Tampere University

MARJAANA KARHU

Utilization of Mineral Side Streams in High Temperature Ceramic Materials

Tampere University Dissertations 327

Tampere University Dissertations 327

MARJAANA KARHU

Utilization of Mineral Side Streams in High Temperature Ceramic Materials

ACADEMIC DISSERTATION
To be presented, with the permission of
the Faculty of Engineering and Natural Sciences
of Tampere University,
for public discussion in the auditorium pieni sali 1
of the Festia building, Korkeakoulunkatu 8, Tampere,
on 4th December 2020, at 12 o'clock.

ACADEMIC DISSERTATION
Tampere University, Faculty of Engineering and Natural Sciences, Finland
VTT Technical Research Centre of Finland Ltd

Responsible supervisor and Custos	Erkki Levänen Tampere University Finland	
Supervisor	Research Professor Elina Huttunen-Saarivirta VTT Technical Research Centre of Finland Ltd Finland	
Pre-examiners	Professor Leena Hupa Åbo Academi University Finland	Associate Professor Yiannis Pontikes KU Leuven Belgium
Opponents	Professor Timo Fabritius University of Oulu Finland	Associate Professor Yiannis Pontikes KU Leuven Belgium

The originality of this thesis has been checked using the Turnitin OriginalityCheck service.

Copyright ©2020 author

Cover design: Roihu Inc.

ISBN 978-952-03-1736-2 (print)
ISBN 978-952-03-1737-9 (pdf)
ISSN 2489-9860 (print)
ISSN 2490-0028 (pdf)
http://urn.fi/URN:ISBN:978-952-03-1737-9

PunaMusta Oy – Yliopistopaino
Vantaa 2020

PREFACE

The work presented in this thesis has been conducted at VTT Technical Research Centre of Finland Ltd. The work was part of research projects CeraTAIL (2015-2019, funded by Academy of Finland), REslag (2015-2019, funded by the European Union's H2020 Programme) and CloseLoop (2015-2019, funded by the Strategic Research Council at the Academy of Finland).

I wish to express my gratitude to my supervisor Prof. Erkki Levänen for all the guidance and fruitful conversations during my thesis project and my instructor, Research Professor Elina Hutunen-Saarivirta for all her instructions and help; you have always time for discussions. I wish also to express my gratitude to the opponents and pre-examiners of the thesis.

I would also like to express my gratitude to all my co-authors for contributing to the publications. I want to acknowledge VTT for giving me tools and support to finalize my PhD. I am especially thankful for my current Research Team Leader Päivi Kivikytö-Reponen to initially pushing me towards PhD studies and my previous Research Team Leader Tomi Lindroos giving me a possibility to work in several project during these years. I would like to express my gratitude to all my co-workers and colleagues at VTT. I am particularly grateful for my colleague Juha Lagerbom for all the help during these years. I also want to thank my co-workers Pertti Lintunen, Hanna-Mari Sinilehto and Kati Salonen for all your support to my work. I thank my colleagues and friends, Jonna Ukonjärvi, Heidi Peltola and Elina Yli-Rantala, for all the conversations to support me in my PhD studies.

Finally, I want to thank my parents to all your support and encouragement during these years and especially to my father for inspiring me to Materials Science. I want to thank my husband Heikki for standing by me in good and bad days, and my greatest inspires my daughter Emma and my son Oliver. I love you.

Tampere

Marjaana Karhu

ABSTRACT

Mineral raw materials are solid chemical compounds used in a wide range of industrial processes and end-uses being fundamental to our modern society. Mineral materials, such as oxides, silicates and carbonates, are present in nature, and many of these compounds are also industrially synthesized. Typically, mineral materials are imported in Europe and transported for long distances, resulting in high greenhouse gas emissions. Additionally, in some cases, suitable primary raw material reserves are dwindling and concentrated in certain countries which causes supply problems and price fluctuations. Simultaneously, European industry produces huge and ever-increasing amounts of mineral materials as side streams, which in many cases end up as waste. Side streams from mining processes present the highest proportion of solid mineral residues produced by industry worldwide, with tens of thousands million tons produced annually. Utilization of mineral side streams as secondary raw materials complements the circular economy by closing the material loops, which enables the replacement of imported feedstock and reduces the environmental impact of processes and products.

In recent years, scattered reports on the utilization of mine tailings have indicated their application in civil engineering purposes and as sources of critical metals. In general, the mining industry side streams are still largely viewed as a waste rather than as a resource. This thesis concentrates on the utilization of mineral side streams as raw materials for structures in less studied application field: high temperature ceramic materials. The main objective of this thesis was to increase understanding of the potential and limiting factors for the utilization of mineral side streams in added value ceramic materials with high thermal resistance. To reach this goal, the study focused on investigating, how the variation in mineral side stream composition due to natural impurities influences the formation of ceramic material microstructure and achieved properties in comparison to pure raw material counterparts. Additionally, it was of interest whether it is possible to tailor the mineral side stream composition by mixing different secondary raw material streams. Ceramic structures based on two typical high temperature compounds,

mullite ($3Al_2O_3 \cdot 2SiO_2$) and magnesium aluminate spinel ($MgAl_2O_4$), were targeted in synthesis experiments.

As a conclusion, it was observed that in the case of side stream based ceramic materials, the achieved properties rather than chemical composition dictated their usability. The properties' characterization proved that utilization of mineral side streams in ceramic materials show properties comparable with and in some cases even better as compared to pure raw material counterparts. For example, magnesite rich mine tailings together with aluminum anodizing process side stream resulted in glass-bonded magnesium aluminate spinel ceramic coatings with electrical insulation capability at the same level compared to pure magnesium aluminate spinel coatings. Additionally, abrasive wear test results revealed considerably lower wear rate for these glass-bonded coatings than for the pure raw material coatings. Thus, formation of amorphous phase compensated the inferior effect of impurities but also limited the maximum operating temperatures. As an overall conclusion, investigated mineral side streams could potentially substitute pure raw materials in ceramic materials taking into account their maximum operating temperatures due to the softening point of the amorphous phase. The properties of mineral side stream based ceramic materials presented in this thesis set a basis for material property databank creation. This kind of databank, including materials composition and volume information about the side streams, can be used as a starting point for the designing new side stream based materials.

TIIVISTELMÄ

Mineraaliset raaka-aineet ovat kiinteitä kemiallisia yhdisteitä, joita käytetään laajasti eri teollisuuden aloilla ja käyttökohteissa. Mineraalisia materiaaleja, esimerkiksi oksideja, silikaatteja ja karbonaatteja, esiintyy luonnossa, mutta niitä voidaan myös valmistaa teollisesti. Tyypillisesti mineraalisia materiaaleja tuodaan Eurooppaan jopa toiselta puolelta maapalloa, jolloin kuljetusten aiheuttamat kasvihuonepäästöt ovat suuret. Lisäksi joidenkin mineraalisten materiaalien kohdalla sopivat primääriset raaka-ainevarannot hupenevat maapallolla ja keskittyvät tiettyihin maihin, mikä aiheuttaa raaka-aineiden saatavuusongelmia sekä hinnanvaihteluita. Samanaikaisesti eurooppalainen teollisuus tuottaa valtavat määrät mineraalista materiaalia sivuvirtana, ja niistä suurin osa päätyy jätteeksi kuormittamaan ympäristöä. Kaivosjätteet muodostavat suurimman osuuden teollisuuden tuottamista jätteistä maailmanlaajuisesti: vuosittain kaivosjätettä syntyy kymmeniä tuhansia miljoonia tonneja. Tämän vuoksi mineraaliset sivuvirrat nähdään yhtenä kiinnostavimpana materiaalivirtana, joka tulisi saada uudelleen kiertoon ja hyötykäyttöön. Tämä mahdollistaisi maahantuotujen mineraalisten materiaalien korvaamisen ja primääristen raaka-ainevarantojen turvaamisen pienentäen samalla prosessien ja tuotteiden ympäristövaikutuksia.

Kaivosjätteiden hyödyntämisen tutkimus on pääasiassa keskittynyt maanrakennussovelluksiin, jossa niiden uudelleenkäyttöarvo on suhteellisen alhainen, mutta kuitenkin vakiintunut. Tästä huolimatta kaivosjätteet mielletään edelleen suurelta osin jätteeksi, eikä niiden arvoa raaka-aineena tunnisteta. Tässä väitöskirjassa tutkimus keskittyi mineraalisten sivuvirtojen hyödyntämiseen korkeamman jalostusasteen sovelluksissa, korkean lämpötilan keraamimateriaalien raaka-aineena. Työn päätavoitteena oli tutkia ja lisätä ymmärrystä mineraalisten sivuvirtojen hyötykäytön mahdollisuuksista sekä rajoitteista tällä uudella ja vähemmän tutkitulla sovellusalueella. Tavoitteen saavuttamiseksi tutkimuksessa keskityttiin siihen, kuinka mineraalisten sivuvirtojen epäpuhtauksia sisältävä koostumus ja rakenne vaikuttavat syntyvien keraamisten materiaalien mikrorakenteeseen sekä sitä kautta saavutettuihin ominaisuuksiin verrattuna vastaaviin primäärisistä raaka-aineista valmistettuihin materiaaleihin. Lisäksi

selvitettiin mahdollisuutta sivuvirtojen koostumuksen räätälöintiin yhdistämällä eri virtoja keskenään. Työssä keskityttiin tavoittelemaan kahta tyypillistä korkean lämpötilan keraamiyhdistettä, mulliittia ($3Al_2O_3 \cdot 2SiO_2$) ja magnesium aluminaatti spinelliä ($MgAl_2O_4$).

Työssä esitettyjen tulosten perusteella tarkastellut mineraaliset sivuvirrat soveltuvat korvaamaan puhtaita raaka-aineita korkean lämpötilan keraamisovelluksissa. Sivuvirtojen tapauksessa niiden hyödynnettävyys perustuu saavutettuihin ominaisuuksiin koostumuksen sijasta. Sivuvirroista valmistetuilla keraamimateriaaleilla saavutetut ominaisuudet olivat suurelta osin vastaavalla tasolla ja joidenkin ominaisuuksien osalta jopa parempia kuin vastaavilla puhtaista raaka-aineista valmistetuilla materiaaleilla. Esimerkiksi yhdistämällä kaivosteollisuuden tuottamaa magnesiittirikasta sivuvirtaa alumiinin anodisointiprosessista syntyvän sivuvirran kanssa valmistettiin lasia sisältäviä keraamipinnoitteita, joiden sähköneristävyys oli samaa luokkaa kuin puhtaista raaka-aineista valmistetuilla pinnoitteilla. Lisäksi sekundääriraaka-ainepohjaisten pinnoitteiden abrasiivinen kulumiskestävyys osoittautui paremmaksi kuin vastaavilla puhtaista raaka-aineista valmistetulla pinnoitteilla. Muodostuvien mikrorakenteiden tutkiminen loi pohjaa saavutettujen ominaisuuserojen ymmärtämiselle. Tässä väitöskirjassa esitetyt sivuvirtapohjaisten keraamimateriaalien ominaisuudet toimivat pohjana tietopankille, jota voidaan jatkotutkimuksissa hyödyntää sivuvirtapohjaisten materiaalien suunnittelussa.

CONTENTS

ABBREVIATIONS

ABS	air cooled blast furnace slag
Al	aluminum
$3Al_2O_3 \cdot 2SiO_2$	mullite
Al_2O_3	aluminum oxide, alumina
$Al(OH)_3$	aluminum trihydroxide, mineral gibbsite
AlO(OH)	aluminum oxide hydroxide
$Al_2(SO_4)_3$	aluminum sulfate
$Al_2Si_2O_5(OH)_4$	kaolinite
Al_2SiO_5	sillimanite
$Al_2O_3SiO_2$	andalusite
APS	atmospheric plasma spraying
AsB	angle selective backscattered electron detector in scanning electron microscope
BOS	basic oxygen furnace slag
B_2O_3	boron oxide
Ca	calcium
CaO	calcium oxide
$CaCO_3$	calcium carbonate, mineral calcite
$CaAl_2Si_2O_8$	anorthite
$(Ca,Na)Al_2Si_2O_8$	andesine
$CaMg(CO_3)_2$	dolomite
$CaMgSiO_4$	monticellite
CCS	cold compressive strength, cold crushing strength
CE	circular economy
Cr_2O_3	chromium oxide
DBS	dielectric breakdown strength
DC	direct current
DIL	dilatometer
DSC	differential scanning calorimetry

EAF	electric arc furnace
EAF C	electric arc furnace slag from carbon steel production
EAF S	electric arc furnace slag from stainless/ alloy steel production
EBSD	electron backscatter diffraction
EDS	energy-dispersive spectrometry
Fe	iron
$FeCO_3$	siderite
FeCr	ferrochrome
FeO	iron(II) oxide, wüstite
Fe_2O_3	iron(III) oxide, hematite
FMT1	felsic mine tailings from molybdenum ore mine
FMT2	felsic mine tailings from gold ore mine
FMT3	felsic mine tailings from quartz ore mine
FESEM	field emission scanning electron microscopy
FIBSEM	focused ion beam scanning electron microscopy
GBS	granulated blast furnace slag
HCFeCr	high-carbon ferrochrome
H_2SO_4	sulfuric acid
$KAlSi_3O_8$	potassium feldspar, K-feldspar
K_2O	potassium oxide
$K(Mg,Fe)_3(Al,Fe)Si_3O_{10}(OH,F)_2$	biotite
LFA	laser flash analysis
Mg	magnesium
$MgAl_2O_4$	magnesium aluminate spinel
MgO	magnesium oxide, magnesia
$MgCO_3$	magnesium carbonate, magnesite
Mg_2SiO4	forsterite
$Mg_3Si_4O_{10}(OH)_2$	talc
$(Mg,Fe)_3(Si, Al)_4O_{10}$	chlorite
$(Mg,Fe)_2Al_4Si_5O_{18}$	cordierite
MgMT1	magnesite rich mine tailings from talc ore
Na	sodium
$NaAlSi_3O_8$	albite
Na_2O	sodium oxide

NaOH	sodium hydroxide
PEG	polyethylene glycol
RH	relative humidity
S	sulphur
SE	secondary electron detector in scanning electron microscope
SEM	scanning electron microscopy
SiO_2	silicon oxide, silica, quartz
SMS	secondary metallurgical slag
TGA	thermogravimetric analysis
TG	thermogravimetry
ZrO_2	zirconium oxide
XRF	X-ray fluorescence spectrometry
XRD	X-ray diffractometry
QMS	qualitative mass spectrometer

ORIGINAL PUBLICATIONS

Publication I Karhu, Marjaana; Lagerbom, Juha; Kivikytö-Reponen, Päivi; Ismailov, Arnold; Levänen, Erkki. Reaction Heat Utilization in Aluminosilicate-Based Ceramics Synthesis and Sintering. Journal of Ceramic Science and Technology 08 (01) (2017) 101-112, DOI: 10.4416/JCST2016-00094

Publication II Karhu, Marjaana; Lagerbom, Juha; Solismaa, Soili; Honkanen, Mari; Ismailov, Arnold; Räisänen, Marja-Liisa; Huttunen-Saarivirta, Elina; Levänen, Erkki; Kivikytö-Reponen, Päivi. Mining tailings as raw materials for reaction-sintered aluminosilicate ceramics: Effect of mineralogical composition on microstructure and properties. Ceramics International 45 (2019) 4840–4848, DOI: 10.1016/j.ceramint.2018.11.180

PublicationIII Karhu, Marjaana; Lagerbom, Juha; Solismaa, Soili; Huttunen-Saarivirta, Elina. Magnesite-rich mining tailings as a raw material for refractory ceramics – microstructural and thermal analysis. Proceedings of the Estonian Academy of Sciences 68 (2) (2019) 145–149, DOI: 10.3176/proc.2019.2.05.

Publication IV Karhu, Marjaana; Lagerbom, Juha; Honkanen, Mari; Huttunen-Saarivirta, Elina; Kiilakoski, Jarkko; Vuoristo, Petri; Solismaa, Soili; Kivikytö-Reponen, Päivi. Mining tailings as a raw material for glass-bonded thermally sprayed ceramic coatings: microstructure and properties. Journal of the European Ceramic Society 40 (2020) 4111-4121, DOI: 10.1016/j.jeurceramsoc.2020.04.038.

Publication V Karhu, Marjaana; Talling, Bob; Piotrowska, Patrycja; Matas Adams, Alba; Sengottuvelan, Abirami; Huttunen-Saarivirta, Elina; Boccaccini, Aldo R.; Lintunen, Pertti. Ferrochrome slag feasibility as a raw material in refractories: evaluation of thermophysical and high temperature mechanical properties. Waste and Biomass Valorization (2020), DOI: 10.1007/s12649-020-01092-4.

AUTHOR'S CONTRIBUTION

Marjaana Karhu is the main author of all the five **Publications (I-V)**. She planned, organized and analyzed the results presented in each publication, and prepared the manuscripts. She was the main responsible person for recipe formulation presented in publications and she conducted all thermal analyses as well as X-ray diffraction measurements and analyses.

Professor Erkki Levänen, Docent Elina Huttunen-Saarivirta, Lic. Sc. (Tech). Juha Lagerbom and Dr. Päivi Kivikytö-Reponen gave advice and commented the manuscripts. Juha Lagerbom also provided guidance and helped for planning and organizing the research work.

Dr. Mari Honkanen conducted electron microscopy studies in **Publications II, III, IV and V.** M.Sc. Soili Solismaa was responsible for the interpretation of mineralogical and chemical analyses in **Publications II, III and IV**. Additionally, in **Publication II**, Dr. Marja-Liisa Räisänen give guidance on behaviour of different minerals. M.Sc. Arnold Ismailov conducted the dilatometric measurements in **Publications I and II**. In **Publication IV**, M.Sc. Jarkko Kiilakoski and Professor Petri Vuoristo gave advice about thermal spray tests, which were performed in co-operation with Thermal Spray Center Finland. In **Publication V**, the selection of raw materials and recipe formulation was made in close collaboration with Mr. Bob Talling and Dr. Patrycja Piotrowska from Renotech Oy. Patrycja Piotrowska conducted also the cold crushing strength measurements. Dr. Alba Matas Adams conducted all high temperature mechanical testing and M.Sc. Abirami Sengottuvelan was responsible for thermophysical testing with assistance of Professor Aldo R. Boccaccini. Lic. Sc. (Tech) Pertti Lintunen gave advice and commented the manuscript. All manuscripts were commented by all the co-authors.

1 INTRODUCTION

Mineral raw materials are solid chemical compounds used in wide range of industrial processes and end-uses being fundamental to our modern society. Mineral materials, such as oxides, silicates and carbonates, are present in nature, and many of these compounds are also industrially synthesized. Mineral raw materials are usually grouped into industrial minerals, metallic minerals and construction minerals based on their different characteristics and their intended use [1]. Industrial minerals are defined as minerals mined or processed, either from natural sources or synthetically processed, for the value of their non-metallurgical properties [2]. Metallic minerals, on the other hand, yield metals or metallic substances. Construction minerals are defined as minerals used by the construction such as aggregates [1].

Earth's crust contains abundantly different kind of minerals raw materials resources and reserves. However, they are geographically unevenly distributed and economic issues constraint the exploitation of small and lower-grade deposits. In most cases, mineral materials are imported in Europe and transported for long distances resulting in high greenhouse gas emissions [3]. For example, for bauxite the largest producers are Australia (29%), China (18%), Brazil (13%) and Indonesia (12%). Within the EU, bauxite is mined in Greece (0.8% of global total), Hungary, France and Croatia (< 0.1% each). Europe is then highly dependent on the import of bauxite [4]. Bauxite is mainly used for aluminum production but it is also an important mineral for refractory ceramic and cement production [4]. Additionally, certain mineral raw materials are considered as "critical raw materials" because they are economically important and have a high risk with their supply. One example of critical raw material is magnesium (Mg). The supply of Mg for the EU industry entirely relies on imports from China and there is no extraction of magnesium nor processing of pure magnesium in the EU [5]. Magnesite ($MgCO_3$) mineral can be used to produce magnesium metal and magnesia/magnesium oxide (MgO) which is an important raw material for ceramic industry. China dominates also the global magnesite supply (64%) and EU represents about 12% of the global magnesite extraction. In EU, all magnesite is used for magnesia processing. [4, 5].

At the same time, European industry produces huge and increasing amounts of mineral side streams that end up as waste status or landfill. [6] Residue generated from mining industry presents the highest proportion of solid residue produced by industry, with approximately world annual production of 20 000–25 000 Mt [6]. In Finland, the mining sector produces ca 35–40 Mt of mine tailings as residue each year [7]. Another example is steel industry: globally 1.6 Gt of steel was produced creating 250 Mt of slag as residue (2014) [8]. Additionally, in most cases the amount of slag is higher than the actual product. For example, ferrochrome (FeCr) slag, the residue generated from stainless steel production, amounted 1.1-1.6 t / t FeCr depending on feed materials [9].

In order to decrease environmental impacts, inefficient use of natural resources and dependency on resources from outside of Europe, there exists increasing pressure to move from linear to circular economy in EU [10][11][12]. The main idea in circular economy ideology is that the value of materials and products is kept as high as possible for as long as possible helping to minimize the need for the input of new raw material and energy together with minimization of waste generation (Figure 1) [10][11]. The benefits of 'the inner circle' approaches (reuse, repair, redistribution, refurbishment and remanufacturing) are higher than for 'the outer circle' (recycling, energy recovery), because of the losses during collection and processing [10].

As a concrete action towards a more circular economy, the European Commission published its Circular Economy Action Plan in 2015 identifying supporting actions for circular economy [13]. That action plan has been just recently updated, on March 2020 [14]. The action plan includes the mix of voluntary initiatives and regulatory actions, being a concrete operational plan to 'closing the loop' of product life cycles by resource-efficient raw materials management, reuse of components and recycling of waste or by-products into secondary raw materials, bringing benefits for both the environment and the economy. However, regardless of the initiatives and pressures towards circular economy, the Platform for Accelerating the Circular Economy (PACE) has just recently, in 2019, published The Circularity Gap Report [15] telling that our global economy is currently only 9% circular. From the total material inputs of 92.8 Gt only 8.4 Gt of materials are coming from cycled resources and rests are coming from primarily extracted resources. Mineral materials cover 41% of all global resource inputs. Thus, there is a high motivation towards greater circularity and due to the huge volumes, 'closing the loop' of mineral raw materials will have a huge impact.

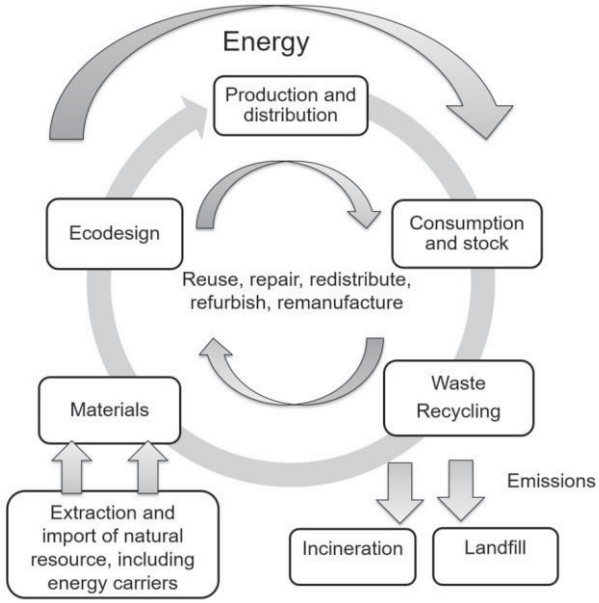

Figure 1. Conceptual principle of circular economy for materials and energy, figure adapted from [10]

In recent years, the utilization of mineral side streams has mainly concentrated on civil engineering purposes in high-volume solutions. Mineral side streams generated from ore processing in mining industry, are typically utilized for civil engineering purposes at the mining site [16]. For steel slags, the situation is better and they are mainly utilized for cement production or concrete addition or as aggregate in road construction in some cases [17]. However, the utilization rate depends highly on slag type. The utilization of mineral side streams as raw materials for higher value solutions for specialized ceramic industry, more specifically, for high temperature ceramic applications, has received far less attention in research community so far.

This thesis is a compilation dissertation based on five scientific publications in the area of the utilization of secondary raw materials, mineral side streams, in high temperature stable ceramic compounds for added value, which enables the replacement of imported feedstock and reduces the environmental impact of processes and products. Ceramic structures based on two typical high temperature compounds, mullite ($3Al_2O_3{\cdot}2SiO_2$) and magnesium aluminate spinel ($MgAl_2O_4$), were targeted in synthesis experiments. In mineral side streams selection, the criteria was to concentrate on such compositions that hold potential to be used as

raw materials in thermally stable ceramic compounds. The first part of this dissertation (Chapter 2) comprises a short theoretic background of the investigated mineral side stream materials, their volumes and properties and state of the art of their current utilization. The second part (Chapter 3) concentrated to ceramic compositions aimed for as high temperature ceramic materials, mullite and magnesium aluminate spinel, their typical raw materials, processing methods, properties and effect of impurities on their properties. The aim and scheme of this thesis, including the research questions stated, are presented in Chapter 4. The experimental procedures to characterize the mineral side streams, their processing to ceramic materials, formed microstructures and properties evaluation are presented in Chapter 5. The most important results obtained are collected from the publications and presented and discussed in Chapter 6. Finally, the concluding remarks are stated in Chapter 7.

2 SECONDARY RAW MATERIALS (RESIDUES)

Generally, waste streams can be divided into two main categories: material streams (for example metals, glass, plastics, textiles, etc.) and product streams (for example electronic waste, end-of-life vehicles, construction and demolition waste, etc.)[18]. The Waste Framework Directive for the EU 2008/98/EC [19] sets the basics for waste management and the recycling targets. In 2013, the 7th Environment Action Programme [20] set the following priority objectives for waste policy in the EU, simultaneously forming targets for circular economy adaptation too:

- To reduce the amount of waste generated;
- To maximize recycling and re-use;
- To limit incineration to non-recyclable materials;
- To phase out landfilling of non-recyclable and non-recoverable waste;
- To ensure full implementation of the waste policy targets in all Member States.

The waste hierarchy establishes a priority order in waste management starting from prevention, reuse, recycling and ending to energy recovery [13]. Landfilling is considered as the least preferred option being divided into three categories: landfills for hazardous waste, landfills for non-hazardous waste, and landfills for inert waste [21]. Thus, waste management is setting the basis for circular economy adaption by determining how successfully the waste hierarchy is put into practice. In circular economy, reusable and recyclable materials are returning back into the economy as "secondary raw materials" to be used in manufacturing processes substituting virgin, primary raw materials [13][22]. Through industrial symbiosis, waste or by-products of one industry stakeholder or sector can become inputs for another industrial operator [13]. In ideal case, secondary raw materials, i.e., residues must be traded and shipped in equal ways to primary raw materials [22].

The use of secondary raw materials shows a number of advantages, including increased security of supply, reduced material and energy use, reduced impacts on the climate and the environment, and reduced manufacturing costs [22]. However, the use of secondary raw materials faces also a number of challenges. One of the main challenges to the use of secondary raw materials is uncertainty about their quality and the lack of EU-wide standards. Uncertainty about the quality of secondary raw materials can relate to variation in their composition (chemical or mineralogical) as compared to primary raw materials with constant composition. Additionally, there can exist variation also in residue stream itself when accumulating and stored as heaps, i.e., between the surface and the interior. The quality uncertainty can also relate to residues non-desirable physical state, e.g. in slurry state or big lumps, which implies post-processing. Another issue in the use of secondary raw materials is the potential presence of undesirable elements or harmful species in material streams [13] [22]. For this reason, a lot of effort is put to improve the tracking of chemicals in products and to boost non-toxic material cycles [22]. Additionally, in order to provide secondary raw material operators more certainty, more harmonized rules to determine secondary raw material classification as either waste, product or by-product need to be established [13]. For example, the legal status of ferrous slags has been discussed worldwide for more than 25 years. In 2012, EUROSLAG published a Position Paper [17] on the status of ferrous slags. The main outcome was that ferrous slag could be grouped into two categories: as a by-product already in the liquid state, directly after its manufacture, with or without processing steps, or it is first considered as waste, but turns to a product/secondary raw material after the specific recovery measures.

In this study, three types of mineral material side streams generated by industry were investigated: mine tailings generated by mineral processing at mining sites, ferrous slag generated by steel making processes in metallurgical industry and aluminum anodizing process side streams generated by aluminum profile manufacturing industry.

2.1 Mine tailings

Mining is defined as the extraction of material from the ground in order to recover one or more component of the mined material [6]. Mineral processing or beneficiation refer to actions to physically separate and concentrate the ore

minerals [6]. Metallurgical extraction covers actions, which aims to destroy the crystallographic bonds in the ore mineral in order to recover the targeted elements or compounds [6]. At mining sites, mining is always associated with some mineral processing, e.g., crushing, grinding, separation by different means (gravity, magnetic or electrostatic forces) and flotation. Sometimes it is also accompanied by metallurgical extraction of elements already at the mining site. All three mining industry operations: mining, mineral processing and metallurgical extraction produce residues. Residues generated from the mining industry could be defined as solid, liquid and gaseous by-products of mining, mineral processing, and metallurgical extraction [6]. From the viewpoint of circular economy, they can be classified as residues from solid mining, residues from processing and metallurgical extraction and residues from mine waters. Schematic presentation of product and residues streams at a metal mine are presented in Figure 2. Mining residues should be carefully managed and stored, often accumulating as heaps and bonds at mining sites [6].

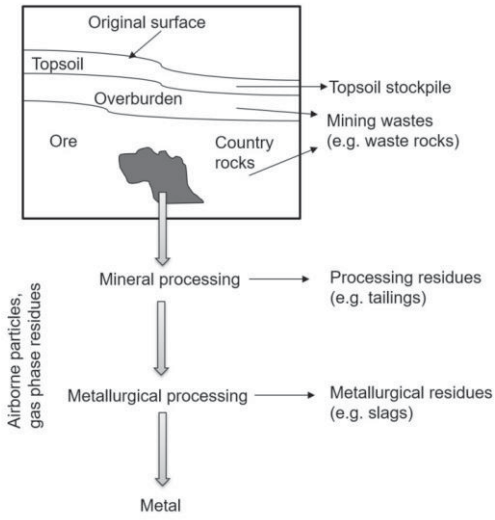

Figure 2. Schematic presentation of the product and residue streams at a metal mine, adapted from [6]

Mineral processing of metal ores as well as industrial mineral deposits involves size reduction and separation of the individual minerals. In mineral processing, the blocks of rock ore which could be up to a meter in diameter scale are made

smaller, down to a few millimeters or microns in diameter, first by crushing and then by grinding and milling [6]. The aim in size reduction is to break down the ore so that the targeted ore minerals are liberated from residue phases. Consequently, the products generated by ore or industrial mineral processing are a concentrate and a residue, known as mine tailings [6]. The tailings consist of the fine-grained residue, typically between 1-600 μm in diameter, from which most of the valuable minerals have been removed. What is retained in the mine tailings is the minerals, such as silicates, oxides, hydroxides, carbonates, and sulphides [6][23]. Most of the mined material ends up as mine tailings and the extracted elements represent only a small fraction of the whole ore mass. Indeed, mine tailings represent the most voluminous industrial residue produced annually worldwide approximately 20 000–25 000 Mt [6]. Such amounts of tailings occupy large areas of land and cause costly construction and maintenance activities as well as increased environmental load [16][24]. Mine tailings may also contain hazardous substances, such as heavy metals, acids and residues of process chemicals, therefore they require monitoring, treatment, and secure disposal [6]. However, many mine tailings do not contain or release contaminants, and are called as inert mine tailings.

The increasing volume of inert mine tailings has encouraged research into their utilization potential. There is great diversity of applied mining and mineral processing methods and additionally there exist compositional differences in the mined ore. For these reasons, every mine produces its own unique residues [6][23]. Thus, the utilization of mine tailings is dependent on their chemical and mineralogical characteristics, particle size and physical form (dry, slurry) [6].

Reuse of mine tailings may be defined as the new use of the mine tailings as such, in its original form, without any reprocessing. Typically, in this case, mine tailings are used a civil engineering purposes at the mining site [16]. Recycling, on the other hand, makes use of the included raw materials, that is, uses the mine tailings as feedstock and converts it into a new valuable material, product or application with reprocessing. During reprocessing, the material is used for producing new valuable products such as recovered minerals and metals [6][23][25]. Several publications may be found about the reprocessing of mine tailings into bricks for construction and building industry based on the geopolymerization technology, e.g. [26][27][28][29][30], and into glass-ceramics and glass- and rock-wool fibre in [31]. Additionally, metal recovery from tailings has attracted research effort, e.g., in [32][33][34][35][36]. However, still most mines around the world use conventional tailings disposal approach, storing them into tailing dams in impoundments [16] or in a slurry form [23].

2.2 Ferrous slag

Major part of metallurgical side streams are different kind of slags. Ferrous slag is generated as a side stream of iron and steel making processes in metallurgical industry. Depending on the production process, different types of slags are formed. Overall, the following types of slag families can be identified [17]:

- -blast furnace slag, either as granulated blast furnace slag (GBS) or air-cooled blast furnace slag (ABS)
- -basic oxygen furnace slag or converter slag (BOS)
- -electric arc furnace slag from carbon steel production (EAF C) or electric arc furnace slag from stainless/ alloy steel production (EAF S)
- -secondary metallurgical slag (SMS)

Usually, granulated blast furnace slag and air-cooled blast furnace slag are summarized as "blast furnace slag" or "ferrous metallurgy slag" because they are manufactured during the production of iron. Basic oxygen furnace slag, converter slag, electric arc furnace slag and secondary metallurgical slag are summarized as "steel slags" or "steel making slags". Steel slags are formed in steelmaking processes: converter slag is formed during the conversion of liquid iron into steel, electric arc furnace slags from melting (steel scrap, reduced iron) in an electric arc furnace. The chemical composition of ferrous slag varies from source to source but primarily they consist of calcium oxide (CaO), magnesium oxide (MgO), silicon oxide (SiO_2), and iron oxide (FeO) [37][38].

Globally 1.6 Gt of steel was produced creating 250 Mt of slag as residue (2014) [8]. About 24.6 Mt of blast furnace slag was generated in Europe (2016) [39]. Most European countries have the utilization rate for blast furnace slag about 100% [17][39]. About 80% of the generated blast furnace slag is used as a component in cement production or as concrete addition and the rest is used as aggregate in road construction [39]. About 18.4 Mt of steel making slag was generated in Europe (2016) from which about 57% was basic oxygen furnace slag , 25% was electric arc furnace slag from carbon steel production (EAF C) and 7% was electric arc furnace slag from stainless/ alloy steel production (EAF S) [39]. 14.2 Mt of the produced steel slag was utilized, about 46% as aggregates for road construction [39]. Still about 14 % of steel slag goes for landfill as final deposit [17]. Ferrochrome slag is one example of electric arc furnace slag from stainless steel production. High-carbon ferrochrome (HCFeCr) is the most common alloying

material used for stainless steel production. Overall, 1.1-1.6 t ferrochrome slag was formed per each FeCr t, depending on feed materials [9].

Numerous studies are available about FeCr slag utilization in road and civil construction purposes, like as coarse aggregate in concrete applications and pavement layers, e.g., [40][41][42][43][44], and as partial substitution of fine aggregate sand in concrete, e.g., [45][46]. New possibilities for FeCr slag utilization are continuously searched for, especially for fine aggregates. For example in concrete, aggregates makes 70% of its volume being the principal component material in concrete production. Typically, the aggregate could be classified as coarse aggregate with 4.75 mm particle size or more and fine aggregate with 4.75 mm particle size or less [46].

2.3 Aluminum anodizing process side stream

Aluminum anodizing is an electrochemical process in which an oxide film is formed on the aluminum alloy to provide hardness and corrosion resistance. The anodizing process is composed of several pre- and post-treatment steps: rinsing, etching, desmutting, anodizing, possible coloring, and sealing [47]. Acid and basic bath streams are generated from the cleaning steps following the anodizing process. These bath streams contain mainly sulfuric acid (H_2SO_4), sodium hydroxide (NaOH), and aluminum (Al). Typically, these acid and basic residue streams are mixed as a neutralization step, where a solid phase is precipitated. The solid precipitate, a side stream from anodizing process, is predominantly composed of aluminum hydroxide ($Al(OH)_3$) possibly accompanied by a small amount of aluminum sulfate ($Al_2(SO_4)_3$) in water (up to 85wt.%). Regardless of the origin, Al, sulphur (S), and sodium (Na) or calcium (Ca) are the main chemical elements in solid side stream from aluminum anodizing process.[48]

Aluminum hydroxide-based side stream from aluminum anodizing process is usually disposed in landfills [48]. In the recent work of Souza et al. (2019) [48], the potential applications of Al anodizing residues were reviewed. Alumina (Al_2O_3) is an important raw material used in a wide range of industrial segments, because of its advantageous properties, such as inertness, hardness, temperature resistance, and electrical resistance. For that reason, many works have explored the possibility of obtaining alumina from anodizing process side stream by using a calcination step. Another approach to utilize anodizing process residue is by exploring the uses

of its main compound, aluminum hydroxide, as such. It was suggested by of Souza et al. (2019) [48] that one opportunity of utilization is thermal dehydration at the temperatures below 800°C to produce an activated alumina, which can then be used as a drying agent, adsorbent, catalyst, and catalysts carrier. Several studies of aluminum rich residues similar to aluminum anodizing side streams have examined the material to be utilized in wastewater treatments as coagulants and adsorbents, like in municipal wastewater treatment [49] and phosphorus adsorption [50][51]. Another potential application reported for aluminum anodizing process side streams is the production of hydraulic binders and chemically bonded ceramics [48]. Aluminum anodizing side streams together with other residues have also been reported in the production of hydraulic binders [52] and for geopolymer synthesis [53][54]. There exist also studies [55][56][57] about utilization of aluminum anodizing residues in refractory ceramics based on cordierite ($(Mg, Fe)_2Al_4Si_5O_{18}$) and mullite phases revealing that aluminum anodizing side stream material is potential feedstock material when compared with commercial primary raw materials.

3 CERAMICS

Ceramics are inorganic non-metallic materials typically characterized by their high strength, texture, longevity, chemical inertness and electrical resistance. Their most distinguishing feature is that they generally can withstand very high temperatures. Ceramics are a very diverse group of products and ceramics sector could be divided as sub-sectors e.g. to tableware and ornamentalware, sanitaryware, technical ceramics, vitreous clay pipes, expanded clay products, refractory products, wall and floor tiles and bricks and roof tiles [58]. The EU ceramics industry accounts for 27.8 billion euros in production value [59]. Dependency on imported raw materials concerns the especially the refractories sub-sector, where certain non-EU countries correspond to 90% of the raw materials production resulting in high greenhouse gas emissions from transport [59]. The European refractory industry produces 5.5 Mt of refractory ceramics annually, with the value of 3.6 billion euros [60].

Refractory ceramics are ceramic materials that withstand a variety of harsh conditions, including high temperatures, corrosive liquids and gases, abrasive wear as well as mechanical and thermal stresses [61]. They are necessary to all high-temperature processes in the production of metals, cement, glass and ceramics as lining materials for furnaces, kilns, incinerators and reactors. Refractories are mostly (70%) used in basic metal industries [58]. There exist several methods to classify refractory materials, for example, based on their chemical composition (acid, basic), method of implementation (shaped, unshaped/monolithic), and porosity level (porous, dense) [62]. Refractory materials are mainly based on six oxides: SiO_2, Al_2O_3, MgO, CaO, chromium oxide (Cr_2O_3), zirconium oxide (ZrO_2) and some of their combined minerals [63].

A huge variety of refractory materials exists, designed and manufactured to meet the temperature and process requirements of each application. In some applications, resistance to corrosion and abrasion may be the most important selection criteria, while in other cases the melting temperature and thermal conductivity are the key properties for a refractory material. The high strength of a refractory material is generally an indication of materials suitability for use in construction applications. Low thermal conductivity is particularly important for

insulating refractories, where thermal gradients between hot and cold surfaces dictate the use of a refractory material. In applications where solid particle impacts are common, such as fluidized-bed systems, erosion resistance is one of the most important characteristics of refractories. Prior to refractory materials use in the application, the most important properties (physical, thermal, chemical) need to be defined at room temperature and at operation temperature, to validate their suitability. The high-temperature performance of refractory materials, is directly related to the texture and richness of mineral refractories, such as magnesium minerals. The major properties of the refractory materials are closely connected to their mineralogical composition and, therefore, the different phases formed need to be identified and microstructures evaluated. [62][64]

Bauxite and magnesite present examples of imported mineral raw materials for industrially synthesized mullite and magnesium aluminate spinel refractory ceramics [3]. Bauxite is a heterogeneous material composed primarily of aluminum minerals with varying quantities of iron oxides and its supply is dominated by Australia, China and Brazil [4]. Magnesite, the mineral magnesium carbonate is mainly used for magnesium oxide or magnesia processing. On average between 2010 and 2014, net imports of magnesia were of 540 000 tons and China is the main country supplying magnesia [5]. Additionally, within the last years, there has been a significant increase in raw material prices, thus for refractory industry, the need to secure the availability of raw materials at competitive prices has created a strong incentive for the alternatives to substitute imported primary raw materials [60] [63].

3.1 Mullite

Mullite is the only stable intermediate phase in the Al_2O_3–SiO_2 system (Figure 3) at atmospheric pressure [65][66][67]. The high thermal stability of mullite makes it a superior ceramic material in high-temperature refractory applications and mullite based refractories represent one of the main groups of acid refractories [65][68]. The wide technical applicability of mullite ceramics results from their excellent properties, such as high thermal stability and good thermal insulation capability, low density and thermal expansion [69].

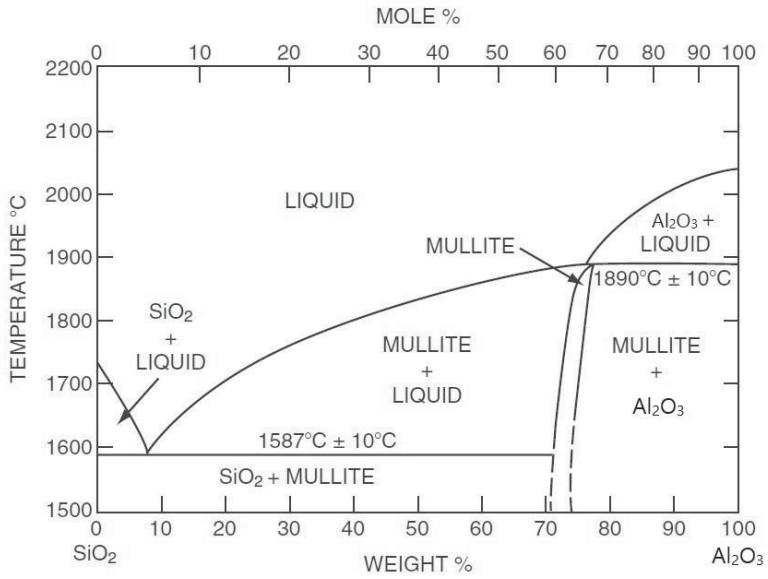

Figure 3. Phase diagram of the system Al_2O_3-SiO_2, adapted from [65]

Different processing routes for mullite refractory ceramics have been suggested in literature [62]: °C

- Mullite processing from clays when mullite is obtained by reaction between alumina and silica. Kaolinite ($Al_2Si_2O_5(OH)_4$), is commonly used clay mineral for mullite synthesis [70][71].

- Mullite processing from bauxite and sillimanite (Al_2SiO_5) containing minerals.

- Advanced processing routes, e.g. sol-gel, precipitation and hydrolysis.

Starting raw materials, environmental conditions and the applied synthesis and production routes significantly influence the mullite formation, development of the mullite crystals and achieved properties [69]. Mullite crystals, which are grown from melt, are typically acicular or columnar. The dimensions of mullite grains produced by reaction sintering typically range between 1 μm and 100 μm, with the crystal morphologies between acicular and equiaxed. Aluminosilicate refractories performance can be significantly affected by impurities, mainly alkalis and iron. The high temperature behavior of a refractory material is strongly dependent on the mineralogical composition and in particular, the amount and the nature of the

amorphous phase which influences the properties. The presence of impurities contributes to the formation of an amorphous phase and the viscosity of this amorphous phase is decreased by the presence of impurities, particularly alkalis, such as potassium oxide (K_2O) and sodium oxide (Na_2O), and is thus responsible for lowering the softening point of the material. [68]

Recently, also some industrial residues rich in alumina are shown to be useful raw materials in the processing of mullite. Choo et al. (2019) [72] presented a review article about the preparation of mullite ceramics utilizing industrial residues, including aluminum anodizing process residues [73][74][75] and coal fly ash from coal combustion process [76][77], as starting materials. When aluminum anodizing process residue was combined with common commercial ceramic raw materials, such as kaolinite [73] [74], the best performing compositions had properties that indicated potential for aluminum anodizing process residue use as a component of low grade refractory and/or electrical insulating bodies [73]. However, the impurities prevented their use at high temperatures [74]. When aluminum anodizing process residue was combined with waste glass, mullite-based glass ceramics were produced [75]. During sintering of the mixture consisting of natural bauxite and fly ash, the bauxite-derived alumina dissolved into liquid glass phase. Glass phase was formed from the melted fly ash due to different metal oxide impurities [77]. Bouchetou et al. (2005) [78] studied mullite growth from fired andalusite ($Al_2O_3SiO_2$) grains during heating, where andalusite was converted into mullite and silica-rich glass phase. The presence of impurities, iron and alkalis, in andalusite increased the amount of the liquid phase. Bouchetou et al. (2005) concluded that the presence of a liquid phase influences the behavior of fired andalusite grains under thermal shocks. During the mullitization, the liquid phase heals initial cracks of the andalusite grains when the mullite-glass composite stays uncracked. Thus, the formation of this specific microstructure leads to an excellent thermal shock resistance in comparison with monocrystalline mullite.

3.2 Magnesium aluminate spinel

Magnesium aluminate spinel is another excellent refractory oxide having good physical, chemical, and thermal properties: a high melting point (2135°C), resistance against chemical attack and very good thermal characteristics both at ambient and elevated temperatures, thus it is used typically in refractory ceramic

applications [79] [80]. Due to their particular combination of resistance to steel-making slag corrosion, thermal shock resistance and excellent hot strength magnesium aluminate spinel ceramics are typically used in steel-making as lining materials for furnaces [81]. Additionally, $MgAl_2O_4$ has a wide range of applications in structural, chemical, optical and electrical industries [82]. $MgAl_2O_4$ is the only compound in the binary system MgO-Al_2O_3 (Figure 4). A stoichiometric spinel presents a molar ration of 1 MgO to 1 Al_2O_3 [83].

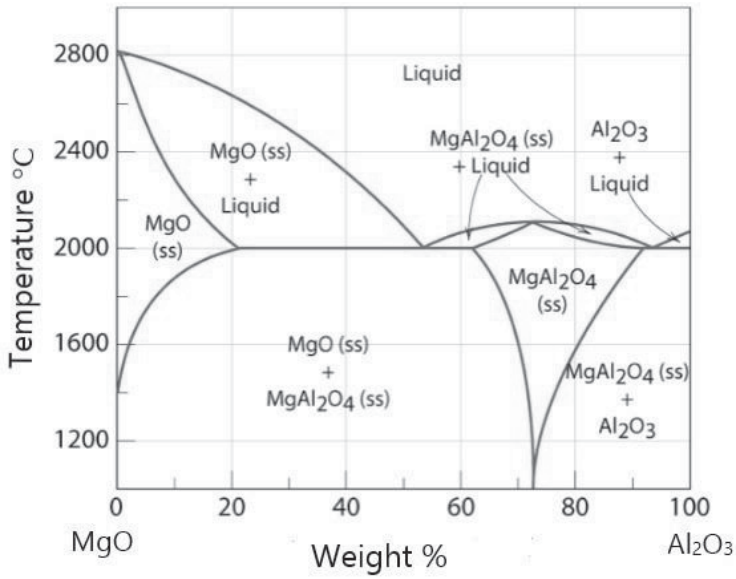

Figure 4. Phase diagram of the system MgO-Al_2O_3, adapted from [83]

The most popular method in the commercial production of $MgAl_2O_4$ is the conventional solid state reaction of Mg- and Al-bearing precursors, such as oxides, hydroxides and carbonates [82]. During synthesis, solid-state reactions between the grains of starting materials happen, being highly dependent on the size of the used powders [72]. The two main routes for refractory $MgAl_2O_4$ production are sintering and fusion. For sintered spinel, synthesis occurs in a shaft kiln, whereas for fused spinel it takes place in an electric arc furnace. Very fine and reactive raw materials are needed for spinel synthesis due to the solid state reactions which are kinetically difficult.[81][83]

The impurities commonly detected in refractory $MgAl_2O_4$ raw materials, such as dead-burnt magnesia, are SiO_2, CaO, FeO, Al_2O_3 and boron oxide (B_2O_3). These

impurities could react with MgO or each other, leading to the formation of new phases, for example Ca-Mg-silicate phases. High SiO_2 amount could lead to monticellite ($CaMgSiO_4$) and forsterite (Mg_2SiO_4) formation. When the SiO_2 content increases, the initial melting temperature of MgO particles decreases. Generally, certain mineralizers could be employed for $MgAl_2O_4$ synthesis to accelerate the phase formation and densification. One type of mineralizers lowers the spinel formation temperature, while the other type reduces the sintering temperature. However, mineralizers certainly restrict $MgAl_2O_4$ applications to lower temperatures. [82][83][84]

Most refractory grade $MgAl_2O_4$ are made of a combination of high-purity synthetic aluminum oxide and chemical-grade magnesium oxide. Some publications have reported the synthesis of $MgAl_2O_4$ utilizing residue streams concentrating on aluminum dross use, e.g. [85] and [86]. In [87] magnesia-alumina spinel-corundum composite was prepared from residue slide plate and residue magnesia carbon brick and in [88] using chromium slag as a component in synthetic $MgAl_2O_4$ spinel material.

3.2.1 Thermally sprayed magnesium aluminate spinel coatings

One application for magnesium aluminate spinel is in ceramic coatings. Thermally sprayed $MgAl_2O_4$ coatings are used in harsh high-temperature environments and electrical insulation applications, where insulating materials with poorer thermal stability, such as polymers, cannot be used [89][90].

Thermal spraying is defined as the group of coating processes to apply metallic or non-metallic coatings, where thermal energy is generated by chemical (combustion) or electrical (plasma or arc) methods to melt and accelerate fine dispersions of particles or droplets to high speeds (50-1000 m/s). Processes are grouped into flame spray, electric arc spray and plasma arc spray depending on energy sources to be used heating the coating material. The heated particles are accelerated toward substrate by process gases or atomization jets. The achieved high particle temperatures and speeds result in significant droplet deformation on impact at a surface, producing thin layers or lamellae that are called as "splats," which conform and adhere to the substrate surface (Figure 5). Individual splats are generally thin, approximately from 1 to 20 μm, and each metal droplet cools at a

very high rate >10^6 K/s to form uniform, fine-grained, polycrystalline coating. [91][92]

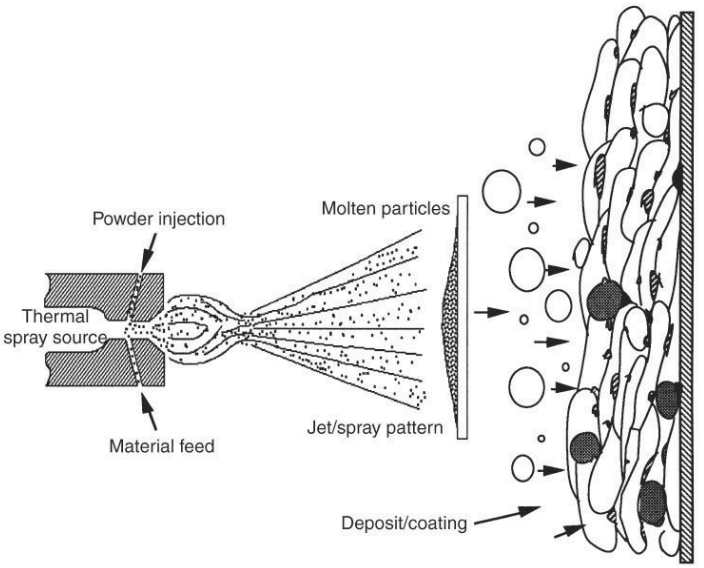

Figure 5. Thermal spray process, adapted from [91]

Ceramics are particularly suited to thermal spraying with atmospheric plasma spraying (APS). In a plasma spray gun, a direct current (DC) power is used for the generation of plasma. Energy is transferred into plasma-forming gases until the energy level is sufficient to ionize the gas. The ionized gas returns to atoms/molecules by recombining when a high amount of energy is released. The gas expands forming an extremely hot and high-velocity gas jet. The powder is injected radially to the plasma jet where the particles of the powder melt and are accelerated. The coating is formed when the melted and accelerated powder particles impact into the substrate surface. [92][93]

The materials used as feed materials in thermal spraying are powders, rods or wires. The powders are injected into a jet or a flame as a suspension in a carrier gas or in a liquid. The industrial methods of powder manufacturing depend mainly on the types of materials used. One of the most versatile powder preparation method is spray drying, also suitable to $MgAl_2O_4$ powder preparation. Organic binder holds together any kind of small material particulates, forming spherical agglomerates. First, a slurry containing finely dispersed precursors, organic binder and water is feed to spray drier. The pump feeds the slurry into an atomizer and the atomized

slurry is then dried in the stream of gas, as the moisture contained in droplets evaporates during flight in the chamber. The gas is then cleaned out in the cyclone and recycled back to the heater, while the solid agglomerated particles can be collected in the powder collector.[92]

4 THE AIM AND SCHEME OF THE THESIS

This thesis concentrates on the utilization of mineral side streams as raw materials for structures in less studied application field: high temperature ceramic materials. In mineral side streams selection, the criteria were to concentrate on such compositions that hold potential to be used as raw materials in thermally stable ceramic compounds. Typically, industrially manufactured pure mineral raw materials for ceramic materials are either enriched or purified, thus homogenous in composition and structure. In contrast to this, side stream mineral raw materials are typically mixtures of multiple minerals and have variation in composition and structure. In order to substitute pure mineral raw materials with secondary mineral side streams in added value ceramic materials, it is important to investigate and understand thoroughly, how the variation in mineral side stream composition due to natural impurities influences the formation of ceramic material microstructure and achieved properties in comparison to pure raw material counterparts. Thus, the main research questions in this thesis are the following:

1. Is the targeted high temperature stable ceramic material structure possible to be achieved using the investigated mineral side stream materials and their mixtures: mine tailings from mining industry processes, side stream from aluminum anodizing process and ferrous slag from steel making processes?
2. How the variation in composition and structure in investigated mineral side stream based materials influences the formed ceramic material structure and achieved properties in comparison to pure raw material products?
3. What is the potential for mineral side streams materials utilization and what factors limit the use in comparison to pure raw materials?

In order to answer these questions, the effects of variation in mineral side streams composition on the structure and properties of the synthesized ceramics need to be fully investigated and understood. Figure 6 shows the flow chart of the publications I-V, the aimed properties for the side streams based ceramics (with

corresponding color-coding to publications) and the aimed knowledge created in this thesis.

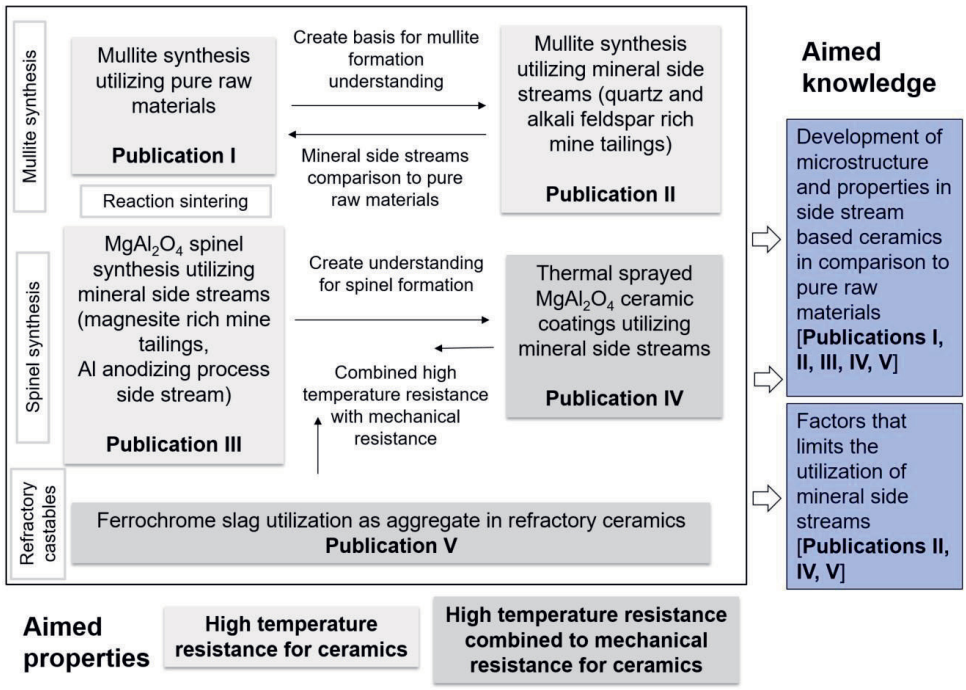

Figure 6. Flow diagram of the publications (left), aimed properties with color-coding to publications (bottom) and the aimed knowledge (right)

In this work, ceramic structures based on two typical high temperature ceramic compounds, mullite and magnesium aluminate spinel, were targeted in synthesis experiments using industrial side streams. Additionally, it was investigated, if it was possible to tailor the mineral side stream composition by mixing different streams. The research work started with mullite synthesis and reaction sintering experiments using commercial, high purity kaolinite ($Al_2Si_2O_5(OH)_4$), and commercial aluminum oxide hydroxide (AlO(OH)) as raw materials [**Publication I**]. The thermal behavior and chemical reactions as well as the formed phase- and microstructures were investigated, generating the basis for mullite formation understanding. The obtained results raised a question if mullite synthesis is possible utilizing mine tailings rich in alumina (Al_2O_3) and silica (SiO_2) as raw materials. This was studied in [**Publication II**] by utilizing quartz and alkali feldspar rich mine tailings as raw materials for mullite synthesis and reaction sintering experiments. The objective was to investigate and especially to increase the

understanding of the effect of chemical and mineralogical composition of mine tailings on the mullite formation.

Possibilities of utilizing magnesite ($MgCO_3$) rich mine tailings in $MgAl_2O_4$ synthesis and reaction sintering experiments were investigated in [**Publication III**]. As alumina source in the spinel synthesis, mineral side stream from aluminum anodizing process, rich in aluminum hydroxide ($Al(OH)_3$), was studied. The results obtained in [**Publication III]** were promising for the feasibility of magnesite rich mining tailings together with aluminum hydroxide rich side stream from anodizing process as raw material in $MgAl_2O_4$ ceramics. This raised a question if in addition to high temperature resistance also comparable mechanical properties could be achieved, because magnesium aluminate spinel often finds use in thermally-sprayed ceramic coatings for high-temperature environments where good electrical insulation is needed. In [**Publication IV],** this was studied by depositing thermally sprayed $MgAl_2O_4$ ceramic coatings utilizing magnesite rich mining tailings together with aluminum hydroxide rich side stream as raw materials for thermal spray powder preparation. The effect of elements other than magnesium and aluminum in mine tailings mineralogy on the resulting coatings was investigated and the electrical insulating properties and wear performance of the secondary and primary coatings were examined and correlated to their microstructures.

High thermal temperature resistance combined with mechanical resistance in side streams based ceramics was also studied in [**Publication V]** where ferrochrome (FeCr) slag utilization as aggregate in refractory ceramics was investigated. The main components of the FeCr slag are SiO_2, MgO and Al_2O_3, thus compositionally it holds potential as aggregate material for refractories. Refractory castable specimens were prepared using ferrochrome slag as an aggregate and commercial calcium aluminate cement as a binder. The effect of FeCr slag on the properties of refractory castable specimens was investigated and compared with commercial refractory castable material targeted for similar applications with requirements of thermal and mechanical stability.

This thesis will summarize the main findings of the attached five scientific publications and combine the information gained in each article into a coherent entity. The scientific novelty of the work arises from created knowledge and increased understanding of the behavior of mineral side streams as raw material in high temperature stable ceramic materials. This thesis focuses solely on the technical feasibility of side stream materials in ceramic applications. Issues related to environmental, economic and legislation aspects of secondary raw materials use are not within the scope of this thesis.

The main scientific goals of this work are:

- Gain knowledge of the feasibility of mineral side streams as raw materials for ceramics if high temperature stable ceramic compounds are targeted.

- Increase understanding about the mineral side streams composition on the formed ceramic material microstructures and achieved properties against those of corresponding pure materials.

- Create understanding of the limiting factors for mineral side streams utilization when high thermal resistance is needed.

5 EXPERIMENTAL PROCEDURE

This chapter describes the experimental procedures used in the thesis. Firstly, the investigated mineral side stream raw materials are introduced along with the pure raw material references. Secondly, the experimental preparation of ceramic materials from the raw materials is introduced, aiming for reaction-sintered mullite ceramics, thermal sprayed magnesium aluminate spinel ceramic coatings and refractory castable ceramics. Lastly, the characterization methods are introduced for the microstructure and properties investigations.

5.1 Raw materials

In mineral side streams selection, the criteria were to focus on compositions, which hold potential to be used as raw materials in high-temperature ceramic compounds. For this reason, this thesis concentrates on the utilization of the following types of mineral side streams: quartz and alkali feldspar rich mine tailings (dominant oxides Al_2O_3 and SiO_2), magnesite rich mine tailings (dominant carbonate $MgCO_3$), aluminum hydroxide rich aluminum anodizing process side stream (dominant hydroxide $Al(OH_3)$) and ferrochrome slag (dominant oxides SiO_2, Al_2O_3 and MgO).

Quartz and alkali feldspar rich mine tailings could be called as felsic mine tailings [94]. From the composition point of view, with alumina source addition, the felsic mine tailings: molybdenum ore tailings FMT1 [95], gold ore tailings FMT2 [96] and quartz ore tailings FMT3 [97] hold potential as starting materials for mullite compositions and were investigated in **Publication II**. Compositions of major elements in feldspars can be expressed in terms of three endmembers: potassium feldspar ($KAlSi_3O_8$), albite ($NaAlSi_3O_8$) and anorthite ($CaAl_2Si_2O_8$).

The talc ore mine tailings MgMT1 is rich in magnesite >80% but contained also other minerals, such as talc ($Mg_3Si_4O_{10}(OH)_2$), chlorite ($(Mg,Fe)_3(Si,Al)_4O_{10}$), and

dolomite ($CaMg(CO_3)_2$) [98]. From the composition point of view, with alumina source addition MgMT1 holds potential as starting material for magnesium aluminate spinel compositions, investigated in **Publication III** and **Publication IV**. As alumina source, a side stream from aluminum anodizing process, aluminum hydroxide precipitate, which consists mainly of gibbsite, $Al(OH)_3$ was studied.

The main components of the FeCr slag are SiO_2, Al_2O_3 and MgO, and it also includes Cr_2O_3, Fe_2O_3 and CaO [9]. Thus from the composition point of view, it holds potential as aggregate material for refractory castables, investigated in **Publication V**.

Table 1 presents the chemical composition of studied side streams, FMT1, FMT2, FMT3, MgMT1 and FeCrSlag as oxides, measured by X-ray fluorescence spectrometry (XRF) method. For the XRF measurement, samples were ground to particle size below 10 μm and pressed into powder pellets. When chemical composition is represented as oxides, the proportion of the volatile compounds (e.g. carbon dioxide from carbonate and water from hydrates) is missing. Table 2 shows side streams compositions converted to elemental compositions.

Table 1. Chemical composition of the studied side stream materials as oxides (wt.%).

Side stream	SiO_2	Al_2O_3	MgO	Fe_2O_3	CaO	Cr_2O_3	Na_2O	K_2O	Publication
FMT1	73.2	11.1	4.84	2.93	1.95	-	3.45	1.51	II
FMT2	57.3	14.3	3.14	5.03	5.36	-	3.91	4.66	II
FMT3	89.8	5.16	0.11	0.57	0.04	-	0.11	1.20	II
MgMT1	10.1	0.61	38.5	8.20	0.80	-	-	-	III,IV
FeCrSlag	30	26	23	4	2	8	-	-	V

Table 2. Elemental composition of studied side stream materials (wt.%).

Side stream	O	Si	Al	Mg	Fe	Ca	Cr	S	Na	K	Publication
FMT1	48.8	34.2	5.87	2.92	2.05	1.39	-	-	2.56	1.25	II
FMT2	43.4	26.7	7.57	1.89	3.52	3.83	-	-	2.90	3.87	II
FMT3	51.4	41.9	2.73	0.07	0.40	0.03	-	-	0.08	1.00	II
MgMT1	23.7	4.71	0.32	23.2	5.74	0.57	-	-	-	-	III,IV
$Al(OH)_3$ precipitate	62.2	0.18	27.8	0.04	0.07	0.11	-	3.82	0.78	0.05	III, IV
FrCrSlag	41.7	14.0	13.8	13.9	2.80	1.43	5.47	-	-	-	V

Table 3 provides a summary of the investigated mine tailings in terms of the most important minerals included in them as wt%. Mineralogical characterization was performed by Geological Survey of Finland (GTK) in Academy of Finland CeraTail project and all the details of performing mineralogical analysis is described in [94]. Mineralogical analyses included the identification and quantification as wt.% of mineral phases. The mineral composition was analyzed with scanning electron microscopy (FESEM) together with elemental composition analyses (EDS). The mineral identification was based on matching the numerical elemental composition converted from EDS spectra to GTK's internal mineral database. Approximately 5-10% of analyses were categorized as unclassified, which included mixed analyses of different mineral phases. Amorphous content was not detected. Magnesite detected in MgMT1 was not stoichiometric $MgCO_3$ but had a varying amount of iron substituting Mg in the lattice, being likely breunnerite rather than pure magnesite, more detailed studied in [99]. There exists a series of solid solutions between $MgCO_3$ and siderite, $FeCO_3$, and iron carbonate content in magnesite could lie between 0 and 5%. If iron carbonate content falls within the range between 5% and 30%, the mineral is called breunnerite [100].

Table 3. Main minerals of the side streams included in the thesis (wt.%), determined by Geological survey of Finland [**Publications II, III, V**]

Mineral group	Mineral	FMT1	FMT2	FMT3	MgMT1
Quartz	Quartz, SiO_2	40	11	64	-
Alkali feldspars	Albite, $NaAlSi_3O_8$	23	31	-	-
	Andesine, $(Ca,Na)Al_2Si_2O_8$	12	3	-	-
	K-feldspar, $KAlSi_3O_8$	6	15	-	-
K-micas	Biotite, $K(Mg,Fe)_3(Al,Fe)Si_3O_{10}(OH,F)_2$	6	20	-	-
	Muscovite, $KAl_2(Si_3Al)O_{10}(OH,F)_2$	3	2	27	-
Clay minerals	Kaolinite, $Al_2(Si_2O_5)(OH)_4$	-	-	4	-
Carbonate minerals	Calcite, $CaCO_3$	-	6	-	
	Magnesite, $MgCO_3$	-	-	-	80
	Dolomite, $CaMg(CO_3)_2$	-	-	-	2
Mg-Fe silicates	Talc, $Mg_3Si_4O_{10}(OH)_2$	-	-	-	9
	Chlorite, $(Mg,Fe)_3(Si,Al)_4O_{10}$	-	-	-	5

A side stream from aluminum anodizing process, aluminum hydroxide precipitate consists mainly of gibbsite, $Al(OH)_3$ [48]. The mineralogy of FeCr slag was characterized in detail by Makkonen and Tanskanen (2005) [101] suggesting the common phases in the slag are Fe-Mg-Cr-Al-spinels, forsterite (Mg_2SiO_4), magnesium silicates and metal iron (Fe) as droplets. FeCr slag was also detailed characterized by Karhu et al. (2017) [102] and (2018) [103]. With fast cooling rates, the slag is not totally crystalline, with amorphous phase being solidified between the grains. The amount of amorphous phase depends on the cooling rate, being typically between 60-70% in FeCr slag [101].

In **Publications I** and **II**, the 3:2 mullite ($3Al_2O_3 \cdot 2SiO_2$) composition was aimed for in synthesis experiments. As a reference, a stoichiometric 3:2 mullite was prepared using commercially available high-purity kaolinite ($Al_2Si_2O_5(OH)_4$) and aluminum oxide hydroxide (AlO(OH)). In Publications III and IV, the magnesium aluminate spinel ($MgAl_2O_4$) composition was aimed for when the reference was prepared using commercially available high-purity magnesium oxide (MgO) and aluminum oxide hydroxide. In Publication V, the properties were compared to those of a commercial refractory castable as the reference material. In castable formulation, commercially available calcium aluminate cement was used. Calcium aluminate cements are typically used as refractory castables because of their good refractory properties in comparison with Portland cements. When heating, the reactive components of the Portland cement, are liberated and can absorb moisture from the atmosphere upon cooling, causing expansion and deterioration of the refractory component. Calcium aluminates are not so susceptible to this phenomenon and can be used to form monolithic castables and refractory cements [79]. Table 4 shows the details of the commercial reference materials used as benchmarks.

Table 4. Details of the commercial raw materials

Raw material	Provider	Specifications	Publication
Kaolinite, $Al_2Si_2O_5(OH)_4$	Merck	high purity	I, II
Aluminum oxide hydroxide AlO(OH)	Sasol Germany GmbH	99.99% purity	I, II, III, IV
Magnesium oxide, MgO	Inframat	99.9% purity	III, IV
Calcium aluminate cement	Kerneos	Secar 71	V
Refractory castable	Calderys	Calde Flow LF50A	V

5.2 Ceramic materials preparation

The mine tailings side streams used in **Publications II**, **III** and **IV** were received in powder form, having particle size distributions (PSD) shown in Table 5. The aluminum anodizing process side stream precipitate was received as sediments after filter pressing with 80 wt.% moisture. In **Publication V**, the ferrochrome slag fine aggregates 0-4 mm were used. For the particle size analysis, aggregates 0-4mm were sieved through 2 mm screen. Approx. 40 wt.% of aggregates were above 2 mm. Particle size and its distribution for under 2 mm sieved fraction was shown in Table 5. All particle size analyses were determined using laser diffractometer (Malvern Mastersizer).

Table 5. Particle sizes as µm of the as received side streams

Side stream	d10 [µm]	d50[µm]	d90[µm]	Publication
FMT1	100	264	467	II
FMT2	25.6	80.8	187	II
FMT3	26.7	108	276	II
MgMT1	10.7	102	213	III,IV
$Al(OH)_3$ precipitate	0.37	1.76	4.04	III,IV
FeCrSlag	411	1230	2410	V

Mine tailing side streams were first ground by jet milling into the particle size below 10 µm, in order to increase the reactivity and ensure the mixing of ingredients in **Publications II, III and IV**. In **Publication II**, the correct Al:Si ratio for mullite composition was balanced by adding commercially available AlO(OH), details were shown in Table 4. The targeted amount of AlO(OH) additions was calculated based on the chemical composition analysis of mining tailings presented in Table 1. Powder mixtures were prepared by ball milling in an attrition mill for 30 min in air atmosphere. In **Publications I** and **II**, as a reference, a stoichiometric 3:2 mullite sample was prepared using commercially available high purity kaolinite (51.8 wt.%) and aluminum oxide hydroxide (42.8 wt.%), raw materials details were presented in Table 4. In **Publications III** and **V**, the correct 1:2 Mg to Al molar ratio for $MgAl_2O_4$ composition was balanced by adding aluminum anodizing side stream $Al(OH)_3$ precipitate, which chemical composition was presented in Table 2. Reference $MgAl_2O_4$ spinel powder was prepared using commercially available pure MgO and AlO(OH) powders as raw materials, details presented in Table 4. In **Publication V** recipe formulation,

particle packing optimization was made using an Elkem Materials Mixture Analyser Software (EMMA). Particle packing of refractory castables covers the selection of right size distribution and amount of particles of particular size [104]. The particle size distribution is selected to fill up the voids between large particles with smaller ones and thus to increase the particle packing density. Particle size distribution optimization was based on packing models and curves developed by Andreassen [105]. The optimization curves were combined in such a way that the total particle size distribution of the mixture was closest to an optimum curve with the distribution coefficient (q) value of 0.30.

Table 6 summarizes the main studied mineral side streams based ceramic material formulations. All the supporting formulations studied may be found in **Publications II**, **III, IV and V**.

Table 6. Main studied mineral side streams based ceramic material formulations (wt.%). [**Publications II, III, IV,V**]

Raw material	FMT1_ ceramic	FMT2_ ceramic	FMT3_ ceramic	MgMT1_ ceramic	FeCrSlag_ castable	Publicati-on
FMT1	33.6	-	-	-	-	II
FMT2	-	40.4	-	-	-	II
FMT3	-	-	28.8	-	-	II
MgMT1	-	-	-	35.0	-	III, IV
$Al(OH)_3$ precipitate	-	-	-	65.0	-	III, IV
AlO(OH)	66.4	59.6	71.2	-	-	II
FeCr slag	-	-	-	-	81.8	V
Secar71	-	-	-	-	18.2	V

5.2.1 Reaction-sintering experiments

For mullite reaction-sintering experiments, in **Publication II**, the attrition-milled powders were uniaxially compressed into green pellets of the size of 20 mm ×3 mm using approximately 25 MPa pressure. Heat treatment of green pellets was made in an ENTECH chamber furnace in air atmosphere and ambient air pressure. The heating rate was 3.3°C/min up to 1300 °C, with 3 h holding time at

the maximum temperature before cooling to room temperature at the rate of 5 °C/min.

For $MgAl_2O_4$ reaction-sintering experiments, in **Publication III**, powder mixtures were also uniaxially compressed into green pellets of the size of 20 mm×3 mm using approximately 25 MPa pressure. Green-state pellets were heat treated in an ENTECH chamber furnace in air atmosphere and ambient air pressure at the maximum temperatures of 1000°C, 1100°C, 1200°C, 1300°C, 1400°C and 1500°C. The heating rate was 3.3°C/min up maximum temperatures, with 3 h holding time at the maximum temperature before cooling to room temperature at the rate of 5°C/min.

5.2.2 Powder preparation for thermal spray and coatings deposition

In order to prepare agglomerated powders suitable for thermal spraying in **Publication IV**, water-based ceramic powder suspensions were prepared from raw material mixtures by bead milling for 15 minutes. 2 wt.% addition of Dispex A as dispersing agent was used. Before spray drying, an organic binder, polyethylene glycol (PEG) was added to suspensions at the concentration of 2%. Suspensions were dried with an industrial-scale spray dryer Niro Atomizer to produce agglomerated powders. Spray-dried powders were reaction sintered in an ENTECH air chamber furnace at ambient air atmosphere and pressure at the temperatures between 1075°C and 1150°C.

Atmospheric plasma spraying (APS) technique was used for the deposition of coatings in **Publication IV**. Coatings were sprayed with an APSProPlasma gun using argon/ hydrogen (Ar/H_2) plasma gas mixture. Spray distance was constant, 110 mm. Coatings with the average thickness of 225-300 μm were deposited on grain-blasted carbon steel substrates. The plasma gun was robot-manipulated with 51 m/min surface speed and 3 mm increments.

5.2.3 Refractory castables preparation

In **Publication V**, the refractory castable specimens were prepared according to the standard EN 196-1 [106]. A standard steel mould with the size of 40 mm x 40 mm x 160 mm was used for mixed compositions. Specimens were first cured for 24h in the moulds in a curing cabinet with relative humidity (RH)>95% at room

temperature. Then the specimens were removed from the molds and left for another 24h in the curing cabinet in a plastic bag at room temperature. After that, specimens were moved to drying oven and kept there for 7 hours at 105°C. The dried specimens were then sintered in air atmosphere by slowly heating them to 540°C and kept at this temperature for 3 hours, then heated to 1200°C and kept there for another 3 hours.

5.3 Characterization

This chapter introduces the main characterization techniques used in this thesis.

5.3.1 Microstructure

Microstructural analysis in all **Publications I-V** covered the determination of phase structure and the overall microstructure with compositional analysis of the microstructural details. For side streams compositional and mineralogical characterization was described details already in Section 3.1. Raw materials in this thesis.

Phase structure analyses of the materials, in all **Publications I-V**, were performed using X-ray diffractometry (XRD, Empyrean, PANalytical B.V. device, ALMELO) and a CuKα radiation source, and analysed using HighScore Plus software with ICDD database. The XRD was operated at 45 kV and 40 mA with the scanning rate of 3° 2θ/min. Microstructural and compositional investigations of the materials were conducted by field emission scanning electron microscopy (FESEM, Zeiss ULTRAplus) together with energy-dispersive spectrometry (EDS). For microstructural analyses, metallographic cross sections were prepared by casting the cut sections of specimens in Epofix cold setting resin under reduced pressure. The casts were then ground, polished and carbon coated for electrical conductivity. For imaging, secondary electron (SE) detector or angle selective backscattered electron (AsB) detector was used. In **Publication IV**, in addition to the visual inspection of particle size distribution, these were determined for the powders with a laser diffractometer (Malvern Mastersizer). Additionally in **Publication IV**, an electron backscatter diffraction (EBSD) system (Oxford

Instruments), Symmetry EBSD detector based integrated into FESEM was employed for crystal structure analysis. The cross-sectional EBSD samples were prepared by moulding the sections of specimens in epoxy, followed by grinding and polishing down to the final finish by colloidal silica suspension (0.04 μm). After the final polishing, the samples were removed from epoxy. In **Publication IV,** after the dry abrasion wear tests, the surfaces and cross sections of the worn surfaces were investigated. The cross sections were prepared with focused ion beam SEM (FIBSEM, Zeiss Crossbeam 540) first by depositing a platinum (Pt) protection layer on top of the region of interest and then using gallium (Ga) ions to mill the cross section under the Pt covering layer. Prior to FIBSEM studies, the samples were carbon coated to avoid the sample charging during the milling process.

5.3.2 Structural integrity and strength

In **Publications II** and **V**, apparent solid density, bulk density and open porosity were investigated according to Archimedes principle following the ISO18754 standard [107]. In **Publication II**, compressive strength values were determined using an INSTRON testing system according to the standard ISO 20504:2006 [108]. Rectangular samples with the dimensions of 15 mm × 40 mm were employed in the compression tests, with the used compression speed being 1 mm/min. In **Publication V**, cold crushing strength of the specimens was tested based on the standard EN 196-1 using uniaxial strength tester [106]. The compression tests were carried out at the constant load rate of 2.4 kN/s as indicated in the standard. For high temperature mechanical tests in **Publication V**, cubic samples were prepared from sintered castables. To obtain the desired sample size (10 mm x 10 mm x 10 mm), a diamond saw with a blade thickness of 0.5 mm was used using a slow cutting speed. The tests were done under argon atmosphere at 1200ºC, with the initial pinchload of -0.05 kN and the heating rate of 10°C/min. Once the target temperature was reached, compression was performed at the displacement rate of 0.2 mm/min. All the measurements were done in a furnace using an INSTRON testing system frame with a 4 MPa loading cell.

5.3.3 Thermal behavior

In all **Publications I-V**, in order to understand the differences in behavior between the compositions, the thermal behavior of raw materials and raw material mixtures was studied using thermogravimetric analysis (TGA, Netzsch STA449 F1 Jupiter) in differential scanning calorimetry (DSC) and thermogravimetry (TG) modes. A qualitative mass spectrometer (QMS, Netzsch QMS 403 D Aeolos) coupled directly to the TG device exhaust was used for evolved gas analysis.

In **Publications I** and **II**, the thermal expansion and sintering shrinkage behaviors were studied using horizontal pushrod dilatometers (Adamel Lhomargy DI- 24 and Netzsch DIL 402 Expedis). In **Publication V**, the thermal expansion coefficient α for the specimens was measured by dilatometry using a Netzsch Dilatometer DIL 402C. Additionally, in **Publication V**, specific heat capacity and thermal conductivity of materials were measured by laser flash analysis (LFA 457 Microflash, Netzsch) in argon atmosphere using the samples size of 10 mm x 10 mm x 2 mm. Samples were prepared by a hollow drill and measured in the temperature range from 21°C up to 1000°C.

5.3.4 Electrical insulation

In **Publication IV**, the electric insulation properties of the coating samples were measured using a breakdown voltage method. Breakdown voltage electrode areas (Ø=11 mm) and silver electrodes (Ø=11 mm) were painted on the coating surface as described in [109]. Silver paint penetration into the coating has been studied from cross-sectional images taken by optical microscopy, and it has been observed that the utilized silver paint does not penetrate into the coating [109]. After painting the electrodes, the samples were first dried at 120°C for 2 h, followed by conditioning in a climate room at 20°C/RH 20% for at least 12 h before the measurements. The breakdown measurements were performed in the climate room at 20°C/RH 20%. In the breakdown tests, a stainless steel rod electrode (Ø=11 mm, edge rounding 1 mm), was placed on the top of a coating surface while the steel substrate of the sample acted as the other electrode. Direct current (DC) breakdown voltage measurements were performed by utilizing linearly increased DC voltage (ramp rate of 100 V/s throughout the test) [109]. The voltage source control and data recording were performed using a LabVIEW-based software [109]. The voltage source was Spellman SL1200 (U_{max}=20 kV) and the voltage

level was measured using a resistive voltage divider (Spellman HVD-100-1, divider ratio 10000:1) [109]. Dielectric breakdown strength (DBS) of the coatings was calculated by dividing the breakdown voltage by the corresponding coating thickness at the painted electrode (Ø=11 mm) location. Seven measurements were performed per each coating.

5.3.5 Wear resistance

In **Publication IV**, sand abrasion tests by a rubber wheel tester were performed using quartz sand with the particle size of 0.32 mm and the feed of 350 g/min based on the ASTMG65 standard (procedure D, modified) [110]. A static contact force of 45 N against the rubber wheel, 233 mm in diameter, was used. Prior to the wear tests, the surfaces of samples were ground with a P1200 grinding disk to eliminate the effect of as-sprayed surface quality. Two samples per coating were tested and their mass loss was measured at four time intervals (5, 10, 20 and 30 min) to ensure the linear wear performance during rubber wheel abrasion tests. Hardness of the coatings was measured with a hardness tester (DuraScan 20 Struers) and a Vickers intender in order to evaluate how the hardness correlates to wear resistance.

6 RESULTS AND DISCUSSION

This chapter summarizes the most important results of this thesis, presented in detail in the attached five publications. First, the thermal behavior of studied mineral side stream materials are analyzed through thermogravimetric analyses in order to investigate the raw materials response to the heat treatment and gain understanding of their phase transformations and chemical reactions. For comparison, mullite and magnesium aluminate spinel syntheses are also studied using corresponding pure raw materials in order to support the evaluation of phase transformations and reactions during the heat treatments.

After that, the success of targeted structure (mullite, magnesium aluminate spinel and refractory castable) formation is evaluated based on the XRD, FESEM and EDS studies. The factors influencing the formed structure during the heat-treatments are discussed, aiming to understand the reasons behind the different behaviors.

The last part concentrates on presenting the summary of the achieved properties of mineral side stream based ceramic materials. Achieved properties are compared to references prepared using pure raw materials. As a summary, utilization potential of studied mineral side stream materials as high-temperature ceramic raw material are evaluated and the limiting factors for utilization are discussed.

6.1 Thermal behavior analyses and response to heat-treatments

This chapter evaluates the thermal behavior of studied mineral side stream materials and their response to the heat treatments. Focus is on phase transformations and reactions occurring during the heat treatment. For comparison, also thermal behavior of pure raw materials is evaluated.

In **Publications I and II**, the mullite composition was aimed for in synthesis and reaction sintering experiments. As a reference, a stoichiometric 3:2 mullite sample was prepared using commercially available high purity kaolinite and aluminum oxide hydroxide. Behavior of pure raw material mixture during heat-treatment was studied in detail in **Publication I.** TG/DSC measurement curves of the pure raw material mixture are presented in (Figure 7).

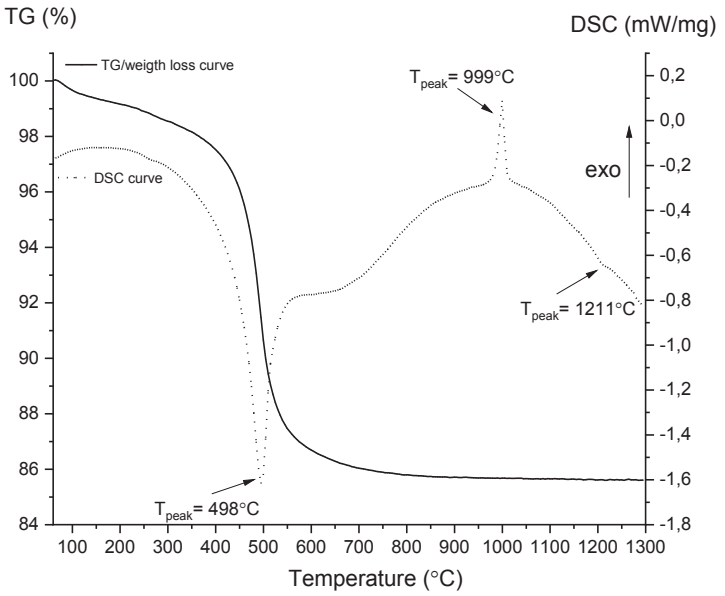

Figure 7. TG/DSC curves of the mixture of kaolinite and aluminium oxide hydroxide [**Publication I**]

DSC curve revealed the first transformation peak at 498°C combined to over 10% weight loss in TG curve, being related to the dehydratation reactions of kaolinite into metakaolin, as suggested earlier by Yung-Feng et al. [71] (Equation 1), and of aluminum oxide hydroxide, AlO(OH), into alumina (Equation 2):

$$Al_2O_3 \cdot 2SiO_2 \cdot 2H_2O \rightarrow Al_2O_3 \cdot 2SiO_2 + 2H_2O \quad (1)$$

$$2AlO(OH) \rightarrow Al_2O_3 + H_2O \quad (2)$$

At 999°C, DSC curve revealed an exothermic peak. It was likely related to the reorganization of the metakaolin into the Al-Si spinel, $Si_3Al_4O_{12}$, and amorphous silica (SiO_2) phases, as presented by Yung-Feng et al. [71] (Equation 3):

$$2(Al_2O_3 \cdot 2SiO_2) \rightarrow Si_3Al_4O_{12} + SiO_2 \quad (3)$$

At 1211°C, mullite formation was started according to the reaction presented by Yung-Feng et al. [71], resulting in mullite $3Al_2O_3{\cdot}2SiO_2$ and amorphous silica phases (Equation 4):

$$3Si_3Al_4O_{12} \rightarrow 2(3Al_2O_3 \cdot 2SiO_2) + 5SiO_2 \quad (4)$$

Because of the higher silica content in kaolinite than in mullite, the addition of alumina was needed to synthesize stoichiometric mullite. Thus, aluminum oxide hydroxide was added to recipe to balance the aluminum amount. An aluminum oxide resulting from (Equation 2) reacted with extra silicon oxide forming a mullite phase structure (Equation 5):

$$3Al_2O_3 + 2SiO_2 \rightarrow (3Al_2O_3 \cdot 2SiO_2) \quad (5)$$

Above 495°C, any notable weigh loss was not more observed in TG curve that supports that DSC curve observations were connected to solid state phase transformations and reactions. Thus, the following total reaction (Equation 6) was assumed to take place during reaction sintering of powder mixture of kaolinite and aluminum oxide hydroxide:

$$Al_2O_3 \cdot 2SiO_2 \cdot 2H_2O + 4AlO(OH) \rightarrow 3Al_2O_3 \cdot 2SiO_2 + 4H_2O \quad (6)$$

In **Publication II**, the mullite synthesis was studied utilizing quartz and feldspar rich mine tailings FMT1, FMT2 and FMT3 balanced with aluminum oxide hydroxide additions. DSC measurement curves for mine tailings (FMT1, FMT2 and FMT3) and their mixtures balanced with AlO(OH) (FMT1_ceramic, FMT2_ceramic and FMT3_ceramic) are presented in Figure 8. Figure 9 shows the corresponding TG curves.

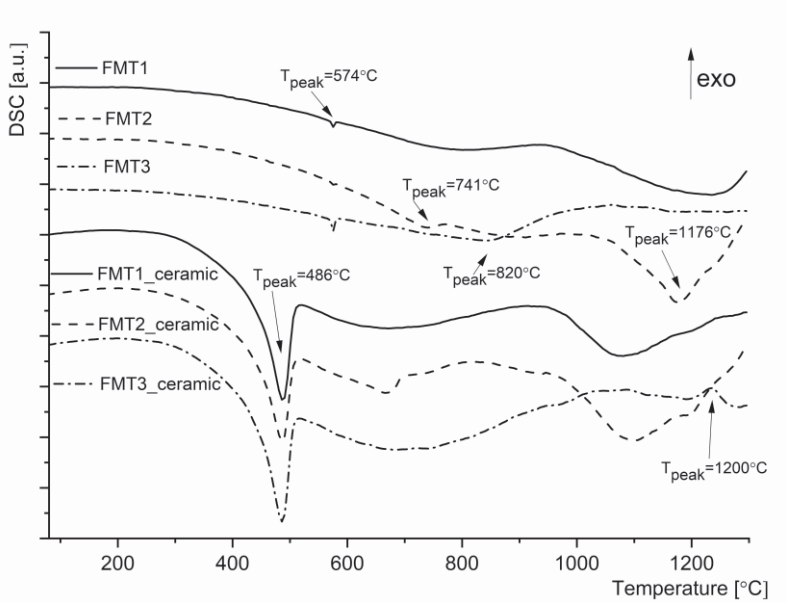

Figure 8. DSC curves of mine tailings (FMT1, FMT2 and FMT3) and their ceramic mixtures balanced with AlO(OH) [**Publication II**]

For all mine tailings FMT1, FMT2 and FMT3, the first phase transformation occurred above 574°C, as a small endothermic peak for all three tailing samples was detected in DSC curves (Figure 8), being the most visible in highest quartz content containing FMT3. No notable weight change was related to this phase transformation in TG curves (Figure 9), based on which the peak could be associated with quartz alfa-beta phase transition, described in literature [111]. For FMT2 weight loss was detected approximately at 750°C relating to peak in DSC curve, most probable due to calcite decomposition. Similarly, for FMT3 weight loss was detected approximately at 880°C relating to peak in DSC curve, most probable due to dehydratation of muscovite.

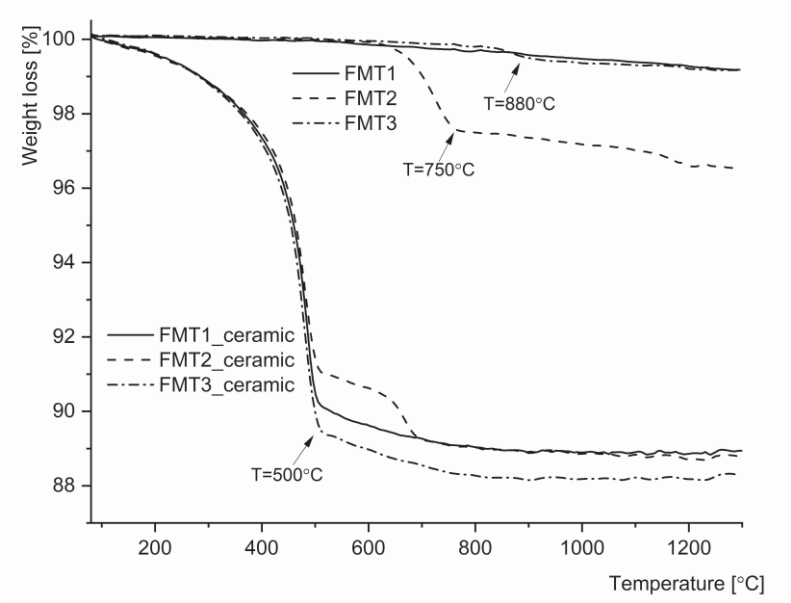

Figure 9. TG curves of mine tailings (FMT1, FMT2, FMT3) and their ceramic mixtures with AlO(OH) **[Publication II]**

In high-alkali content mine tailings FMT1 and FMT2, a liquid phase was formed. DSC curves (Figure 8) showed for FMT1 and FMT2 a slope decline starting above 900°C and featuring a clear peak approximately at 1176°C for FMT2 and about 30°C higher temperature for FMT1. This transformation was related to the formation of a liquid phase, i.e., melting of FMT1 and FMT2. For FMT3 behavior was not detected. For FMT2 the decline in the DSC curve slope was steeper as compared to that for FMT1, most probably referring to a higher liquid phase amount. A quite large variation in the melting temperatures of feldspar minerals is shown in literature, for example, for albite, of which FMT1 contains 21% and FMT2 31%, the following melting temperatures have been suggested: between 1105°C and 1145°C [112], 1134°C [113] and 1180°C [114]. The compressed pellets of mine tailings were visually examined after the reaction sintering experiments at 1300°C/3 h in **Publication II**. The compressed pellets of FMT1 and FMT2 had melted completely, losing their shape in the heat treatment due to melting, which supports the observations in DSC curves of the liquid phase formations. For the pellet of FMT3, any melting was observed, but the specimen was clearly fractured during the heat treatment. The DSC curves (Figure 8) for mine tailings mixtures balanced with AlO(OH) additions (FMT1_ceramic, FMT2_ceramic and FMT3_ceramic) all contained phase transformation peak at approximately 486°C,

connected with a significant weight loss by approximately 10% in TG curves (Figure 9). This transformation was associated with dehydratation reaction of aluminum oxide hydroxide, AlO(OH), into alumina (Equation 2). A liquid phase was suggested to form in mining tailings FMT1 and FMT2 above 1000°C. Similar transformations were observed also in FMT1_ceramic, FMT2_ceramic mixtures as response to heat-treatment but approximately 50°C lower temperatures than for pure mine tailings FMT1 and FMT2. One explanation for this difference could be that SiO_2 in mine tailings started to react with Al_2O_3. Then alkali content in the remaining mine tailings increased, decreasing the melting temperature in the mixtures.

In **Publications III and IV**, the magnesium aluminate spinel composition was aimed for when the reference was prepared using commercially available high-purity magnesium oxide and aluminum oxide hydroxide. For the reference mixture, TG/DSC/QMS curves are presented in Figure 10.

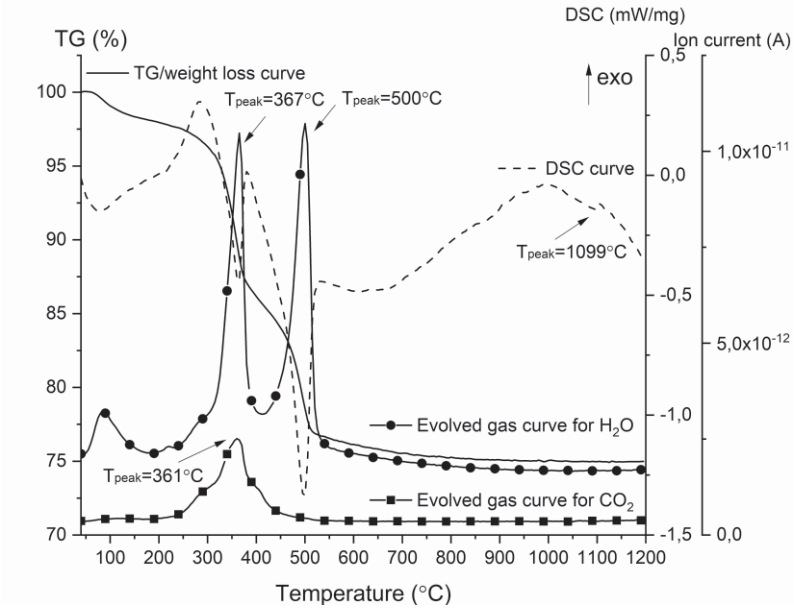

Figure 10. TG/DSC/QMS curves of the mixture of MgO and AlO(OH) [**Publication IV**]

At 367°C, the dehydration of magnesium hydroxide $Mg(OH)_2$ (Equation 7) occurred, suggested also by Yoshida et al. [115] at corresponding temperatures:

$$Mg(OH)_2 \rightarrow MgO + H_2O \quad (7)$$

Magnesium hydroxide was likely formed from the raw material, MgO, by the reaction with water during the spray-drying step. Above 500°C, the dehydration of aluminum oxide hydroxide, AlO(OH), (Equation 2) occurred, similar values for dehydration temperatures was presented also by Wilson [116]. After completion of the dehydration of aluminum oxide hydroxide, the reaction between Al_2O_3 and MgO was possible, resulting in $MgAl_2O_4$ formation (Equation 8). An exothermic peak detected at 1099 °C in DSC curve was probably related to this spinel formation. Magnesium aluminate spinel formation has been reported to be a heat releasing reaction with similar temperatures [117].

$$Al_2O_3 + MgO \rightarrow MgAl_2O_4 \quad (8)$$

In Figure 11, TG/DSC/QMS curves are presented for magnesite rich mine tailings (MgMT1) mixture balanced with $Al(OH)_3$ precipitate from aluminum anodizing process, studied in **Publication IV**.

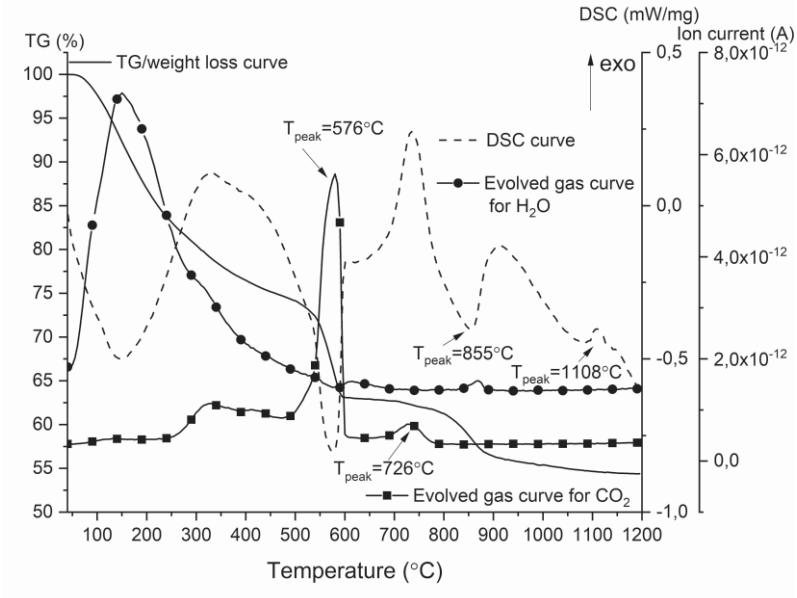

Figure 11. TG/DSC/QMS curves of magnesite rich mine tailings (MgMT1) ceramic mixture with $Al(OH)_3$ precipitate [**Publication IV**]

According to the observations in TG/DSC/QMS curves (Figure 11) for the mixture of magnesite rich mine tailings (MgMT1) and $Al(OH)_3$ precipitate, the following reactions were likely during the heat treatment. Below 500°C, $Al(OH)_3$ dehydration occurred, as suggested earlier by Živković and Dobovišek [118] (Equation 9, Equation 10):

$$2Al(OH)_3 \rightarrow 2AlOOH + 2H_2O \quad (9)$$

$$2AlOOH + H_2O \rightarrow Al_2O_3 + 2H_2O \quad (10)$$

It is suggested that both reactions proceeded in the diffusion region, the first (Equation 9) up to the temperature of 253°C and the second (Equation 10) up to 427°C in TG curves. Vusikhis et al. [100] reported that carbonates begun to dissociate in the temperature range of 500–584°C. They explained the presence of two separate peaks in the DSC curve by the following reactions, forming besides MgO the spinel $MgFe_2O_4$ (Equation 11, Equation 12):

$$(Mg_{1-x}Fe_x)CO_3 = (Mg_{1-x}Fe_x)O + CO_2 \quad (11)$$

$$2(Mg_{1-x}Fe_x)O + 0.5xO_2 = (2-3x)MgO + xMgFe_2O_4 \quad (12)$$

The transformation observed above 800°C was probably associated with the decomposition of hydrated magnesium silicates that were present as impurities in the mine tailings sample. Eventually at 1108°C, an exothermic peak was detected, probably related to the formation of magnesium aluminate spinel by the reaction between magnesium oxide formed from mine tailings sample magnesite and aluminum oxide formed from $Al(OH)_3$ precipitate.

In **Publication V**, refractory castables utilizing ferrochrome slag as aggregates were aimed for. TG/DSC measurement curves of the FeCr slag (in Figure 12) revealed a notable phase transformation above 1200°C, probably related to liquid slag phase formation, with increase in temperature increasing the content of the liquid phase. In the study by Zelic´ [40], the melting point of FeCr slag was reported to fall in the temperature range of 1200–1400°C. In order to confirm the liquid phase formation, which was observed in DSC curves for FeCr aggregates,

sintered castable specimens were re-heated up to temperatures 1260°C and 1320°C. Reheating to 1320°C revealed clearly the melting of both slag aggregates and the surrounding binder phases, which strengthens the observation that the maximum service temperature should be kept below 1200°C.

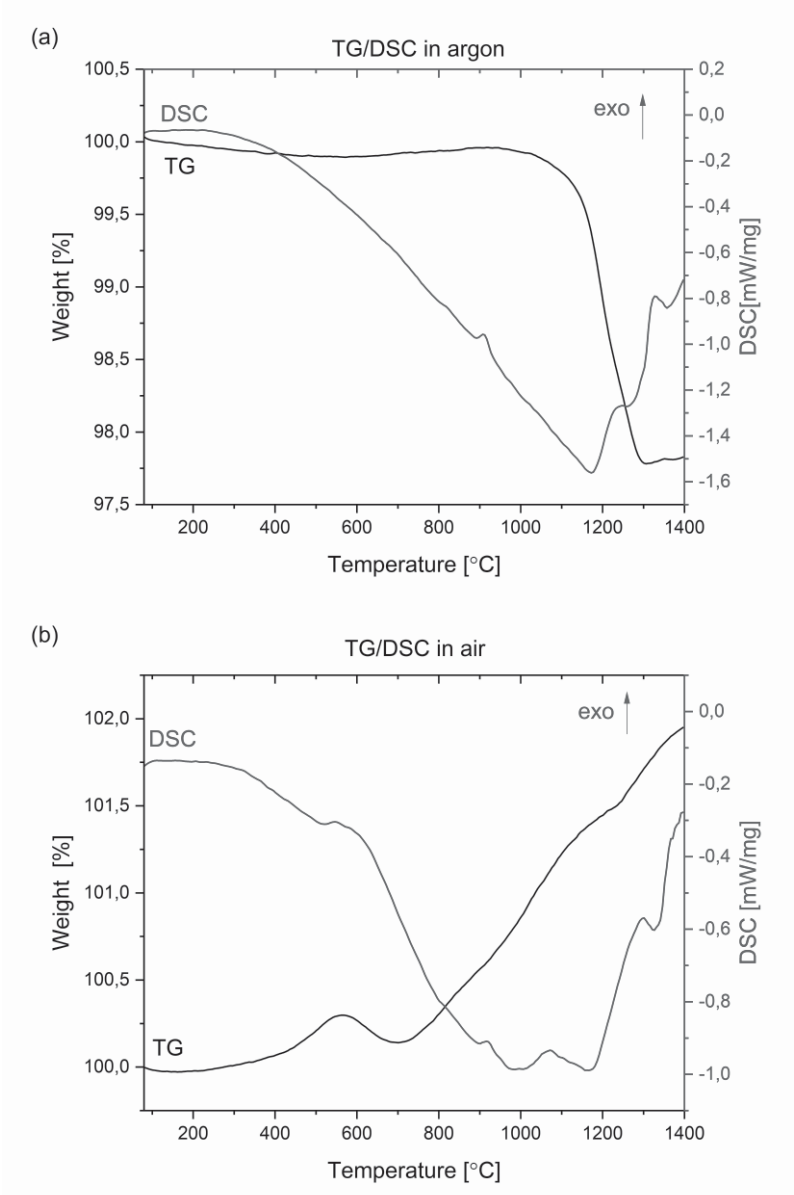

Figure 12. TG/DSC curves of FeCr slag in argon (a) and in air (b) [**Publication V**]

6.2 Success of synthesis experiments and formed microstructures

In this section, the success of synthesis experiments utilizing studied mineral side streams is reviewed and the formed ceramic material microstructures are introduced. The reactions during the heat treatments are discussed, trying to establish the factors that influence the formed microstructures.

6.2.1 Mullite synthesis

XRD, FESEM and EDS analyses in **Publication II** suggested that the quartz and alkali feldspar rich mine tailings (FMT1, FMT2, FMT3) balanced with AlO(OH) additions and subjected to reaction sintering at 1300 °C for 3 h resulted in the formation of following structures.

FMT1 (main minerals alkali feldspars 41%, quartz 40% and K-micas 9%) containing mixtures with AlO(OH) yielded acicular mullite structure. FESEM examination (Figure 13) revealed that the microstructure formed in reaction sintering consisted of evenly distributed and networked needle-shaped crystals. Networked needle-shaped crystals were surrounded by an amorphous phase (seen as uniform areas between the networked needles).

According to EDS analyses together with XRD results (Figure 14) the crystalline needle network was identified as the mullite phase (with Al/Si ratio according to elemental analyses of the 3:1, corresponding to 3:2 mullite). Figure 13 revealed that microstructure also involved separate randomly distributed clusters of nearly-equiaxed crystals. These were identified as the corundum phase according to combined EDS and XRD analyses. Glass phase was aluminosilicate-based with traces (~ 2 wt%) of Na, K and Ca. Porosity, seen in black contrast, was also present. It was suggested that during the heat treatment of FMT1 containing mixtures, the original minerals in the tailings, i.e. alkali feldspars and K-micas, converted into a liquid form, i.e., melted. Higher temperature increases the solubility of quartz/silica to the melt, which subsequently enables the reaction of silica with alumina (resulting from AlO(OH)) into mullite. Thus, mullite phase crystallized from the aluminosilicate melt.

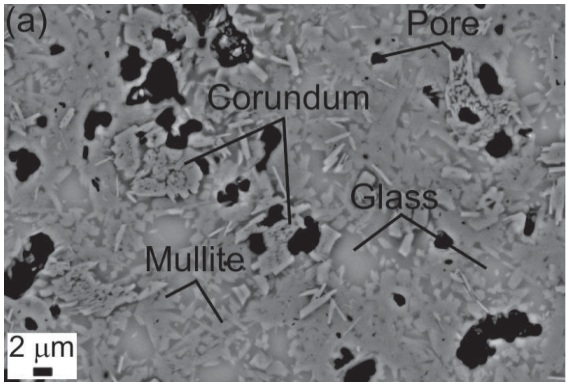

Figure 13. SEM image, showing the microstructure formed in FMT1 containing mixture during reaction sintering [**Publication II]**

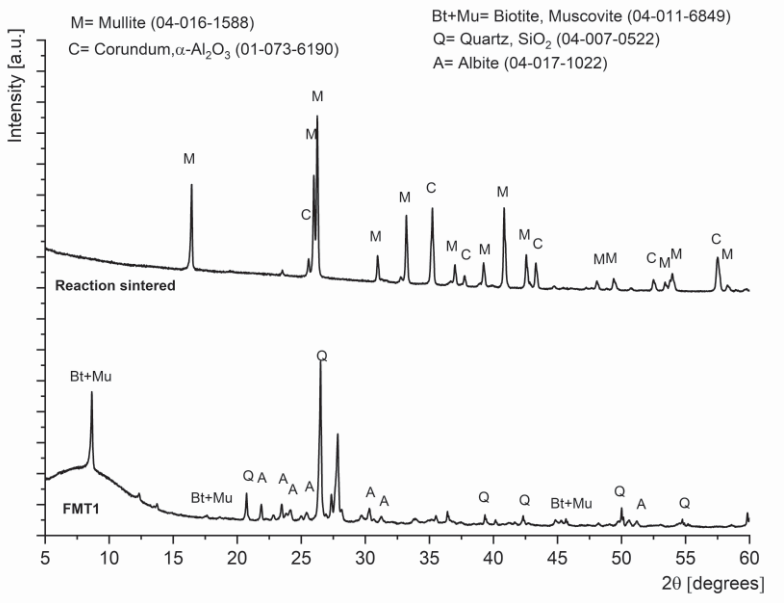

Figure 14. XRD patterns for FMT1 and reaction sintered mixture of FMT1 balanced with AlO(OH) additions [**Publication II**]

In FMT2 (main minerals alkali feldspars 49%, quartz 11%, K-micas 22% and calcite 6%) containing mixtures with AlO(OH) mullite did not form. FESEM

studies (Figure 15 (a)) revealed that the formed microstructure contained needle-shaped crystals with the length of approximately 5–10 μm, which were surrounded by an amorphous phase. In FMT3 (main minerals quartz 64 %, K-micas 27% and kaolinite 4%) containing mixtures with AlO(OH), only occasional single mullite needles were identified. FESEM investigations (Figure 15 (b)) revealed that in the case of FMT3, the developed microstructure consisted mainly of coarse grains.

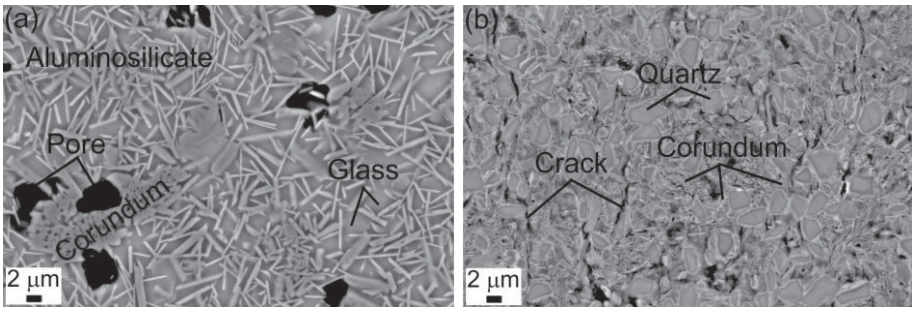

Figure 15. SEM images, showing the microstructure formed in (a) FMT2 containing mixture during reaction sintering and (b) FMT3 containing mixture during reaction sintering [**Publication II**]

According to EDS analyses for FMT2 containing mixtures balanced with AlO(OH) additions, the crystal needles were identified as an Al-rich aluminosilicate phase. According EDS combined to XRD analyses (Figure16), randomly-distributed crystal clusters appeared in occasional areas were identified as corundum. In FMT2 containing mixtures, the aluminosilicate melt formed during the heat treatment, similarly to FMT1 case. However, mullite was not formed regardless of the correct Al:Si ratio, as it was not detected by any of the used characterization methods. Original minerals in the FMT2 tailings: alkali feldspars, K-micas and quartz have melted and formed a new crystalline aluminosilicate phase. One possibility for the development of this aluminosilicate phase was that calcite reacted in the feldspar melt and crystallized into anorthite.

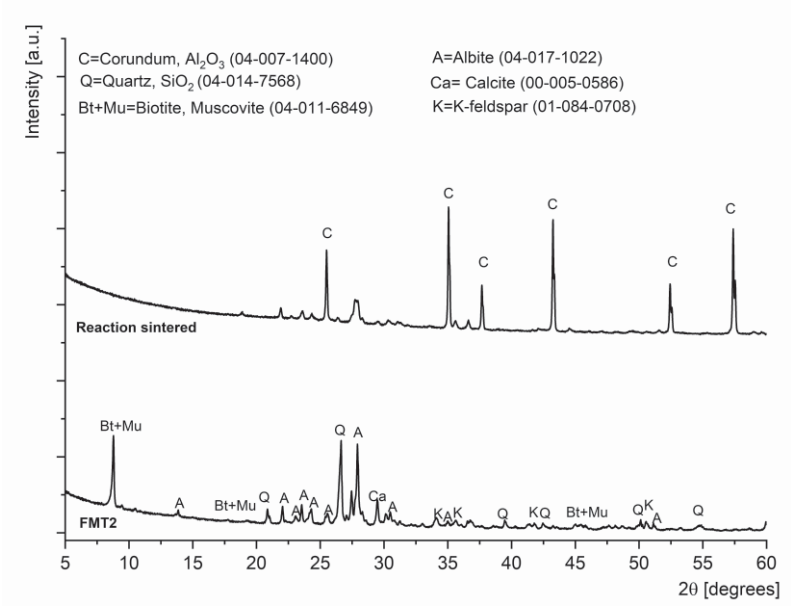

Figure 16. XRD patterns for FMT2, and reaction-sintered mixture of FMT2 balanced with AlO(OH) additions [**Publication II**]

According to EDS analyses supported by XRD analyses shown in (Figure 17) for FMT3 containing mixtures balanced with AlO(OH) additions, the coarse grains were identified as quartz grains. Corundum crystals were identified between the quartz grains and, to some extent, their clustering was observed. Also visible macro cracks were observed in the structure. According to EDS analyses, only occasional single mullite needles were identified, probably resulting from kaolinite heating. In FMT3, aluminosilicate melt did not form and thus mullite was not crystallized from the melt. The quartz was retained largely unreacted in the reaction sintering experiments. It may be possible to facilitate the mullite formation with notably higher sintering temperatures or longer times via solid-state reaction between Al_2O_3 and SiO_2 particles.

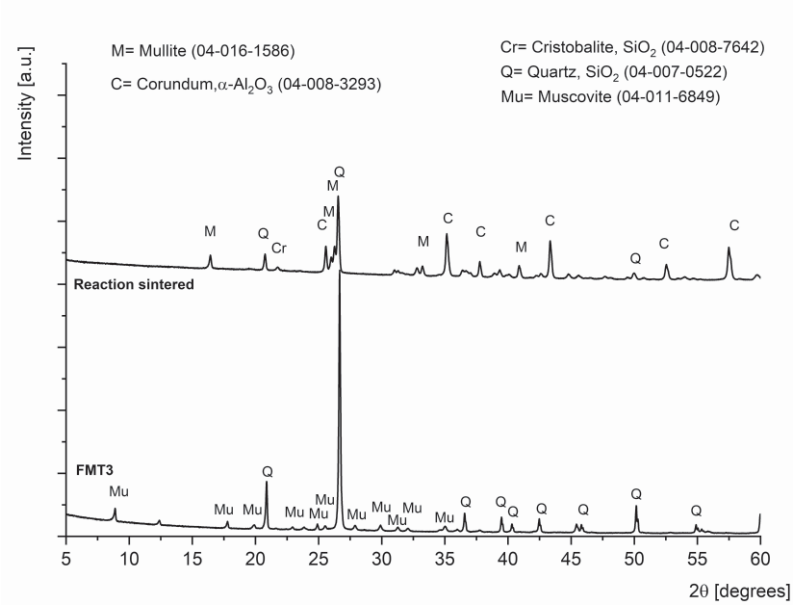

Figure 17. XRD patterns for FMT3, and reaction sintered mixture of FMT3 balanced with AlO(OH) additions [**Publication II**]

6.2.2 Spinel synthesis

Magnesium aluminate spinel formation capability utilizing magnesite rich mine tailings was studied in reaction sintered specimens in **Publication III** and in thermal sprayed ceramic coatings in **Publication IV**.

XRD, FESEM and EDS analyses in **Publication III** suggested that the compacted mixture of pure raw materials MgO and AlO(OH) resulting from reaction sintering at 1300 °C for 3 h featured a very fine structure of $MgAl_2O_4$ spinel crystals (Figure 18). The only difference between the applied six heat treatments temperatures (1000–1500 °C) was the peak widths in XRD spectrum (Figure 19), indicating that the crystal size increased with the increasing temperature.

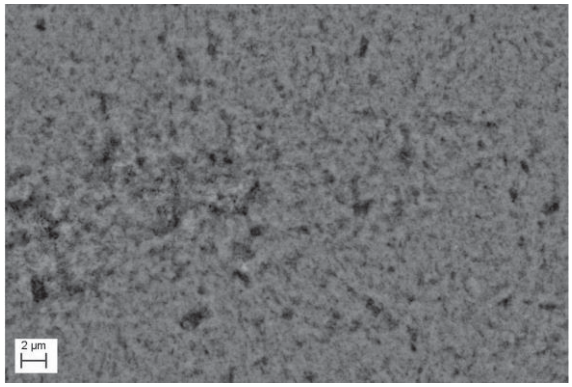

Figure 18. Reaction sintering of the mixture of pure raw material MgO and AlO(OH) resulted in very fine $MgAl_2O_4$ microstructure [**Publication III**]

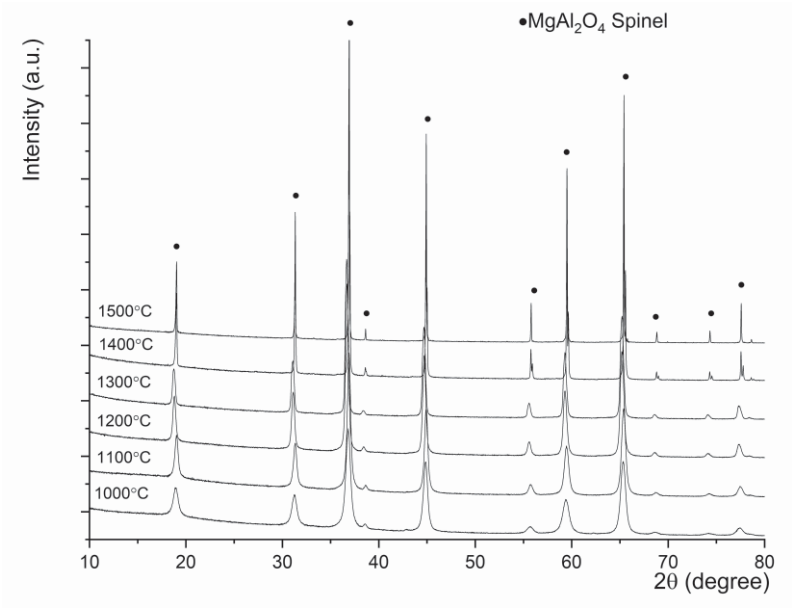

Figure 19. XRD patterns for reaction sintered pieces of the mixture of pure raw material MgO and AlO(OH) [**Publication III**]

In the case of compacted mixture of magnesite mining tailings (MgMT1) balanced with $Al(OH)_3$ precipitate additions and subjected to reaction sintering at 1300 °C for 3 h, the formation of $MgAl_2O_4$ spinel crystals surrounded by an amorphous phase, seen in darker grey than the spinel phase, was evident (Figure 20) and confirmed by XRD studies (Figure 21). Also another crystalline phase was

observed in areas with a bright contrast, most likely the ferroan forsterite, (Mg, $Fe)_2SiO_4$, phase. According to EDS analyses, it is challenging to draw any definite conclusion about the compositional characteristics of small areas, due to their microstructural complexity and fine crystal size compared to the electron beam size.

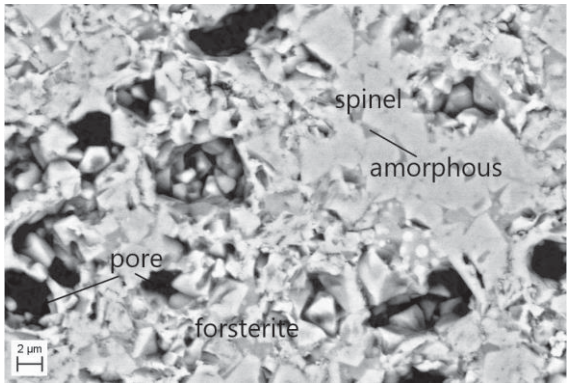

Figure 20. Mixture of MgMT1 balanced with $Al(OH)_3$ precipitate resulted $MgAl_2O_4$ spinel crystals surrounded by an amorphous phase [**Publication III**]

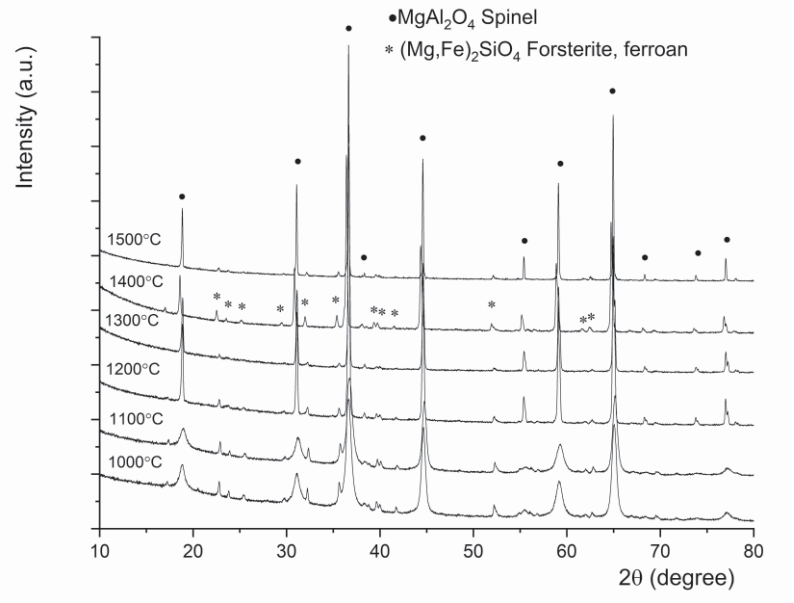

Figure 21. XRD patterns for reaction sintered pieces of mixture of MgMT1 balanced with $Al(OH)_3$ precipitate [**Publication III**]

In **Publication IV**, XRD, FESEM and EDS analyses confirmed that agglomerated $MgAl_2O_4$ based powders can be synthesized by spray drying and subsequent reaction sintering using magnesite rich mine tailings, MgMT1, and $Al(OH)_3$ precipitate from aluminum anodizing process as raw materials. SEM examinations of spray-dried particles (Figure 22) confirmed the results from laser diffraction measurements that particle size distributions for agglomerated powders were with d10 of approximately 10 μm and d90 of 40 μm, thus the powders were suitable for APS spraying.

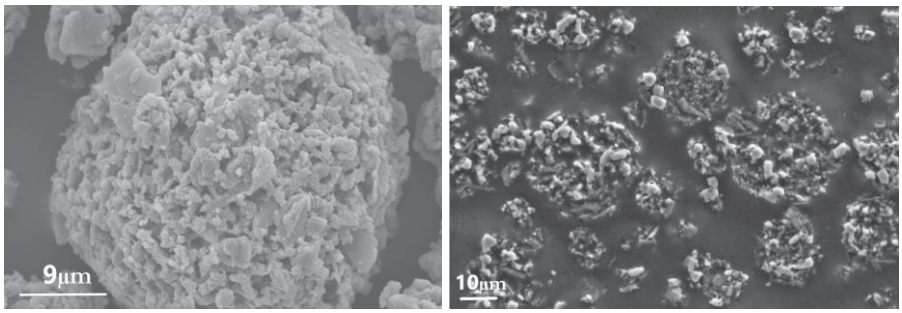

Figure 22. SEM images showing the powder morphology (left) and powder cross-section (right) for synthesized powders utilizing MgMT1 and $Al(OH)_3$ precipitate as raw materials [**Publication IV**]

XRD analyses (Figure 23) suggested that in the case of reference powder prepared from commercial pure raw materials MgO and AlO(OH), atmospheric plasma spraying resulted formation of $MgAl_2O_4$ coating with the cubic $MgAl_2O_4$ spinel phase as the only crystalline phase. In the case of powder prepared from the mixture of mineral side streams, MgMT1 and $Al(OH)_3$ precipitate, XRD pattern reveal that atmospheric plasma spraying resulted in the formation of coating having a partly amorphous phase and partly crystalline $MgAl_2O_4$ structure.

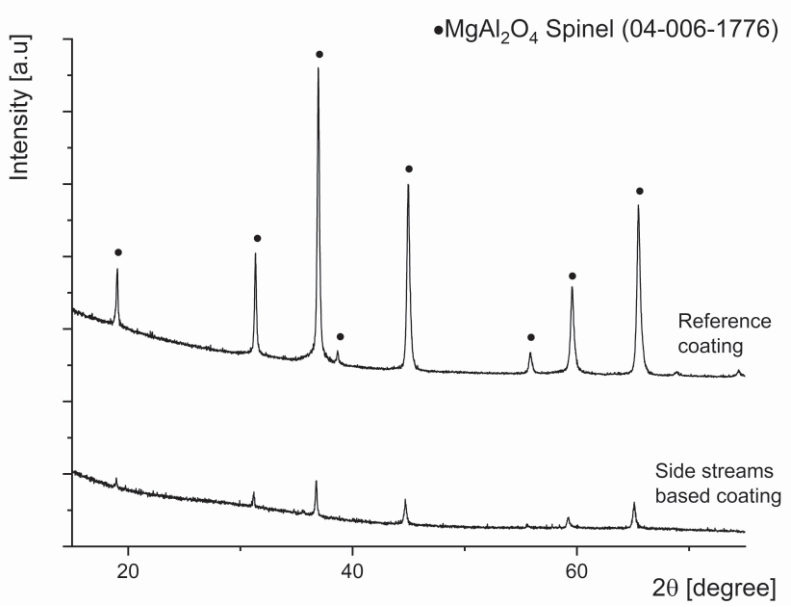

Figure 23. XRD patterns for APS sprayed coatings [**Publication IV**]

In the case of Reference coating, resulted microstructure was lamellar, typical for APS spayed coatings (Figure 24). Indeed, the formation of coatings by APS technique occurs by stacking the lamellae one by one, resulting from the impact, flattening, and finally solidification of the colliding molten particles.

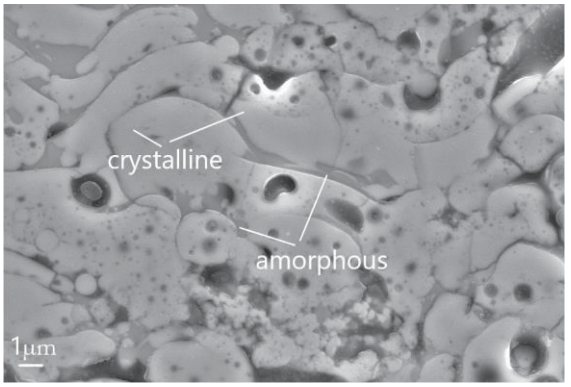

Figure 24. SEM image showing the APS coating microstructure, pure $MgAl_2O_4$ spinel coating [**Publication IV**]

The lamellas were crystalline, but some inter-lamellar areas contained small amounts of amorphous phase, confirmed by FESEM-EBSD investigations (Figure 25). Crystalline lamella thickness was in the order of 1 to 4 μm, but amorphous sections between the crystalline lamellas were only 1 μm or less in thickness.

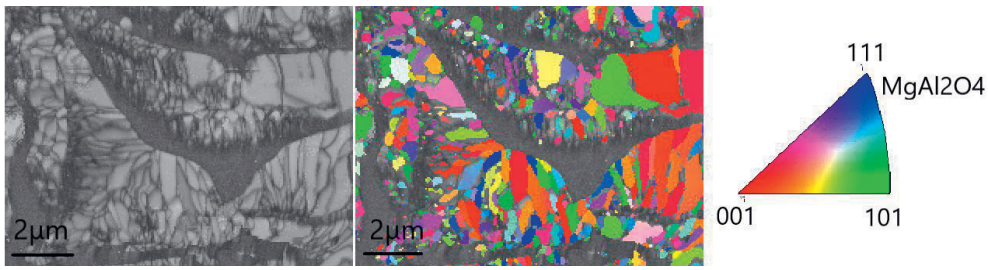

Figure 25. SEM mage and BC maps for the APS spayed coating, pure $MgAl_2O_4$ spinel coating [**Publication IV**]

In the case of powder prepared from the mixture of mineral side streams, magnesite rich mine tailings MgMT1 and $Al(OH)_3$ precipitate from aluminum anodizing process atmospheric plasma spraying resulted, according to FESEM micrographs (Figure 26), to the formation of coating having a partly amorphous and partly crystalline structure. The amorphous phase bound together the cluster of separate $MgAl_2O_4$ crystals. Amorphous phase in the structure is seen as the darker grey contrast in FESEM images. Crystalline phase was concentrated on separate areas with a fine structure and seen in lighter grey contrast than the amorphous phase in FESEM images. Coating also contained some lamellar areas, which had a similar morphology to the reference coating. Due to the complex shape and small thickness, it was not possible to reliably analyze and identify the chemistry of the phases.

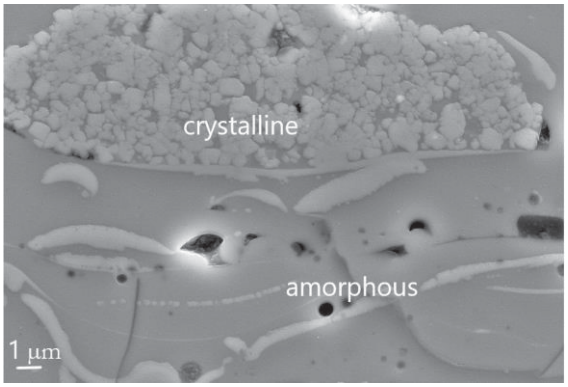

Figure 26. SEM image showing APS sprayed coating microstructure; side streams based $MgAl_2O_4$ spinel coating [**Publication IV**]

6.2.3 Slag as aggregate in refractory castables

In **Publication V**, FESEM analyses revealed that in the case of commercial refractory castable reference, the microstructure was typical refractory material cross section, including aggregates and the surrounding binder phase (Figure 27). The compatibility between the binder and the aggregates was good, as judged based on continuous and dense binder/aggregate interface. This was likely the result from a long development and surface optimization work for commercial product.

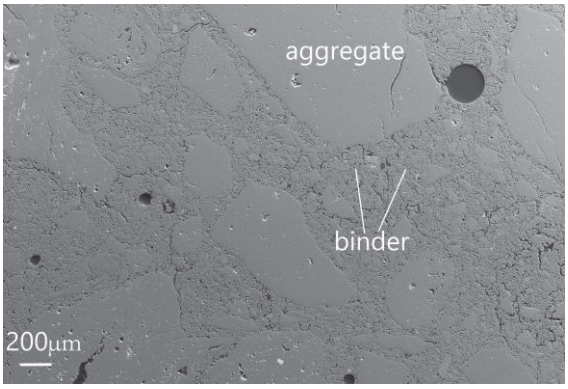

Figure 27. SEM image showing microstructure of the commercial refractory castable reference. [**Publication V**]

In the case of castable prepared using FeCr slag as aggregate and commercial calcium aluminate cement as binder, the formed microstructure also showed a typical refractory material cross section, including aggregates and the surrounding binder phase (Figure 28). However, clear cracks at the binder-aggregate interfaces were detected. The binder was evenly distributed between the aggregates of different size fractions.

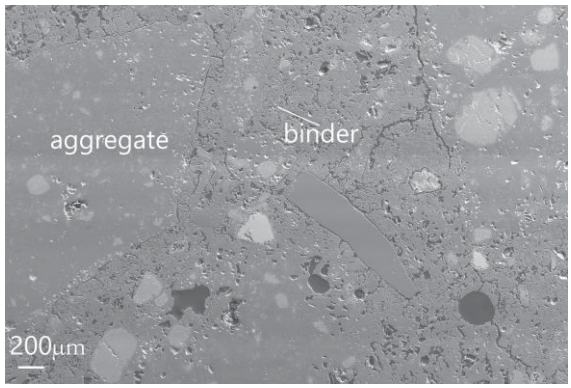

Figure 28. SEM image, showing the Microstructure of the FeCr slag based refractory castable. [**Publication V**]

6.3 Properties of mineral side stream based ceramics

In this section, a summary of the achieved properties for mineral side stream based ceramics is provided. Properties are compared to the corresponding property values of pure references. Additionally, the potential for mineral side streams' utilization as ceramic raw material as well as the limiting factors for utilization are discussed.

Property requirements for ceramic materials for certain application are primarily dictated by the maximum operating temperature, applied stress and operating environment. The quartz and alkali feldspar rich mine tailings based ceramics are intended for applications with high thermal resistance, such as refractory bricks or protective layers. In order to obtain understanding of where the synthesized materials could find use, their melting point, linear thermal expansion, compressive strength and density were determined. The magnesite rich mine tailings based

ceramic coatings are intended for high-temperature electrical insulation applications. For the synthesized coatings, the values of dielectric breakdown strengths were determined. Coatings hardness and abrasion wear resistance were also determined to evaluate their use in harsh environments in addition to electrical insulation. Ferrochrome slag are intended to be used as an aggregate material for refractory castables e.g., insulating secondary layers or bottom zones in metallurgical processes to substitute virgin refractories where both high-temperature and mechanical resistance is needed. Thermo-physical and mechanical properties of FeCr slag based castables were characterized comprehensively including determining their cold crushing strength, density, porosity, linear thermal expansion and thermal conductivity values.

6.3.1 Quartz and feldspar rich mine tailings based ceramics

Properties achieved for quartz and alkali feldspar rich mine tailings based ceramics (FMT1_ceramic, FMT2_ceramic, FMT3_ceramic) are summarized in Table7. Here, the 3:2 mullite ($3Al_2O_3 \cdot 2SiO_2$) composition was aimed for synthesis and reaction sintering experiments. Thus for comparison, properties for pure mullite as a reference are included in a property summary table. Values for pure mullite are gathered from several literature sources and from **Publication II**, in which reference mullite was prepared using commercially available high purity kaolinite ($Al_2Si_2O_5(OH)$) and aluminum oxide hydroxide (AlO(OH)) and the properties were experimentally determined.

Table 7. Summary of properties determined for the quartz and feldspar rich mine tailings based ceramics in comparison to pure mullite [**Publication II**]

Property	FMT1_ceramic	FMT2_ceramic	FMT3_ceramic	Mullite
Main chemical components [wt. %]	FMT1: 33.6 AlO(OH): 66.4 FMT1: alkali feldspars 41%, quartz 40% K-micas 9%	FMT2: 40.4 AlO(OH): 59.6 FMT2: alkali feldspars 49%, K-micas 22%, quartz 11% calcite 6%	FMT3: 28.8 AlO(OH): 71.2 FMT3: quartz 64% K-micas 27% kaolinite 4%	$Al_2Si_2O_5(OH)_4$: 51.8 AlO(OH): 48.2
Melting point [°C]	>1450 (*)	~1100	>1450 (*)	1850 [66] 1830 [67]
Compressive strength [MPa]	62 ±17	65±20	55±21	61±6.7 180 [66] (Bending) 200 [67] (Bending)
Linear thermal expansion [*10^{-6} 1/K]	10.9 (20-1200°C)	10.8 (20-1200°C)	12.7 (20-1000°C)	4.4 [66] 4.5[67] 4.5 - 6.5 [68] (20-1400°C)
Density [g/cm^3]	2.7± 0.02	3.0 ± 0.01	3.1 ± 0.01	3.1± 0.01 3.1 [66] 3.2 [67]

(*) dilatometer test results up to 1450°C

The quartz and alkali feldspar rich, i.e. felsic mine tailings based ceramics, are intended for high-temperature applications, such as refractory bricks or protective layers, thus the melting point/softening point sets the ultimate limit for maximum service temperature for them. Characterization results showed that high alkali-feldspar content caused pure mine tailings FMT1 (main minerals alkali feldspars 41%, quartz 40% and K-micas 9%) and FMT2 (main minerals alkali feldspars 49%, K-micas 22%, quartz 11% and calcite 6%) to melt already above 1100°C. By modifying the chemical composition of the FMT1 with aluminum oxide hydroxide addition (FMT1_ceramic) and after reaction sintering microstructure that included acicular mullite network surrounded by an amorphous phase was generated. The formation of mullite network improves the thermal resistance and enable use at higher temperatures of the formed ceramic materials when compared to pure mine tailings that melt already above 1100°C. In order to prove the improved thermal

resistance, the reaction-sintered specimens (FMT1_ceramic, FMT2_ceramic and FMT3_ceramic) were subjected to dilatometric measurements, which were conducted up to 1450°C (Figure 29). During reheating FMT2_ceramic specimen, where mullite structure was not formed, phase transformation still occurred, first above 1100°C and second above 1300°C, most probably due to liquid phase formation. Thus, the maximum operating temperature for FMT2_ceramic materials is limited below 1100 °C. In contrast, the reheating of FMT1_ceramic and FMT3_ceramic specimens introduced homogenous and linear thermal expansion of the specimen. Thus for those materials, operating temperatures up to 1450 °C are possible. This is below the melting point for pure mullite presented in literature [66] [67] but over 300°C higher than for pure mine tailings.

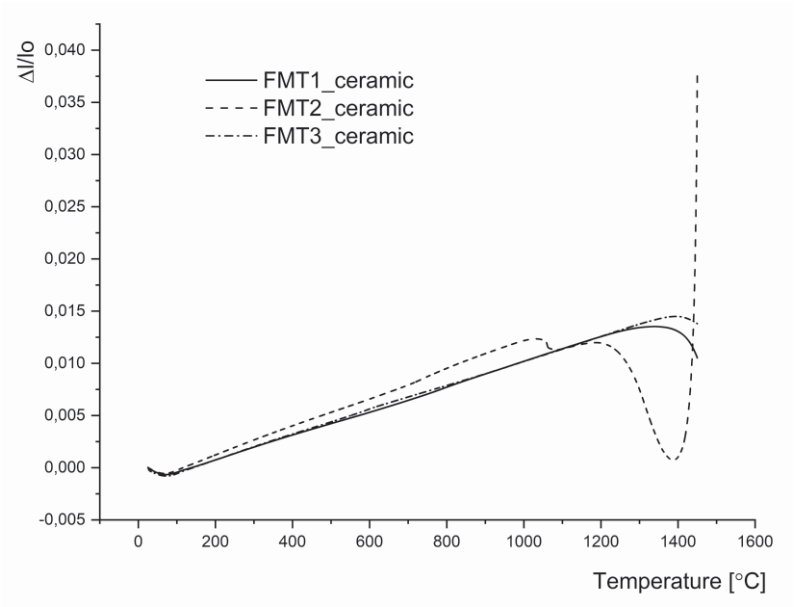

Figure 29. Dilatometer measurement up to 1450°C for FMT1_ceramic, FMT2_ceramic and FMT3_ceramic specimens [**Publication II**]

The strength results in (Table 7) show that sufficient strength values (average 60.7 MPa ± 19.3) in the mine tailings based ceramic specimens were reached, being of the same magnitude than for the 3:2 mullite reference (61.7 ±6.7 MPa). However, compressive strength values for mine tailings based ceramics were considerably lower than bending strength values represented for the pure 3:2 mullite in the literature. The quartz and feldspar rich mine tailings based ceramics are intended for applications, such as refractory bricks or protective layers when the

compressive strength is more informative than the bending strength. Nevertheless, as is well known, the strength of ceramic materials depends on their microstructure and particularly on flaws, like pores, cracks, defects or inclusions in the material. These may act as the points of fracture and easily have an effect on strength values [66]. The consequent range of strength values depends on the flaw distribution parameters, and is the result of both processing and raw material powder characteristics [66]. Linear thermal expansion values for quartz and feldspar rich mine tailings based ceramic are higher (10.8 -12.7x10^{-6} 1/K) than reported for pure mullite (4.4 - 4.5x10^{-6} 1/K) but more closer to values reported for glasses. Density values are in the same order (2.7-3.1 g/cm^3) than for the reference mullite sample (3.1 g/cm^3).

In the case of targeting mullite formation with quartz and feldspar rich mine tailings, the limiting factor for their utilization is firstly the appropriate mineral composition enabling mullite structure formation. It is suggested that only with the particular mineralogical composition the mullite formation is possible regardless of the correct Al:Si ratio in the mixture. One important factor in tailings' mineralogical composition with respect to mullite formation is the amount of alkali feldspars in relation to quartz. Also DSC results shown in (Figure 7) revealed that melting temperatures decrease for the FMT1 and FMT2 mixtures balanced with AlO(OH) additions. Too high alkali content in FMT2 (alkali feldspars 49%, quartz 11%, K-micas 22% and calcite 6%) resulted melt formation when SiO_2 was not able to react with alumina to form mullite. Excess amount of iron-rich mica minerals may also prevent the mullite formation. For this approach, the composition, i.e., the amount of alkalis, plays an important role. If the mullite formation was successful, the second limiting factor for quartz and feldspar rich mine tailings utilization is the softening point/melting point of the amorphous phase surrounding the networked needle-shaped mullite grains in the ceramic microstructure. Thus, the softening point/melting point of this amorphous phase i.e. amount of alkalis defines the maximum operating temperature for quartz and feldspar rich mullite based ceramics. In this study, thermal resistance up to temperature of 1450°C was proved with dilatometer measurements. In future work, the properties are planned to be studied up to higher temperatures.

6.3.2 Magnesite rich mine tailings based ceramic coatings

Properties achieved for atmospheric plasma sprayed magnesite rich mine tailings based ceramic coatings (MgMT1_ceramic coating) are collected in Table 8. For magnesite rich mine tailings based ceramic coatings, the magnesium aluminate spinel ($MgAl_2O_4$) composition was aimed for. The reference $MgAl_2O_4$ coating was prepared using commercially available high purity magnesium oxide (MgO) and aluminum oxide hydroxide (AlO(OH)) as thermal spray powder constituents. Table 8 gathered results show that the values of dielectric breakdown strength measured for MgMT1_ceramic coatings, 24 V/μm, are at the same level as those for pure magnesium aluminate coatings, 23 V/μm, and also close to the DC breakdown strength values of alumina and spinel coatings reported in different literature sources [119][120][109][121][122][123]. Hardness results reveal that the hardness values for MgMT1_ceramic coatings (687±50) are approximately 20% lower than those for the Reference $MgAl_2O_4$ coatings (885±63) from pure commercial raw materials. Abrasive wear test results reveal considerably lower wear rate for MgMT1_ceramic coating than for the pure $MgAl_2O_4$ coating counterparts. These results suggest that the coating hardness is not the only decisive factor for the abrasive wear resistance of the side stream based coatings. Reference $MgAl_2O_4$ coatings were worn through already after 5 min of test duration. When compared to literature of abrasion wear resistance of plasma sprayed ceramic coatings, the values are comparable: ref. [124] reported the weight losses of 156 mg after abrasion wear test of the duration of 60 min for Al_2O_3 coatings, with corresponding values reported also in refs. [125] and [126].

Table 8. Summary of properties for the APS sprayed magnesite rich mine tailings based ceramic coatings in comparison to pure $MgAl_2O_4$ coatings. [**Publication IV**]

Property		**MgMT1_ceramic coating**	**Pure $MgAl_2O_4$ coating**
Main chemical components [wt. %]		MgMT1: 35 $Al(OH)_3$: 65 MgMT1: magnesite 80%, talc 9.4%, chlorite 4.9%	MgO:25.1 AlO(OH):74.9
Dielectric breakdown strength [V/µm]		24.2± 3.8	23± 1.5
Hardness, HV 0.3kg		687±50	885±63
Weight loss [mg] in wear tests	**5min**	17±1.6	100± 3.3
	10min	33±3.5	worn trough
	20min	53±3.3	worn trough
	30min	73±7.2	worn trough

Because abrasive wear tests revealed such a remarkable differences between the mine tailings based MgMT1_ceramic coating and pure $MgAl_2O_4$ coating, the worn surfaces were investigated after the abrasion wear tests using FESEM (Figure 30 (a-b)). For the reference $MgAl_2O_4$ coatings the wear tracks featured a high surface roughness. The large smooth area in the middle of (Figure 30 (a)) indicated the material removal by a lamella-by-lamella mechanism. In the case of MgMT1_ceramic coating (Figure 30 (b)), the wear surface was much smoother than in the case of reference coating, indicating that material losses occurred through the removal of only small fractions of the coating at a time and equally in all areas of the coating.

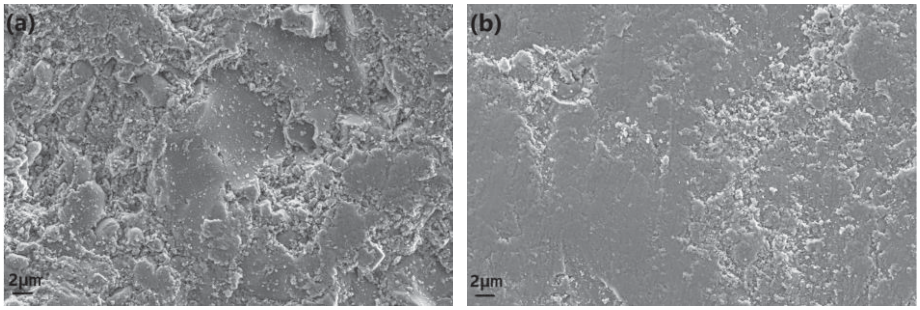

Figure 30. Top-view images of the worn surfaces of coatings for (a) reference $MgAl_2O_4$ coatings and (b) MgMT1_ceramic coating. [**Publication IV**]

The worn surfaces were investigated also in cross sections using FIBSEM (Figure 31 (a-b)). For reference $MgAl_2O_4$ coating (Figure 31 (a)) the cracks were often connected through the lamellar structure, which likely caused the removal of large pieces of the coating when exposed to abrasive wear. This suggests that the lamella boundaries may be the weak point of the material under abrasive wear. On the contrary, in MgMT1_ceramic coating (Figure 31 (b)), there were also visible cracks but these were not systematically connected, thus when exposed to abrasive wear, material losses occurred only locally and mass losses were lower.

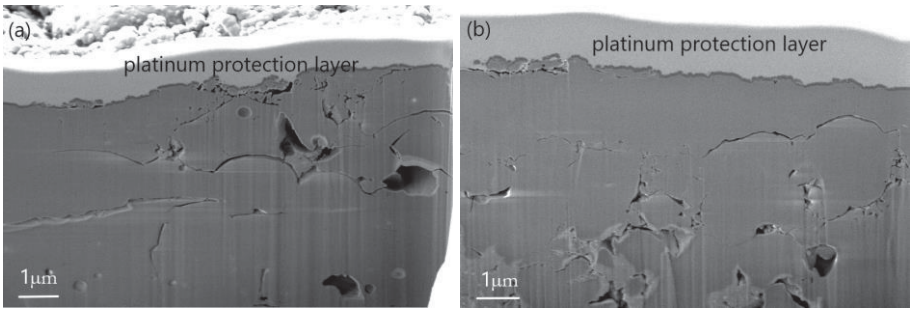

Figure 31. FIBSEM images of the cross-sections of the worn surfaces of coatings (a) reference $MgAl_2O_4$ coatings and (b) MgMT1_ceramic coating. [**Publication IV**]

The values of dielectric breakdown strength of these MgMT1_ceramic coatings were at the same level as for pure $MgAl_2O_4$ coating. Thus, these results suggest,

that the electrical insulation capability of the atmospheric plasma sprayed $MgAl_2O_4$ coatings was hardly affected by the compositional differences between magnesite-rich mine tailings (magnesite 80%, talc 9.4%, chlorite 4.9%) as compared to pure raw materials counterpart. Abrasive wear test results revealed considerably lower wear rate for MgMT1_ceramic coating as compared to pure $MgAl_2O_4$ counterparts. However, hardness values for MgMT1_ceramic coatings were approximately 20% lower than the reference $MgAl_2O_4$ coatings. These results suggested that the coating hardness is not the only decisive factor for the abrasive wear resistance of the side stream based coatings. It was suggested, that the different structure of the MgMT1_ceramic coatings in comparison to pure $MgAl_2O_4$ coatings, particularly the high degree of amorphous phase binding the separate crystalline $MgAl_2O_4$ clusters together, can cause the higher abrasive wear resistance of the coating by changing the wear mechanism. It seems to be possible that inferior mechanical properties of impure $MgAl_2O_4$ spinel is compensated by the introduction of glass phase in plasma spray coatings. These results suggest that mineral side stream materials: magnesite rich mine tailings and $Al(OH)_3$ precipitate use as raw materials, can potentially substitute virgin raw materials in high-temperature electrical insulation ceramic coating applications. However, in the case of utilization of these side stream materials, the limiting factor for their utilization is the softening point of amorphous phase found in the coatings microstructure. The amorphous phase seems to be the origin of the better wear performance of the mining tailing based coatings as comparison to the pure counterparts but at the same time, it also limits the maximum utilization temperature for the side streams based ceramic coatings.

6.3.3 Ferrochrome slag aggregate based refractories

Ferrochrome slag holds potential to be used as an aggregate material for refractory castables e.g., insulating secondary layers or bottom zones in metallurgical processes to substitute virgin refractories. Mechanical and thermo-physical properties of FeCr slag based castables were characterized comprehensively including determining their cold crushing strength, density and porosity, linear expansion, thermal expansion coefficients and thermal conductivity values. Properties achieved for ferrochrome slag aggregate based refractory ceramic castables (FeCrSlag_castable) are gathered in Table 9. For slag based refractory

castables, the maximum slag utilization was aimed for but simultaneously sustaining the good properties, comparable to those of virgin raw material refractory products. Thus, the properties were compared to commercial refractory castable as a reference.

Table 9. Summary of the achieved properties for FeCr slag based refractory castable in comparison to commercial reference [**Publication V**]

Property	**FeCrSlag_castable**	**Commercial reference**
Cold crushing strength [MPa]	91±5.4	149±8.2
Compressive strength at 1200°C [MPa]	9.2±0.5	16±0.5
Apparent solid density [g/cm3]	2.92±0.03	2.78±0.01
Bulk density [g/cm3]	2.39±0.07	2.33±0.02
Open porosity [%]	17.33±1.28	16.12±0.64
Thermal expansion coefficient $\alpha_{RT-1100°C}$ [1/K]	$8.55x10^{-6}$	$6.80x10^{-6}$
Thermal diffusivity αRT-1000°C [mm²/s]	0.80-0.38	1.30-0.73
Thermal conductivity λRT-1000°C [W/m·K]	1.34-0.92	2.41-2.11
Specific heat CpRT-1000°C [J/g·K]	0.69-0.99	0.85-1.3
Maximum service temperature [°C]	1200	1500

According to Table 9 results, cold crushing strength values for FeCrslag_castable are as high as 90 MPa. The cold compressive strength or cold crushing strength (CCS) of a refractory material is an indication of its suitability for the use as refractory, being a combined measure for the strength of the aggregate grains and the bonding system [64]. Recorded strength values for FeCrSlag_castable are clearly below those recorded for the commercial refractory reference material, 149 MPa, but notably higher than the highest strength value, 60 MPa, reported in the studies by Kumar et al. [127] [128] for experimental slag-utilizing castables. Recorded strength values at 1200°C are one tenth of corresponding values at room temperature, but show relatively a similar performance than in CCS values: 9.2±0.5 MPa for the FeCr slag based castable and 16.0±0.5 MPa for the commercial

reference. Density and porosity values for FeCr slag based castable are comparable to those of the commercial reference. These values are typical for the aluminosilicate-based dense refractory castables used as structural components in heat-treatment furnaces and kilns [64]. FeCrSlag_castable specimens exhibit linear expansion and the recorded thermal expansion coefficient values ($8.55 \cdot 10^{-6}$ 1/K) being at approximately 20% higher level than those for the commercial reference ($6.80 \cdot 10^{-6}$ 1/K). FeCrSlag_castable specimens exhibit low thermal diffusivity (from 0.80 to 0.38 mm^2/s) and conductivity (from 1.3 to 0.9 W/m·K) values, which are lower than those for the commercial reference (1.30-0.73 mm^2/s; 2.4-2.1 W/m·K). Thermal conductivity values for the FeCr slag based castables are comparable to values shown in literature for alumina-based insulating castables, with thermal conductivity values of 1.2 W/ m·K at 200°C but having much lower density value of 1.2 g/cm^3 [64]. The liquid phase formation above 1200°C in FeCrSlag_castable specimens sets the maximum service temperature below 1200°C. This is lower than for the studied commercial reference but comparable to, for instance, commercial insulating castable products having the maximum temperature limit of 1100°C [129].

As a summary, thermal insulation properties of the FeCrSlag_castable specimens were even better than those of commercial refractory reference, showing thermal conductivity values as low as $\lambda_{RT\text{-}1000°C}$=1.3 - 0.9 W/m·K. Such a good thermal insulation capability for FeCr slag based castables proved FeCr slag suitability in the use as aggregate in refractory castables for insulation purposes. Furthermore, simultaneously these FeCrSlag_castable have a sufficient strength (60 MPa) to be used in structural components. Typically, insulating refractory materials are designed for low thermal conductivity and not for mechanical strength. The majority of insulating castables are aluminosilicate-based or high-alumina castables, having densities between 0.4-1.45 g/cm^3 and the corresponding porosities of 45-85% [64]. Thus, typical insulating castables show much lower densities and higher porosities than the castables designed for mechanical applications, because generally when density increases and porosity decreases, thermal conductivity will increase. Possible applications for this kind of novel slag-based refractory materials are, e.g., insulating secondary layers or bottom zones in metallurgical process equipment to substitute virgin refractories. A direct contact to molten metal must be avoided (due to temperatures higher than the maximum service temperature of the material), but they are applicable as, e.g. floorings typically exposed to only occasional melt droplets. Indeed, the liquid phase formation at high temperatures is the limiting factor for the use of FeCr slag based materials in structural

applications, suggesting that maximum service temperature for these type of novel FeCr slag based refractory material is 1200°C.

7 CONCLUDING REMARKS

Minerals raw materials are abundant in Earth's crust. However, they are geographically unevenly distributed and economic and political issues constraint the exploitation of small and low-grade deposits. For these reasons, mineral raw materials are often imported in Europe and transported for long distances, resulting in high greenhouse gas emissions particularly in the transportation phase. Additionally, certain mineral raw materials, considered as "critical raw materials" for EU, pose a risk of poor availability and price volatility because some countries outside of the European Union dominate the markets. At the same time, European industry produces large volumes of mineral side streams that end up as waste status or landfill. E.g. side streams from mining processes present the highest proportion of solid mineral residue produced by industry worldwide, with tens of thousands million tons produced annually. Scattered reports on the utilization of mine tailings have indicated their application in construction purposes and as sources for critical metals. In general, the mine tailings are still largely viewed as a waste rather than as a resource.

This thesis concentrates on the utilization of mineral side streams as raw materials for structures in less studied application field: high temperature ceramic materials. The main objective of this thesis was to increase understanding of the potential and limiting factors for the utilization of mineral side streams in added value ceramic materials with high thermal resistance. To reach this goal, the study focused on investigating, how the variation in mineral side stream composition due to natural impurities influences the formation of ceramic material microstructure and achieved properties in comparison to pure raw material counterparts. Ceramic structures based on two typical high temperature compounds, mullite ($3Al_2O_3 \cdot 2SiO_2$) and magnesium aluminate spinel ($MgAl_2O_4$), were targeted in synthesis experiments.

7.1 Novel scientific conclusions

As a general conclusion, it was observed that in the case of mineral side stream based ceramic materials, the achieved properties rather than chemical composition dictated their usability. The properties' characterization proved that utilization of mineral side streams in ceramic materials show properties comparable with and in some cases even better as compared to pure raw material counterparts. In many applications, we consume unnecessarily pure raw materials, if comparable properties can be reached also by utilizing side streams. Thus, the investigated mineral side streams could potentially substitute pure raw materials in ceramic materials taking into account their limitations for maximum operating temperatures.

This thesis provides novel knowledge of the potential of mineral side streams as raw materials for high temperature ceramic materials. The properties of mineral side stream based ceramic materials presented in this thesis set a basis for material property databank creation in future. This kind of databank, including materials composition and volume information about the side streams, can be used as a starting point for the designing new side stream based materials. Variations in side streams compositions can change the ceramic structure and achieved properties. The governing factors presented in this thesis apply in the specific cases presented. Other influencing factors may exist and the variation in composition can also affect the influencing factors. For these reasons, in future studies, it is crucial to concentrate on developing tools to handle side stream materials compositional variation in the material design and manufacturing processes.

The results obtained in this thesis enable the following specific conclusions to be drawn. More detailed revisit of research questions are presented in next section.

1. Quartz and alkali feldspar rich mine tailings have potential to be used as raw materials for mullite-based ceramics intended for operating temperatures up to 1450°C Mullite formation is possible with the investigated sintering conditions (1300°C for 3 hours) if the aluminosilicate melt is formed at suitable temperature range for mullite crystallization. Too high alkali content can cause melt formation at too low temperatures. Factors that affects the formation of aluminosilicate melt and its formation temperature, and, accordingly, the mullite crystallization, are the amount of

alkali feldspars in relation to quartz and the amount of Fe-containing micas. For this approach, the composition, i.e., the amount of alkalis, plays an important role. If mullite formation is successful, the formed microstructure consists of acicular mullite network surrounded by amorphous phase. The softening /melting point of this amorphous phase defines the maximum operating temperature for ceramic material. It may be possible to facilitate the mullite formation with notably higher sintering temperatures or longer times than in this work via solid-state reaction but that need to be solved in future studies.

2. Magnesite-rich mine tailings together with aluminum hydroxide precipitate from aluminum anodizing process have potential as raw materials for thermally sprayed $MgAl_2O_4$ spinel ceramic coatings, having equal level of electrical insulation capability and a higher abrasive wear resistance than pure $MgAl_2O_4$ counterparts. The formed microstructure consists of a partly amorphous structure, in which the amorphous phase binds together the separate crystalline $MgAl_2O_4$ clusters. The different structure in comparison to pure $MgAl_2O_4$ coatings, particularly the high degree of amorphous phase can cause the higher abrasive wear resistance of the coating by changing the wear mechanism. The softening /melting point of this amorphous phase defines the maximum operating temperature and set the limits for the utilization.

3. Ferrochrome slag proves to be a potential aggregate raw material for refractory castables up to the temperature of 1200 °C, with comparable physical and mechanical properties to the commercial reference. Thermal insulation properties of the FeCr slag based specimens are even better than for the commercial dense refractory reference, being at a comparable level to commercial thermally insulating castables. The formed microstructure showed a typical refractory material cross-section, where binder was evenly distributed between the aggregates. The liquid phase formation in FeCr slag is the limiting factor for their use as aggregate in refractory castables.

7.2 Research questions revisited

Figure 32 show the summary of the main results of this thesis, presenting the main causalities between side streams materials and the formed structures and reachable properties.

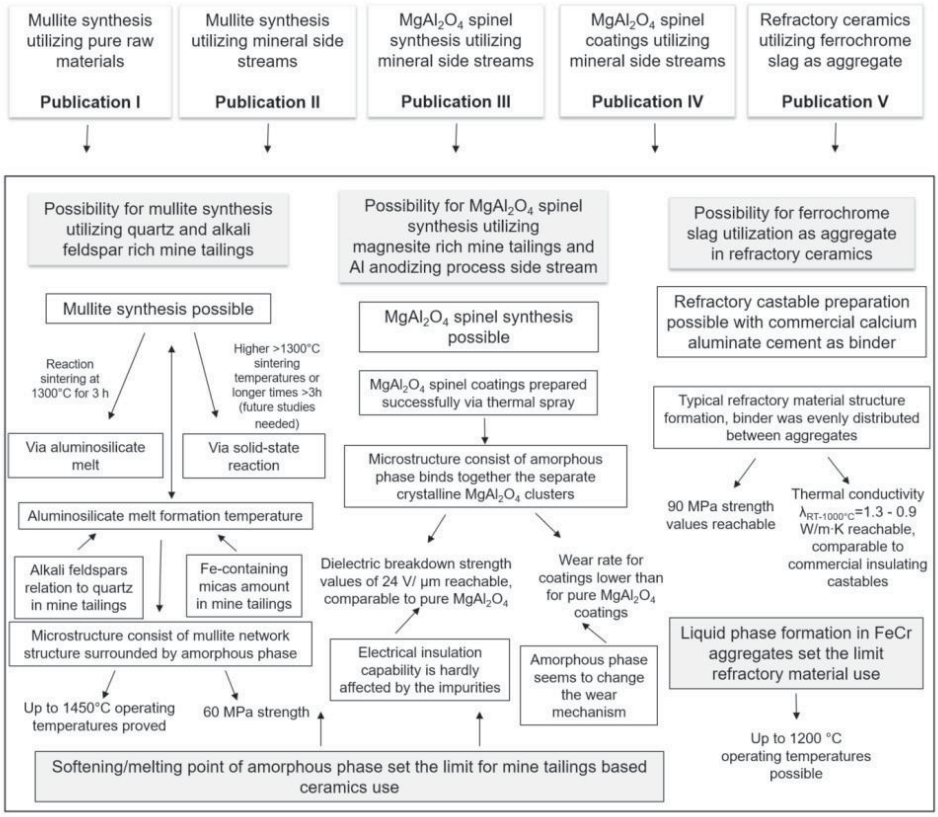

Figure 32. Summary of the main results of this thesis

1. *Is the targeted in high temperature stable ceramic material structure possible to achieve using investigated mineral side stream materials: inert mine tailings from mining industry processes, side stream from aluminum anodizing process and ferrous slag from steel making processes?*

Firstly, results presented in this thesis proved that mullite synthesis is possible utilizing inert quartz and feldspar rich mine tailings from mining industry processes as raw materials. The critical point for mullite synthesis seems to be the formation of aluminosilicate melt. Here, the amount of alkali feldspars in relation to quartz and the amount of Fe-containing micas seems to influence the formation of the aluminosilicate melt and, accordingly, the mullite crystallization. For this approach, the composition, i.e., the amount of alkalis, plays an important role. Without formation of the aluminosilicate melt, mullite crystallization is not possible at the investigated sintering conditions (1300°C for 3 hours). Mullite formation via solid-state reaction at higher sintering temperatures or longer sintering times than in this work needs to be solved in future studies.

Secondly, results presented in this thesis also proved, that $MgAl_2O_4$ spinel synthesis is possible utilizing inert magnesite rich mine tailings and aluminum anodizing process side stream as raw materials. Ceramic coatings with the cubic $MgAl_2O_4$ spinel phase as the only crystalline phase were successfully prepared using atmospheric plasma spraying for coating deposition.

Thirdly, results presented in this thesis prove, that FeCr slag, residues from stainless steel production, can be utilized as aggregate in rectory ceramics. Refractory castables were successfully prepared using FeCr slag as aggregates together with commercial calcium aluminate cement as binder.

2. *How the variation in composition and structure in investigated mineral side streams influences the structure and properties of targeted high- temperature ceramic materials in comparison to pure raw material products?*

Firstly, when utilizing quartz and alkali feldspar rich mine tailings as a raw material, the formed microstructure consists of acicular mullite network surrounded by amorphous phase, if mullite synthesis is successful. Up to 1450°C operating temperatures was proved in this thesis. Up to 1450°C operating temperatures lay below the melting point for pure mullite ceramics being above 1800°C according to literature [66] [67] but still sufficient for several high thermal resistance ceramic applications such as protective layers. Compressive strength values achieved were over 60 MPa being of the same magnitude than for the 3:2 mullite reference.

Secondly, when magnesite rich mine tailings and aluminum anodizing process side stream were utilized as raw materials in thermal spray powder production, atmospheric plasma spraying resulted in the formation of coatings having a partly

amorphous structure in which the amorphous phase binds together the separate crystalline $MgAl_2O_4$ spinel clusters. The values of dielectric breakdown strength of the coatings were at the same level, 24 V/μm, as for pure $MgAl_2O_4$ spinel coatings, and close to DC breakdown strengths of alumina and spinel coatings reported in literature, suggesting that the electrical insulation capability is hardly affected by the impurities in raw materials. Abrasive wear test results revealed considerably lower wear rate for the side stream based coatings as compared to pure $MgAl_2O_4$ counterparts. However, hardness values for the side stream based coatings were approximately 20% lower than for the reference $MgAl_2O_4$ coatings. Thus, the coating hardness is not the only decisive factor for the abrasive wear resistance of the side stream based coatings. The different structure in comparison to pure $MgAl_2O_4$ coatings, particularly the high degree of amorphous phase binding the separate crystalline $MgAl_2O_4$ clusters together, can cause the higher abrasive wear resistance of the coating by changing the wear mechanism. The investigations of worn surfaces after abrasion tests reveal that the amorphous structure seems to be more resistant to abrasive wear compared to lamellar structure. It seems to be possible that inferior mechanical properties of impure $MgAl_2O_4$ spinel can be compensated by the introduction of glass phase in plasma spray coatings.

Thirdly, when utilizing FeCr slag as an aggregate and commercial calcium aluminate cement as a binder in refractory castables preparation, the formed microstructure showed typical refractory material cross sections, including aggregates and surrounding binder phases. Thermal insulation properties of the FeCr slag based specimens were even better than those of commercial refractory reference, showing thermal conductivity values as low as $\lambda_{RT\text{-}1000°C}$=1.3 - 0.9 W/m·K. Thermal insulation properties achieved for FeCr slag based castables were comparable to commercial insulating castables, which typically have a lower density and strength.

3. *What is the potential for the utilization of mineral side streams and what factors limit the use in comparison to pure raw materials?*

Quartz and feldspar rich mine tailings offer potential raw material substitutes for ceramics in certain refractory applications, such as protective layers, where operating temperatures are below 1450°C. However, in future work, the properties are planned to be studied to higher operating temperatures. The limiting factor for quartz and feldspar rich mine tailings utilization is firstly the appropriate mineral

composition that enables mullite structure development via aluminosilicate melt formation. If mullite formation is successful, the softening /melting point of amorphous phase formed in the structure defines the maximum operating temperature of these kind of ceramic materials use.

Magnesite rich mining tailings and aluminum anodizing process side stream can potentially substitute virgin raw materials in high-temperature electrical insulation ceramic coating applications. Thermally sprayed $MgAl_2O_4$ ceramic coatings have an equal level of electrical insulation capability and a higher abrasive wear resistance than pure raw materials counterparts. However, the limiting factor for the utilization of these side streams is the softening point/melting point of the amorphous phase found in the coatings microstructure.

FeCr slag can be used to substitute commercial aggregates in in refractory castables for thermal insulation purposes and simultaneously having sufficient strength for structural components too. Possible applications for this kind of refractory materials are, e.g., insulating secondary layers or bottom zones in metallurgical process equipment A direct contact to molten metal must be avoided, they are applicable to, e.g. floorings when exposed only to occasional melt droplets. The liquid phase formation in FeCr slag aggregates is the limiting factor for their use, limiting that the maximum service temperature below 1200°C.

7.3 Suggestions for future work

In order to reach true circular use of mineral raw materials and secure the markets for secondary raw materials, the barriers related to secondary raw materials use need to overcome. First of all, more harmonized rules need to be established by clarifying the existing rules, when a secondary raw material is no longer legally considered as waste and starts to be a by-product/product. Secondly, one of the main obstacles to the use of secondary raw materials are the uncertainty of their quality and the absence of EU-wide standards for secondary raw materials. Uncertainty about secondary raw materials quality can relate to variation in their composition (chemical or mineralogical) as compared to primary raw materials with constant composition. Additionally, there can exist variation in residue stream itself when accumulating and stored as heaps, i.e., between the surface and the interior. Also, the quality uncertainty can relate to a residues non-desirable physical state, e.g. in slurry state or big lumps, which implies post-processing. Another issue

is the potential presence of undesirable elements or harmful species in material streams. For these reason, it is essential in the future work to concentrate on developing tools to handle this compositional variation in the material design processes. In the case of pure raw materials, standards are based on their chemical composition. For the side streams utilization, the achieved properties rather than chemical composition of the raw materials dictate their usability. Thus, property-based standards need to be developed for secondary raw materials. In addition, methods to increase the traceability of chemicals of concerns need to be developed in the future.

When designing a ceramic material for a certain application, care has to be taken that the maximum temperature attainable in the system is lower than the softening or melting temperature of the ceramic material constituents. In this thesis, the formation of amorphous phase is detected to be the limiting factor for the use of side stream based ceramic materials. In the future work, the stability of this amorphous phase needs to be studied more thoroughly. In this thesis, generic material properties of mineral side stream based ceramics is presented, but the actual operating environment sets the final limits and requirements. In the future work, more application-specific property characterization needs to be provided for these side stream based materials.

In this thesis presented mineral side stream based ceramic materials properties set basis for future material property databank creation However, as mentioned, the mineral side streams can have a great variation in the composition. Thus, the most essential in the future work is to concentrate on developing tools to handle this variation in the material design processes. Thermodynamics is a promising starting point for the development of such tools but also kinetics needs to be taken into account.

REFERENCES

[1] European Commission, 'Minerals and non-energy extractive industries', [Online]. Available: https://ec.europa.eu/growth/sectors/raw-materials/industries/minerals_en. [Accessed: 08-Oct-2019].

[2] G. E. Christidis, 'Industrial minerals: Significance and important characteristics', *Adv. Charact. Ind. Miner. EMU Notes Mineral.*, vol. 9, pp. 1–12, 2011.

[3] M. O'Driscoll, 'Industrial Minerals Basics', *Mines Money, London 2015*, pp. 1-43, 2015.

[4] European Commission, 'Study on the review of the list of Critical Raw Materials - Non-critical Raw Materials Factsheets', pp. 1-476, 2017.

[5] European Commission, 'Study on the review of the list of Critical Raw Materials - Critical Raw Materials Factsheets', pp. 1-515, 2017.

[6] B. G. Lottermoser, *Mine Wastes (third edition): Characterization, treatment and environmental impacts*. Springer, pp. 1-393, 2010.

[7] Tukes, 'Tilastotietoja vuoriteollisuudesta 2017', [Online]. Available: https://tukes.fi/documents/5470659/6373016/Vuoriteollisuustilasto+2017/4d8e29bd-6377-4e7e-9057-a3a89211a38a/Vuoriteollisuustilasto+2017.pdf [Accessed: 17-Mar-2020].

[8] R. McCaffrey, 'Review of 11th Global Slag Conference', [Online]. Available:https://www.globalslag.com/conferences/global-slag/review/global-slag-review-2016. [Accessed: 22-Jun-2019].

[9] P. Niemelä and M. Kauppi, 'Production, characteristics and use of ferrochromium slags', in *INFACON XI, New Delhi, India, 2007*, pp. 171–179, 2007.

[10] European Environment Agency, 'Circular by design', pp. 1-52, 2017.

[11] European Commission, 'Report on Critical Raw Materials and the Circular Economy', pp. 1-80, 2018.

[12] Ellen MacArthur Foundation, 'Growth within: a circular economy vision for a competitive europe', pp. 1-98, 2015.

[13] European Commission, 'Communication from the Commission to the European Parliament, the Council, the European Economic and Social Committee, and the Committee of the Regions. Closing the loop - An EU action plan for the Circular Economy. COM/2015/0614 final', 2015.

[14] European Commission, 'Circular Economy Action Plan - For a cleaner and more competitive Europe', pp. 1-18, 2020.

[15] PACE Platform for Accelerating the Circular Economy, 'The Circularity Gap Report 2019', pp. 1-56, 2019.

[16] P. Kauppila, M. L. Räisänen, and S. Myllyoja, 'Best Environmental Practices in Metal Ore Mining (Metallimalmikaivostoiminnan parhaat ympäristökäytännöt)', pp. 1-222, 2013.

[17] EUROSLAG and EUROFER, 'Position Paper on the status of Ferrous Slag complying with the Waste Framework Directive 2008/98/CE (Articles 5 / 6) and the REACH Regulation', 2012.

[18] European Parliament, 'Understanding waste streams', 2015. [Online]. Available: http://www.europarl.europa.eu/EPRS/EPRS-Briefing-564398-Understanding-waste-streams-FINAL.pdf. [Accessed: 01-Oct-2019].

[19] European Union, 'Directive 2006/21/EC of the European Parliament and of the council of 15 March 2006', 2006.

[20] European Union, 'DECISION No 1386/2013/EU OF THE EUROPEAN PARLIAMENT AND OF THE COUNCIL of 20 November 2013', 2013.

[21] G. Blengini *et al.*, 'Recovery of critical and other raw materials from

mining waste and landfills', European Union, pp. 1-130, 2019.

[22] European Parliament, 'Strategy for secondary raw materials', [Online]. Available: ttps://ec.europa.eu/environment/green-growth/raw-materials/index_en.htm. [Accessed: 10-Jan-2020].

[23] M. Edraki, T. Baumgartl, E. Manlapig, D. Bradshaw, D. M. Franks, and C. J. Moran, 'Designing mine tailings for better environmental, social and economic outcomes: A review of alternative approaches', *J. Clean. Prod.*, vol. 84, no. 1, pp. 411–420, 2014.

[24] A. Akcil and S. Koldas, 'Acid Mine Drainage (AMD): causes, treatment and case studies', *J. Clean. Prod.*, vol. 14, no. 12-13 SPEC. ISS., pp. 1139–1145, 2006.

[25] C. Driussi and J. Jansz, 'Technological options for waste minimisation in the mining industry', *J. Clean. Prod.*, vol. 14, no. 8, pp. 682–688, 2006.

[26] S. Ahmari and L. Zhang, 'Production of eco-friendly bricks from copper mine tailings through geopolymerization', *Constr. Build. Mater.*, vol. 29, pp. 323–331, 2012.

[27] S. Ahmari and L. Zhang, 'Durability and leaching behavior of mine tailings-based geopolymer bricks', *Constr. Build. Mater.*, vol. 44, pp. 743–750, 2013.

[28] J. Kiventerä, L. Golek, J. Yliniemi, V. Ferreira, J. Deja, and M. Illikainen, 'Utilization of sulphidic tailings from gold mine as a raw material in geopolymerization', *Int. J. Miner. Process.*, vol. 149, pp. 104–110, 2016.

[29] L. Zhang, 'Production of bricks from waste materials - A review', *Constr. Build. Mater.*, vol. 47, pp. 643–655, 2013.

[30] D. Feng, J. L. Provis, and J. S. J. Van Deventer, 'Thermal activation of albite for the synthesis of one-part mix geopolymers', *J. Am. Ceram. Soc.*, vol. 95, no. 2, pp. 565–572, 2012.

[31] A. M. Marabini, P. Plescia, D. Maccari, F. Burragato, and M. Pelino, 'New materials from industrial and mining wastes: Glass-ceramics and glass-and rock-wool fibre', *Int. J. Miner. Process.*, vol. 53, no. 1–2, pp. 121–134, 1998.

[32] J. Huisman *et al.*, 'Prospecting Secondary Raw Materials in the Urban Mine and mining wastes (ProSUM) - Final Report', 2017.

[33] L. Weber, T. Leek, and A. Alzubairi, 'An Economic Analysis of the Extraction of Rare Earth Elements from WPPA Sand Tailings Waste Stream', *Univ. Tennessee Honor. Thesis Proj.*, pp. 1–36, 2015.

[34] C. Falagán, B. M. Grail, and D. B. Johnson, 'New approaches for extracting and recovering metals from mine tailings', *Miner. Eng.*, vol. 106, pp. 71–78, 2017.

[35] N. Johansson, J. Krook, M. Eklund, and B. Berglund, 'An integrated review of concepts and initiatives for mining the technosphere: Towards a new taxonomy', *J. Clean. Prod.*, vol. 55, pp. 35–44, 2013.

[36] K. Binnemans, Y. Pontikes, P. T. Jones, T. Van, and B. Blanpain, 'Recovery of Rare Earths From Industrial Waste Residues : a Concise Review', *3rd Int. Slag Valoris. Symp.*, pp. 191–205, 2013.

[37] Y. N. Dhoble and S. Ahmed, 'Review on the innovative uses of steel slag for waste minimization', *J. Mater. Cycles Waste Manag.*, vol. 20, no. 3, pp. 1373–1382, 2018.

[38] İ. Yüksel, 'A review of steel slag usage in construction industry for sustainable development', *Environ. Dev. Sustain.*, vol. 19, no. 2, pp. 369–384, 2017.

[39] EUROSLAG, *Statistic 2016*, no. June. 2016.

[40] J. Zelić, 'Properties of concrete pavements prepared with ferrochromium slag as concrete aggregate', *Cem. Concr. Res.*, vol. 35, no. 12, pp. 2340–2349, 2005.

[41] B. B. Lind, A. M. Fällman, and L. B. Larsson, 'Environmental impact of ferrochrome slag in road construction', *Waste Manag.*, vol. 21, pp. 255–264, 2001.

[42] C. R. Panda, K. K. Mishra, K. C. Panda, B. D. Nayak, and B. B. Nayak, 'Environmental and technical assessment of ferrochrome slag as concrete aggregate material', *Constr. Build. Mater.*, vol. 49, pp. 262–271, 2013.

[43] P. K. Acharya and S. K. Patro, 'Utilization of ferrochrome wastes such as ferrochrome ash and ferrochrome slag in concrete manufacturing', *Waste Manag. Res.*, vol. 34, no. 8, pp. 764–774, 2016.

[44] A. Yilmaz and M. Karaşahin, 'Mechanical properties of ferrochromium slag in granular layers of flexible pavements', *Mater. Struct. Constr.*, vol. 43, no. 3, pp. 309–317, 2010.

[45] M. K. Dash and S. K. Patro, 'Effects of water cooled ferrochrome slag as fine aggregate on the properties of concrete', *Constr. Build. Mater.*, vol. 177, pp. 457–466, 2018.

[46] M. K. Dash, S. K. Patro, and A. K. Rath, 'Sustainable use of industrial-waste as partial replacement of fine aggregate for preparation of concrete – A review', *Int. J. Sustain. Built Environ.*, vol. 5, no. 2, pp. 484–516, 2016.

[47] C. . Grubbs, 'Anodizing of aluminium', *Met. Finish.*, vol. 105, no. 10, pp. 397–412, 2007.

[48] M. T. Souza, L. Simão, O. R. K. Montedo, F. Raupp Pereira, and A. P. N. de Oliveira, 'Aluminum anodizing waste and its uses: An overview of potential applications and market opportunities', *Waste Manag.*, vol. 84, pp. 286–301, 2019.

[49] A. Correia *et al.*, 'Municipal wastewater treatment with anodizing solid waste', *Desalination*, vol. 185, no. 1–3, pp. 341–350, 2005.

[50] J. F. Fu, Y. Q. Zhao, M. Razali, and M. Bruen, 'Response surface optimization of phosphorus species adsorption onto powdered alum sludge', *J. Environ. Sci. Heal. - Part A Toxic/Hazardous Subst. Environ. Eng.*, vol. 43, no. 9, pp. 1100–1107, 2008.

[51] Y. Q. Zhao, M. Razali, A. O. Babatunde, Y. Yang, and M. Bruen, 'Reuse of aluminum-based water treatment sludge to immobilize a wide range of phosphorus contamination: Equilibrium study with different isotherm models', *Sep. Sci. Technol.*, vol. 42, no. 12, pp. 2705–2721, 2007.

[52] F. Raupp-Pereira, R. J. Ball, J. Rocha, J. A. Labrincha, and G. C. Allen, 'New waste based clinkers: Belite and lime formulations', *Cem. Concr. Res.*, vol. 38, no. 4, pp. 511–521, 2008.

[53] S. Onutai, S. Jiemsirilers, P. Thavorniti, and T. Kobayashi, 'Aluminium hydroxide waste based geopolymer composed of fly ash for sustainable cement materials', *Constr. Build. Mater.*, vol. 101, pp. 298–308, 2015.

[54] M. B. Ogundiran, H. W. Nugteren, and G. J. Witkamp, 'Geopolymerisation of fly ashes with waste aluminium anodising etching solutions', *J. Environ. Manage.*, vol. 181, pp. 118–123, 2016.

[55] F. Raupp-Pereira, D. Hotza, A. M. Segadães, and J. A. Labrincha, 'Ceramic formulations prepared with industrial wastes and natural sub-products', *Ceram. Int.*, vol. 32, no. 2, pp. 173–179, 2006.

[56] F. Raupp-Pereira, M. J. Ribeiro, A. M. Segadães, and J. A. Labrincha, 'Extrusion and property characterisation of waste-based ceramic formulations', *J. Eur. Ceram. Soc.*, vol. 27, no. 5, pp. 2333–2340, 2007.

[57] M. J. Ribeiro, D. U. Tulyaganov, J. M. Ferreira, and J. A. Labrincha, 'Recycling of Al-rich industrial sludge in refractory ceramic pressed bodies', *Ceram. Int.*, vol. 28, no. 3, pp. 319–326, 2002.

[58] European Commission, 'FWC Sector Competitiveness Studies-Competitiveness of the Ceramics Sector. Within the Framework Contract of Sectoral Competitiveness Studies – ENTR/06/054 Final report, 13 October 2008', 2008.

[59] European Commission, 'Raw materials, metals, minerals and forest-based industries - Ceramics', [Online]. Available: https://ec.europa.eu/growth/sectors/raw-materials/industries/non-metals/ceramics_en. [Accessed: 10-Oct-2019].

[60] EUROPEAN REFRACTORIES PRODUCERS' and FEDERATION, *Refractory Ceramics and Industrial Minerals are Critical for European Industry*, vol. 32. 2009.

[61] H. Fang, J. D. Smith, and K. D. Peaslee, 'Study of spent refractory waste recycling from metal manufacturers in Missouri', *Resour. Conserv. Recycl.*, vol. 25, no. 2, pp. 111–124, 1999.

[62] C. Sadik, I. E. El Amrani, and A. Albizane, 'Recent advances in silica-alumina refractory: A review', *J. Asian Ceram. Soc.*, vol. 2, no. 2, pp. 83–96, 2014.

[63] E. Guéguen, J. Hartenstein, and C. Fricke-begemann, 'Raw material challenges in refractory application', *Proc. Berliner Konf. Miner. Nebenprodukte und Abfaelle*, pp. 489–502, 2014.

[64] C. A. (ed) Schacht, *Refractories handbook*. Taylor & Francis Group, LLC, pp. 1-491, 2004.

[65] J. F. Shackelford and R. H. Doremus, Eds., *Ceramic and Glass Materials - Structure, Properties and Processing*. Springer, 2008.

[66] K. Komeya and M. Matsui, *High Temperature Engineering Ceramics*. WILEY-VCH Verlag GmbH & Co KGaA, 2006.

[67] H. Schneider, J. Schreuer, and B. Hildmann, 'Structure and properties of mullite-A review', *J. Eur. Ceram. Soc.*, vol. 28, no. 2, pp. 329–344, 2008.

[68] D. Frulli, 'Production and Properties of Refractory Raw Materials Based on Andalusite and Mullite - Influence of Impurities in the Refractory Behaviour', *Refract. Worldforum*, vol. 8, no. 3, pp. 1–4, 2016.

[69] H. Schneider, R. X. Fischer, and J. Schreuer, 'Mullite: Crystal Structure and Related Properties', *J. Am. Ceram. Soc.*, vol. 98, no. 10, pp. 2948–2967, 2015.

[70] C. Y. Chen, G. S. Lan, and W. H. Tuan, 'Preparation of mullite by the reaction sintering of kaolinite and alumina', *J. Eur. Ceram. Soc.*, vol. 20, no. 14–15, pp. 2519–2525, 2000.

[71] Y. F. Chen, M. C. Wang, and M. H. Hon, 'Phase transformation and growth of mullite in kaolin ceramics', *J. Eur. Ceram. Soc.*, vol. 24, no. 8, pp. 2389–2397, 2004.

[72] Choo, Mohd Salleh, Kok, and Matori, 'A Review on Synthesis of Mullite Ceramics from Industrial Wastes', *Recycling*, vol. 4, no. 3, p. 39, 2019.

[73] M. J. Ribeiro and J. A. Labrincha, 'Properties of sintered mullite and cordierite pressed bodies manufactured using Al-rich anodising sludge', *Ceram. Int.*, vol. 34, no. 3, pp. 593–597, 2008.

[74] M. J. Ribeiro, D. U. Tulyagavov, J. M. Ferreira, and J. A. Labrincha, 'High temperature mullite dissolution in ceramic bodies derived from Al-

rich sludge', *J. Eur. Ceram. Soc.*, vol. 25, no. 5, pp. 703–710, 2005.

[75] A. Francis and S. Vilminot, 'Crystallisation kinetics of mullite glass-ceramics obtained from alumina-silica wastes', *Int. J. Sustain. Eng.*, vol. 6, no. 1, pp. 74–81, 2013.

[76] J. S. Jung, H. C. Park, and R. Stevens, 'Mullite ceramics derived from coal fly ash', *J. Mater. Sci. Lett.*, vol. 20, pp. 1089 – 1091, 2001.

[77] Y. Dong, X. Feng, X. Feng, Y. Ding, X. Liu, and G. Meng, 'Preparation of low-cost mullite ceramics from natural bauxite and industrial waste fly ash', *J. Alloys Compd.*, vol. 460, no. 1–2, pp. 599–606, 2008.

[78] M. L. Bouchetou, J. P. Ildefonse, J. Poirier, and P. Daniellou, 'Mullite grown from fired andalusite grains: The role of impurities and of the high temperature liquid phase on the kinetics of mullitization and consequences on thermal shocks resistance', *Ceram. Int.*, vol. 31, no. 7, pp. 999–1005, 2005.

[79] J. F. Shackelford and R. H. Doremus, Eds., *Ceramic and Glass Materials - Structure, Properties and Processing*. Springer, pp. 1-199, 2008.

[80] R. Dal Maschio, B. Fabbri, and C. Fiori, 'Industrial Applications of Refractories Containing Magnesium Aluminate Spinel', *Ind. Ceram.*, vol. 8, no. 3, pp. 121–126, 1988.

[81] D. Schmidtmeier, G. Büchel, and A. Buhr, 'Magnesium aluminate spinel raw materials for high performance refractories for steel ladles', *Ceram. Mater.*, vol. 61, no. 4, pp. 223–227, 2009.

[82] I. Ganesh, 'A review on magnesium aluminate (MgAl2O4) spinel: Synthesis, processing and applications', *Int. Mater. Rev.*, vol. 58, no. 2, pp. 63–112, 2013.

[83] M. A. L. Braulio, M. Rigaud, A. Buhr, C. Parr, and V. C. Pandolfelli, 'Spinel-containing alumina-based refractory castables', *Ceram. Int.*, vol. 37, no. 6, pp. 1705–1724, 2011.

[84] I. Ganesh, S. Bhattacharjee, B. P. Saha, R. Johnson, and Y. R. Mahajan, 'A new sintering aid for magnesium aluminate spinel', *Ceram. Int.*, vol. 27, no. 7, pp. 773–779, 2001.

[85] Y. Zhang, Z. hui Guo, Z. yu Han, X. yuan Xiao, and C. Peng, 'Feasibility of aluminum recovery and MgAl2O4 spinel synthesis from secondary aluminum dross', *Int. J. Miner. Metall. Mater.*, vol. 26, no. 3, pp. 309–318, 2019.

[86] Z. A. M. T. Hashishin, Y. Kodera, T. Yamamoto, M. Ohyanagi, 'Synthesis of (Mg,Si)Al2O4 Spinel from Aluminum Dross', *J. Am. Ceram. Soc.*, vol. 87, no. 3, pp. 496–499, 2004.

[87] W. L. Bi, 'Synthesis of MgAl2O4 Spinel-Corundum Composite with Waste Refractory', *Adv. Mater. Res.*, no. 287–290, pp. 467–471, 2011.

[88] J. Meng, W. Chen, J. Zhao, and L. Liu, 'Study of the synthesis of MgAl2O4 spinel refractory from waste chromium slag of a chrome plant in China', *Miner. Met. Mater. Ser.*, vol. Part F6, pp. 341–355, 2018.

[89] G. Bertrand, C. Meunier, P. Bertrand, and C. Coddet, 'Dried particle plasma spray in-flight synthesis of spinel coatings', *J. Eur. Ceram. Soc.*, vol. 22, no. 6, pp. 891–902, 2002.

[90] M. Niittymäki, K. Lahti, T. Suhonen, and J. Metsäjoki, 'Dielectric Breakdown Strength of Thermally Sprayed Ceramic Coatings: Effects of Different Test Arrangements', *J. Therm. Spray Technol.*, vol. 24, no. 3, pp. 542–551, 2015.

[91] J. R. Davis, Ed., *Handbook of Thermal Spray Technology*. ASM International, pp. 1-332, 2004.

[92] L. Pawlowski, *The Science and Engineering of Thermal Spray Coatings, Second Edition*. John Wiley & Sons Ltd, 2008.

[93] P. Vuoristo, 'Thermal Spray Coating Processes', *Compr. Mater. Process.*, pp. 229–276, Jan. 2014.

[94] S. Solismaa *et al.*, 'Valorization of Finnish mining tailings for use in the ceramics industry', *Bull. Geol. Soc. Finl.*, vol. 90, no. 1, pp. 33–54, 2018.

[95] I. Haapala and O. T. Rämö, 'Mineral Deposits Related to Granitic Rocks', *Miner. Depos. Finl.*, pp. 531–556, Jan. 2015.

[96] P. B. Sorjonen-Ward *et al.*, 'Exploration Targeting and Geological

Context of Gold Mineralization in the Neoarchean Ilomantsi Greenstone Belt in Eastern Finland', *Miner. Depos. Finl.*, pp. 435–466, Jan. 2015.

[97] M. Lehtinen, 'Industrial minerals and rocks', *Miner. Depos. Finl.*, pp. 658–705, 2015.

[98] M.-L. Räisänen, *Magnesiittirikastushiekan ympäristökelpoisuus. Geological Survey of Finland, 2004 (in Finnish)*. 2004.

[99] A. Ismailov, N. Merilaita, S. Solismaa, M. Karhu, and E. Levänen, 'Utilizing mixed-mineralogy ferroan magnesite tailings as the source of magnesium oxide in magnesium potassium phosphate cement', *Constr. Build. Mater.*, vol. 231, 2020.

[100] A. S. Vusikhis, R. I. Gulyaeva, L. I. Leont'ev, L. A. Ovchinnikova, and E. N. Selivanov, 'Kinetic features of breunnerite decarbonization', *Russ. Metall.*, vol. 2016, no. 9, pp. 793–797, 2016.

[101] H. T. Makkonen and P. Tanskanen, *Outokumpu Chrome Oy:n Ferrokromikuonan mineralogia ja liukoisuusominaisuudet*. University of Oulu, 2005.

[102] T. Karhu, M., Lintunen, P., Lagerbom, J., & Lindroos, 'Characterisation of steel industry slag suitability as raw material for refractory castables', *Conf. Proc. 5th Int. Slag Valoris. Symp. KU Leuven.*, pp. 71–74, 2017.

[103] P. Karhu, M., Piotrowska, P., Talling, B., Hum, J., Boccaccini, A. R., & Lintunen, 'Valorization of the steel industry slag and by-products as raw material asset for innovative refractories', *Conf. Proc. 10th Int. Conf. Environ. Tech. Implic. Constr. with Altern. Mater. WASCON 2018, Tampere, Finl.*, pp. 218–225, 2018.

[104] S. A. A. M. Fennis and J. C. Walraven, 'Using particle packing technology for sustainable concrete mixture design', *Heron*, vol. 57, no. 2, pp. 73–101, 2012.

[105] B. Myhre and A. M. Hundere, 'The use of particle size distribution in development of refractory castables', *Proc. XXV ALAFAR Congr.*, pp. 1–4, 1996.

[106] European Standard, 'EN 196-1, Methods of testing cement; Determination of strenght'. 1987.

[107] ISO (the International Organization for Standardization), 'ISO 18754:2013 Fine Ceramics (advanced ceramics, advanced technical ceramics) - Determination of density and apparent porosity', 2013.

[108] ISO (the International Organization for Standardization), 'ISO 20504:2006, Fine Ceramics (Advanced Ceramics, Advanced Technical Ceramics) - Test method for compressive behaviour of continuous fibre reinforced composites at room temperature', 2006.

[109] M. Niittymaki, K. Lahti, T. Suhonen, and J. Metsajoki, 'DC conduction and breakdown behavior of thermally sprayed ceramic coatings', *IEEE Trans. Dielectr. Electr. Insul.*, vol. 24, no. 1, pp. 499–510, 2017.

[110] ASTM, 'ASTM G65-16e1, Standard Test Method for Measuring Abrasion Using the Dry Sand/Rubber Wheel Apparatus, ASTM International, West Conshohocken, PA, 2016, www.astm.org', 2016.

[111] H.-R. Wenk and A. Bulakh, *Minerals - Their Constitution and Origin*. Cambridge University Press, Cambridge, pp. 1-666, 2003.

[112] A. Navrotsky, C. Capobianco, and J. Stebbins, 'Some thermodynamic and experimental constraints on the melting of albite at atmospheric and high pressure', *J. Geol.*, vol. 90, pp. 679–698, 1982.

[113] L. A. Johnson and R. A. McCauley, 'The thermal behavior of albite as observed by DTA', *Thermochim. Acta*, vol. 437, no. 1–2, pp. 134–139, 2005.

[114] R. Sokolář and L. Vodová, 'Sintering of feldspar rocks from czech quarries', *J. Ceram. Soc. Jpn.*, vol. 123, pp. 62–67, 2015.

[115] T. Yoshida, T. Tanaka, H. Yoshida, T. Funabiki, S. Yoshida, and T. Murata, 'Study of dehydration of magnesium hydroxide', *J. Phys. Chem.*, vol. 99, no. 27, pp. 10890–10896, 1995.

[116] S. J. Wilson, 'The dehydration of boehmite, γ-AlOOH, to γ-Al2O3', *J. Solid State Chem.*, vol. 30, no. 2, pp. 247–255, Nov. 1979.

[117] P. Orosco, L. Barbosa, and M. D. C. Ruiz, 'Synthesis of magnesium aluminate spinel by periclase and alumina chlorination', *Mater. Res. Bull.*, vol. 59, pp. 337–340, 2014.

[118] Ž. . Živković and B. Dobovišek, 'Kinetics of aluminium hydroxide dehydration', *J. Therm. Anal.*, vol. 12, no. 207, 1977.

[119] F. L. Toma, S. Scheitz, L. M. Berger, V. Sauchuk, M. Kusnezoff, and S. Thiele, 'Comparative study of the electrical properties and characteristics of thermally sprayed alumina and spinel coatings', *J. Therm. Spray Technol.*, vol. 20, no. 1–2, pp. 195–204, 2011.

[120] M. Niittymaki, I. Rytoluoto, K. Lahti, J. Metsajoki, and T. Suhonen, 'Role of microstructure in dielectric properties of thermally sprayed ceramic coatings', *Proc. 2016 IEEE Int. Conf. Dielectr. ICD 2016*, vol. 2, pp. 1102–1105, 2016.

[121] M. Niittymaki, T. Suhonen, K. Lahti, J. Metsajoki, and U. Kanerva, 'Influence of humidity and temperature on the dielectric properties of thermally sprayed ceramic $MgAl_2O_4$ coatings', *IEEE Conference on Electrical Insulation and Dielectric Phenomena, CEIDP, 19 Oct - 22 Oct, 2014, Des Moines, IA, USA.* pp. 94–97, 2014.

[122] M. Niittymaki, K. Lahti, T. Suhonen, and J. Metsajoki, 'Effect of temperature and humidity on dielectric properties of thermally sprayed alumina coatings', *IEEE Trans. Dielectr. Electr. Insul.*, vol. 25, no. 3, pp. 908–918, 2018.

[123] F. L. Toma *et al.*, 'Comparison of the microstructural characteristics and electrical properties of thermally sprayed Al 2O 3 coatings from aqueous suspensions and feedstock powders', *J. Therm. Spray Technol.*, vol. 21, no. 3–4, pp. 480–488, 2012.

[124] V. Matikainen, K. Niemi, H. Koivuluoto, and P. Vuoristo, 'Abrasion, erosion and cavitation erosion wear properties of thermally sprayed alumina based coatings', *Coatings*, vol. 4, no. 1, pp. 18–36, 2014.

[125] R. S. Lima, C. Moreau, and B. R. Marple, 'HVOF-sprayed coatings engineered from mixtures of nanostructured and submicron Al2O3-TiO2 powders: An enhanced wear performance', *J. Therm. Spray Technol.*, vol. 16, no. December, pp. 866–872, 2007.

[126] E. H. Jordan *et al.*, 'Fabrication and evaluation of plasma sprayed nanostructured alumina-titania coatings with superior properties', *Mater. Sci. Eng. A*, vol. 301, no. 1, pp. 80–89, 2001.

[127] A. Kumar, Pattem Hemanth Srivastava, V. Kumar, and V. K. Singh, 'Implementation of industrial waste ferrochrome slag in conventionaland low cement castables: Effect of calcined aluminao Title', *J. Asian Ceram. Soc.*, vol. 2, pp. 371–379, 2014.

[128] P. H. Kumar, A. Srivastava, V. Kumar, M. R. Majhi, and V. K. Singh, 'Implementation of industrial waste ferrochrome slag in conventional and low cement castables : Effect of microsilica addition', *J. Asian Ceram. Soc.*, vol. 2, no. 2, pp. 169–175, 2014.

[129] 'ALLIED MINERAL PRODUCTS- Global Refractory Solutions'. [Online].Available:https://alliedmineral.com/wp-content/uploads/2017/12/Formatted-POWER-product-tables_CASTABLES.pdf. [Accessed: 15-Oct-2019].

PUBLICATIONS

PUBLICATION I

Reaction Heat Utilization in Aluminosilicate-Based Ceramics Synthesis and Sintering

Marjaana Karhu, Juha Lagerbom, Päivi Kivikytö-Reponen, Arnold Ismailov, Erkki Levänen

Journal of Ceramic Science and Technology 08 (01) (2017) 101-112

https://doi.org/10.4416/JCST2016-00094

Publication reprinted with the permission of the copyright holders.

Journal of
Ceramic Science
and Technology

J. Ceram. Sci. Tech., **08** [01] 101-112 (2017)
DOI: 10.4416/JCST2016-00094
available online at: http://www.ceramic-science.com
© 2017 Göller Verlag

Reaction Heat Utilization in Aluminosilicate-Based Ceramics Synthesis and Sintering

M. Karhu*[1], J. Lagerbom[1], P. Kivikytö-Reponen[1], A. Ismailov[2], E. Levänen[2]

[1]VTT Technical Research Centre of Finland Ltd, Sinitaival 6, P.O. Box 1300, FI-33101 Tampere, Finland
[2]Tampere University of Technology, Korkeakoulunkatu 10, P.O. Box 527, FI-33101 Tampere, Finland

received November 2, 2016; received in revised form December 16, 2016; accepted January 19, 2017

Abstract

Self-propagating high-temperature synthesis (SHS) is a widely known and extensively studied highly exothermic-reaction-utilizing technique for making certain advanced composites and intermetallic compounds. However, only few studies have been published about the SHS of pure aluminosilicate ceramics. In the current work, possibilities for aluminosilicate ceramic synthesis and sintering requiring less energy based on the utilization of SHS in air was studied. Kaolinite powder and exothermically reactive metallic aluminium powder were used as raw materials. Thermodynamic calculations for the possible reactions and reaction paths were performed to show the theoretical possibilities for SHS utilization. The chemical reactions, thermal expansion behaviour and formed phase- and microstructures after SHS were compared to the conventional reaction sintering of mullite. Results conclude that highly exothermic reactions above 900 °C relating mainly to aluminium oxidation can ignite the SHS reaction in air atmosphere. After initialization, the reaction proceeded in a self-sustaining manner through entire test pieces, resulting in the formation of an Al_2O_3 - Si phase structure. Thermodynamic calculations showed the total energy balance for mullite formation from aluminium and kaolinite mixtures as highly exothermic in nature only if sufficient oxygen is available to complete the reactions. However, future research is needed to fully utilize SHS in aluminosilicate ceramics processing.

Keywords: Aluminosilicate ceramics, self-propagating high-temperature synthesis, SHS, exothermic reactions, synthesis, sintering

I. Introduction

Ceramics processing, e.g. mullite reaction sintering, normally requires high temperatures and long processing times that consume a lot of energy, increasing the cost of the products and leading to a high environmental impact. One process technology opportunity to lower processing energy is to utilize the reaction heat released from exothermic ceramic compound reactions. A lower overall energy consumption can then be achieved by producing part of the heat internally in the process and utilizing this extra heat in ceramic material processing and synthesis. One widely known and extensively studied technique utilizing highly exothermic reactions is self-propagating high temperature synthesis (SHS). SHS is based on a system's ability to react exothermally and proceed when ignited. The high activation energy and high compound formation enthalpy of the synthesis reaction is utilized to run a self-sustained reaction; thus, once ignited, the reaction continues on its own [1,2]. When the initial reagents are ignited, they spontaneously transform into products and a reaction front is formed that propagates through the reactants in the form of a combustion wave. Owing to the exothermic heat of reaction and subsequent high temperature of the reaction products, it is possible to combine the synthesis and densification steps into one process. The SHS process is traditionally limited only to highly exothermic reactions for making certain advanced composites and intermetallic compounds [3,4].

Mullite is one example of an advanced aluminosilicate ceramic material for high-temperature applications owing to its favourable properties such as high melting point (1830 °C), moderate thermal expansion coefficient (4.5×10^{-6} 1/K), good resistance to thermal shock, good chemical durability, excellent creep resistance and sufficient mechanical strength [5,6]. The stoichiometric 3:2 mullite ($3Al_2O_3$ $2SiO_2$) is the only thermodynamically stable phase in the $SiO_2 \pm Al_2O_3$ system [7]. Various starting materials and preparation methods have been used to prepare mullite ceramics. For the conventional fabrication method, the solid-state reaction of high-purity Al_2O_3 and SiO_2 (quartz), the mullitization temperature is as high as 1600 °C [8]. Kaolinite powder is commonly used as a raw material for mullite synthesis owing to its low cost, and upon heating it reacts to form mullite and silica [9]. There are several studies on mullite reaction sintering, for example in the study by Chen *et al.* [7], it was demonstrated that mullite specimens can be prepared by reaction sintering of mechanically mixed kaolinite and alumina powders.

Few studies have been published about the SHS synthesis of mullite-based composites: zirconia-mullite/TiB_2 composite [6], mullite/TiB_2 composite [8] and TaB/TaB_2/mullite composites [10]. However, only few studies have been pub-

* Corresponding author: marjaana.karhu@vtt.fi

lished about exothermic-assisted synthesis and sintering of pure aluminosilicate-based ceramics. In the recent study by Esharghawi *et al.* [11], porous mullite-based bodies were produced in flowing oxygen by means of SHS starting from kaolin, Al and Mg powder mixtures. They found out that the heat of the aluminium oxidation reaction in a pure oxygen atmosphere could be used to ignite the SHS reaction. A sufficient amount of oxygen was not obtained using air. Pure mullite was not obtained, but in addition to mullite, Si and Al in metallic phases, quartz, α-alumina and $MgAl_2O_4$ spinel were also present after SHS. In the work by Podbolotov *et al.* [12], preparation of aluminosilicate coatings with a mullite weight content of 61 – 72 % by means of SHS was studied using aluminium powder, quartz sand and kaolinite clay as raw materials together with different binders and additives. The exact compositions and SHS synthesis steps were not exactly given in the study. In the studies by Kazhikenova *et al.* [13] and by Zharmenov *et al.* [14, 15], the theoretical principles behind the SHS of refractory materials (magnesia, chromite-magnesia, forsterite, dolomite and chamotte refractories) were studied. Only theoretical calculations were reported and pure aluminosilicate refractories were not considered in these studies. A recently published study by Mansurov *et al.* [16] reported the influence of mechanochemical treatment of $CaO\text{-}SiO_2\text{-}Al_2O_3$ system minerals used as components in a mixture for SHS synthesis of ceramics. But pure aluminosilicate ceramics were not considered in this study either. There are also few studies presented by Balmori-Ramirez *et al.* [17], Erharghawi *et al.* [18], Khabas *et al.* [19] and Anggono *et al.* [20] where the aluminium powder was successfully utilized as the raw material for mullite powder synthesis, but the possibilities of SHS utilization were not studied.

In the current work, the possibilities for energy savings in pure aluminosilicate ceramic synthesis and sintering by utilizing SHS were studied. Kaolinite and exothermically reactive aluminium powder were used as raw materials. The aim of the study was to synthesize low-energy-intensity pure aluminosilicate-based ceramic bodies by means of SHS in air atmosphere, which has not been previously reported. Air atmosphere enables a more economical and sustainable option for synthesis atmosphere compared to using pure oxygen. Thermodynamic calculations for the possible reactions and reaction paths were performed beyond earlier publications in this field to show the theoretical possibilities for SHS utilization in pure aluminosilicate ceramics processing. The thermal reactions, thermal expansion and formed phase- and microstructures after SHS were evaluated and compared to conventional reaction sintering of mullite. The effects of kaolinite powder heat-treatment and aluminium particle size on chemical reactions that were not previously reported with these raw material mixtures were also studied.

II. Experimental Procedure

(1) Starting materials

Commercially available kaolinite powder ($Al_2O_3{\cdot}2SiO_2{\cdot}2H_2O$ or $Al_2Si_2O_5(OH)_4$), aluminium oxide hydroxide (AlO(OH, boehmite) powder and aluminium (Al) powder were used as raw materials. Kaolinite was provided by Merck (average grain size < 6.68 μm, high kaolin purity), aluminium oxide hydroxide by Sasol Germany GmbH (average grain size < 0.77 μm) and aluminium powder by ECKA Granules (average grain sizes < 27 μm and the same air classified to 17 μm, purity 99 %). Four mixtures were prepared from the selected raw materials. Recipes were calculated for stoichiometric 3:2 mullite synthesis; details are presented in Table 1. The endothermic dehydration reaction in kaolinite was assumed to consume the exothermic heat of the SHS reaction. In order to study this effect, in Mixture 2 kaolinite powder was first heat-treated at 850 °C for 30 min in order to decompose the aluminosilicate hydrate, kaolinite, to metakaolin ($Al_2Si_2O_5$). Raw materials were mixed by means of high-energy attrition milling for 10 min in argon atmosphere. A short milling time was chosen in order to avoid any reactions during milling.

Table 1: Test matrix for mullite synthesis experiments.

Mixture no	Raw material 1	wt%	Raw material 2	wt%
1	Kaolinite powder	51.8	Aluminium oxide hydroxide	48.2
2	Heat-treated kaolinite powder	67.3	Al powder (27 μm)	32.7
3	Kaolinite powder	70.5	Al powder (27 μm)	29.5
4	Kaolinite powder	70.5	Al powder (17 μm)	29.5

(2) Compaction and sintering

For mullite reaction sintering experiments, attrition-milled mixtures were uniaxially cold pressed to pellets of the size 20*3 mm using approximately 25 MPa pressure. The pellets were then reaction-sintered in an ENTECH air chamber furnace. Sintering was performed in air atmosphere and in ambient air pressure with a heating rate of 3.3 °C/min up to 1600 °C. which was maintained for 1 h before cooling to room temperature with cooling rate of 5 °C/min.

For the SHS experiments, aluminium-containing attrition-milled mixtures were packed in a steel mould with diameter of 70 mm and with powder bed thickness of 25 mm. The packing pressure of the powder mixtures was about 26 MPa. The steel mould was coated with 2 mm graphite foil in order to reduce heat losses and facilitate mould release. A thermocouple was inserted into the powder bed to a depth of about 3 mm from the upper surface to measure the temperature during the process, and to indicate the reaction front propagation. The powder bed with the mould was preheated at 500 °C in a separate furnace in air atmosphere. The mould was then quickly transferred from the furnace and the preheated packed powder bed surface was then ignited in air atmosphere from the top surface using resistance heating.

(3) Characterization techniques

The thermal behaviour and reaction paths of raw materials and attrition-milled powder mixtures were studied using thermogravimetric analysis (TGA, Netzsch STA 449 F1 Jupiter) giving a simultaneous Differential Scanning Calorimetry signal (DSC). Tests were conducted in air atmosphere with a temperature range from 40 °C to 1400 °C with the heating rate of 10 °C/min. A qualitative mass spectrometer (QMS, Netzsch QMS 403 D Aëolos) coupled directly to the TGA device exhaust was used for evolved gas analysis. The thermal expansion of uniaxially pressed (5 kN) pellets with a diameter of 11.62 mm was measured in air atmosphere with temperature range of 20 °C to 1550 °C using a horizontal pushrod dilatometer (Adamel Lhomargy DI-24). Qualitative phase analyses were performed for raw materials and final products by using an X-ray diffractometer (XRD, Empyrean, PANalytical B.V., ALMELO, Netherlands) with CuKα radiation source, and analysed using HighScore Plus software. Microstructures of the final sintered bodies were observed using a scanning electron microscope (SEM, Jeol JSM 6360LV) equipped with electron-dispersive spectroscopy (EDS). SEM investigations were conducted on polished cross-sections coated with gold. Thermodynamic calculations for the possible reactions, reaction enthalpies and adiabatic temperatures were performed using FactSage thermochemical software with FToxid database.

III. Results and Discussion

(1) Characterization of starting materials

(a) *Phase composition*

XRD patterns of untreated kaolinite powder and kaolinite powder after heat-treatment at 850 °C for 30 min are presented in Fig. 1. XRD patterns reveal that untreated kaolinite powder mainly consists of kaolinite $Al_2O_3{\cdot}2SiO_2{\cdot}2H_2O$ phase, alternatively presented as $Al_2Si_2O_5(OH)_4$. The kaolinite powder heat-treated at 850 °C for 30 min. mainly showed aluminium silicate $Al_2O_3{\cdot}SiO_2$ (Al_2SiO_5) phase forming from kaolinite caused by dehydration, i.e. water release.

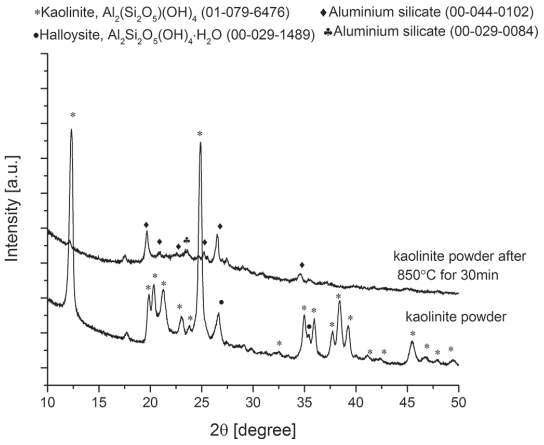

Fig. 1: XRD patterns of kaolinite and heat-treated kaolinite powders.

(b) *Thermal behaviour*

Fig. 2 shows the TGA/DSC/QMS-curve of kaolinite powder. An endothermic peak relating to the dehydration of the kaolinite into metakaolin phase can be seen at 510 °C (T_1). This includes water release according to following reaction, Eq. (1), presented by Yung-Feng *et al.* [9]:

$$Al_2O_3 \cdot 2SiO_2 \cdot 2H_2O \rightarrow Al_2O_3 \cdot 2SiO_2 + 2H_2O \quad (1)$$

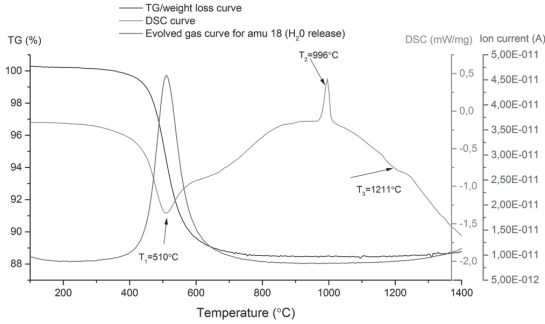

Fig. 2: Thermal behaviour of kaolinite powder.

At 996 °C (T_2), an exothermic peak related to the reorganization of the metakaolin into the Al-Si-spinel phase, $Si_3Al_4O_{12}$, and amorphous silica (SiO_2) phase, can be seen according to reaction Eq. (2) presented by Yung-Feng *et al.* [9]:

$$2(Al_2O_3 \cdot 2SiO_2) \rightarrow Si_3Al_4O_{12} + SiO_2 \quad (2)$$

At 1211 °C (T_3), mullite formation is starting according to the reaction in Eq. (3) presented by Yung-Feng *et al.* [9], resulting in mullite $3Al_2O_3{\cdot}2SiO_2$ and amorphous silica phases:

$$3Si_3Al_4O_{12} \rightarrow 2(3Al_2O_3 \cdot 2SiO_2) + 5SiO_2 \quad (3)$$

Because of the higher silica content in kaolinite than in mullite, an addition of alumina is needed to synthesize stoichiometric mullite. Eq. (4) presents a balanced reaction with a stoichiometric amount of alumina:

$$Si_3Al_4O_{12} + 5SiO_2 + 10Al_2O_3 \rightarrow 4(3Al_2O_3 \cdot 2SiO_2) \quad (4)$$

Fig. 3 shows the TGA/DSC-curve of aluminium powder ($d_{50} = 27\,\mu m$). Solid-state aluminium oxidation can be seen starting after 560 °C according to Eq. (5) and increase in weight:

$$4Al + 3O_2(g) \rightarrow 2Al_2O_3 \quad (5)$$

This is followed by aluminium melting at 660 °C. An exothermic peak is seen again at 996 °C, which could be attributed to accelerated liquid-state aluminium oxidation. The weight gain revealed that aluminium oxidation continues at high temperatures from 660 °C up to upper temperature limit of 1400 °C. After the accelerated oxidation after 1000 °C, oxidation continues with increasing rate as a function of the temperature. Trunov *et al.* [21] showed that, in aluminium powder oxidation, four distinct stages could be observed in the temperature range from 300 °C to 1500 °C. At the first stage, at temperatures below about 550 °C there was slow oxidation. At

about 550 °C, a transformation of amorphous alumina into γ-Al_2O_3 occurred, when the oxide layer thickness exceeded the critical thickness of amorphous alumina. The density of the γ - Al_2O_3 was greater than that of amorphous alumina, thus the γ-Al_2O_3 covered the aluminium surface only partially. At the second stage in the temperature range, about 550 – 660 °C, the oxidation rate increases rapidly until the γ-Al_2O_3 coverage becomes multilayered and continuous. At the third stage from about 650 °C to 1000 – 1100 °C, the oxidation rate continuously increased, related to the growth of a continuous γ-Al_2O_3 layer and its partial transformations into the structurally similar θ - Al_2O_3 polymorph. Finally, at the fourth oxidation stage above 1100 °C, there was also increase of the oxidation rate, related to the formation and growth of the α-Al_2O_3 oxide. All these four stages can be identified in Fig. 3.

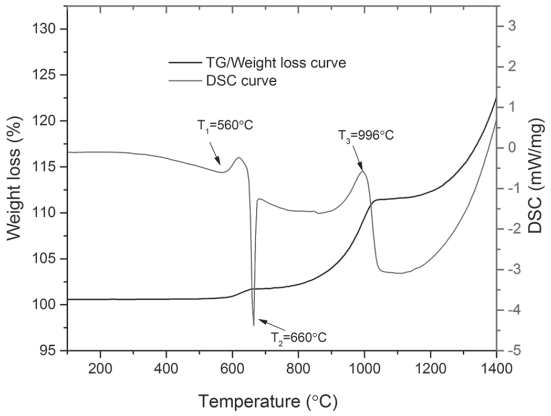

Fig. 3: Thermal behaviour of aluminium powder.

(2) Characterization of milled mixtures

(a) *Thermal behaviour, phase structure evolution*

Fig. 4 shows DSC-curves of the milled Mixtures 1 – 4. For Mixture 1, which does not contain aluminium, the DSC results show a first endothermic peak at 498 °C (T_1). That peak could be the dehydration of the kaolinite into the metakaolin according to presented Eq. (1) and also dehydration of aluminium oxide hydroxide, AlO(OH), according to following reaction (6):

$$2AlO(OH) \rightarrow Al_2O_3 + H_2O \qquad (6)$$

Obviously, for Mixture 2 containing heat-treated kaolinite, the kaolinite hydration reaction at 498 °C is missing. For Mixtures 3 and 4, the dehydration of the kaolinite into the metakaolin is observed at 498 °C according to Eq. (1). A different shape of the endothermic peak compared to Mixture 1 can be seen, because aluminium oxide hydroxide dehydration is missing. Aluminium-containing Mixtures 2 – 4 show exothermic solid-state aluminium oxidation starting at about 580 °C (T_2) according to Eq. (5) and endothermic aluminium melting at 660 °C (T_3). Exothermic peaks are seen again at 953 °C (T_4) which could be attributed to liquid-state aluminium oxidation. DSC results suggest that with the decrease in the aluminium particle size (difference between Mixture 3 and 4) aluminium oxidation accelerates, which seems obvious because of higher surface area. For all Mixtures 1 – 4, exothermic peaks observed at 993 °C (T_5) are probably caused by the reorganization of the metakaolin into the Al-Si-spinel phase according to Eq. (3). For aluminium-containing Mixtures 2 – 4, an exothermic peak is observed again at 1219 °C (T_6). For Mixture 2, which contains heat-treated kaolinite, the DSC signal stabilizes after the 1219 °C peak. Contrary to untreated kaolinite-containing Mixtures 3 and 4, it seems that the reaction is not finished within the measured temperature range. Contrary to the initial assumption, the dehydration of kaolinite does not significantly affect the heat balance of the reactions, as it occurs before, i.e. at lower temperature than other (exothermic) reactions. Thus, the kaolinite dehydration reaction occurring *in situ* in Mixtures 3 and 4 may even enhance the reactivity of the formed metakaolin phase.

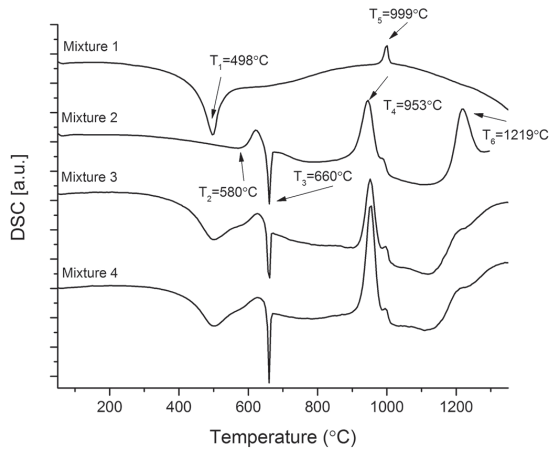

Fig. 4: DSC results of milled mixtures, presented in Table 1.

Fig. 5 shows TG-curves for the milled Mixtures 1 – 4. Mixture 1 and aluminium-containing Mixtures 3 and 4 show weight loss at about 498 °C (T_1) related to the dehydration reaction observed in the DSC curves. For Mixture 2 that contained heat-treated kaolinite this reaction is missing in the DSC curve and there is no weight loss observed for that mixture at that temperature. For aluminium-containing mixtures, aluminium oxidation starting approximately at 600 °C is seen as an increase in the weight loss curve. Another increase in the weight loss curve is observed after 900 °C and after 1200 °C relating to aluminium oxidation. TG-curves support the observation in DSC curves that with finer aluminium particle size (Mixture 4) the oxidation rate is quicker compared to Mixture 3. DSC results suggest that for heat-treated kaolinite oxidation stabilizes after 1219 °C. According to the TG-curves, the oxidation degree seems to be a little higher for heat-treated kaolinite powder in the temperature range from 600 °C to 1000 °C. After 1000 °C, oxidation seems to be higher for Mixtures 3 and 4 than for Mixture 2.

In their study [11], Esharghawi *et al.* have shown DTA curves for a mixture containing calcined kaolinite (heat-treated at 650 °C for 1 hour) and aluminium powder (average grain size < 45 μm). In our study, the DSC results

in Fig. 4 are similar to their results related to aluminium oxidation around 600 °C, aluminium melting at 660 °C and above 900 °C observed two exothermic peaks related to aluminium oxidation and the reorganization of the metakaolin. In contrast to their results, in our study, DSC results also reveal an exothermic peak at 1219 °C for Mixtures 2 – 4. This observed difference could be related to the use of finer aluminium in our study (average grain size < 27 μm and < 17 μm) which promotes aluminium oxidation.

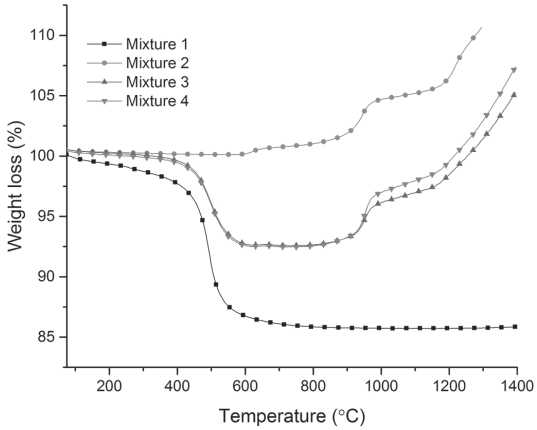

Fig. 5: TG-curves of the milled mixtures, presented in Table 1.

(a) ***Thermal expansion characteristics***

The thermal expansion behaviour of the compressed material from Mixtures 1 – 4 is presented in Fig. 6. Mixture 1, where aluminium oxide hydroxide AlO(OH) was used as the source of aluminium instead of metallic Al, clearly shows shrinkage that accelerates when the temperature reaches 1000 °C. The first unique shrinkage step for this mixture visible at 500 °C can be attributed to the dehydration of kaolinite into metakaolin, but more importantly to the dehydration of AlO(OH). Significant sintering of the aluminosilicate powder at 1000 – 1200 °C is quite evident, followed by a step above 1250 °C most likely caused by a combination of mullite formation and phase transformation of aluminium oxide into the α-phase.

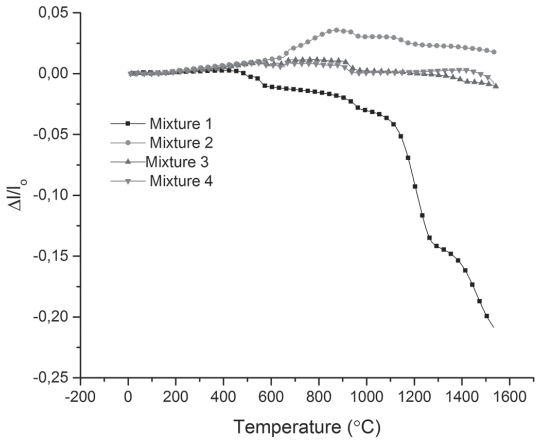

Fig. 6: Dilatometric curves of milled mixtures, presented in Table 1.

For mixtures containing metallic Al, despite showing very little length variation overall, some of the events described in the TG-curves and DCS results above are discernible in dilatometric curves as well. Mixtures 3 and 4 show a small dip above 540 °C followed by a sudden rise at 650 – 675 °C, the latter of which is also present for Mixture 2 and is probably caused by melting of the aluminium. Since Mixture 2 does not show clear events at 540 – 600 °C, it is safe to assume that the previously mentioned dip starting at 540 °C for Mixtures 3 and 4 is due to kaolinite dehydration. Other minute variations between the behaviour of Mixtures 2, 3 and 4 above 1000 °C are inconclusive.

All of the mixtures showed a minor shrinkage event below 1000 °C, most likely caused by reorganization of metakaolin into spinel phase. The large differences in the dimensional change between mixtures that either do or do not contain metallic Al, suggests that there is either a very large difference in compressibility of these powders, or that the powders containing Al do not densify in high temperatures and thus exhibit no sintering shrinkage associated with more conventional ceramic powder mixtures.

(3) Phase and microstructure analysis of the sintered bodies

(a) ***Phase structure analysis of reaction-sintered specimens***

Phase structure analysis of the final products after reaction sintering of Mixtures 1 – 4 is presented in Fig. 7. It was observed that after reaction sintering there were differences in the specimen's phase structure homogeneity between different mixtures. Reaction sintering of Mixture 1 and 2 resulted in uniform phase structure, but for Mixtures 3 and 4, there was a difference between the interior and the surface phase structure. XRD patterns for test Mixtures 1 and 2 showed stoichiometric mullite as major phase and minor aluminium oxide phase. XRD patterns for test Mixtures 3 and 4 showed aluminium oxide in both the surfaces. For these mixtures, the specimen's interiors showed metallic silicon and aluminium phases in addition to aluminium oxide. These results suggest that mullite formation is possible by reaction sintering by using heat-treated kaolinite and aluminium powder as raw materials. When using untreated kaolinite and aluminium as starting material, only very minor mullite peaks are detected and the resulting final phase structure is aluminium oxide after reaction sintering at 1600 °C for 1 h. It should be noted that amorphous SiO_2 detection from XRD curves is challenging so probably the final phase structure in Mixtures 3 and 4 also contains amorphous SiO_2. It could be the assumed that also in Mixtures 3 and 4 aluminium oxide and silicon oxide will eventually react to form mullite, only if it is kinetically possible. Additionally, after reaction sintering kaolinite and aluminium mixtures, the formed specimen's phase structure is not homogenous and its interior showed metallic silicon and residual aluminium phases.

(b) ***Phase structure analysis of SHS specimens***

Preheated packed powder bed surfaces of Mixtures 2 – 4 were ignited in air atmosphere from the top surface using

resistance heating. The exothermic reaction detected in the DSC results (in Fig. 4) at above 900 °C related to aluminium oxidation seems to ignite the SHS reaction for all aluminium-containing Mixtures 2 – 4. After initialization the reaction proceeded in self-sustaining manner through the entire test specimens from the top surface to the bottom. The highest measured temperature of the specimens during the SHS reaction was 1675 °C according to the thermocouple. Thus, in comparison to an earlier publication of Esharghawi *et al.* [11] where the SHS experiments were performed in flowing oxygen, our experiment proves that the SHS also succeeded in air atmosphere using similar raw materials mixtures. An air atmosphere is a more economic and sustainable option for synthesis compared to using pure oxygen.

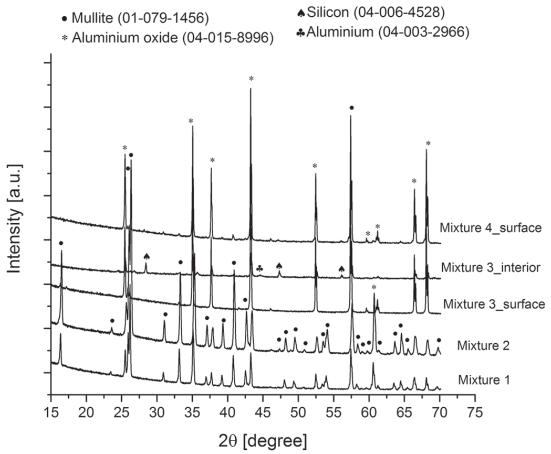

Fig. 7: XRD curves for reaction sintered mixtures, presented in Table 1.

Fig. 8 shows the XRD patterns of final test pieces after SHS. For all test Mixtures 2 – 4, the resulting phase structure after SHS was aluminium oxide and metallic silicon. Also small metallic aluminium peaks were seen for kaolinite-powder-containing Mixtures 3 and 4. The difference between the aluminium particle size in Mixtures 3 and 4 was attributed to the amount of metallic aluminium: with finer aluminium particle size the metallic aluminium peak intensities were smaller. It could therefore be suggested that with finer aluminium particle size the aluminium oxidation is more effective, and less metallic aluminium is left unreacted. For heat-treated kaolinite containing test Mixture 2, it seems that metallic aluminium has reacted with metallic silicon, because aluminium silicon peaks are visible in the XRD pattern.

Esharghawi *et al.* [11] have reported in their study the significant phases as being mullite, quartz, α-alumina and silicon metal with traces of aluminium metal after SHS experiments in flowing oxygen. Thus, flowing oxygen and air atmosphere seem to result in different phase structures after SHS, because mullite and quartz peaks are not visible after SHS in air. This could result from there being more oxygen available for the reaction to be completed.

Comparison to other previous publications in this field is not unequivocal because similar raw material combinations do not exist in other publications. Podbolotov *et al.* [12] have reported a mullite phase structure together with potassium aluminosilicate, corundum and microcline when 85 % kaolin and 15 % aluminium were used as raw materials together with potassium water glass (potassium metasilicate) as binder and different additives such as boric acid and sodium silicon fluoride.

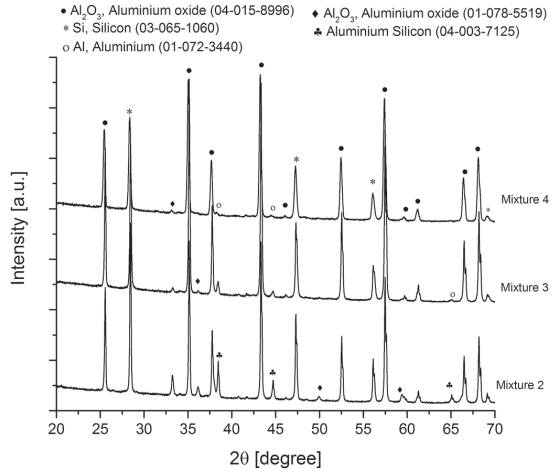

Fig. 8: XRD patterns after SHS for milled mixtures, presented in Table 1.

In order to confirm the reactions leading to the formation of mullite, SHS test pieces were post-treated at 1600 °C for 1 h. The XRD results after that post-treatment are shown in Fig. 9. After this post-treatment, all pieces corresponding to the test Mixtures 2 – 4 resulted in a mullite and aluminium oxide phase structure.

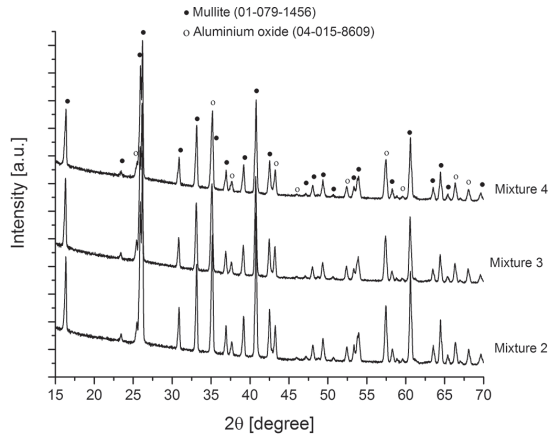

Fig. 9: XRD patterns of post-treated SHS pieces.

The difference between tthe reaction sintering and SHS results indicate that it is possible to affect the reaction path by employing SHS. Fast ignition of the reactions results in different phases than with slow heating. Bigger specimen sizes in the SHS test results in lower heat losses which make the SHS reaction possible but also change the reactions and the end result.

(c) ***Microstructural analysis of reaction-sintered specimens***

The SEM micrographs in Fig. 10 (a-d) show the microstructure cross-sections after reaction sintering experiments for (a) Mixture 1 of kaolinite and aluminium oxide hydroxide (b) Mixture 2 of heat-treated kaolinite and aluminium (27 μm) (c) Mixture 3 of kaolinite and aluminium (27 μm) and (d) Mixture 4 of kaolinite and aluminium (17 μm). The micrographs reveal much higher porosity in the aluminium-containing Mixtures 2, 3, and 4 than in Mixture 1 containing aluminium oxide hydroxide as the aluminium source. These micrographs support the differences in sinterability between these mixtures as detected in the dilatometer curves. For Mixture 1 the dilatometer curve showed first densification and then the reactions. For the aluminium-containing mixtures, the reactions dominated and the densification phase was absent, resulting in a more porous microstructure.

(d) ***Microstructural analysis of SHS specimens***

Fig. 11 (a-b) shows the SEM micrographs of aluminium (d_{50} =27 μm)-containing mixtures with (a) heat-treated (Mixture 2) and (b) untreated (Mixture 3) kaolinite after SHS. The microstructures seemed to be quite similar and a high fraction of porosity was observed. Two different phase areas were seen: denser areas of few tens of micrometres and finer particles with porosity. According to EDS analysis the denser areas are silicon rich and the finer particles are, on the contrary, aluminium oxide rich areas.

(4) Thermodynamic calculations

Thermodynamic calculations for the possible reactions and reaction paths were performed beyond earlier publications in this field to show the theoretical possibilities for SHS utilization in pure aluminosilicate ceramics processing. Thermodynamic calculations for the possible reactions, reaction enthalpies and adiabatic temperatures were performed using FactSage thermochemical software with FToxid database.

(a) ***Reaction sintering experiments***

Reaction sintering of the powder Mixture 1 of kaolinite and aluminium oxide hydroxide, resulted in mullite phase structure formation, thus the following reactions were assumed:

After 495 °C: $$Al_2O_3 \cdot 2SiO_2 \cdot 2H_2O \rightarrow Al_2O_3 \cdot 2SiO_2 + 2H_2O \quad (1)$$

$$2AlO(OH) \rightarrow Al_2O_3 + H_2O \quad (6)$$

After 999 °C: $$2(Al_2O_3 \cdot 2SiO_2) \rightarrow Si_3Al_4O_{12} + SiO_2 \quad (2)$$

After 1211 °C: $$3Si_3Al_4O_{12} \rightarrow 2(3Al_2O_3 \cdot 2SiO_2) + 5SiO_2 \quad (3)$$

Aluminium oxide resulting in Eq. (6) could react with silicon oxide resulting from Eq. (2) forming a mullite phase structure according to Eq. (7):

$$3Al_2O_3 + 2SiO_2 \rightarrow (3Al_2O_3 \cdot 2SiO_2) \quad (7)$$

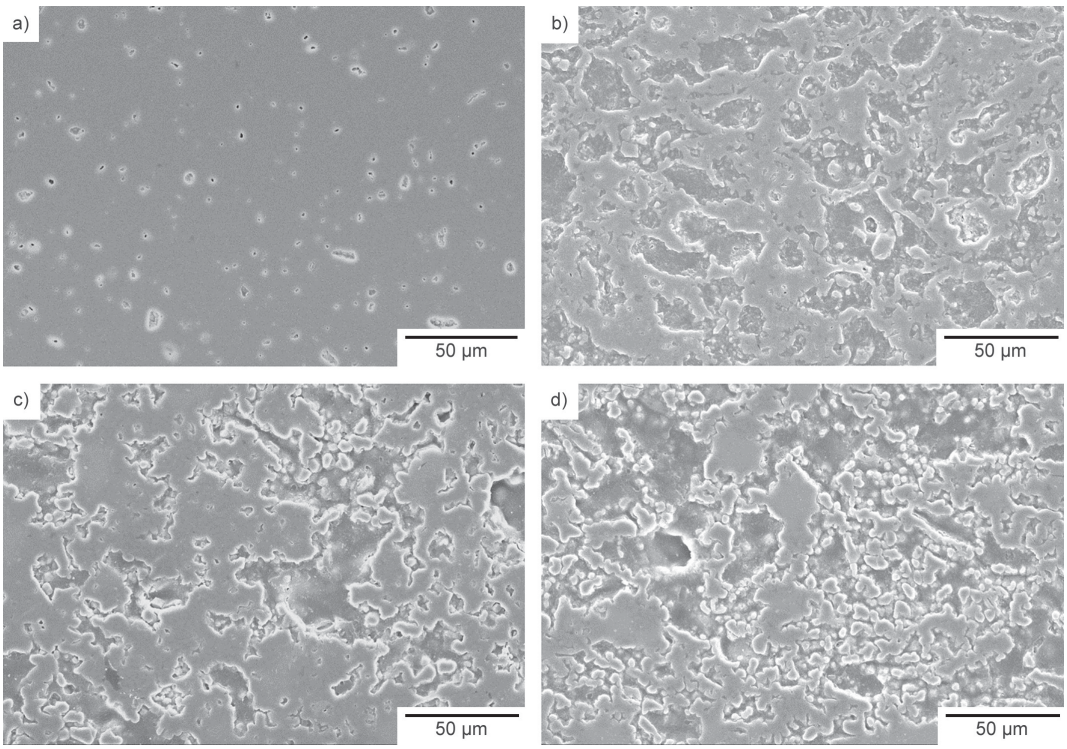

Fig. 10: SEM images of cross-sections of reaction-sintered specimens: (a) Mixture 1 (b) Mixture 2 (c) Mixture 3 and (d) Mixture 4 with 500x magnification.

Thus, the following total reaction was assumed to take place during reaction sintering of powder Mixture 1 of kaolin and aluminium oxide hydroxide:

$$Al_2O_3 \cdot 2SiO_2 \cdot 2H_2O + 4AlO(OH) \rightarrow 3Al_2O_3 \cdot 2SiO_2 + 4H_2O \quad (8)$$

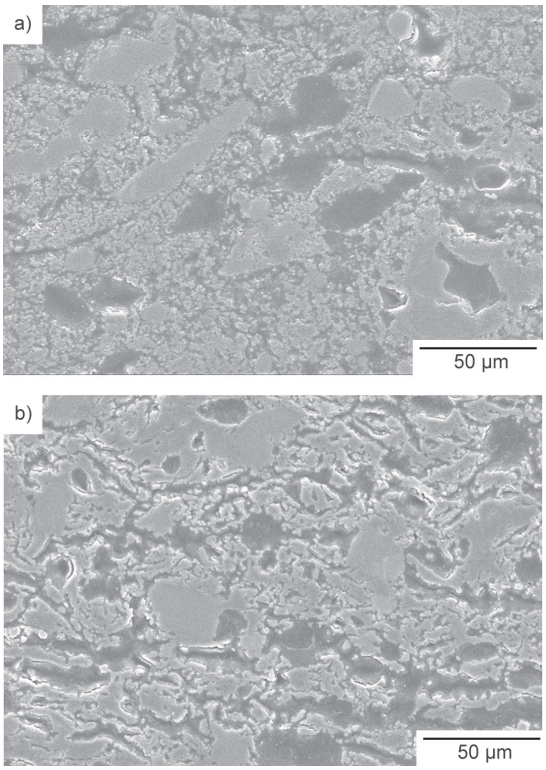

Fig. 11: SEM images of cross-sections after SHS for (a) Mixture 2 and (b) Mixture 3 with 500x magnification.

Table 2 summarizes the calculated reaction enthalpies for presented reactions for Mixture 1. The conclusion from this is that the mullite formation of the kaolinite and aluminium oxide hydroxide mixture is endothermic in nature and thus external heat is required. For the reactions (2) and (3), thermodynamic data was not available in the database used.

Table 2: Calculated reaction enthalpies for assumed reactions during reaction sintering of Mixture 1.

Reaction	Reaction enthalpy, ΔH [kJ]
(1)	+191
(6)	+ 25
(7)	+29
(8)	+115

In order to the define the reaction routes for aluminium-containing mixtures, all the Mixtures 1 – 4 were heat-treated at 1100 and 1300 °C. Fig. 12 (a-d) shows XRD curves after 1100 °C, 1300 °C and 1600 °C for (a) Mixture 1, (b) Mixture 2, (c) Mixture 3 and (d) Mixture 4. Mixture 1 showed aluminium silicate and aluminium oxide phase at 1100 °C, and at 1300 °C mullite phase in addition to aluminium oxide phase, which supported the above-suggested reaction paths for Mixture 1.

According to Fig. 12 XRD, patterns at 1100 °C for Mixture 2, which contain heat-treated kaolinite and aluminium, showed aluminium oxide phase structure containing also metallic silicon and aluminium phases. This observation suggests that aluminium reduces SiO_2 to metallic silicon according to Eq. (9):

$$4Al + 3SiO_2 \rightarrow 3Si + 2Al_2O_3 \quad (9)$$

Perhaps it could also be possible that aluminium reduces SiO_2 from metakaolin as well, according to Eq. (10):

$$Al_2O_3 \cdot 2SiO_2 + 2Al \rightarrow 2Si + 2Al_2O_3 \quad (10)$$

According to Fig. 12, at 1300 °C the XRD pattern for Mixture 2 already showed mullite peaks in addition to aluminium oxide phase. There were still metallic silicon peaks, but the metallic aluminium peaks had disappeared, so it could be concluded that the aluminium was fully oxidized. At 1600 °C the metallic silicon peaks disappeared and the phase structure consisted of mullite and aluminium oxide phases. Thus, after 1300 °C it was assumed that metallic silicon can further oxidize to silicon oxide according to (11):

$$Si + O_2(g) = SiO_2 \quad (11)$$

The formed silicon oxide can then react with aluminium oxide in the structure to finally form mullite according to Eq. (7):

$$3Al_2O_3 + 2SiO_2 \rightarrow (3Al_2O_3 \cdot 2SiO_2) \quad (7)$$

The total reaction route during the reaction sintering of Mixture 2 could be suggested to be the following:

After 953 °C: $4Al + 3O_2(g) \rightarrow 2Al_2O_3(s)$ (5)

After 996 °C: $2(Al_2O_3 \cdot 2SiO_2) \rightarrow Si_3Al_4O_{12} + SiO_2$ (2)

$4Al + 3SiO_2 \rightarrow 3Si + 2Al_2O_3$ (9)

After 1219 °C: $Si + O_2 \rightarrow SiO_2$ (11)

$$3Si_3Al_4O_{12} \rightarrow 2(3Al_2O_3 \cdot 2SiO_2) + 5SiO_2 \quad (3)$$

$$3Al_2O_3 + 2SiO_2 \rightarrow (3Al_2O_3 \cdot 2SiO_2) \quad (7)$$

According to Fig. 12, at 1100 °C for Mixtures 3 and 4, which contain kaolinite, the XRD patterns show aluminium oxide phase structure involving also metallic silicon and aluminium. For these mixtures at 1300 °C metallic silicon and aluminium peaks were still visible in addition to aluminium oxide as a major phase. Unlike for metakaolin-containing Mixture 2, there were no mullite peaks at 1300 °C but the peaks of θ - Al_2O_3 appeared. At 1600 °C, all the metallic silicon and aluminium peaks disappeared and the major phase was aluminium oxide while very minor mullite peaks started to appear. The total reaction route during the reaction sintering of Mixture 3 and 4 could be suggested to be similar to that for Mixture 2, although in Mixtures 3 and 4 there was also kaolinite dehydration that occurs according to Equation (1) after 495 °C. But it could be detected that during the reac-

tion sintering mixture of kaolinite and aluminium, mullite formation seems to be much slower than is the case when metakaolin and aluminium are used. This could be due to the differences in reactivity between kaolinite and metakaolin. One possibility is that the kaolinite dehydration reaction occurring *in situ* may enhance the reactivity of the formed metakaolin phase and thus it could also be possible that aluminium reduces SiO_2 from metakaolin according to Equation (10) in Mixtures 3 and 4 too. It could also be assumed that in Mixtures 3 and 4 aluminium oxide and silicon oxide will eventually react to form mullite, provided that it is kinetically possible. Mechanical properties of metakaolin could be also different to those of kaolinite and because of that grinding and mixing during attrition milling could be more efficient in the case of the heat-treated kaolinite. It could be also possible that kaolinite dehydrates in the attritor mill to some extent, hindering the mixing process.

Table 3 summarizes the calculated reaction enthalpies and adiabatic temperatures for presented reactions for Mixtures 2 – 4. For the reactions (2) and (3), the thermodynamic data was not available in the database used. For Mixture 2, the endothermic dehydration reaction (1) was missing. The aluminium oxidation reaction (5), the aluminium-reducing silicon oxide to metallic silicon reaction (9) and the further oxidizing of silicon (11) are all exothermic reactions. The kaolinite dehydration (1) and mullite formation reactions (7) are only endothermic reactions requiring external energy. According to these thermodynamic calculations, the reaction energy balance for mullite formation from aluminium and kaolinite mixtures is highly exothermic in nature only if sufficient oxygen is available for the reactions to be completed.

Table 3: Calculated reaction enthalpies for assumed reactions during reaction sintering of Mixtures 2 – 4, presented in Table 1.

Reaction	Reaction enthalpy, ΔH [kJ]	T_{ad} [°C]
(1)	+191	-
(5)	-3351	9439
(9)	-619	1902
(11)	-960	-
(7)	+29	-

In the study by Podbolotov *et al.* [12], aluminium powder, quartz sand and kaolin were used as raw materials for mixtures. They have suggested similar chemical processes corresponding to our Eqs. (7), (9) and (11). In their study, the reaction enthalpies and adiabatic temperatures for the presented reactions were missing.

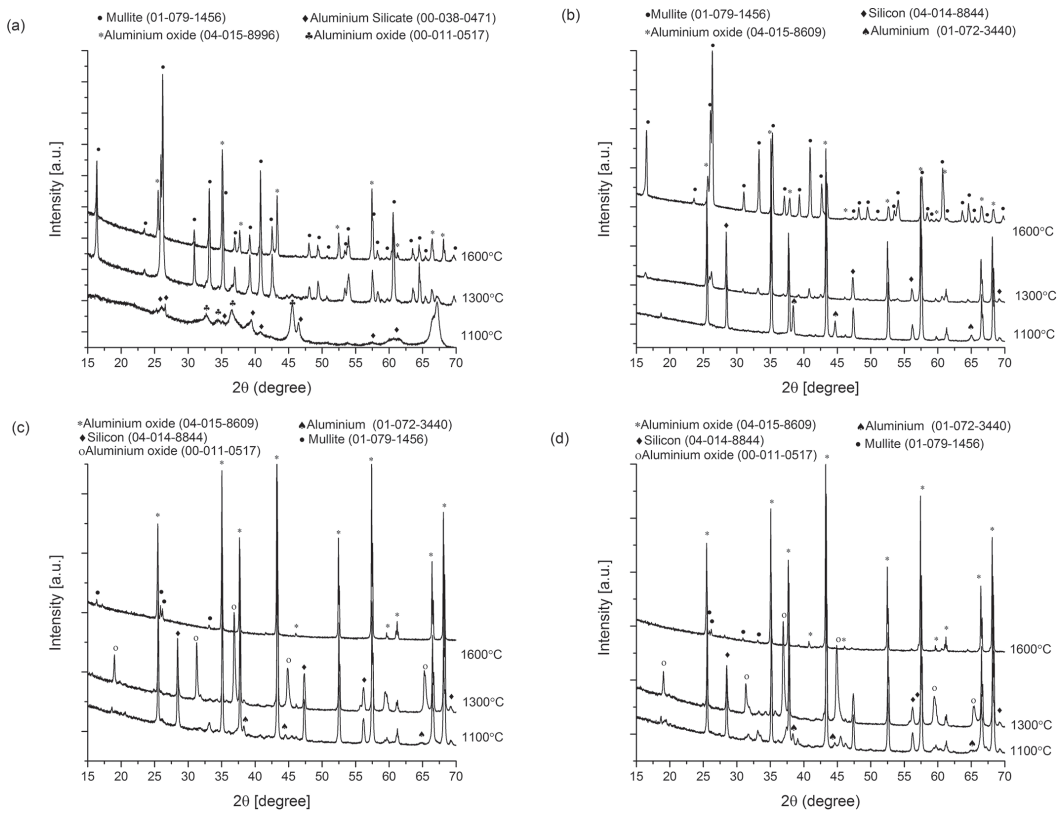

Fig. 12: XRD results after 1100 °C, 1300 °C and 1600 °C for (a) Mixture 1 (b) Mixture 2 (c) Mixture 3 and (d) Mixture 4.

(b) ***SHS experiments***

As the results in Table 3 show, the aluminium oxidation is a highly exothermic reaction only if sufficient oxygen is available for the reaction. In addition, the aluminium-reducing silicon oxide to metallic silicon reaction is exothermic as is the further oxidizing of silicon. The kaolinite dehydration and mullite formation reactions are only endothermic, requiring external energy. The dehydration of kaolinite does not significantly affect the heat balance of the reactions as it occurs before, i.e. at a lower temperature than other (exothermic) reactions. The energy balance in the total reactions indicates the release of energy, thus in energy terms there is great potential for aluminosilicate-based ceramic synthesis when aluminium is used as a raw material. Theoretically, the saving in heating energy could be as high as 70 % if the furnace temperature could be decreased from 1600 °C to 900 °C.

However, the resulting SHS materials from Mixtures 2 – 4 were inhomogeneous and porous, with inadequate mechanical properties. Reasons for this could relate to the inadequate densification mechanism related, for example, to the absence of clear liquid phase. In addition, the specimens were not densified by pressing after SHS. Future research is needed to enable the full utilization of SHS to obtain solid pieces with acceptable mechanical properties. One possibility is to add oxidizing raw materials to provide sufficient oxygen for the reactions to be completed.

After post-treatment of the SHS specimens, the XRD results show a mullite- and aluminium-oxide-containing phase structure. Thus, the following reactions are assumed to have taken place during the post-treatment:

$$Si + O_2 \rightarrow SiO_2 \quad (11)$$

$$3Al_2O_3 + 2SiO_2 \rightarrow (3Al_2O_3 \cdot 2SiO_2) \quad (7)$$

After SHS and post-treatment, all the aluminium-containing mixtures showed a mullite and aluminium oxide phase structure. After reaction sintering of kaolinite and aluminium, the mixtures showed mainly aluminium oxide phase structure. In addition, the formed phase structure was heterogeneous and the specimen's interior also showed metallic silicon and aluminium phases. Thus, it seems that mullite is formed quicker after SHS than in conventional reaction sintering if aluminium and untreated kaolinite are used as raw materials.

IV. Conclusions

In the current work, the possibilities were studied for saving energy in pure aluminosilicate-based ceramic synthesis and sintering based on the use of SHS in air atmosphere. Kaolinite powder, aluminium oxide hydroxide and exothermically reactive aluminium powder were used as raw materials. Four mixtures were prepared from the selected raw materials for the stoichiometric 3:2 mullite synthesis. The thermal reactions and formed phase- and microstructures were compared to the conventional reaction sintering of mullite. The role of the alumina source, the effect of kaolinite heat-treatment and aluminium particle size were studied. The endothermic dehydration reaction in kaolinite was assumed to consume the exothermic heat of the SHS reaction. To study this, in one mixture kaolinite powder was first heat-treated at 850 °C for 30 min in order to effect decomposition of the aluminosilicate hydrate, kaolinite, to metakaolin. All the mixtures were prepared by means of attrition milling in argon atmosphere.

Reaction sintering of the kaolinite and aluminium oxide hydroxide mixture resulted in mullite ceramic pieces. Reaction sintering of the heat-treated kaolinite, metakaolin, and aluminium powder also resulted in mullite ceramic pieces. But reaction sintering of the untreated kaolinite and aluminium powder mixture resulted in aluminium- and silicon oxide phase structures and only minor mullite phase was detected. Additionally, after reaction sintering of the kaolinite and aluminium mixture, the phase structures of the formed pieces were not homogeneous and their interiors showed metallic silicon and residual aluminium phases. This could result from the differences in reactivity between kaolinite and heat-treated kaolinite. One possibility is that the kaolinite dehydration reaction occurring *in situ* may enhance the reactivity of the formed metakaolin phase and thus it could be possible that aluminium reduces SiO_2 from metakaolin as well, which affects the reaction rate. Dilatometer results showed huge differences in the thermal expansion behaviour and sinterability between aluminium oxide hydroxide and aluminium powder as the alumina source. Aluminium oxide hydroxide clearly showed shrinkage and significant sintering, but the mixtures containing metallic Al showed very little variation in length overall. The large differences in dimensional change between mixtures that either do or do not contain metallic Al suggest that there is either a very large difference in the compressibility of these powders or that the powders containing Al do not densify in high temperatures and thus do not exhibit the sintering shrinkage associated with more conventional ceramic powder mixtures. It should be also noted that the particle size of the aluminium oxide hydroxide is much smaller than for aluminium, which promotes sinterability.

On the basis of the thermal behaviour analysis and thermodynamic calculations performed, it is apparent that mullite formation from kaolinite and aluminium oxide hydroxide as the alumina source is endothermic in nature, thus external energy is needed. When exothermically reactive raw material is used, i.e. aluminium powder, the DSC results reveal a highly exothermic reaction starting above 900 °C. This reaction, which is related to aluminium oxidation, ignited the SHS reaction and after initialization the reaction proceeded in a self-sustaining manner through entire test pieces in air atmosphere. The highest recorded temperature during SHS reaction was 1675 °C. According to thermodynamic calculations, in addition to the aluminium oxidation reaction, the aluminium-reducing silicon oxide to metallic silicon reaction and the further oxidization of silicon are exothermic. Thus, the total energy balance for mullite formation from aluminium and kaolinite mixtures is highly exothermic in nature only if sufficient oxygen is available for the reactions to be completed. SHS results in Al_2O_3 - Si phase structure formation in the test pieces. The difference between the reaction sintering and SHS results indicate that it is possible to affect the reaction path by employing SHS. Contrary to the first assumption, the dehydration of kaolinite does not signif-

icantly affect the heat balance of the reactions as it occurs before, i.e. at lower temperature than other (exothermic) reactions. Thus, this affects the total energy balance, but not the SHS reaction itself or reaction sintering. Fast ignition of the reactions results in different phases than with slow heating. Bigger specimen sizes in the SHS tests not only make the SHS reaction possible owing to lower heat losses but also changes the reactions and the end-result. Theoretically, the saving in heating energy could be as high as about 70 % if the furnace temperature could be reduced from 1600 °C to 900 °C. Thus, in energy terms, potential exists for utilizing SHS in aluminosilicate-based ceramic synthesis. However, the resulting SHS materials were inhomogeneous, porous and did not exhibit acceptable mechanical properties, so future research is needed to properly utilize SHS. One possibility is to add oxidizing raw materials in order to provide sufficient oxygen for the reactions to be completed.

Acknowledgements

The research was funded by the Academy of Finland, project CeraTail. The authors would like to thank Mr Mika Heikkinen for his part in the experimental work.

References

1 Kang, T.S., Park, C-H., Kim, S.H.: Characteristics of exothermic reaction fronts in the gasless combustion system, *Ceram. Int.,* **37**, 825 – 833, (2011).

2 Merzhanov, A.G.: History and recent developments in SHS, *Ceram. Int.*, **21**, [5], 371 – 379, (1995).

3 Cao, G., Orrù, R.: Self-propagating reactions for environmental protection: State of the art and future directions, *Chem. Eng. J.,* **87**, [2], 239 – 249, (2002).

4 Mossino, P.: Review some aspects in self-propagating high-temperature synthesis, *Ceram. Int.*, **30**, 311 – 332, (2004).

5 Dong, Y., Feng, X., Feng, X., Ding, Y., Liu, X., Meng, G.: Preparation of low-cost mullite ceramics from natural bauxite and industrial waste fly ash, *J. Alloy. Compd.*, **460**, 599 – 606, (2008).

6 Zaki, Z.I., Ewais, E.M.M., Rashad, M.M.: Review novel route for combustion synthesis of zirconia-mullite/TiB_2 composites, *J. Alloy. Compd.*, **467**, 288 – 292, (2009).

7 Chen, C.Y., Lan, G.S., Tuan, W.H.: Preparation of mullite by the reaction sintering of kaolinite and alumina, *J. Eur. Ceram. Soc.*, **20**, 2519 – 2525, (2000).

8 Zaki, Z.I.: Combustion synthesis of mullite-titanium boride composite, *Ceram. Int.*, **35**, 673 – 678, (2009).

9 Chen, Y-F., Wang, M-C., Hon, M-H.: Phase transformation and growth of mullite in kaolin ceramics, *J. Eur. Ceram. Soc.*, **24**, 2389 – 2397, (2004).

10 Yeh, C.L., Kao, W.C.: Preparation of TaB/TaB_2/mullite composites by combustion synthesis involving aluminothermic reduction of oxide precursors, *J. Alloy. Compd.*, **615**, 734 – 739, (2014).

11 Esharghawi, A., Penot, C., Nardou, F.: Elaboration of porous mullite-based materials via SHS reaction, *Ceram. Int.*, **36**, [1], 231 – 239, (2010).

12 Podbolotov, K.B., Dyatlova, E.M., Popov, R. Yu.: Ceramic refractory SHS-coatings based on the system, Al-SiO_2, *Refract. Ind. Ceram.,* **54**, [5], 31 – 36, (2014).

13 Kazhikenova, S. Sh., Nurkenov, O.A., Satbaev, B.N.: Theoretical aspects of the creation of highly efficient refractories on the basis of SHS technology, *Refract. Ind. Ceram.,* **52**, [1], 55 – 60, (2011).

14 Zharmenov, A.A., Satbaev, B.N., Kazhikenova, S. Sh., Nurkenov, O.A.: Development of refractory materials prepared by SHS technology, *Refract. Ind. Ceram.* **52**, [4], 40 – 48, (2011).

15 Zharmenov, A.A., Satbaev, B.N., Kazhikenova, S. Sh., Nurkenov O.A.: Development of new refractory material by SHS-technology based on kazakhstan republic raw material resources, *Refract. Ind. Ceram.*, **53**, [3], 47 – 54, (2012).

16 Mansurov Z.A., Mofa N.N., Sadykov B.S., Sabaev Zh. Zh., Bakkara A.E: Mechanochemical treatment, structural peculiarities, properties, and reactivity of SHS systems based on natural materials. 4. Production of SHS ceramics based on mechonoactivated materials, *J. Eng. Phys. Thermophys.*, **89**, [1], 230 – 237, (2016).

17 Balmori-Ramirez, H.: Dense mullite from attrition-milled kyanite and aluminum metal, *J. Am. Ceram. Soc.,* **87**, [1], 144 – 146, (2004).

18 Esharghawi, A., Penot, C., Nardou, F.: Contribution to porous mullite synthesis from clays by adding al and mg powders, *J. Eur. Ceram. Soc.,* **29**, [1], 31 – 38, (2009).

19 Khabas, A., Nevvonen, O.V., Vereshchagin, V.I.: Synthesis of mullite in the presence of nanodisperse aluminium powder, *Refract. Ind. Ceram.*, **46**, [1], 71 – 75, (2005).

20 Anggono, J., Derby, B.: Mullite formation from the pyrolysis of aluminium-loaded polymethylsiloxanes: the influence of aluminium powder characteristics, *J. Eur. Ceram. Soc.*, **26**, [7], 1107 – 1119, (2006).

21 Trunov, M.A., Schoenitz, M., Zhu, X., Dreizin, E.L.: Effect of polymorphic phase transformations in Al_2O_3 film on oxidation kinetics of aluminum powders, *Combust. Flame,* **140**, 310 – 318, (2005).

PUBLICATION II

Mining tailings as raw materials for reaction-sintered aluminosilicate ceramics: Effect of mineralogical composition on microstructure and properties

Marjaana Karhu, Juha Lagerbom, Soili Solismaa, Mari Honkanen, Arnold Ismailov, Marja-Liisa Räisänen, Elina Huttunen-Saarivirta, Erkki Levänen, Päivi Kivikytö-Reponen

Ceramics International 45 (2019) 4840–4848

https://doi.org/10.1016/j.ceramint.2018.11.180

Publication reprinted with the permission of the copyright holders.

Ceramics International 45 (2019) 4840–4848

Contents lists available at ScienceDirect

Ceramics International

journal homepage: www.elsevier.com/locate/ceramint

Mining tailings as raw materials for reaction-sintered aluminosilicate ceramics: Effect of mineralogical composition on microstructure and properties

Marjaana Karhu[a,*], Juha Lagerbom[a], Soili Solismaa[b], Mari Honkanen[c], Arnold Ismailov[d], Marja-Liisa Räisänen[b], Elina Huttunen-Saarivirta[a], Erkki Levänen[d], Päivi Kivikytö-Reponen[a]

[a] VTT Technical Research Centre of Finland Ltd (VTT), P.O.Box 1300, FI-33101 Tampere, Finland
[b] Geological Survey of Finland (GTK), P.O.Box 1237, FI-70211 Kuopio, Finland
[c] Tampere University of Technology, Tampere Microscopy Center, P.O. Box 692, FI-33101 Tampere, Finland
[d] Tampere University of Technology, Laboratory of Materials Science, P.O. Box 589, FI-33101 Tampere, Finland

ARTICLE INFO

Keywords:
Mining tailings
Utilization
Mullite
Refractory ceramics
Reaction sintering

ABSTRACT

This paper presents studies on the utilization of aluminosilicate-based mining tailings as raw materials for mullite-based ceramics. Based on the 3:2 stoichiometric composition, mullite was synthesised by reactive sintering with a series of powder mixtures with alumina additions. X-ray diffractometry and scanning electron microscopy analyses revealed that, at the specific mineralogical composition, mullite structure formed surrounded by an amorphous glass phase in reaction-sintered powder mixtures. Results demonstrated that the chemical and mineralogical composition of mining tailings do have an effect on mullite formation possibilities and, only with the particular mineralogical composition, the mullite formation is possible regardless of the correct Al:Si ratio in tailings. Physical and mechanical properties of the formed ceramics were defined, showing comparable values to 3:2 mullite reference. Mullite structure formation enables a better thermal resistance up to above 1450 °C of the formed tailings-based ceramics compared to other aluminosilicates, reflecting their utilization potential for refractory ceramic applications.

1. Introduction

Mining tailings are major waste materials from ore processing. In current practice, tailings are transported in a slurry form and stored in impoundments [1]. This causes occupation of large areas of land, costly construction and maintenance activities, potential environmental and ecological risks, e.g. acid mine drainage, and loss of energy and valuable raw materials [2]. In the path towards circular economy, mining tailings are one key resource to be put into reuse and recycling, because of large volumes, environmental impact and need for the efficient exploitation of natural resources [3]. The valorisation of secondary raw materials reduces the risk of poor resource availability while simultaneously decreasing the amount of waste and providing cost-effective reactants for processes [4]. Development of high-value material solutions from secondary raw materials besides high-volume solutions, such as utilization in earth construction, enhances the economic viability of secondary raw materials utilization along with environmental benefits [5].

Mullite, $3Al_2O_3{\cdot}2SiO_2$, is one of the most important aluminosilicate refractory ceramic materials for high-temperature applications such as for refractory bricks, kiln furnitures or protective coatings [6–8]. Mullite is the only stable crystalline aluminosilicate phase in the SiO_2–Al_2O_3 binary system, shown detailed in study of Klug et al. [9]. Mullite has a special combination of properties, such as low density (~ 3.2 g/cm^3), high melting point (~ 1830 °C) and a low coefficient of thermal expansion (~ 4.5*10^{-6} K^{-1}) [6]. During the recent years, plenty of research effort has been put on aluminosilicate containing waste utilization in the manufacturing of mullite-based ceramics. In the studies of Alves et al. [5,10], mullite-based ceramics were prepared by reaction sintering of mixtures containing kaolin clay and kaolin waste. The results showed that the samples derived at 1500 °C from formulations containing kaolin waste were composed of acicular mullite and glass phases. In the studies of Dong et al. [11–13], mullite ceramics were prepared from the mixtures of natural bauxite and industrial waste fly ash. It was suggested that below 1300 °C cristobalite reacted with alumina to form secondary mullite. At higher temperatures,

* Corresponding author.
E-mail address: marjaana.karhu@vtt.fi (M. Karhu).

https://doi.org/10.1016/j.ceramint.2018.11.180
Received 17 October 2018; Received in revised form 22 November 2018; Accepted 22 November 2018
Available online 23 November 2018
0272-8842/ © 2018 Elsevier Ltd and Techna Group S.r.l. All rights reserved.

bauxite-derived alumina dissolved into a liquid glassy phase, which was formed from the melted fly ash under the action of different metal oxide impurities. In the study of Jung et al. [14], mullite ceramics were manufactured from appropriate mixtures of coal fly ash and Al_2O_3 powder by reaction sintering at 1500 °C. Vieira et al. [15], reported mullite preparation from a mixture of wastes with high contents of silica and aluminium hydroxide: wastes from slate rocks and aluminium sludge from the physicochemical treatment of the wastewaters.

Existing studies suggest the potential of utilizing aluminosilicate-based waste in mullite formation, but further research is needed to fully understand the effects of waste materials composition, particularly the role of impurities, on mullite formation. This paper will provide an insight into the use of aluminosilicate-based mining tailings in mullite synthesis and bridge the most fundamental gaps in the present understanding. Felsic mining tailings (FMT) are side flows rich in quartz and alkali feldspars and, in terms of chemical composition, the dominant oxides are silica (SiO_2) followed by alumina (Al_2O_3) [16]. From the composition point of view, with alumina source addition, the felsic mining tailings hold potential as starting materials for mullite-based ceramics. In the present study, beyond to earlier publications in this field, the utilization of selected felsic mining tailings as raw materials for mullite-based ceramics is examined. The underlying research hypothesis is that, by modifying the raw material chemistry, it is possible to generate mullite-based ceramics from felsic mining tailings. The motivation for the work is that the formation of mullite structure in ceramic materials enables better high-temperature properties compared to other aluminosilicates. The objective in this paper is to investigate and especially to increase the understanding of the effect of chemical and mineralogical composition of felsic-mining tailings on the mullite formation.

2. Experimental procedure

2.1. Mining tailings

Three Finnish felsic mining tailings were selected for investigation: Molybdenum ore tailings [17], FMT1, Gold ore tailings [18], FMT2, and Quartz ore tailings [19], FMT3. The samples do not represent the whole mining tailings area of their origin, but only the shallow tailings at one sampling point. Surface of the tailing dumpling may differ from the overall composition of the tailing deposit. Table 1 shows the mineralogical analyses of the three mining tailings. Mineralogical characterization included the identification and quantification of mineral phases with scanning electron microscopy (SEM) together with elemental analyses. Table 2 presents the total concentrations of oxides (calculated as oxides) in the tailings, measured with X-ray fluorescence spectrometry (XRF) method. The more detailed explanation of mineralogical analyses, geochemical analyses and sampling procedure are described elsewhere [16]. The mining tailings were selected on the basis of notable differences in quartz and feldspar contents in order to investigate the effects of mineralogy on the mullite formation.

Table 1
Main minerals of the tailing samples (% total area).

Mineral group	Mineral	FMT1	FMT2	FMT3
Quartz	Quartz, SiO_2	40	11	64
Alkali feldspars	Albite, $NaAlSi_3O_8$	23	31	–
	Andesine $(Ca,Na)Al_2Si_2O_8$	12	3	–
	K-feldspar, $KAlSi_3O_8$	6	15	–
K-micas	Biotite, $K(Mg,Fe)_3(Al,Fe)Si_3O_{10}(OH,F)_2$	6	20	–
	Muscovite, $KAl_2(Si_3Al)O_{10}(OH,F)_2$	3	2	27
Clay minerals	Kaolinite, $Al_2(Si_2O_5)(OH)_4$	–	–	4
Carbonate minerals	Calcite, $CaCO_3$	–	6	–

Table 2
Chemical composition of the mining tailing samples. Total oxide concentrations measured with XRF method [16].

Sample code	SiO_2	Al_2O_3	Si/Al molar ratio	Fe_2O_3	MgO	CaO	K_2O	Na_2O
FMT1	73.2	11.1	5.6	2.93	4.84	1.95	1.51	3.45
FMT2	57.3	14.3	3.4	5.03	3.14	5.36	4.66	3.91
FMT3	89.8	5.16	14.8	0.57	0.11	0.04	1.2	0.11

Mineralogical analysis of FMT1 showed the quartz content of 40% was about in balance to the sum of feldspars (albite, andesine, K-feldspar). For FMT2, the quartz content was only 11% and the sum of feldspars was much higher, 49%. FMT2 also contained calcite, which was absent or at trace levels in FMT1 and FMT3. The FMT3 differed from FMT1 and FMT2 with its high quartz content, missing alkali feldspars and the presence of kaolinite.

Table 2 shows the total concentrations of phases in the three types of mining tailings. A more detailed explanation of analyses is described elsewhere [16]. In all three mining tailings, SiO_2 was the dominant oxide phase, followed by Al_2O_3, with the overall variation in Si/Al molar ratio being between 3.4 (FMT2) and 14.8 (FMT3). FMT2 contained the greatest share of impurity oxides among the studied mining tailings: CaO, Fe_2O_3, K_2O Na_2O and MgO (~ 22%), whereas the lowest impurity content was detected for FMT3 (~2%).

2.2. Sample preparation

Aiming at mullite, each mining tailings was mixed with additional alumina source. Recipes shown in Table 3 for reaction sintering experiments were formulated in order to reach the composition of 3:2 mullite ($3Al_2O_3{\cdot}2SiO_2$). The correct Al:Si ratio for mullite composition was balanced by adding commercially available boehmite (aluminium oxide hydroxide, AlO(OH)) powder (provided by Sasol Germany GmbH, average grain size < 0.77 μm) to tailings FMT1, FMT2, FMT3 and the reference sample of kaolinite. Commercial boehmite was used in this study in order to define the behavior differences between the three tailing samples. The portions of boehmite addition were calculated according to chemical composition analysis of mining tailings shown in Table 2. In total, four powder mixtures (one corresponding to stoichiometric mullite composition, three with non-stoichiometric compositions) were formulated for each type of mining tailing by varying the boehmite amount in order to study raw materials composition effects on the formed ceramic structure, Table 3. As a reference, a stoichiometric 3:2 mullite sample was prepared using commercially available kaolinite powder ($Al_2O_32SiO_2{\cdot}2H_2O$ or $Al_2Si_2O_5(OH)_4$)) and aluminium oxide hydroxide (boehmite) powder. Kaolinite was provided by Merck (average grain size < 6.68 μm, high kaolin purity).

The mining tailings were received in powder form, but they were first ground by jet milling into the particle size below 10 μm in order to increase the reactivity. The mining tailings were studied as jet-milled and mixed with the alumina source according to Table 3. Powder mixtures were prepared by ball milling in an attrition mill for 30 min in air atmosphere. The attrition-milled powders were then uniaxially compressed into green pellets of the size of 20 × 3 mm using approximately 25 MPa pressure. Heat treatment of green pellets was performed in an ENTECH air chamber furnace in air atmosphere and in ambient air pressure. The heating rate was 3.3 °C/min up to 1300 °C with 3 h holding time at the maximum temperature before cooling to room temperature at the rate of 5 °C/min.

2.3. Characterization methods

All three types of mining tailings and all powder mixtures were visually examined after the reaction sintering experiments. In order to

Table 3
Recipe formulations for reaction-sintered specimens (wt%).

Recipe code	Stoichiometry	FMT1	FMT2	FMT3	Kaolinite	AlO(OH)
Sint01	stoichiometric	33.6	–	–	–	66.4
Sint02	non-stoichiometric	50.4	–	–	–	49.6
Sint03	non-stoichiometric	67.0	–	–	–	33.0
Sint04	non-stoichiometric	83.5	–	–	–	16.5
Sint05	stoichiometric	–	40.4	–	–	59.6
Sint06	non-stoichiometric	–	55.4	–	–	44.6
Sint07	non-stoichiometric	–	70.5	–	–	29.5
Sint08	non-stoichiometric	–	85.2	–	–	14.8
Sint09	stoichiometric	–	–	28.8	–	71.2
Sint10	non-stoichiometric	–	–	46.4	–	53.6
Sint11	non-stoichiometric	–	–	64.0	–	36.0
Sint12	non-stoichiometric	–	–	82.0	–	18.0
Reference	stoichiometric	–	–	–	51.8	48.2

understand the differences in behavior between the mining tailing compositions, the thermal behavior of FMT1, FMT2, FMT3 and attrition-milled powder mixtures of stoichiometric mullite composition (Sint01, Sint05, Sint09) was studied using thermogravimetric analysis (TGA, Netzsch STA449 F1 Jupiter) in Differential Scanning Calorimetry (DSC) and thermogravimetry (TG) modes. The tests were conducted in air atmosphere in a temperature range from 40 °C to 1300 °C at the heating rate of 10 °C/min. In order to verify the differences in melting behavior between the alkali feldspar-containing tailings FMT1 and FMT2, additional heat treatments were carried out in the temperature range of interest, selected based on DSC results.

The thermal expansion and sintering shrinkage behaviors of the stoichiometric mullite powder mixtures (Sint01, Sint05, Sint09) were studied using horizontal pushrod dilatometers (Adamel Lhomargy DI-24 and Netzsch DIL 402 Expedis). The dilatometers require defined specimen dimensions and geometry, limited by the inner dimensions of the heating chambers, geometry of sample holders and maximum travel of the pushrods. Here, the attrition-milled powder mixtures were uniaxially pressed (5 kN) into pellets with a diameter of 11.6 mm. The dilatation was measured in air atmosphere within the temperature range from 20 °C to 1450 °C and the heating rate of 5 °C/min.

Microstructural analysis of mining tailings and reaction-sintered powder mixtures covered the determination of phase structure and the overall microstructure with compositional analysis of the microstructural details. Phase structure analyses of the materials were performed using X-ray diffractometry (XRD, Empyrean, PANalytical B.V. device, ALMELO) and CuKα radiation source, and analysed using HighScore Plus software with ICDD database. Microstructural and compositional investigations of the materials were conducted with field emission scanning electron microscopy (FESEM, Zeiss ULTRAplus microscope) and energy-dispersive spectrometry (EDS, INCA Energy 350 with INCAx-act silicon drift detector equipped in FESEM, Oxford Instruments). For microstructural analyses, metallographic cross-sections were prepared by casting cut sections of specimens in Epofix cold setting resin under reduced pressure. The casts were then ground, polished and carbon coated for electrical conductivity. The polished cross-sections were studied by angle-selective backscattered electron (AsB) detector in order to maximize the compositional contrast.

Apparent solid density, bulk density and open porosity of reaction-sintered Sint01, Sint05, Sint09, and the reference samples, all with stoichiometric mullite composition, were investigated according to Archimedes principle following the ISO18754 standard. Compressive strength values were determined for the same materials than the density and porosity values. These were measured using an INSTRON testing system according to the standard ISO 20504:2006. Rectangular samples with dimensions of approximately 15 mm × 40 mm were employed in the compression tests, with the used compression speed being 1 mm/min.

3. Results and discussion

3.1. Thermal behavior

Compressed pellets of mining tailings (FMT1, FMT2 and FMT3) and all powder mixtures (Sint01-Sint12) were visually examined after the reaction sintering experiments. The observations made after the heat

Table 4
Visual observations results after the heat-treatments of the specimens.

Specimen	Composition (wt%)			Observations after heat-treatment at 1300 °C/3 h
FMT1	Quartz	Alkali feldspars	K-micas	Melted completely, loosing shape
	40	41	9	
FMT2	11	49	22	Melted completely, loosing shape
FMT3	64	–	27	Retained shape, no melting observed but clearly fractured
Sint01	FMT1		Boehmite	Retained shape, no melting observed
	33.6		66.4	
Sint02	50.4		49.6	Retained shape, no melting observed
Sint03	67.0		33.0	Retained shape, no melting observed
Sint04	83.5		16.5	Retained shape, no melting observed
Sint05	FMT2		Boehmite	Retained shape, no melting observed
	40.4		59.6	Retained shape, no melting observed
Sint06	55.4		44.6	Retained shape, no melting observed
Sint07	70.5		29.5	Melting observed
Sint08	85.2		14.8	Melted completely, loosing shape
Sint09	FMT3		Boehmite	Retained shape, no melting observed, but clearly fractured
	28.8		71.2	
Sint10	46.4		53.6	Retained shape, no melting observed
Sint11	64.0		36.0	Retained shape, no melting observed
Sint12	82.0		18.0	Retained shape, no melting observed

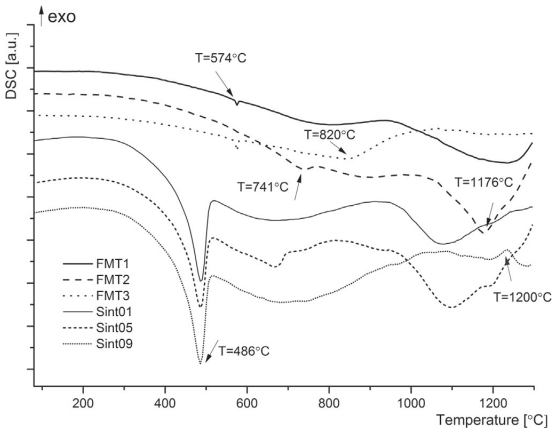

Fig. 1. DSC curves for mining tailings FMT1, FMT2, FMT3 and recipes Sint01, Sint05 and Sint09.

treatments of the specimens are summarized in Table 4. The compressed pellets of pure FMT1 and FMT2 melted completely, losing their shape in the heat-treatment due to melting. On the other hand, no melting was observed for the pellet of FMT3, but the specimen was clearly fractured during the heat treatment. High alkali-feldspar contents of FMT1 and FMT2 tailings compared to that of FMT3 probably caused this difference. As mentioned earlier, feldspars contain alkali metals, which decrease the melting temperature. In the work Raith et al. [20] feldspars melting behavior was studied, that supported the observations. All the FMT1 (Sint01-Sint04) and FMT3 (Sint09-Sint12) containing mixtures balanced with boehmite additions retained their shape during reaction sintering. Among the FMT2 containing powder mixtures, only the mixtures (Sint05 and Sint06) with the highest boehmite additions retained their shape during reaction sintering, thus the mixtures Sint07 and Sint08 experienced melting during the heat treatment.

Fig. 1 shows DSC curves and Fig. 2 TG curves for pure mining tailings FMT1, FMT2 and FMT3 and the stoichiometric mullite powder mixtures with boehmite (recipes Sint01, Sint05 and Sint09). For pure tailings, the first phase transformation occurred at 574 °C as a small endothermic peak for all three tailing samples. No notable weight change was related to this phase transformation, based on which the

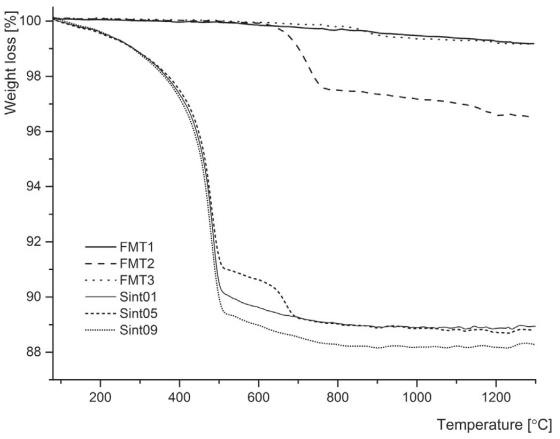

Fig. 2. TG curves for mining tailings FMT1, FMT2, FMT3, and selected recipes Sint01, Sint05 and Sint09.

peak could be associated with quartz alfa-beta phase transition, described by Christidis [21]. With increase in temperature, the DSC curve of FMT2 contained an endothermic peak at approximately 741 °C (Fig. 1), connected with weight change by 2.5% in TG curve (Fig. 2). This transformation was probably related to calcite phase decomposition, because FMT2 includes calcite (according to the mineralogy analysis, Table 2). Both FMT1 and FMT2 curves involved also a peak at approximately at 1176 °C for FMT1 and at slightly (about 20 °C) higher temperature for FMT2, relating most probably to the appearance of the liquid phase for both tailings. The DSC curve for FMT3 further included a transformation peak at 820 °C (Fig. 1), likely relating to quartz to cristobalite transformation as temperature increases [22].

The curves for powder mixtures with boehmite additions (Sint01, Sint05 and Sint09) all contained the first phase transformation peak at approximately 486 °C (Fig. 1) connected with a significant weight change by approximately 10% in TG curve (Fig. 2). This transformation was associated with the boehmite dehydraoxylation (dehydration and simultaneous alumina formation). For powder mixture Sint05, an endothermic peak in a DSC curve appeared at approximately the same temperature than for pure FMT2 tailing and was likely associated with the calcite decomposition process on the basis of the slight further weight loss during the reaction. For the powder mixture Sint_09, the DSC curve included an exothermic peak at slightly above 1200 °C, which could indicate the kaolinite transformation to mullite, as earlier reported by MacKenzie et al. [23].

A liquid phase formed most easily in the presence of high-alkali content mining tailings FMT1 and FMT2. DSC curves (Fig. 1) showed for FMT1 and FMT2 a slope decline starting above 900 °C and featuring a clear peak approximately at 1176 °C for FMT2 and about 30 °C higher temperature for FMT1. FMT3 did not show a similar trend, which could (together with Fig. 1) indicate this transformation was related to the formation of a liquid phase, i.e., melting of FMT1 and FMT2. For FMT2 the decline in the DSC curve slope was steeper as compared to that for FMT1, which could refer to a higher liquid phase amount. Literature shows quite large variation in the melting temperatures of feldspar minerals. For example, for albite, of which FMT1 contains 21% and FMT2 31%, Natrovsky et al. [24] reported the melting temperatures between 1105 and 1145 °C, Johnson & McCauleyn [25] demonstrated the melting temperature of 1134 °C and Sokolář &Vodova [26] showed melting not until 1180 °C. In order to verify the differences in melting behaviors between FMT1 and FMT2, samples were extra heat treated at the temperature range of interest (1000 °C − 1150 °C). Fig. 3 shows compressed FMT1 and FMT2 pellets after heat treatment at three temperatures; 1000 °C, 1100 °C and 1150 °C for 1 h. Figure shows that in FMT2, the liquid phase formed already between 1000 °C and 1100 °C, while in FMT1 the liquid phase formation started at somewhat higher temperatures, between 1100 °C and 1150 °C.

The thermal expansion behavior of the compressed powder mixtures (Sint01, Sint05, Sint09), in the form of dilatometric curves, is presented in Fig. 4. The first shrinkage step for all test materials was visible at 500 °C and was attributed to the dehydration of boehmite, as mentioned also in the context of DSC curves. The second, sintering-derived and thus more significant shrinkage of all FMT mixtures (Sint01, Sint05 and Sint09) occurred above 1100 °C. Since all of the compressed powder mixtures showed clear evidence of sintering, these results promote the use of the sintering temperature of at least 1300 °C for producing dense matter by reaction sintering of raw material mixtures discussed in this paper.

3.2. Phase structure analysis

XRD patterns for FMT1, FMT1 after heat treatment, and FMT1 based reaction-sintered powder mixtures (Sint01-Sint04) are shown in Fig. 5. The XRD curve for FMT1 powder was characterized by peaks related to quartz, biotite/muscovite and albite phases, consistent with the mineralogy presented in Table 1. FMT1 was completely melted during the

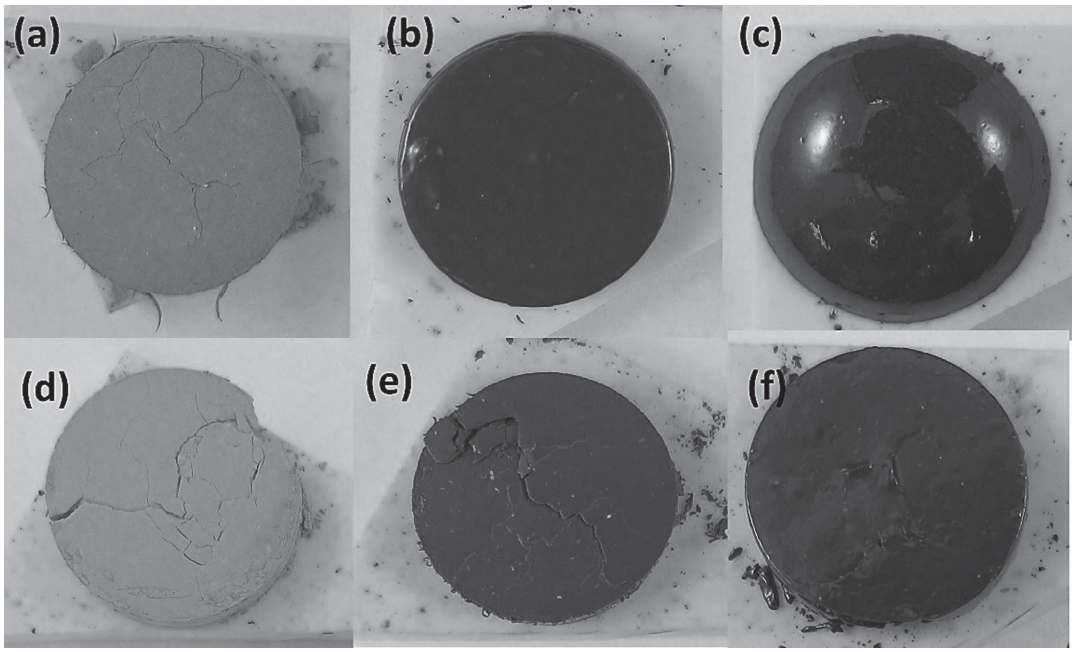

Fig. 3. Precompressed tailings FMT1 pellets after heat treatments at (a) 1000 °C for 1 h, (b) 1100 °C for 1 h, (c) 1150 °C for 1 h, and FMT2 after heat-treatments at (d) 1000 °C for 1 h, (e) 1100 °C for 1 h, and (f) 1150 °C for 1 h.

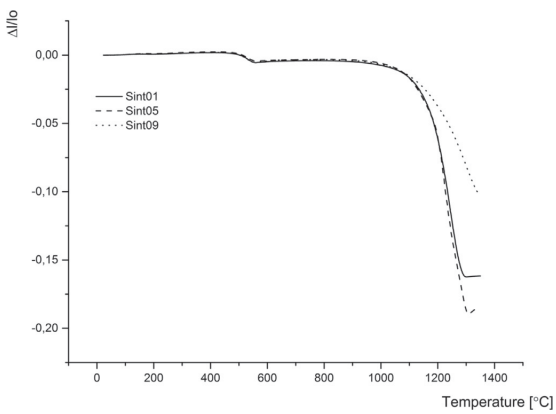

Fig. 4. Dilatometric curves of the mixtures Sint01, Sint05 and Sint09.

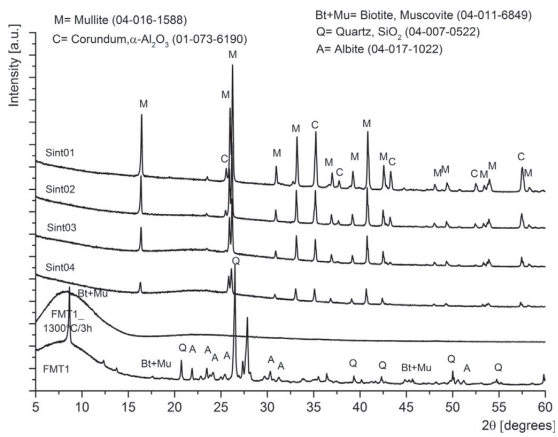

Fig. 5. XRD patterns of jet-milled FMT1, heat-treated FMT1 and reaction-sintered pieces Sint01-Sint04.

heat treatment and, therefore it was crushed in a ball mill before the XRD measurements. The XRD pattern collected for the crushed powder FMT1 after heat treatment showed no peaks of crystalline phases. Hump detected in the curve at low 2θ values may result from the fine structure or even amorphous phase.

All reaction-sintered powder mixtures (FMT1 balanced with boehmite, Table 3) were clearly crystalline and involved mullite as the main crystalline phase. XRD patterns involved also corundum peaks, which indicates some unreacted (dehydrated) boehmite. This finding was further justified by the fact that corundum peak intensities decreased when the boehmite amount in the mixtures decreased. A broad hump between 15° and 30° in XRD patterns indicated the presence of amorphous phase in all reaction-sintered powder mixtures, being most evident in Sint04 curve. According to XRD patterns, the mullite peak intensities decreased and the amorphous phase amounts increased with increase in mining tailings content in the powder mixture recipe. No high-intensity peaks related to the phases identified in the pure tailings: quartz, biotite/muscovite and albite, were seen in XRD spectra for the reaction-sintered mixtures. This is a sign that reaction sintering has been successful.

XRD patterns for FMT2, heat-treated FMT2, and reaction-sintered powder mixture specimens Sint05-Sint08 are shown in Fig. 6. In the XRD pattern for FMT2, analysis identified peaks associated with quartz, albite, biotite/muscovite and calcite, in agreement with mineralogical analysis (Table 1). FMT2 was completely melted in the heat treatment, and for that reason, the melted FMT2 sample was crushed in a ball mill

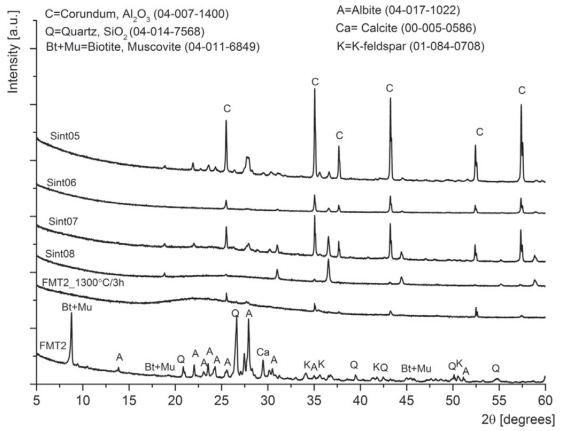

Fig. 6. XRD patterns for jet-milled FMT2, heat-treated FMT2 and reaction-sintered pieces Sint05-Sint08.

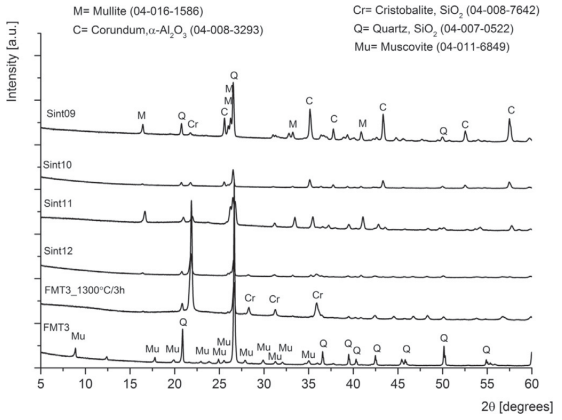

Fig. 7. XRD patterns for jet-milled FMT3, heat-treated FMT3 and reaction-sintered pieces Sint09-Sint12.

into powder form for the XRD measurements. Small corundum peaks detected in the XRD spectrum for melted FMT2 sample were probably due to the contamination from alumina substrate when removing the melted sample.

Conversely to reaction-sintered FMT1 containing mixtures, XRD spectra for FMT2 based powder mixtures (Sint05-Sint08) did not involve mullite peaks after reaction sintering experiments. However, peaks related to at least one crystalline phase could be detected in addition to corundum phase in the XRD patterns for reaction-sintered specimens. Sokolář and Vodova [26] suggested in their study that sodium-calcium-containing mineral mixture (simulating oligoclase) transformed into the combination of a major phase of anorthite and a minor phase of albite when heated above 1275 °C. Also here, anorthite could be suggested as the crystalline phase as a result of andesine transformation or reaction between calcite and albite. A broad hump between 15° and 30° in XRD patterns indicated the presence of an amorphous phase in the reaction-sintered specimens. In addition, for FMT2 containing powder mixtures, no marks from the phases identified in pure FMT2 remained in the sintered mixtures: the peaks related to quartz, albite, biotite/muscovite and calcite had disappeared from the XRD spectra.

XRD patterns for FMT3, heat-treated FMT3 and reaction-sintered powder mixtures containing FMT3 (Sint09-Sint12) are shown in Fig. 7. The XRD curve for FMT3 contained quartz and muscovite peaks, equally to mineralogical analysis (Table 1). After heat treatment, XRD pattern for FMT3 involved cristobalite peaks and some small peaks related to quartz. Also minor mullite peaks were seen in the XRD curve for the heat-treated mining tailing sample, most probably due to muscovite reaction (all muscovite peaks were disappeared after the heat treatment). Aasly [22] has shown that the quartz phase transforms into cristobalite at high temperatures, thus evidently this transformation has occurred here. In addition, XRD analyses for reaction-sintered powder mixtures with boehmite additions revealed cristobalite peaks, the intensities of which decreased with increase in boehmite amount. XRD patterns for reaction-sintered powder mixtures also included quartz peaks, indicating that also unreacted quartz was retained in reaction-sintered specimens. The curves also contained peaks associated with mullite and corundum. Corundum peaks were the highest for the mixture of the highest boehmite addition, thus unreacted corundum was retained in the structure. No amorphous hump was detected in the XRD spectra for FMT3 based samples due to the absence of glass formers, like alkali fluxes.

3.3. Microstructure analysis

FESEM micrographs of reaction-sintered powder mixture specimens (a) Sint01, (b) Sint02, (c) Sint03 and (d) Sint04 consisting of FMT1 with boehmite additions are shown in Fig. 8. FESEM images revealed that the microstructures formed in reaction sintering consisted of evenly distributed and networked needle-shaped crystals surrounded by an amorphous glass phase (seen as uniform areas between the networked needles). Microstructure also involved separate randomly distributed clusters of nearly equiaxed crystals. Porosity, seen in black contrast, was also present in most cases, particularly in Sint01.

EDS analyses together with XRD results enabled to identify the crystalline needle network as the mullite phase (with Al/Si ionic ratio of the 3:1 corresponding to 3:2 mullite). Separate clusters of equiaxed crystals were identified as the corundum phase. Crystalline phases were surrounded by an amorphous aluminosilicate glass phase with traces (~ 2 wt%) of Na, K and Ca. According to EDS analyses, it is challenging to draw any definite conclusion about the Fe distribution, due to complexity of microstructural details and fine crystal size compared to electron beam size and analysis spot dimension exceeding the crystal detail size. According to EDS analyses, Fe was present in the amorphous phase but traces of it were detected also in the mullite needles. FMT1 contained 6% biotite, which is a Fe-rich mineral, which could partly explain the presence of Fe in the mullite needles. Microstructural images support the observations based on the XRD curves that the amount of amorphous phase increased with decrease in the amount of boehmite.

XRD, SEM and EDS analyses suggested that, during the reaction sintering of FMT1 containing mixtures, Sint01, Sint02, Sint03 and Sint04, the original minerals included in FMT1, i.e., alkali feldspars and K-micas, converted into liquid form. Higher temperature increased the solubility of silica to the melt, which enabled silica reaction with alumina (resulting from boehmite). Mullite phase then crystallized from the aluminosilicate melt. According to Schneider et al. [6], mullite crystals that have grown from aluminosilicate melt usually display acicular (needle-shaped) morphology, which also supports this assumption.

Fig. 9 shows FESEM micrographs of reaction-sintered powder mixture specimens of (a) Sint05 consisting of FMT2 and (b) Sint09 consisting of FMT3 with boehmite additions. The microstructure formed from FMT2 containing powder mixture (Fig. 9a) contained needle-shaped crystals with the length of approximately 5–10 μm and surrounded by an amorphous phase. In addition, here, randomly distributed crystal clusters appeared in occasional areas; these were

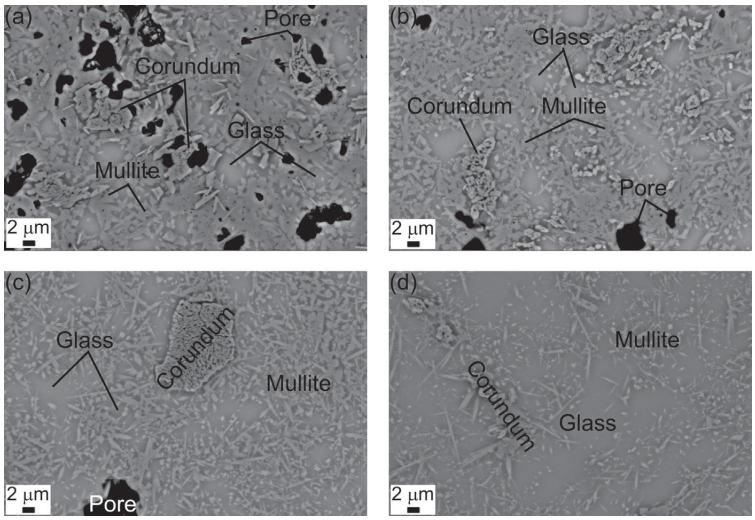

Fig. 8. FESEM images (AsB) of the cross-sections of at 1300 °C for 3 h reaction-sintered (a) Sint01, (b) Sint02, (c) Sint03, and (d) Sint04 specimens.

identified as corundum according to combined EDS and XRD analyses. According to EDS analyses, the crystal needles were identified as an Al-rich aluminosilicate phase. One possibility is that calcite is reacting in feldspar melt and crystallized into anorthite as suggested in XRD results.

As a conclusion, it seems that also in the case of FMT2, the original phases of albite, biotite, K-feldspar and quartz did melt and formed a new aluminosilicate crystalline phase. For some reason, mullite was not detected after the reaction sintering process regardless of the correct Al:Si ratio in the Sint05 mixture. Sint05 contains FMT2, in which the amount of impurities was the highest among the studied mining tailings (FMT1, FMT2, FMT3).

FESEM examinations, Fig. 9(b), revealed that Sint09 specimen that contains FMT3 with boehmite addition had a microstructure consisting mainly of coarse grains. There were also visible macro cracks in the structure. According to EDS analyses, the coarse grains were identified as quartz grains, which is supported by XRD analyses. Corundum crystals were identified between the quartz grains and, to some extent, their clustering was observed. Occasional single mullite needles were identified according to EDS analyses, probably resulting from kaolinite heating. These results suggest for FMT3 with low alkali content and high silica content that much of the quartz phase was retained unreacted in the reaction sintering experiments. It could be possible to facilitate mullite formation with notably higher sintering temperatures. For example, the mullitization temperature for the solid-state reaction between Al_2O_3 and SiO_2 particles can be higher than 1650 °C for the completion of the reaction.

Presented results showed that mullite crystallizes from aluminosilicate melt in alkali-feldspar- and quartz-containing tailing, FMT1, mixed with boehmite. However, mullite does not form in the mixtures of FMT2 bearing higher alkali-feldspar and lower quartz content as compared to FMT1. According to the received results, it is suggested that only with a particular mineralogical composition the mullite formation is possible regardless of the correct Al:Si ratio. It seems that one important factor in mining tailing mineralogical composition for the following mullite formation is the amount of alkali feldspars in relation to quartz. Mineralogical analysis for FMT1 (Tables 1, 2) shows that the quartz content was about equal to the sum of alkali feldspars. For FMT2, the quartz content was only 11% and the alkali feldspars content was relatively much higher. Another mineralogical difference between the studied mining tailings FMT1 and FMT2 was the Fe-containing micas. In FMT2, the amount of mica was relatively much higher (20% compared to 6% in FMT1).

In the study by Sokolář and Vodova [26] it was shown that the melting of feldspars is dependent on many factors, such as the rate of heating and the content of alkali oxides. For the melting of feldspars, not just the total content of feldspar components are important, but also the ratio between potassium and sodium feldspars (i.e. between K_2O and Na_2O). At the appropriate ratio, low-melting eutectics may appear, with a melting temperature substantially lower than the melting temperature of pure feldspars. Results presented here suggest that one explanation for the differences for mullite crystallization between the three felsic tailings with different mineralogical compositions could relate to differences in the melting temperatures of FMT1 and FMT2.

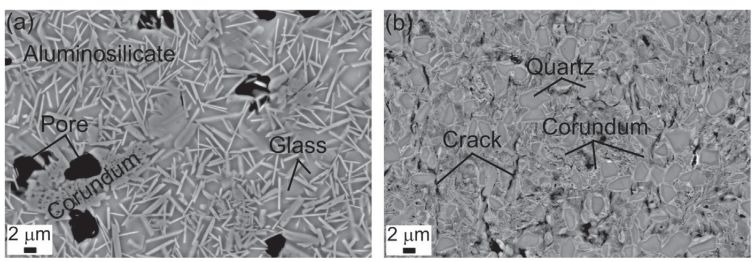

Fig. 9. FESEM images (AsB) of cross-sections of at 1300 °C for 3 h reaction-sintered (a) Sint05, and (b) Sint09 specimens.

Table 5
Apparent density, bulk density and open porosity values of the studied specimens and reference.

Recipe code	Apparent solid density (g/cm^3)	Bulk density (g/cm^3)	Open porosity (%)
Sint01_1300C/3 h	2.7 ± 0.02	2.6 ± 0.05	6.1 ± 1.12
Sint05_1300C/3 h	3.0 ± 0.004	2.9 ± 0.005	2.4 ± 0.06
Sint09_1300C/3 h	3.1 ± 0.007	2.4 ± 0.02	24 ± 0.71
Reference	3.1 ± 0.001	2.3 ± 0.02	25 ± 0.51

Results indicate that mullite crystallization in aluminosilicate melt is possible if the crystallization temperature for mullite is high enough. For this approach, the composition plays an important role, i.e., the amount of alkalis.

3.4. Structural integrity and strenght

Table 5 summarizes apparent density, bulk density and open porosity values for the reaction-sintered powder mixture specimens Sint01, Sint05, Sint09 and the stoichiometric 3:2 mullite used as a reference. Results are average values determined for three parallel samples. The results showed that open porosity was much lower for the specimen Sint01 containing FMT1 and Sint05 containing FMT2 that are rich in alkali feldspars compared to Sint09 containing FMT3 that does not contain alkalis. The formed liquid phase clearly promoted the densification of the structure. No clear trends were detected between density values and the specimen composition.

Fig. 10 shows the compressive strength values for the reaction-sintered specimens containing FMT1 (Sint01), FMT2 (Sint05), FMT3 (Sint09) and for the reference. Results are average values of five measurements. The results disclosed that the strength values (> 60 MPa) of the mining tailing containing specimens were of the same magnitude than for the reference. As porosity results, Table 5, revealed, the formed liquid phase (Sint01 and Sint05) promoted the densification of the specimens, which had a slight positive effect on strength values. Thus, the highest overall strength values were obtained for sample Sint05, with the powder mixtures with the lowest open porosity. Conversely, the lowest strength values were detected for Sint09, being characterized by the highest open porosity. However, the strength values of Sint09 and the reference were still at sufficient level despite of the high porosity in these specimens. The most significant difference between the mining tailing based samples and the reference was the extent of scatter in the strength values: in the case of all mining tailings based samples (Sint01, Sint05, Sint09), the scatter was approximately 2–3 times that in the case of the reference sample. Magnitude of the scatter in strength values was higher than the scatter reported in the works of Alves et al. [5] and Dong et al. [12]. They both reported flexural strength values. This was probably because of a great structural heterogeneity between local areas in the reaction-sintered mining tailing samples, particularly concerning the distribution of the amorphous glass phase.

3.5. Mullite formation and thermal resistance

Characterization results showed that high alkali-feldspar content caused pure FMT1 to melt already above 1100 °C (Fig. 3). By modifying the chemical composition of the mining tailing with boehmite addition it was possible to generate microstructure that included acicular mullite network surrounded by amorphous glass phase. According to the research hypothesis, the formation of mullite would improve the thermal resistance and enable use at higher temperatures of the formed ceramic materials.

In order to prove the improved thermal resistance of the samples containing mullite structure, the reaction-sintered Sint01, Sint05 and Sint09 pellets from the first dilatometer measurements were subjected again to dilatometer measurements, which were conducted at 1450 °C. The results, Fig. 11, show a clear difference between Sint01, which contains the mullite structure, and Sint05, where mullite structure was not formed. During reheating Sint05, a clear transformation still occurred, first after 1100 °C and second after 1300 °C, most probably due to liquid phase formation. In contrast, reheating Sint01 and Sint09 introduced homogenous and linear expansion of the specimen. Small shrinkage occurred after 1300 °C, what indicated that the sintering observed in the previous measurements had not been complete. In the forthcoming works, the optimal reaction sintering time and temperature will be studied in more detail. In addition, the high temperature properties of the mullite containing specimens will be studied more thoroughly in order to establish their applicability for refractory uses.

4. Conclusions

The results of the presented study enable the following conclusions:

1. High alkali-feldspar contents cause molybdenum ore tailings (FMT1) and gold ore tailings (FMT2) to melt already slightly above 1100 °C. Therefore, these tailings as such are not suitable for refractory applications requiring thermal resistance up to higher temperatures.
2. XRD, FESEM and EDS analyses suggest that, by reaction sintering at

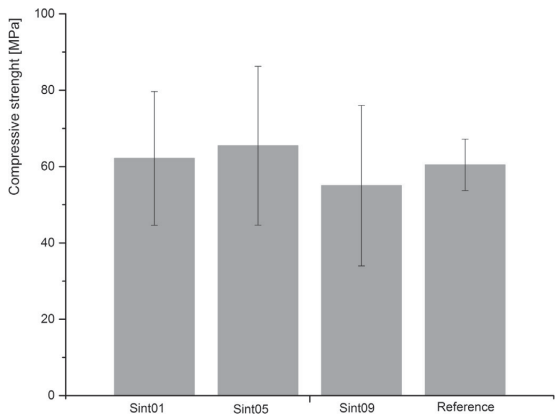

Fig. 10. Compressive strength values at 1300 °C for 3 h reaction-sintered specimens.

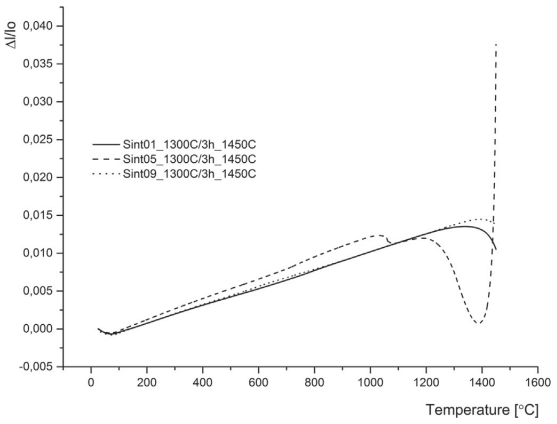

Fig. 11. Dilatometric curves of reheating of the reaction-sintered Sint01, Sint05, and Sint09 pellets.

1300 °C for 3 h with boehmite, molybdenum ore tailings (FMT1) containing powder mixtures yield acicular mullite structure surrounded by amorphous glass phase. During the heat treatment, the original minerals in the tailings: alkali feldspars and K-micas, convert into a liquid form. Higher temperature increases the solubility of silica to the melt, which subsequently enable silica reaction with alumina (resulting from boehmite) into mullite. Thus, mullite phase crystallizes from the aluminosilicate melt.

3. Mullite does not form in the mixtures of gold ore tailings (FMT2), having the highest amount of alkali-feldspars among the three mining tailings, although the aluminosilicate melt forms, similarly to molybdenum ore mining tailing case. According to the results, it is suggested that only with the particular mineralogical composition the mullite formation is possible regardless of the correct Al:Si ratio. One important factor in tailing mineralogical composition with respect to mullite formation is the amount of alkali feldspars in relation to quartz. Excess amount of iron-rich mica minerals may also prevent the mullite formation.
4. In quartz ore tailings (FMT3), aluminosilicate melt does not form and mullite is thus not crystallized from the melt. Reaction-sintered specimens were clearly fractured. For FMT3 with low alkali content and high silica content, the quartz retained largely unreacted in the reaction sintering experiments. It may be possible to facilitate the mullite formation with notably higher sintering temperatures via solid-state reaction between Al_2O_3 and SiO_2 particles.
5. Porosity is much lower in reaction-sintered specimens containing molybdenum ore tailings (< 6%) and gold ore tailings as compared to the quartz ore tailings (24%). The liquid phase that form in the two former systems in the presence of boehmite promote the densification of the structure. Molybdenum ore tailings and gold ore tailings containing specimens show compressive strength values (> 60 MPa) comparable to the corresponding values for the reference, yet with a greater scatter.
6. Mullite network formation enables better thermal resistance up to > 1450 °C for the formed ceramic materials as compared to other aluminosilicate phases in the samples, showing potential to be used for refractory ceramic applications.

Acknowledgement

The research has been supported by the Academy of Finland, project CeraTail funding decision #292563 and by the Strategic Research Council at the Academy of Finland, project CloseLoop, funding decision #303453.

References

[1] P.M. Kauppila, M.L. Räisänen, S. Myllyoja. Best Environmental Practices in Metal Ore Mining. Finnish Environment en29/2 011. 〈http://hdl.handle.net/10138/40006〉 ISSN 978-952-11-3942-0 (PDF).
[2] A. Akcil, S. Koldas, Review article Acid Mine Drainage (AMD): causes, treatment and case studies, J. Clean. Prod. 14 (2006) 1139–1145, https://doi.org/10.1016/j.jclepro.2004.09.006.
[3] B.G. Lottermoser, Recycling, reuse and rehabilitation of mine wastes, Elements 7 (2011) 405–410, https://doi.org/10.2113/gselements.7.6.405.
[4] EllenMacArthurFoundation. Report Growth within: a circular economy vision for a competitive Europe. June, 2015. Available: 〈https://www.ellenmacarthurfoundation.org/assets/downloads/publications/EllenMacArthurFoundation_Growth-Within_July15.pdf〉.
[5] H.P.A. Alves, J.B. Silva, L.F.A. Campos, S.M. Torres, R.P.S. Dutra, D.A. Macedo, Preparation of mullite based ceramics from clay–kaolin waste mixtures, Ceram. Int. 42 (2016) 19086–19090, https://doi.org/10.1016/j.ceramint.2016.09.068.
[6] H. Schneider, J. Schreuer, B. Hildmann, Structure and properties of mullite—a review, J. Eur. Ceram. Soc. 28 (2008) 329–344, https://doi.org/10.1016/j.jeurceramsoc.2007.03.017.
[7] A.H. Paksaresht (Ed.), Production, Properties, and Applications of High Temperature Coatings, IGI Global, 2018(ISSN: 2327-5448).
[8] R. Krishnamurthy, B.W. Sheldon, Stability of mullite protective coatings for silicon-based ceramics, J. Am. Ceram. Soc. 88 (2005) 1099–1107, https://doi.org/10.1111/j.1551-2916.2005.00169.x.
[9] F.J.S. Klug, Prochazka, R.H. Doremus, Alumina–silica phase diagram in the mullite region, J. Am. Ceram. Soc. 70 (1987) 750–759, https://doi.org/10.1111/j.1151-2916.1987.tb04875.x.
[10] H.P.A. Alves, R.A. Junior, L.F.A. Campos, R.P.S. Dutra, J.P.F. Grilo, F.J.A. Loureiro, D.A. Macedo, Structural study of mullite based ceramics derived from a mica-rich kaolin waste, Ceram. Int. 43 (2017) 3919–3922, https://doi.org/10.1016/j.ceramint.2016.12.035.
[11] Y. Dong, X. Feng, X. Feng, Y. Ding, X. Liu, G. Meng, Preparation of low-cost mullite ceramics from natural bauxite and industrial waste fly ash, J. Alloy. Compd. 460 (2008) 599–606, https://doi.org/10.1016/j.jallcom.2007.06.023.
[12] Y. Dong, J. Zhou, B. Lin, Y. Wang, S. Wang, L. Miao, Y. Lang, X. Liu, G. Meng, Reaction-sintered porous mineral-based mullite ceramic membrane supports made from recycled materials, J. Hazard. Mater. 172 (2009) 180–186, https://doi.org/10.1016/j.jhazmat.2009.06.148.
[13] Y. Dong, S. Hampshire, J. Zhou, B. Lin, Z. Ji, X. Zhang, G. Meng, Recycling of fly ash for preparing porous mullite membrane supports with titania addition, J. Hazard. Mater. 180 (2010) 173–180, https://doi.org/10.1016/j.jhazmat.2010.04.010.
[14] J.S. Jung, H.C. Park, Mullite ceramics derived from coal fly ash, J. Mater. Sci. Lett. 20 (2001) 1089–1091.
[15] S.C. Vieira, A.S. Ramos, M.T. Vieira, Mullitization kinetics from silica- and alumina-rich wastes, Ceram. Int. 33 (2007) 59–66, https://doi.org/10.1016/j.ceramint.2005.07.015.
[16] S. Solismaa, A. Ismailov, M. Karhu, H. Sreenivasan, M. Lehtonen, P. Kinnunen, M. Illikainen, M.-L. Räisänen, Valorization of Finnish mining tailings for the use of ceramic industry, Bull. Geol. Soc. Finl. 90 (2018) 33–54, https://doi.org/10.17741/bgsf/90.1.002.
[17] I. Haapala, O. Rämö, Mineral deposits related to granitic rocks, in: W.D. Maier, R. Lahtinen, H. O'Brien (Eds.), Mineral Deposits of Finland, Elsevier Scientific Publ. Co, Amsterdam, 2015, pp. 531–556, , https://doi.org/10.1016/B978-0-12-410438-9.00021-2.
[18] P. Sorjonen-Ward, A. Hartikainen, P. Nurmi, K. Rasilainen, P. Scaubs, Y. Zhang, J. Liikanen, Exploration targeting and geological context of gold mineralization in the neoarchean ilomantsi greenstone belt in eastern Finland, in: W.D. Maier, R. Lahtinen, H. O'Brien (Eds.), Mineral Deposits of Finland, Elsevier Inc, 2015, pp. 435–466.
[19] M. Lehtinen, Industrial minerals and rocks, in: W. Maier, R. Lahtinen, H. O'Brien (Eds.), Mineral deposits of Finland, Elsevier Inc, 2015, pp. 658–705.
[20] M.M. Raith, R. Hoffbauer, R. Spiering, M. Shinoto, N. Nakamura, Melting behaviour of feldspar clasts in high-fired Sue ware, Eur. J. Mineral. 28 (2016) 385–407, https://doi.org/10.1127/ejm/2016/0028-2514.
[21] G.E. Christidis (Ed.), Advances in the characterization of Industrial Minerals, 9 Mineralogical Society of Great Britain and Ireland, 2010, , https://doi.org/10.1180/EMU-notes.9.
[22] K. Aasly, Properties and Behavior of Quartz for the Silicon Process (Thesis for the degree of philosophiae doctor), (2008) https://core.ac.uk/download/pdf/52098782.pdf.
[23] K.J.D. MacKenzie, et al., The thermal reactions of muscovite studied by high-resolution solid state 29-Si and 27-Al NMR, J. Mater. Sci. 22 (1987) 2645–2654, https://doi.org/10.1007/BF01082158.
[24] A. Navrotsky, C. Capobianco, J. Stebbins, Some thermodynamic and experimental constraints on the melting of albite at atmospheric and high pressure, J. Geol. 90 (1982) (1982) 679–698 〈https://www.jstor.org/stable/i30081028〉.
[25] L. Johnson, R. McCauley, The thermal behavior of albite as observed by DTA, Thermochim. Acta 437 (2005) (2005) 134–139.
[26] R. Sokolář, L. Vodová, Sintering of feldspar rocks from czech quarries, J. Ceram. Soc. Jpn. 123 (2015) 62–67 (1).

PUBLICATION III

Magnesite-rich mining tailings as a raw material for refractory ceramics – microstructural and thermal analysis

Marjaana Karhu, Juha Lagerbom, Soili Solismaa, Elina Huttunen-Saarivirta

Proceedings of the Estonian Academy of Sciences 68 (2) (2019) 145–149

https://doi.org/10.3176/proc.2019.2.05

Publication reprinted with the permission of the copyright holders.

Proceedings of the Estonian Academy of Sciences,
2019, **68**, 2,
https://doi.org/10.3176/proc.2019.2.05
Available online at www.eap.ee/proceedings

MATERIALS
ENGINEERING

Magnesite-rich mining tailings as a raw material for refractory ceramics – microstructural and thermal analysis

Marjaana Karhu[a*], Juha Lagerbom[a], Soili Solismaa[b], and Elina Huttunen-Saarivirta[a]

[a] VTT Technical Research Centre of Finland Ltd, Visiokatu 4, P.O. Box 1300, 33101 Tampere, Finland
[b] Geological Survey of Finland, P.O. Box 1237, 70211 Kuopio, Finland

Received 9 January 2019, accepted 4 March 2019, available online

© 2019 Authors. This is an Open Access article distributed under the terms and conditions of the Creative Commons Attribution-NonCommercial 4.0 International License (http://creativecommons.org/licenses/by-nc/4.0/).

Abstract. In this paper, we present results of a study about the possibilities of utilizing talc ore mining tailings as a refractory raw material aiming at magnesium aluminate $MgAl_2O_4$ spinel composition. The mine tailings are rich in magnesite but contain also other minerals such as talc, chlorite, dolomite, and iron sulphides. As alumina source for spinel synthesis, we studied also another secondary raw material, an aluminium hydroxide precipitate, a by-product generated from the pickling process of aluminium anodizing. The goal of this paper is to study and compare a pure Mg–Al–O system and the corresponding Mg–Al–O system with some impurities. The formed phase and microstructures were examined by XRD, FESEM, and EDS studies. The thermal behaviour was studied using thermogravimetric analysis.

Key words: mining tailings, refractory ceramics, magnesium aluminate spinel, value from waste.

1. INTRODUCTION

Magnesium aluminate ($MgAl_2O_4$), spinel is the only intermediate compound in the phase diagram of the system MgO–Al_2O_3 [1]. It is an excellent refractory oxide having useful physical, chemical, and thermal properties: a high melting point (2135 °C), excellent resistance against chemical attack, and very good thermal characteristics both at ambient and elevated temperatures. Due to these desirable properties, $MgAl_2O_4$ spinel has a wide range of applications in the structural, chemical, optical, and electrical industries [2,3]. As a refractory material, $MgAl_2O_4$ spinel has applications in the form of sintered ceramics or coatings, e.g. for surfacing furnace parts. In particular, porous $MgAl_2O_4$ spinel ceramic is used as a thermally insulating material at high temperatures for the steel-making industry [4]. Due to its high melting point and high chemical inertness, $MgAl_2O_4$ spinel has also been used to replace traditional chromite-based refractories in cement rotary kilns and steel ladles [5].

Calcination of magnesite ($MgCO_3$) is the principal route by which magnesia (MgO) is formed for the use as a refractory ceramic raw material [6]. In Europe, magnesite is extremely scarce and in high demand, thus it was included in the 2014 EU 'Critical Raw Materials' list [7]. China, North Korea, and Russia account for 65% of the global magnesite reserves with China being the largest magnesite producer [8]. In the path towards resource efficiency, mining tailings are a key resource to take advantage of considering their large volumes, environmental impact, and the need for the efficient exploitation of natural resources [9].

In this paper, we discuss possibilities of utilizing mine tailings from talc ore mining as a refractory raw material aiming at magnesium aluminate ($MgAl_2O_4$)

* Corresponding author, marjaana.karhu@vtt.fi

spinel composition. The main goal of the research was to examine the possibility of utilizing mining tailings containing impurities as low-cost, but presumably non-ideal, raw materials in an effective way. Mine tailings from talc ore mines are rich in magnesite (70–80%). Other minerals are 10–15% talc, 5–10% chlorite, 2–10% dolomite, and 0.5–1% iron sulphides [10]. As the alumina source for spinel synthesis, we used another secondary raw material, an aluminium hydroxide precipitate, a by-product generated from the pickling process of aluminium anodizing. As a reference, a stoichiometric $MgAl_2O_4$ spinel was synthesized by using commercially available MgO and AlO(OH) powders. The goal was to compare a pure Mg–Al–O system and an analogous Mg–Al–O system with some impurities (Si^{4+}, Fe^{3+} cations) present. The formed phase and microstructures were examined by X-ray diffraction (XRD), field emission scanning electron microscopy (FESEM), and energy dispersive spectroscopy (EDS) studies. The ultimate aim of the research was to examine the possibility of utilizing impurity containing mining tailings as economical but presumably non-ideal raw materials in an effective way.

2. EXPERIMENTAL PROCEDURE

2.1. Raw materials

The raw materials selected for the investigation were mining tailings from a talc ore mine and aluminium hydroxide precipitate, a by-product generated from the pickling process of aluminium anodizing. The mining tailings sample was taken from one point of a temporary storage pile; therefore, it is not necessarily representative of the whole mining tailings area of its origin as the mineralogy, grain size, and chemistry of tailings may vary in different parts of the deposit. Table 1 shows the mineralogical composition of the talc ore tailings. Mineralogical characterization included the identification and quantification of mineral phases with scanning electron microscopy (SEM) together with elemental analyses. Table 2 presents the total concentrations of cations (calculated as oxides) in the tailings sample, measured with X-ray fluorescence spectrometry (XRF).

Table 1. Main identified minerals in the talc ore tailings sample (% of total volume)

Mineral	Content, vol%
Magnesite, $MgCO_3$	80.4
Talc, $Mg_3Si_4O_{10}(OH)_2$	9.4
Chlorite, $(Mg,Fe)_5Al(Si_3Al)O_{10}(OH)_8$	4.9
Dolomite, $CaMg(CO_3)_2$	1.8

Table 2. Chemical composition of the talc ore tailings sample as revealed by XRF

	MgO	SiO_2	Fe_2O_3	Al_2O_3
Tailings content, %	38.5	10.1	8.16	0.61

The more detailed explanation of the mineralogical analyses, geochemical analyses, and sampling procedure is presented in [11].

As the alumina source, aluminium hydroxide precipitate, a by-product generated from the pickling process of aluminium anodizing, consisting mainly of gibbsite (aluminium oxide trihydroxide, $Al(OH)_3$) with traces of Na_2SO_4, was used. As a reference, pure magnesium aluminate $MgAl_2O_4$ spinel was prepared using commercially available powders of MgO and boehmite (aluminium oxide hydroxide, AlO(OH)), average grain size < 0.77 μm. The MgO powder was provided by Inframat and the boehmite powder, by Sasol Germany GmbH.

2.2. Synthesis experiments

Experimental powder mixtures were prepared aiming at magnesium aluminate ($MgAl_2O_4$) spinel composition. Recipes shown in Table 3 were formulated with 1 : 2 Mg to Al molar ratio. The talc ore tailings were received in powder form, but the powder was first ground by jet milling into the particle size below 10 μm in order to increase its reactivity and ensure a good mixing of the ingredients. Ceramic powder suspensions (water-based) were prepared from raw material mixtures by bead milling for 15 min. Suspensions were dried with an industrial scale spray dryer Niro Atomizer to produce agglomerated powders. Agglomerated powders were uniaxially compressed into green pellets of 20 mm × 3 mm using approximately 25 MPa pressure. Green state pellets were heat treated in an ENTECH air chamber furnace in ambient air atmosphere and pressure. The powders were heat treated at six different temperatures: 1000, 1100, 1200, 1300, 1400, and 1500 °C. The heating rate was 3.3 °C/min up to the maximum temperature. After 3 hours of holding time, the mixtures were cooled to room temperature at the rate of 5 °C/min.

Table 3. Test matrix recipes for the spinel experiments (wt%)

Recipe code	MgO	AlO (OH)	Talc ore tailings	Aluminium hydroxide precipitate
Recipe1	25.1	74.9	0	0
Recipe2	0	0	35	65

2.3. Characterization methods

The thermal behaviour of agglomerated powders was studied using thermogravimetric analysis (TG, Netzsch STA449 F1 Jupiter) giving a simultaneous differential scanning calorimetry (DSC) signal. The tests were conducted in air atmosphere in a temperature range from 40 to 1500 °C with the heating rate of 10 °C/min. The phase structure was analysed for agglomerated powders and heat-treated pellets by using an X-ray diffractometer (XRD, Empyrean, PANalytical B.V., ALMELO, Netherlands) with a CuKα radiation source, and analysed using HighScore Plus software with ICDD database. The XRD was operated at 45 kV and 40 mA with a scanning rate of 3° 2θ/min. Compressed pellets were characterized after heat treatments.

For microstructural analyses, metallographic cross-sections were prepared by casting cut sections of specimens in Epofix cold setting resin under reduced pressure. The casts were then ground, polished, and carbon coated for electrical conductivity. Microstructural and compositional investigations of the materials were conducted with FESEM (Zeiss ULTRAplus microscope) and EDS and operating on a Noran NSS software. The polished cross-sections were studied by SEM using an angle-selective backscattered electron (AsB) detector in order to maximize the compositional contrast.

3. RESULTS AND DISCUSSION

3.1. Agglomerated powders

The TG and DSC curves of agglomerated powders for the two recipes are presented in Fig. 1. For Recipe1 powder (Fig. 1a), the DSC curve showed an endothermic peak centred at 382 °C and accounting for approximately 12% of the initial weight loss in the TG curve. This was probably caused by the dehydration of magnesium hydroxide, which was formed by the reaction with the spray drying water. Prior to that transformation, evaporation of water occurred (below 290 °C). The second endothermic peak, at 504 °C in the DSC curve, accounted for approximately 10% of the weight loss in the TG curve and was attributed to boehmite dehydraoxylation. The exothermic peak at 1012 °C was most probably related to the spinel crystallization. No weight change was related to this phase transformation. For Recipe2 (Fig. 1b), approximately 36% weight loss was observed already below 600 °C, most likely due to the decomposition of $Al(OH)_3$ and $MgCO_3$. The peak at 853 °C is related to the weight loss of approximately 7%; these findings could be connected to the decomposing of talc. The DSC curve showed also transformation above 1200 °C, with no accompanying weight change in the TG curve. Thus, above 1200 °C the peaks can most likely be attributed to the solid–solid phase transformations.

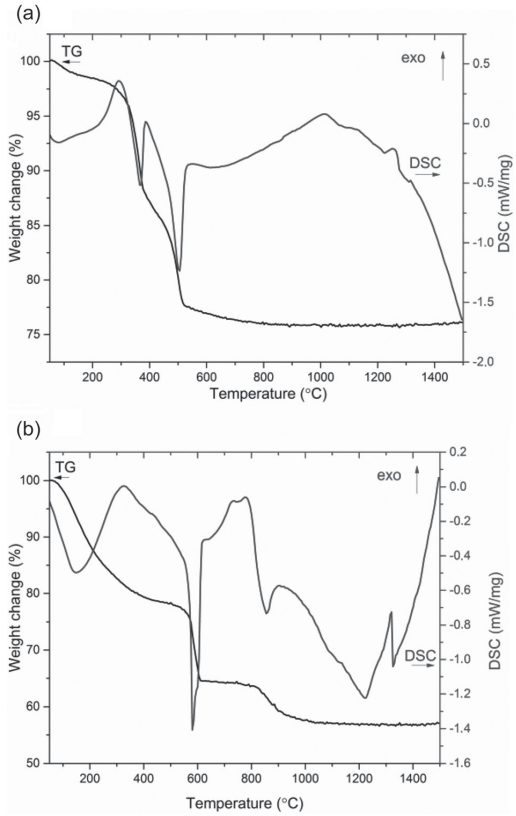

Fig. 1. Thermogravimetric (TG) and differential scanning calorimetry (DSC) curves for agglomerated powders: (a) Recipe1 and (b) Recipe2.

3.2. Sintered pellets

Figure 2 illustrates the phase structure evolution for compressed pellets of both recipes after heat treatments at 1000–1500 °C. For Recipe1 pellets, the $MgAl_2O_4$ spinel phase was the only crystalline phase at all temperatures. The only difference between the applied six temperatures was the peaks widths, indicating that the crystal size increased with the increasing temperature. For Recipe2 compressed pellets, the $MgAl_2O_4$ spinel phase was the main crystalline phase at all temperatures, but also minor peaks related to the ferroan forsterite phase, $(Mg, Fe)_2SiO_4$, were detected at all temperatures. The peaks of forsterite were of lower intensity at higher temperatures. Peak widths, indicating the crystal size,

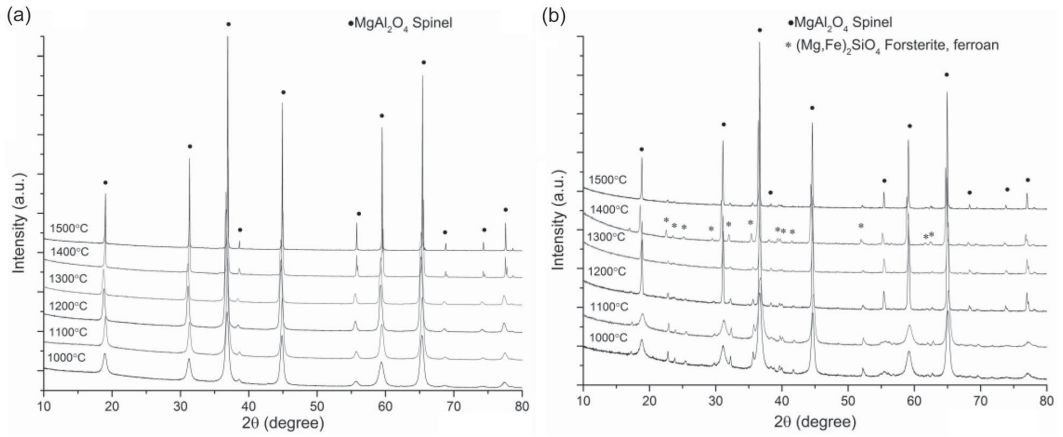

Fig. 2. XRD patterns for powder pellets heat treated at different temperatures: (a) Recipe1 and (b) Recipe2.

were smaller at high temperatures. Additionally, the XRD spectra related to heat-treated pellets of Recipe2 showed a slight increase in the overall intensity of the curve at low 2θ values; thus the presence of an amorphous phase was possible.

Figure 3 shows FESEM images of pellets treated at 1300 °C. Recipe1 produced a very fine structure of $MgAl_2O_4$ spinel crystals. Recipe2 introduced $MgAl_2O_4$ spinel crystals surrounded by an amorphous phase, seen in darker grey than the spinel phase. Also another crystalline

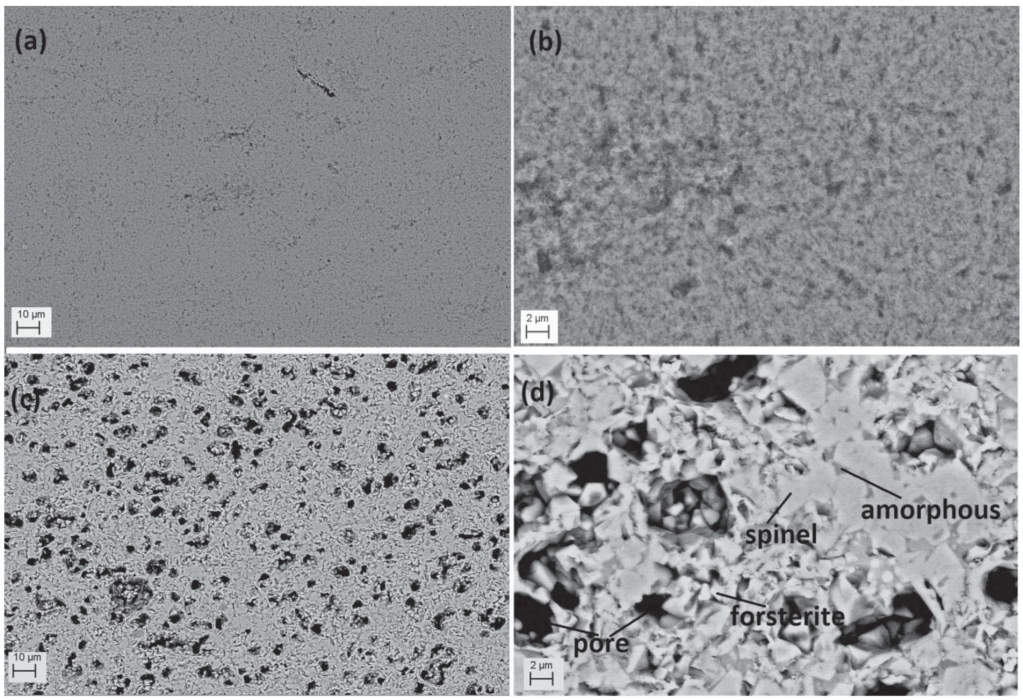

Fig. 3. FESEM images of cross-sections of pellets treated at 1300 °C (a,b) Recipe1 and (c,d) Recipe 2.

phase was observed in areas with a bright contrast, most likely it was the ferroan forsterite, $(Mg, Fe)_2SiO_4$, phase. According to EDS analyses, it is challenging to draw any definite conclusion about the compositional details, due to their microstructural complexity and fine crystal size compared to the electron beam size. Nevertheless, these characterization results suggest that Fe^{3+} cations were concentrated on crystal phases, most likely to the ferroan forsterite, $(Mg, Fe)_2SiO_4$, phase. Partly Si^{4+} cations were also included in the forsterite phase and partly in the amorphous phase. Porosity, seen in black contrast, was also present in both samples, particularly in Recipe2. The more porous structure in Recipe2 pellets evolved due to a relatively higher fraction of evaporating phases (inducing weight losses) consistent with observations on TG/DSC curves (Fig. 1).

4. CONCLUSIONS

The results from this research suggest that synthesis of magnesium aluminate $MgAl_2O_4$ spinel is possible using secondary raw material sources, such as mining tailings from talc ore mining and a by-product from the aluminium anodizing process. Mine tailings from a talc ore mine are rich in magnesite but contain also other minerals such as talc, chlorite, dolomite, and iron sulphides. According to the results, both Si^{4+} and Fe^{3+} cations could be included in the crystalline forsterite phase. Additionally, presence of Si^{4+} cations induced the formation of an amorphous phase. Future work will concentrate on a more detailed characterization of the properties of the secondary raw material-based spinel ceramics.

ACKNOWLEDGEMENTS

The research was supported by the Academy of Finland, project CeraTail funding decision # 292563, and by the Strategic Research Council at the Academy of Finland, project CloseLoop, funding decision #303453. The publication costs of this article were covered by the Estonian Academy of Sciences.

REFERENCES

1. Dal Maschio, R., Fabbri, B., and Fiori, C. Industrial applications of refractories containing magnesium aluminate spinel. *Ind. Ceram.*, 1988, **8**(3), 121–126.
2. Li, H., Wei, H-Y., Cui, Y., Sang, R-L., Bu, J-L., Wei, Y-N., et al. Synthesis and characterisation of $MgAl_2O_4$ spinel nanopowders via nonhydrolytic sol–gel route. *J. Ceram. Soc. Jpn.*, 2017, **125**(3), 100–104.
3. Yan, W., Lin, X., Chen, J., Li, N., Wei, Y., and Han, B. Effect of TiO_2 addition on microstructure and strength of porous spinel ($MgAl_2O_4$) ceramics prepared from magnesite and $Al(OH)_3$. *J. Alloys Compd.*, 2015, **618**, 287–291.
4. Ganesh, I. Fabrication of magnesium aluminate ($MgAl_2O_4$) spinel foams. *Ceram. Int.*, 2011, **37**, 2237–2245.
5. Ganesh, I. A review on magnesium aluminate ($MgAl_2O_4$) spinel: synthesis, processing and applications. *Int. Mater. Rev.*, 2013, **58**(2), 63–112.
6. Walling, S. A. and Provis, J. L. Magnesia-based cements: a journey of 150 years, and cements for the future? *Chem. Rev.*, 2016, **116**, 4170−4204.
7. *Report on Critical Raw Materials for the EU: Report of the Ad Hoc Working Group on Defining Critical Raw Materials*. European Commission, Brussels, Belgium, 2014.
8. Magnesium compounds. In *Mineral Commodity Summaries 2015*. U.S. Geological Survey, Reston, VA, 2015, 96−97.
9. Lottermoser, B. G. Recycling, reuse and rehabilitation of mine wastes. *Elements*, 2011, **7**, 405–410.
10. Räisänen, M-L. *Magnesiittirikastushiekan ympäristökelpoisuus*. Report Dnro K43/41/02. Geological Survey of Finland, 2004 (in Finnish).
11. Solismaa, A., Ismailov, M., Karhu, H., Sreenivasan, M., Lehtonen, P., Kinnunen, M., et al. Valorization of Finnish mining tailings for the use of ceramic industry. *Bull. Geol. Soc. Finl.*, 2018, **90**, 33–54.

Magnesiidirikka kaevandusjäätme kui rasksulava keraamika tooraine kasutamine – mikrostruktuuri- ja termoanalüüs

Marjaana Karhu, Juha Lagerbom, Soili Solismaa ja Elina Huttunen-Saarivirta

On uuritud talgimaagi kaevandusjäätmete kasutamise võimalusi toorainena magneesiumaluminaadi valmistamiseks. Kaevandusjääde on magnesiidirikas, kuid sisaldab ka teisi materjale, nagu talk, kloriit, dolomiit ja raudsulfiid. Alumiiniumoksiidi allikana uuriti ka teisest tooret alumiiniumhüdroksiidi kui sadestist alumiiniumi anodeerimise kaasproduktina. Töö eesmärgiks on uurida ja võrrelda puhast Mg-Al-O ning mõningaid lisandeid sisaldavaid Mg-Al-O süsteeme. Moodustunud faase ja mikrostruktuure uuriti XRD-, FESEM- ning EDS-meetodiga. Termilist käitumist uuriti termograafilise analüüsi meetodit kasutades. Uuriti lisandeid sisaldavate kaevandusjäätmete kasutamist kui ökonoomset, kuid eeldatavalt mitteideaalset toorainet efektiivsel teel. Töö tulemusena selgitati, et magneesium-aluminaadi $MgAl_2O_4$ süntees on võimalik, kasutades teisese toorme ressursse.

PUBLICATION IV

Mining tailings as a raw material for glass-bonded thermally sprayed ceramic coatings: microstructure and properties

Marjaana Karhu, Juha Lagerbom, Mari Honkanen, Elina Huttunen-Saarivirta, Jarkko Kiilakoski, Petri Vuoristo, Soili Solismaa, Päivi Kivikytö-Reponen

Journal of the European Ceramic Society 40 (2020) 4111-4121

https://doi.org/10.1016/j.jeurceramsoc.2020.04.038

Publication reprinted with the permission of the copyright holders.

Journal of the European Ceramic Society 40 (2020) 4111–4121

Contents lists available at ScienceDirect

Journal of the European Ceramic Society

journal homepage: www.elsevier.com/locate/jeurceramsoc

Original Article

Mining tailings as a raw material for glass-bonded thermally sprayed ceramic coatings: Microstructure and properties

Marjaana Karhu[a,*], Juha Lagerbom[a], Mari Honkanen[b], Elina Huttunen-Saarivirta[a], Jarkko Kiilakoski[c], Petri Vuoristo[c], Soili Solismaa[d], Päivi Kivikytö-Reponen[a]

[a] VTT Technical Research Centre of Finland Ltd, Visiokatu 4, P.O. Box 1300, 33101 Tampere, Finland
[b] Tampere Microscopy Center, Tampere University, Korkeakoulunkatu 3, 33014 Tampere University, Finland
[c] Thermal Spray Center Finland (TSCF), Tampere University, Faculty of Engineering and Natural Sciences, P.O. Box 589, 33014 Tampere, Finland
[d] Geological Survey of Finland, P.O. Box 1237, 70211 Kuopio, Finland

ARTICLE INFO

Keywords:
$MgAl_2O_4$ spinel
Mining tailings
Circular economy
Thermal spray
Ceramic coating

ABSTRACT

Magnesium aluminate, $MgAl_2O_4$, spinel powders for thermal spraying, were synthesized from secondary raw materials by spray drying and subsequent reaction sintering. Talc ore mining tailings and aluminium hydroxide precipitate from aluminium anodizing process were studied. A stoichiometric $MgAl_2O_4$ spinel coating was prepared as a reference using pure raw materials. Atmospheric plasma spraying resulted in the formation of ceramic coatings. Microstructural investigations revealed that the reference coatings exhibited crystalline lamellar microstructure of $MgAl_2O_4$ but secondary coatings contained amorphous areas between the crystalline $MgAl_2O_4$ clusters. Abrasive wear test results revealed considerably lower wear rate for secondary coatings. It is suggested that the different structure of coatings, particularly the high degree of amorphous phase between the isolated crystalline $MgAl_2O_4$ clusters caused the higher abrasive wear resistance by changing the wear mechanism. The dielectric breakdown strength of the secondary coatings were at the same level, 24 V/μm, as compared to reference coating, 23 V/μm.

1. Introduction

Magnesium aluminate spinel, $MgAl_2O_4$, is the only intermediate compound in the MgO-Al_2O_3 system [1]. It is a refractory oxide having useful physical, chemical and thermal properties, such as a high melting point (2135 °C), excellent resistance against chemical attack and very good thermal characteristics, both at ambient and elevated temperatures. Due to these desirable properties, sintered $MgAl_2O_4$ spinel has a wide range of applications in structural, chemical, optical, and electrical industries, for example as a high-performance refractory material [2]. Magnesium aluminate spinel is also used in thermally sprayed ceramic coatings for harsh high-temperature environments and in electrical insulating applications where normal insulating materials, such as polymers, cannot be used [3,4]. It has been shown that magnesium aluminate spinel is stable during the thermal spraying process [5] and the only phase determined in the resulting coatings, as cubic $MgAl_2O_4$ [6]. Additionally to the good electrical insulation properties of spinel coatings [7–10], the coatings have been reported to exhibit good mechanical properties [11].

Calcination of magnesite, $MgCO_3$, is the principal route to produce magnesium oxide, MgO, for the use as a ceramic raw material [12]. China, North Korea, and Russia account for 65% of global magnesite reserves, with China being the largest magnesite producer. For these reasons, magnesite was included in the 2014 EU "Critical Raw Materials" list [13,14]. Simultaneously, as the consequence of the growth of mining and mineral processing industry, large volumes of mining wastes are being produced. Mining waste typically refers to an unwanted mining by-product but may still contain valuable constituents [15]. Mining tailings consist of fine-grained (1–600 μm) ground-up rock residue after minerals of value have been extracted from mined ore. The physical and chemical characteristics of mining tailings vary considerably with ore type [16]. Overall, mining tailings are seen as one potential resource to be utilized on the way towards circular economy and resource efficiency [17].

In this paper, the sample of talc ore mining tailings was studied. Talc ore mining tailings are rich in magnesite [18] and then can be seen as potential ceramic raw material source. This paper investigates the feasibility of talc ore mining tailings as raw material source for thermally sprayed ceramic coatings. Here, $MgAl_2O_4$ spinel composition was aimed for. Because the sample of mining tailings does not contain

* Corresponding author.
E-mail address: marjaana.karhu@vtt.fi (M. Karhu).

https://doi.org/10.1016/j.jeurceramsoc.2020.04.038
Received 2 October 2019; Received in revised form 19 April 2020; Accepted 20 April 2020
Available online 01 May 2020
0955-2219/ © 2020 Elsevier Ltd. All rights reserved.

aluminium enough for spinel composition, another secondary raw material, precipitate of aluminium hydroxide, $Al(OH)_3$, a by-product generated by aluminium anodizing process was studied. As a research hypothesis, agglomerated $MgAl_2O_4$ spinel-based powders, ideal for thermal spraying, could be synthesized by spray drying and subsequent reaction sintering using these secondary Mg and Al sources as raw materials. In order to investigate and establish a direct comparison in powders and resulting coatings, a stoichiometric $MgAl_2O_4$ spinel coating was prepared using commercially available primary raw materials. The sample of talc ore mining tailings was rich in magnesite > 80% but contained also other minerals, such as talc, chlorite, dolomite and iron sulphide [18].The effect of constituents other than Mg and Al in mining tailings mineralogy on the resulting coatings was investigated as the main research question in this study. Finally, the properties and wear performance of the secondary and primary coatings were examined and correlated to their microstructures.

2. Experimental procedure

2.1. Raw materials

The mining tailings sample (10 l bucket) from talc ore mine was taken from one point of the temporary storage pile. However, it should be noted that there exist to some extend quality variation for the entire mining tailings area as the mineralogy, grain size and chemistry of the tailings may vary in different parts of deposit due to differences in the original ore composition and separation during storage. Table 1 shows the mineralogical analysis of the used talc ore tailings sample presenting the main identified minerals. Mineralogical characterization included the identification and quantification of mineral phases with scanning electron microscopy (SEM) together with elemental analyses by energy-dispersive spectrometry (EDS). The more detailed explanation of mineralogical analysis, chemical composition analysis, geochemical analysis and sampling procedure are described elsewhere [19]. Ismailov et al. [20] have shown that magnesite in the talc ore tailings was not stoichiometric $MgCO_3$ but had a varying amount of iron substituting magnesium in the lattice. Indeed, there exists a series of solid solutions between $MgCO_3$ and siderite, $FeCO_3$ [21]. Iron carbonate content in magnesite could lie between 0 and 5%. If iron carbonate content increases to the level between 5% and 30%, mineral is then called breunnerite [21].

Table 2 presents the total concentration of cations (calculated as oxides) in the tailings sample, measured with X-ray fluorescence spectrometry (XRF). Loss of ignition (LOI) value presents the loss in weight after being heated to 1000 °C.

Because the sample of talc ore tailings does not contain enough aluminium for synthesizing magnesium aluminate, $MgAl_2O_4$, spinel, another secondary raw material, an aluminium hydroxide precipitate, a by-product from aluminium anodizing process, was studied as alumina source. The precipitate composed mainly of gibbsite, aluminium oxide trihydroxide $Al(OH)_3$ and the elemental composition is shown in Table 3.

As a reference, pure magnesium aluminate $MgAl_2O_4$ spinel powder was prepared using commercially available MgO (99.9% purity) and boehmite, aluminium oxide hydroxide, AlO(OH) (99.99% purity) powders as raw materials. MgO powder was provided by Inframat and AlO(OH) powder was provided by Sasol Germany GmbH.

Table 1
The main identified minerals of the talc ore tailings sample (% total volume).

Mineral	Sample vol%
Magnesite, $MgCO_3$	80.0
Talc, $Mg_3Si_4O_{10}(OH)_2$	9.4
Chlorite, $(Mg,Fe)_3(Si, Al)_4O_{10}$	4.9
Dolomite, $CaMg(CO_3)_2$	1.8

Table 2
Chemical composition of the talc ore tailings sample (wt.%).

	MgO	SiO_2	Fe_2O_3	CaO	Al_2O_3	LOI
Talc ore tailings sample	38.5	10.1	8.2	0.8	0.61	42.7

Table 3
Elemental composition of aluminium hydroxide precipitate (wt.%).

	O	Al	H	S	Na
Aluminium oxide precipitate	62.2	27.8	3.9	3.8	0.8

Table 4
Test matrix compositions for the spinel powder synthesis experiments (wt. %).

Recipe code	MgO (commercial)	AlO(OH) (commercial)	Talc ore tailings sample (secondary)	By-product $Al(OH)_3$ (secondary)
Reference	25.1	74.9	–	–
SC30	16.8	50.0	11.7	21.7
SC60	8.40	25.0	23.4	43.4
SC100	–	–	35.0	65.0

2.2. Powder preparation

Four experimental powder mixtures were prepared aiming at the synthesis of magnesium aluminate, $MgAl_2O_4$, spinel. Mixtures shown in Table 4 were formulated with 1:2 Mg to Al molar ratio. Reference powder represents the reference composition, $MgAl_2O_4$ spinel powder, prepared using commercially available pure MgO and AlO(OH), as raw materials. SC100 powder represents the secondary $MgAl_2O_4$ powder composition, prepared using 100% only secondary raw materials, talc ore tailings sample and anodizing by-product aluminium hydroxide, $Al(OH)_3$. SC30 powder and SC60 powder represent compositional points between the composition of Reference and Secondary100 powders, prepared using both commercial and secondary sources of raw materials, approximately 30% secondary raw materials in SC30 powder and approximately 60% in SC60 powder.

The talc ore mining tailings sample was received in powder form having 90% (D90) of particle size below 140 μm. For powder mixture compositions, it was first ground by jet milling into the particle size below 10 μm in order to increase the reactivity and ensure mixing of the ingredients. Secondary alumina source had the particle size of 6.70 μm (D90). The average grain size of commercial reference MgO was below 1 μm, while that of AlO(OH) powder was below 0.77 μm, thus there was notable difference in the particle sizes of the raw material powders. In order to prepare agglomerated powders suitable for atmospheric plasma spraying, water-based ceramic powder suspensions (2% Dispex A) were prepared from raw material mixtures by bead milling for 15 min. Before spray drying, an organic binder polyethylene glycol, PEG, 2%, was added to suspensions. Suspensions were dried with an industrial- scale spray dryer Niro Atomizer to produce agglomerated powders. Spray-dried powders were reaction-sintered in an ENTECH air chamber furnace in ambient air atmosphere and pressure at the temperatures between 1075 °C and 1150 °C.

2.3. Coating deposition

Atmospheric plasma spraying (APS) technique was used for the deposition of coatings. In a plasma spray gun, a direct current (DC) power is used for the generation of plasma. Energy is transferred into

Table 5
Main spray parameters.

Parameter	Value
Plasma gas mixtures Ar/H_2 (l/min)	43/12
Arc current (A)	600
Voltage (V)	76
Plasma power (kW)	45.4

plasma-forming gases until the energy level is sufficient to ionize the gas. When the ionized gas returns back to atoms/molecules by recombining, a high amount of energy is released. The gas expands in the atmosphere and forms an extremely hot and high-velocity gas jet. The powder is injected radially to the plasma jet where the particles of the powder melt and get accelerated. The coating is formed when the melted and accelerated powder particles impact onto the substrate surface [22].

In this study, coatings were sprayed with an APS ProPlasma gun (Saint Gobain, 6.5HighPower- mm nozzle) using argon/ hydrogen (Ar/H_2) plasma gas mixture. Spray distance was constant at 110 mm. The main spray parameters are summarized in Table 5. Coatings with the thickness range of 225–300 μm were deposited on grain-blasted carbon steel substrates. The plasma gun was robot-manipulated with 51 m/min surface speed and 3 mm increments.

2.4. Characterization techniques

Phase structure analyses were performed for both synthesized powders and deposited coatings using X-ray diffractometry (XRD, Empyrean, PANalytical B.V. device, ALMELO) and CuK_α radiation source, and analysed using HighScore Plus software with ICDD database. The XRD was operated at 45 kV and 40 mA with the scanning rate of 3° 2θ/min. Microstructures were investigated for both synthesized powders and deposited coatings with scanning electron microscope (SEM, Jeol JSM 6360 L V) and field emission scanning electron microscope (FESEM, Zeiss ULTRAplus) together with energy-dispersive spectrometer (EDS, Oxford Instruments, $XMax^N$ silicon drift detector). For imaging, secondary electron (SE) detector or angle selective backscattered electron (AsB) detector was used. For microstructural analyses, metallographic cross sections were prepared by casting cut sections of the specimens in Epofix cold setting resin under reduced pressure. The casts were then ground, polished and carbon coated for electrical conductivity. Electron backscatter diffraction (EBSD) system (Oxford Instruments, Symmetry EBSD detector based on CMOS technology with AZtecHKL software) integrated into FESEM was employed for crystal structure analysis. The cross-sectional EBSD samples were prepared by moulding the sections of specimens to epoxy followed by grinding and polishing down to the final finish by colloidal silica suspension (0.04 μm). After the final polishing, the samples were removed from epoxy.

The thermal behaviour of agglomerated powders was studied using thermogravimetric analysis (TG, Netzsch STA449 F1 Jupiter) giving a simultaneous differential scanning calorimetry (DSC) signal in order to investigate the differences in raw materials behaviour during the heat treating process. The tests were conducted in air atmosphere in a temperature range from 40 to 1200 °C with the heating rate of 10 °C/min. The final temperature was maintained for 1 h before cooling the powders to the room temperature. A qualitative mass spectrometer (QMS, Netzsch QMS 403 D Aeolos) coupled directly to the TG device exhaust was used for evolved gas analysis.

The physical properties of synthesized powders were investigated. Particle size distributions for the powders were determined with laser diffractometer (Malvern Mastersizer). In addition, apparent densities of the powders were measured using hall flow tester 25 ml cup test.

Electric insulation properties of the coating samples were measured using breakdown voltage method. Prior to the measurements, coating thicknesses were measured with a magnetic measuring device (Elcometer 456B) from the electrode contact points. Breakdown voltage electrode areas (Ø = 11 mm) and silver electrodes (Ø = 11 mm) were painted on the coating surface as described in [9]. Silver paint penetration into the coating has been studied from cross-sectional images taken by optical microscope, and it has been observed that the utilized silver paint does not penetrate into the coating [9]. After painting the electrodes, the samples were first dried at 120 °C for two hours, followed by conditioning in a climate room at 20 °C/RH 20% for at least 12 h before the measurements. The breakdown measurements were performed in the climate room at 20 °C/RH 20%. In the breakdown tests, a stainless steel rod electrode (Ø = 11 mm, edge rounding 1 mm), was placed on the top of a coating surface while the steel substrate of the sample acted as the other electrode. DC breakdown voltage measurements were performed by utilizing linearly increased DC voltage (ramp rate of 100 V/s throughout the test) [9]. The voltage source control and data recording was performed using a LabVIEW-based software [9]. The voltage source was Spellman SL1200 ($Umax$ = 20 kV) and the voltage level was measured using a resistive voltage divider (Spellman HVD-100-1, divider ratio 10,000:1) [9]. Dielectric breakdown strength (DBS) of a coating was calculated by dividing the breakdown voltage by the corresponding coating thickness at the painted electrode (Ø = 11 mm) location. Seven measurements were performed per each coating.

Hardness of the coatings was measured with hardness tester (DuraScan 20 Struers) and a Vickers intender. Sand abrasion tests by a rubber wheel tester were performed using quartz sand with the particle size of 0.32 mm and the feed of 350 g/min. A static contact force of 45 N against the rubber wheel, 233 mm in diameter, was used. Prior to the wear tests, the surfaces of samples were ground with a P1200 grinding disk to eliminate the effect of as-sprayed surface quality. Two samples per coating were tested and their mass loss was measured at four time intervals (5, 10, 20, and 30 min) to ensure the linear wear performance during rubber wheel abrasion tests. After the tests, the surfaces and cross sections of the worn surfaces were investigated with SEM. The cross sections were prepared with focused ion beam SEM (FIBSEM, Zeiss Crossbeam 540) first by depositing a platinum (Pt) protection layer on top of the region of interest and then using gallium (Ga) ions to mill the cross-section under the Pt covering layer. Prior to FIBSEM studies, the samples were carbon-coated to avoid the sample charging during the milling process.

3. Results and discussion

3.1. Powder characterization

3.1.1. Microstructure

Fig. 1 shows X-ray diffraction (XRD) patterns for the synthesized powders. As identified by XRD patterns, all synthesized powders revealed $MgAl_2O_4$ spinel as the main crystalline phase. Thus, the synthesis of $MgAl_2O_4$ spinel was successful for all the powder mixtures shown in Table 3. For Reference powder, and the intermediate compositions, SC30 and SC60 powders, $MgAl_2O_4$ spinel peaks were the only peaks observed for crystalline phases. Nevertheless, XRD pattern for 100% secondary composition powder, SC100, showed additionally to the peaks related to the spinel phase minor unidentified peaks at the 2theta values of 28°, 33° and 61°. Thus, only the most impure SC100 powder introduced extra peaks in addition to $MgAl_2O_4$ spinel peaks in the XRD curve. Probably these minor crystalline phases were also present in SC30 and SC60 powders, but their amounts were too low to be detected by XRD. Vusikhis et al. [21] suggested that in the case of ferroan magnesite, during the decarbonisation of magnesite, both MgO and spinel $MgFe_2O_4$ were formed. Thus, it is likely that powders synthesized from mining tailings sample: SC30, SC60 and SC100, contained $MgFe_2O_4$ phase in addition to the $MgAl_2O_4$ phase. Spinel $MgFe_2O_4$ is

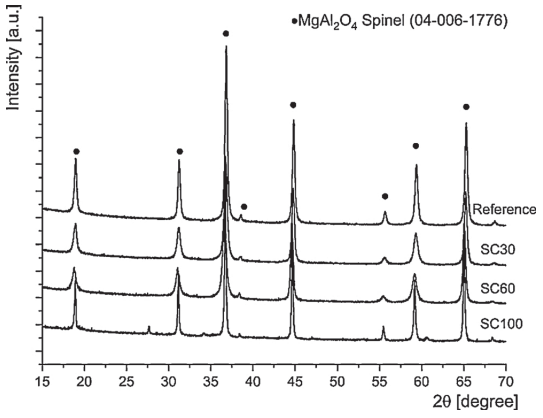

Fig. 1. XRD patterns for synthesized powders Reference, SC30, SC60 and SC100.

also known as magnesioferrite. XRD patterns for $MgAl_2O_4$ and $MgFe_2O_4$ are almost identical, thus according to XRD data it is hard to draw any conclusions about the presence of $MgFe_2O_4$ in the synthesized powders. One possibility is also that there is some dissolution between $MgAl_2O_4$ and $MgFe_2O_4$

Talc ore mining tailings sample contains also silicate minerals as impurities, thus it was assumed that traces of these silicate minerals could also be found in secondary raw material containing powders. As mentioned, XRD pattern for SC100 powder contained minor unidentified peaks at the 2theta values of 28°, 33° and 61°. Another possible explanation for these unidentified peaks is that they were related to some complex silicates formed from the elements which were not dissolved into the $MgAl_2O_4$ spinel. Fig. 1, XRD patterns, revealed also that differences in the widths of $MgAl_2O_4$ peaks exist. This indicates that there were differences in crystal sizes between the 100% secondary SC100 powder and the remaining three powders: Reference, SC30 and SC60. SC100 powder had the most narrow peaks, indicating a relatively more coarse crystal size than the other powders.

Fig. 2 (a–d) shows the surface morphology and Fig. 3 (a–d) the cross-sectional images of the synthesized powders. Figures revealed clear differences in the primary particle size of agglomerated powders. Agglomerates of Reference powder were formed of very fine-grained particles evenly distributed all through the agglomerates. In turn, SC100 powder consisted of much larger primary particles which were essentially dense but formed a coarse agglomerate skeleton. FESEM-EDS analyses revealed that SC100 contained also the traces of Si (~2 wt.%) and Fe (~3 wt.%), which support the two explanations given for extra peaks in the XRD curve. Similarly, the traces of Si and Fe were detected for also other secondary raw materials containing powders SC30 and SC60. However, according EDS analyses, it is challenging to draw any definite conclusion about Si and Fe distribution because of the complexity of microstructural details, fine crystal size as compared to electron beam size and analysis spot dimension exceeding the crystal detail size. Structurally, powders SC30 and SC60 were closer to Reference powder than 100% secondary powder SC100, with essentially a small primary particle size (consistent with XRD data). Nevertheless, SC30 powder (Fig. 3b) contained slightly larger pores than Reference and SC60 powders but the difference of SC30 compared to SC60 and Reference powder is quite marginal. This is resulting most probably from the poorer powder processing rather than the chemical composition in SC30 powder. All the studied powder mixtures were processed with similar processing parameters. As mentioned, there was notable difference in the particle sizes, dispersion and chemistry of the raw material powders.

3.1.2. Thermal behaviour

Thermal behaviour of the agglomerated powders was studied using TG/DSC/QMS in order to investigate the raw materials response to the heat-treatment step aiming at synthesizing $MgAl_2O_4$ powders. Fig. 4 presents the TG/DSC/QMS curves for agglomerated powders in the case of (a) Reference powder (b) SC30 powder (c) SC60 powder and (d) SC100 powder.

In the case of Reference powder, the powder mixture consisted only commercial pure starting materials, MgO and AlO(OH). DSC curves for Reference powder in Fig. 4 (a) revealed an exothermic peak at 367 °C, relating to the dehydration of magnesium hydroxide $Mg(OH)_2$ which introduced water evaporation, detected in evolved gas curve and accounting for approximately 13% weight loss in TG curve (Eq. 1). Magnesium hydroxide was likely formed from starting material source in the powder mixture, MgO, by the reaction with water during the spray-drying step. Another exothermic peak was seen approximately at 500 °C, relating to the dehydration of another starting material in the powder mixture, aluminium oxide hydroxide, AlO(OH). This transformation accounts for approximately 9% weight loss in TG curve due to water release, as indicated by evolved gas curve (Eq. 2) resulting formation of Al_2O_3. Similar values for dehydration temperatures have been presented in literature for $Mg(OH)_2$ [23] and for AlO(OH) [24]. Prior to these reactions, evaporation of water occurred, relating to the removal of moisture from agglomerated powders. Additionally, at the peak temperature of 361 °C, evaporation of carbon dioxide, CO_2, was detected relating to the removal of the organic binder used in spray drying. Similar CO_2 release at approximately the same temperature range was detected in all powder mixtures relating to removal of the organic binder. After completion of the dehydration of aluminium oxide hydroxide (at 500 °C), the reaction between Al_2O_3 and MgO was possible, resulting in $MgAl_2O_4$ formation (Eq. 3). An exothermic peak detected at 1099 °C was probably related to the spinel evolution. Magnesium aluminate spinel formation has been reported to be a heat releasing reaction [25].

$$Mg(OH)_2 \rightarrow MgO + H_2O \quad (1)$$

$$2AlOOH \rightarrow Al_2O_3 + H_2O \quad (2)$$

$$Al_2O_3 + MgO \rightarrow MgAl_2O_4 \quad (3)$$

In the case of SC100 powder, the powder mixture consisted only impure starting materials, talc ore mining tailings sample and secondary $Al(OH)_3$ precipitate. The TG/DSC/QMS curves shown in Fig. 4 (d) revealed transformations as response to the heat-treatment for these impure raw materials showing different behaviour than the pure raw materials in the case of Reference powder shown in Fig. 4 (a). Below 500 °C, the TG curve in Fig. 4 (d) revealed already 25% weight loss related to transformations in DSC curve, most probably relating to starting material in the powder mixture, $Al(OH)_3$ precipitate, dehydration. Živković and Dobovišek [26] have studied the aluminium hydroxide dehydration and they suggest it proceeds according to the following mechanisms (Eqs. 4 and 5):

$$2Al(OH)_3 \rightarrow 2AlOOH + 2H_2O \quad (4)$$

$$2AlOOH + H_2O \rightarrow Al_2O_3 + 2H_2O \quad (5)$$

They suggested that both reactions proceed in the diffusion region, the first (Reaction 4) up to the temperature of 253 °C and the second (Reaction 5) up to 427 °C. Thus based on the water evaporation detected in evolved gas curve it could be confirmed that 25% weight loss in Fig. 4 (d) below 500 °C was related to these $Al(OH)_3$ dehydration reactions resulting in the formation of Al_2O_3.

According to mineralogical analysis, the talc ore mining tailings sample was composed 80% of magnesite $MgCO_3$, about 9.4% of talc $Mg_3Si_4O_{10}(OH)_2$ and about 4.9% of chlorite $(Mg,Fe)_3(Si, Al)_4O_{10}$. As mentioned in raw material section, the magnesite in talc ore tailings was not stoichiometric $MgCO_3$ but has a varying amount of iron

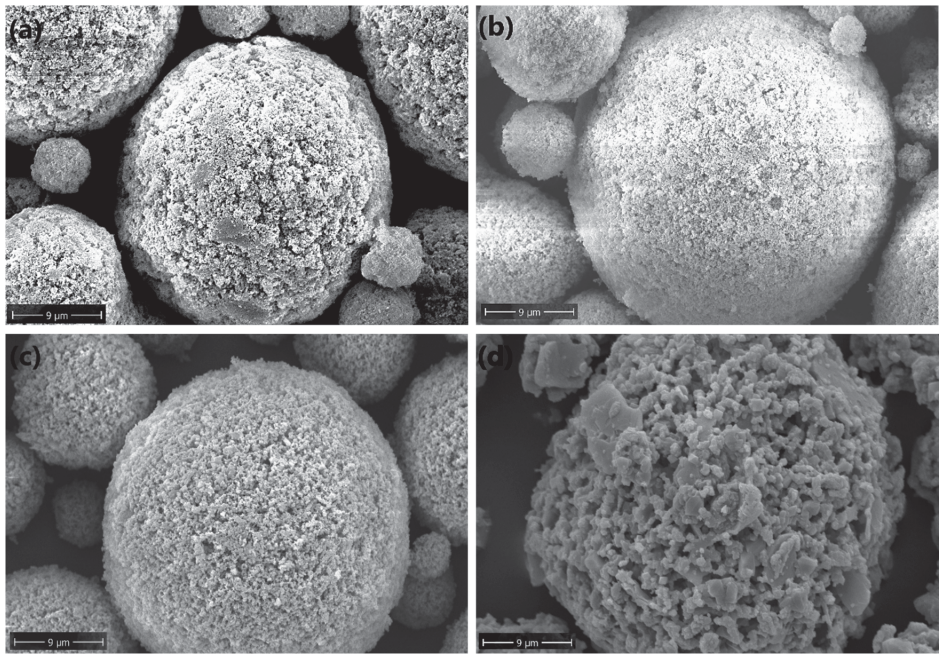

Fig. 2. SEM (SE) images showing the powder morphology for powders (a) Reference (b) SC30 (c) SC60 and (d) SC100.

substituting Mg in the lattice, being likely breunnerite rather than pure magnesite. Vusikhis et al. [21] have studied the kinetic features decarbonisation of breunnerite, the magnesite mineral where iron carbonate content lies between 5% and 30%. They suggested that carbonates begun to dissociate in a temperature range of 500–584 °C. They detected two endothermic transformations in the DSC curve (beginning above 584 °C, with the maxima at 664 °C and 710 °C), connected with the release of CO_2. They explained the presence of two separate peaks in the DSC curve by the following reactions, forming besides MgO the spinel $MgFe_2O_4$ (Eq.6):

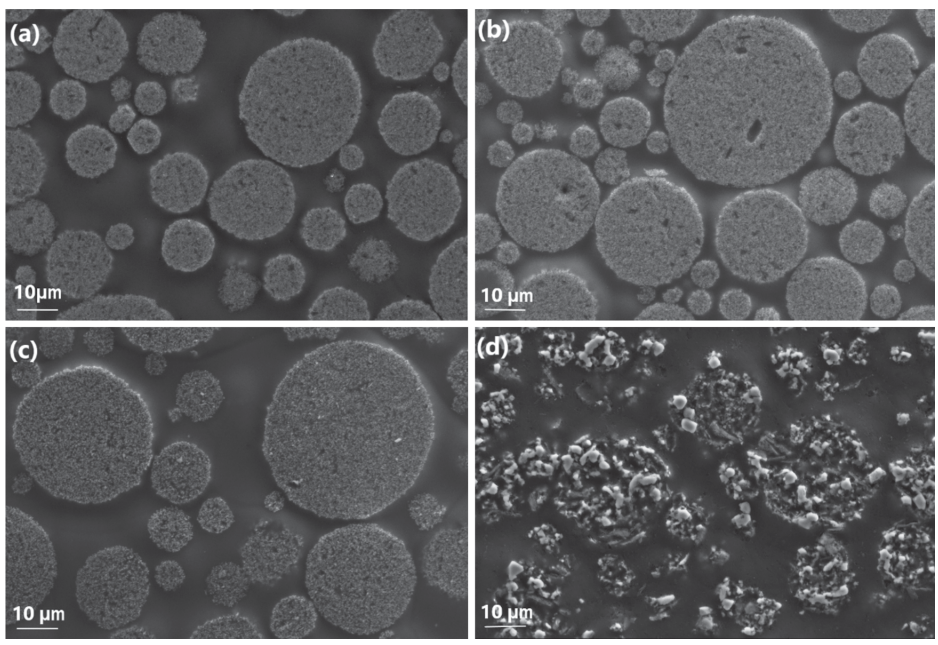

Fig. 3. Cross-sectional FESEM (AsB) images for powders (a) Reference (b) SC30 (c) SC60 and (d) SC100.

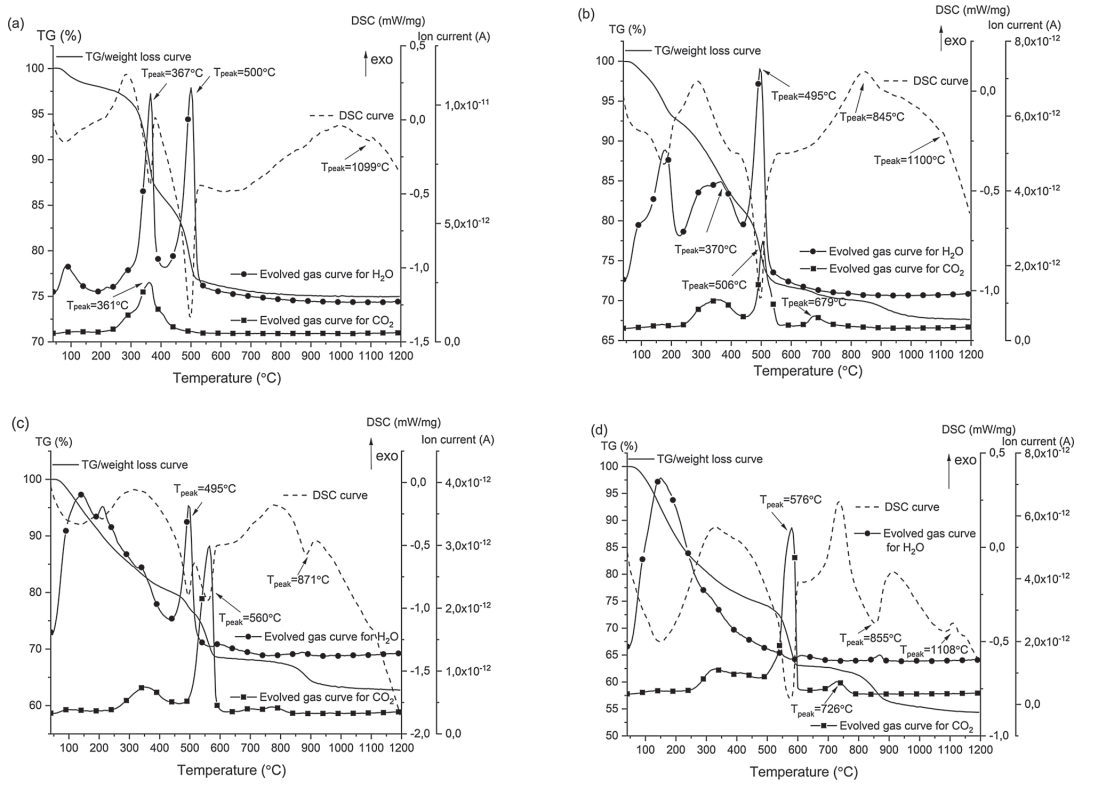

Fig. 4. TG/DSC/QMS curves for (a) Reference powder (b) SC30 powder (c) SC60 powder and (d) SC100 powder.

$$(Mg_{1-x}Fe_x)CO_3 = (Mg_{1-x}Fe_x)O + CO_2, 2(Mg_{1-x}Fe_x)O + 0.5xO_2 = (2-3x)MgO + xMgFe_2O_4 \quad (6)$$

Similarly to observations by Vusikhis et al. [21], DSC curve for SC100 powder in Fig. 4 (d) revealed two transformations, related to the peaks in CO_2 evaporation curve at the temperatures of 579 °C and 726 °C. These transformations could thus be linked with ferrous magnesite decarbonisation (Reaction 6) being present in the talc ore mining tailings sample. SC100 powder showed weight losses again above 800 °C, connected with water evaporation in evolved gas curve. This transformation was most probably associated with the decomposition of hydrated magnesium silicates that were present as impurities in the mining tailings sample. Eventually at 1108 °C, an exothermic peak was detected, probably related to the formation of magnesium aluminate spinel by the reaction between magnesium oxide formed from tailings sample magnesite and aluminium oxide formed from $Al(OH)_3$ precipitate. Thus the main reaction between the starting materials was taken place between the alumina Al_2O_3 formed from $Al(OH)_3$ precipitate and the MgO formed from the tailings sample magnesite $MgCO_3$ resulting in $MgAl_2O_4$ phase formation. The impurities were most probably concentrated in spinel $MgFe_2O_4$ phase as suggested by Vusikhis et al. [21] and the magnesium silicates phases as residues.

In the case of SC30 and SC60 powders, the powder mixtures consisted both commercial and secondary sources of starting materials, approximately 30% secondary raw materials in SC30 powder and approximately 60% in SC60 powder. For that reason, TG/DSC/QMS curves for SC30 powder in Fig. 4 (b) and SC60 powder in Fig. 4 (c) disclosed transformations related to the dehydration of pure $Mg(OH)_2$ and AlO(OH) similarly than for the Reference in Fig. 4 (a). Additionally also transformations related to impure raw materials, talc ore mining tailings sample and secondary $Al(OH)_3$ precipitate were detected similarly than for the SC100 powder in Fig. 4 (d). However, as a difference, decarbonization temperatures of magnesite $MgCO_3$ were lower for powder mixtures, SC30 and SC60, with pure raw materials present as compared to only 100% secondary raw materials containing SC100 powder.

3.1.3. Physical characteristics

Table 6 presents particle size distributions for agglomerated powders, measured with laser diffractometer. Along with the particle size distributions, the density values measured with hall flow tester are given. Particle size distributions for all agglomerated powders were relatively similar with d10 of approximately 10 µm and d90 of 40 µm, thus all were suitable for APS spraying. In density values, a clear difference was detected between the powders. Only secondary raw materials containing powder SC100 featured almost double density values as compared to others powders. This was mostly due to the coarser primary particle size, as disclosed by SEM studies, resulting in a better

Table 6
Characteristics of the synthesized (heat treated) powders.

Powder code	Particle size distribution d10-d90 [µm]	Apparent density [g/cm^3]
Reference	11.9 - 44.8	0.52 ± 0.01
SC30	7.1 - 37.4	0.43 ± 0.02
SC60	12.0 - 45.0	0.40 ± 0.02
SC100	9.9 - 42.6	0.86 ± 0.03

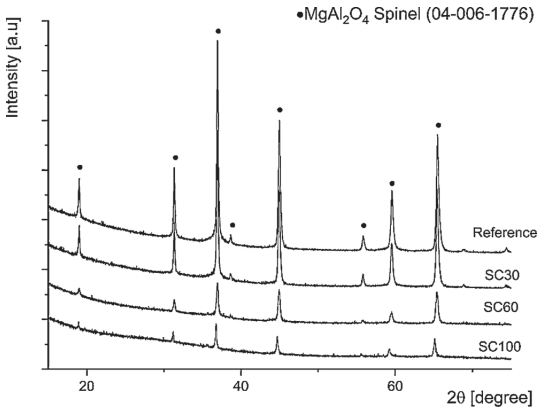

Fig. 5. XRD patterns of the APS coatings Reference, SC30, SC60 and SC100.

packing. Conversely, very fine particles of MgO and AlO(OH) caused loose packing of the remaining powders (Reference, SC30 and SC60). However, as the density of the spinel is from 3.5 to 4.0 g/cm^3, all powder density values indicate high porosity level in the powder agglomerates. This is also supported by SEM studies.

3.2. Coating characterization

3.2.1. Microstructure

Fig. 5 shows the XRD patterns for APS sprayed coatings. For all coatings, only cubic $MgAl_2O_4$ spinel phase was observed as the crystalline phase. XRD pattern revealed that secondary raw material containing coating SC100 coating and SC60 coating were partly amorphous. The intensities of crystalline spinel peaks were highest for Reference coating and the peak intensities decreased with increase in the relative amount of secondary raw materials (i.e., impurity content in raw materials). Similarly, spinel peaks shifted from the original 2θ position following the same order. The intensity decrease was probably due to both increased amount of amorphous phase and less perfect structure of the crystalline phase. Similarly, the shifting of XRD peaks was likely the result of impure composition, i.e., distortion of the lattice due to atomic size discrepancy. The unidentified small peaks that were detected in the XRD pattern for only secondary raw material containing SC100 powder (Fig. 1 d) were not any more visible in the pattern for the corresponding coating. Explanations for this are that this unidentified phase disappeared by dissolution to the spinel phase or to the amorphous glass phase in the coating. This dissolution may also be responsible to the spinel peak shifting. As the plasma spraying process involves the presence of melt, which is not present in powder synthesis, this kind of dissolution is plausible.

Fig. 6 shows cross-sectional FESEM images of the APS sprayed coatings for (a–c) Reference, (d–f) SC30, (g–j) SC60 and (i–k) SC100. The Reference was characterized by a lamellar microstructure typical of APS deposited coatings. Indeed, the formation of coatings by APS technique occurs by stacking the lamellae one by one, resulting from the impact, flattening, and finally solidification of the colliding molten particles [27]. The lamellas were crystalline, but some inter-lamellar areas contained a small amounts of amorphous phase. Crystalline lamella thickness was in the order of 1 to 4 μm, but amorphous sections between the crystalline lamellas were only 1 μm or less in thickness. Coating SC30 (Fig. 6 (d–f)) featured similar lamellar microstructure of the crystalline phase, but the amorphous sections between the lamellas were essentially thicker and more frequent. Microstructures of coatings SC60 (Fig. 6 (g–j)) and SC100 ((Fig. 6 (i–k)) revealed the presence of high amount of the amorphous phase. Based on FESEM investigations, SC100 coating had the highest amount of amorphous phase in the structure (seen as the darker grey contrast in FESEM images), which was already observed in XRD pattern for the coating (Fig. 5). Crystalline phase was concentrated on separate areas with a fine structure and seen in lighter grey contrast than the amorphous phase in FESEM images. SC100 coating also contained some lamellar areas, which had a similar morphology as in Reference coating. Due to the complex shape and small thinness, it was not possible to reliably analyze and identify the chemistry of the phases.

The porosity values of studied APS coatings were defined by image analysis in Fig. 6 shown FESEM micrographs using ImageJ software. The average porosity values defined were the following: for Reference coating 4.9 ± 1.0%, for SC30 coating 6.8 ± 1.0%, for SC60 coating 6.3 ± 0.6% and for SC100 coating 3.5 ± 0.4%. As detected in FESEM images of the Reference coating in Fig. 6 (a–c) the lamellas were crystalline, but some inter-lamellar areas contained small amounts of amorphous phase. This was confirmed by FESEM-EBSD investigations shown in Fig. 7. In the EBSD results, a band contrast (BC) map represents the quality of the Kikuchi diffraction pattern for each measurement pixel. In the BC map, bright signifies that the pattern quality is good, it can be indexed and crystal orientation can be determined. Black/dark grey signifies that the pattern cannot be indexed for example due to amorphous material. Here, also the nonconductive sample complicates the indexing especially in the edges of the crystalline lamellas. The colours in the inverse pole figure (IPF) maps (Z direction) correspond to the crystallographic orientations of $MgAl_2O_4$ parallel to the observed plane as indicated by the coloured stereographic triangle, i.e. an IPF colouring key.

3.2.2. Properties and performance

Table 7 presents the values of dielectric breakdown strengths for the studied coatings. Results revealed that breakdown strength values for all coatings, Reference, SC30, SC60 and SC100 were at the comparable level, at about 20 V/μm, considering the deviation in the results. The reported values are close to the DC breakdown strengths values of alumina and spinel coatings reported in literature [7–10,28,29].

According to results presented, the direct relation between the raw material chemical composition and the resulting breakdown strength values cannot be established. The thermal sprayed coatings manufactured using $MgAl_2O_4$ powder synthesized from secondary sources, talc ore tailings sample and $Al(OH)_3$ precipitate show similar level of breakdown strength values than coatings manufactured using $MgAl_2O_4$ powder synthesized from pure MgO and AlO(OH) sources. The electrical insulation capability was not decreased by the presence of impurities in raw materials. However, the deviation in the breakdown strength values was higher for secondary raw material based coatings. Also, for SC60 coating, slightly lower breakdown strength values than for the remaining three coatings were recorded. Most probable explanation for these lower breakdown strength values could be resulted from the higher amount of defects and porosity level in the coating as shown in SC60 coating microstructure in Fig. 6 (g–j).

Table 8 shows both the hardness values of the coatings and the results from their rubber wheel abrasive wear tests. Hardness results revealed that all the coatings that included secondary raw materials: SC30 coating, SC60 coating and SC100 coating were characterized by the hardness values approximately 20% lower than the Reference coating with pure commercial raw materials. Surprisingly, the differences between the three secondary raw materials containing coatings were only negligible, thus independent of the relative amount of secondary raw materials in the composition. These results suggest that the thermal sprayed coatings manufactured using $MgAl_2O_4$ powder synthesized from pure MgO and AlO(OH) resulted in higher hardness value and impurities in chemical composition of the starting materials decrease the hardness value.

In abrasive wear tests, the specimens of Reference coating, SC30 coating and SC60 coating were worn through already after 5 min test duration. The weight losses after 5 min test duration for the Reference

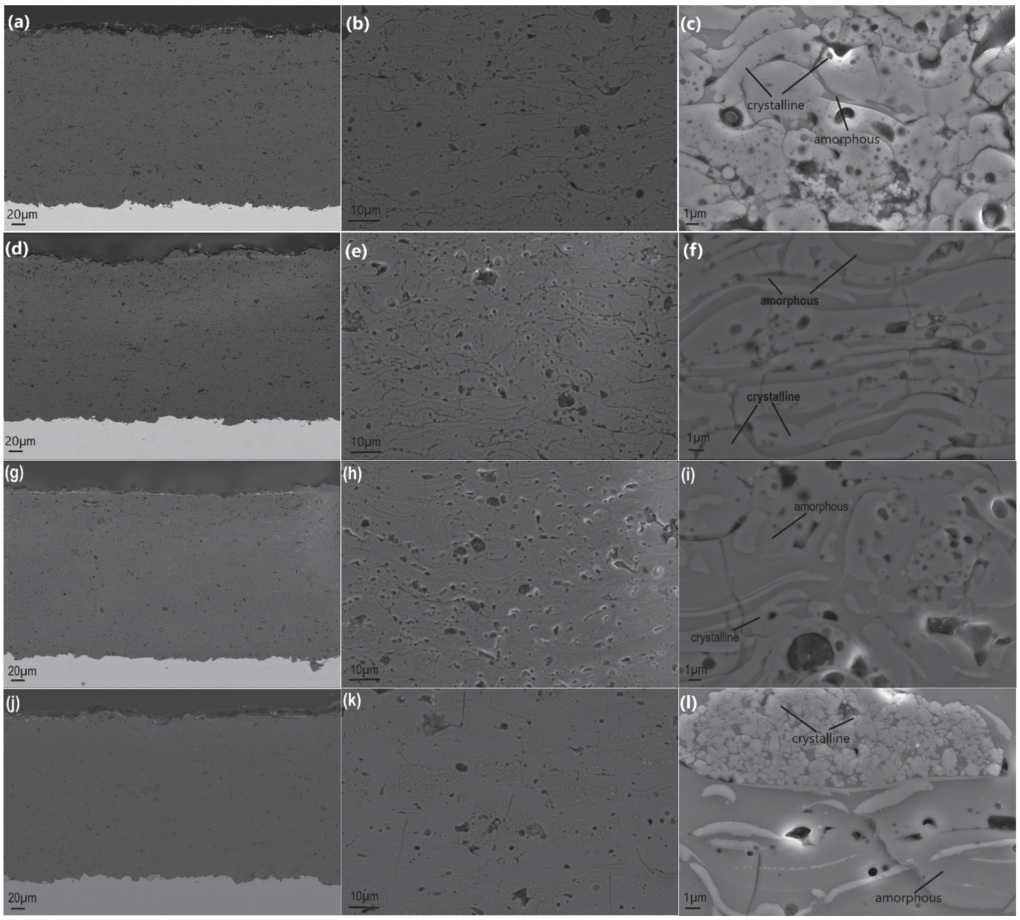

Fig. 6. FESEM (SE or AsB) images of the APS-coatings cross-sections for (a–c) Reference coating (d–f) SC30 coating (g–i) SC60 coating and (j–l) SC100 coating.

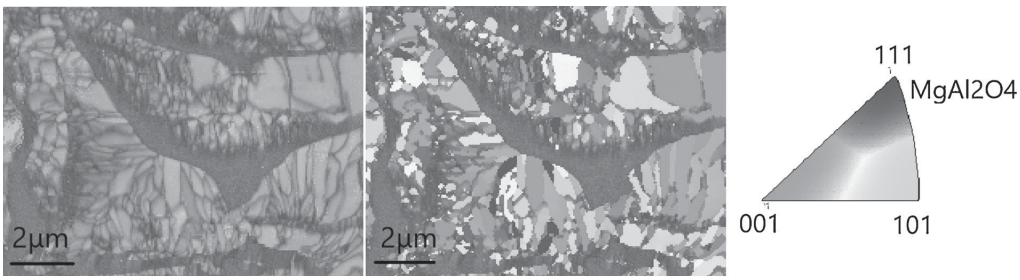

Fig. 7. BC map and inverse pole figure (IPF) map superimposed on the BC map collected from Reference coating. The colours in the IPF maps correspond to the orientations parallel to the observed plane as indicated by the IPF colouring key.

Table 7
Dielectric breakdown strength values for the coatings.

Coating code	Dielectric breakdown strength (V/μm)
Reference	23.0 ± 1.5
SC30	22.6 ± 1.4
SC60	18.1 ± 2.1
SC100	24.2 ± 3.8

coating and SC60 coating specimens were approximately 100 mg taking into account the deviation in the results. The weight loss for SC30 coating specimen after 5 min test duration was higher than for Reference coating and SC60 coating specimens. The most probable reason for that is resulting from the higher porosity level detected for SC30 powder due to poorer processing, discussed in Powder Characterization section. On the contrary, the wear rate was considerably lower for 100% secondary raw material based SC100 coating

Table 8
Hardness of and wear test results for the coatings.

Coating code	Hardness, HV 0.3kg	Weight loss [mg]			
		5 min	10min	20min	30min
Reference	885 ± 63	100 ± 3.3	–	–	–
SC30	670 ± 70	164 ± 3.6	–	–	–
SC60	684 ± 85	96 ± 10	–	–	–
SC100	687 ± 50	17 ± 1.6	33 ± 3.5	53 ± 3.3	73 ± 7.2

than all other studied coatings. For SC100 coating specimens the weight loss detected after 5 min test duration was 17 mg and after 30 min test duration only 73 mg. Thus for SC100 coating specimens the weight loss is lower after 30 min test duration than that all other studied coatings specimens after 5 min test duration. Because only 100% secondary raw material based SC100 coating resulted lower wear rate than all other studied coatings, any evident relation between the wear results with the starting composition cannot be given. It is suggested that the different structure of the coatings, particularly the high degree of amorphous phase binding the separate crystalline $MgAl_2O_4$ clusters, causes the higher abrasive wear resistance of the 100% secondary raw material based coating by changing the wear mechanism. These results suggest that the coating hardness was not the only decisive factor for the abrasive wear resistance of the coating, as the hardest of the coatings (Reference) had a wear performance comparable to that of lower-hardness coatings (e.g., SC30). Conversely, the coating with the highest wear resistance, SC100 coating, featured the same hardness as the two coatings with much poorer wear resistance (SC30, SC60).

The worn surfaces were investigated after the abrasion wear tests using FESEM (top views) in Fig. 8 (a) for the Reference and in Fig. 8 (b) for the 100% secondary raw material based SC100 coating. The wear morphologies of the coatings, Fig. 8, well reflected the results from the wear tests. For the Reference coating the wear tracks featured high surface roughness. The large smooth area in the middle of Fig. 8 (a) indicates that a removal by lamella-by-lamella mechanism is likely. In the case of SC100 coating in Fig. 8 (b), the wear surface was much smoother than for Reference coating, indicating that material losses occurred through the removal of only small fractions of the coating at a time and equally in all areas of the coating.

The worn surfaces were investigated also using FIBSEM (cross-sectional views) shown in Fig. 9 for (a–b) Reference coating and (c–d) SC100 coating. For Reference coating Fig. 9 (a–b), the cracks were often connected through the lamellar structure, which caused the removal of large pieces of the coating when exposed to abrasive wear. This suggests that the lamella boundaries may be the weak point of the material under abrasive wear. On the contrary, in secondary raw material based coating SC100 Fig. 9 (c–d) there were also visible cracks but these were not systematically connected, thus when exposed to abrasive wear, material losses occurred only locally and mass losses were lower than for Reference coating. As detected in the microstructure investigations of APS sprayed coatings, SC100 coating was highly amorphous, with crystalline spinel phase in the structure being concentrated on separate clusters surrounded by the amorphous phase. The amorphous phase binds the individual areas of the crystalline phase together thus there is no typically a direct connection between the crystalline areas. In all other coatings: Reference, SC30 and SC60, the crystalline phase forms the lamellar structure though the coatings. FESEM-EBSD investigations confirmed that in Reference coating, SC30 coating and SC60 coating, the crystalline phase was evenly distributed all through the structure but in SC100 coating, the crystalline phase was concentrated on separate clusters surrounded by the amorphous phase. Thus according to these results, the 100% secondary raw material based impurity-containing amorphous coating (SC100) was more resistant to abrasive wear as compared to pure $MgAl_2O_4$ coating. The presented microstructural results suggest that different structure of the coatings and the particularly the presence of amorphous structure causes the different behavior in abrasive wear test between the coatings by changing the mechanism for wear.

4. Conclusions

The following main conclusion could be drawn from the results:

- Agglomerated $MgAl_2O_4$ spinel based powders for thermal spraying, can be synthesized by spray drying and subsequent reaction sintering using secondary Mg (talc ore mining tailings) and Al (aluminium hydroxide precipitate from aluminium anodizing process) sources as raw materials.
- Atmospheric plasma spraying results in the formation of $MgAl_2O_4$ spinel coatings with the cubic $MgAl_2O_4$ spinel phase as only crystalline phase.
- The Reference coating prepared from commercial pure raw materials exhibits a lamellar microstructure, typical for APS spayed coatings.
- Coatings prepared from only secondary raw materials have a partly amorphous structure in which the amorphous phase binds together the separate crystalline $MgAl_2O_4$ clusters.
- The values of dielectric breakdown strength for the secondary raw material based coatings are at the same level, 24 V/μm, compared to pure magnesium aluminate coating, 23 V/μm, and close to the DC breakdown strengths of alumina and spinel coatings reported in literature. Thus, the electrical insulation capability is hardly affected by the impurities in raw materials.
- Abrasive wear test results reveal considerably lower wear rate for secondary raw materials $MgAl_2O_4$ spinel based coating than for the pure counterpart or the intermediate coating compositions. It is

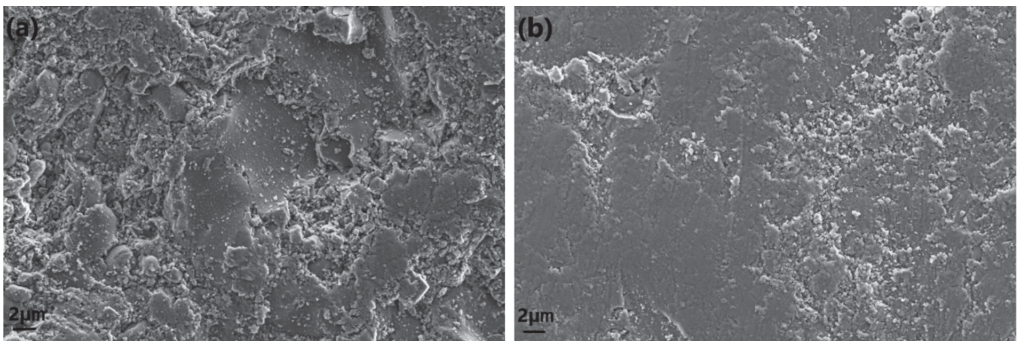

Fig. 8. FESEM (SE) images of the worn surfaces of coatings (a) Reference and (b) SC100.

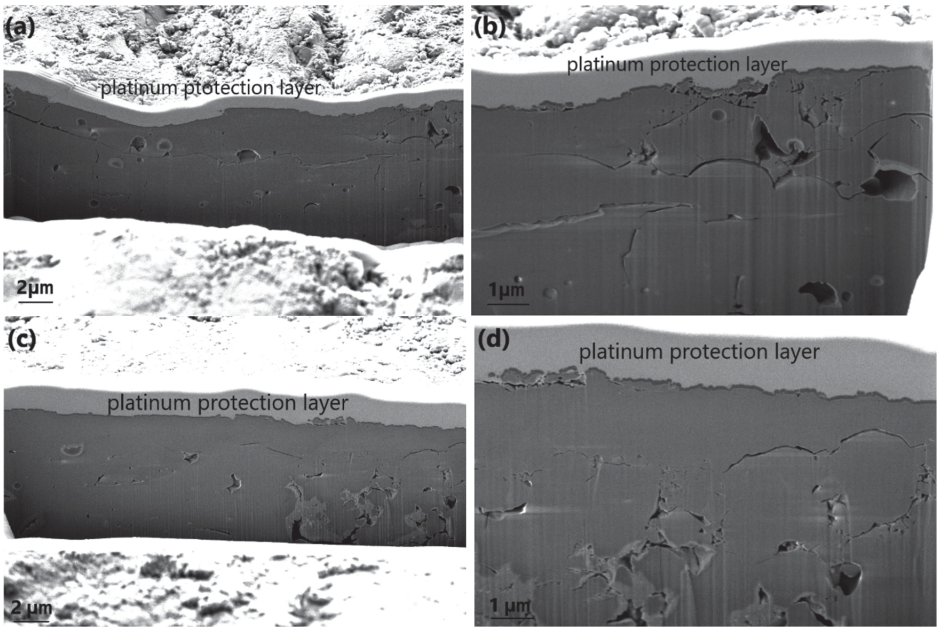

Fig. 9. FIBSEM (SE) images of the worn surfaces for (a–b) Reference coating and (c–d) SC100 coating. Reference coating (a–b) is prepared from commercial pure raw materials and SC100 coating (c–d) using only secondary raw materials.

suggested that the different structure of the coatings, particularly the high degree of amorphous phase binding the separate crystalline $MgAl_2O_4$ clusters, causes the higher abrasive wear resistance of the secondary coating and changes the wear mechanism.

- The investigations of worn surfaces after abrasion tests reveal that the amorphous structure is more resistant to abrasive wear compared to lamellar structure. It seems to be possible that inferior mechanical properties of impure $MgAl_2O_4$ spinel is compensated by the introduction of glass phase in plasma spray coatings.
- These secondary raw materials could potentially substitute virgin raw materials in high-temperature electrical insulation ceramic coating applications.

Declaration of Competing Interest

The authors declare that they have no known competing financial interests or personal relationships that could have appeared to influence the work reported in this paper.

Acknowledgements

The research has been supported by the Academy of Finland, project CeraTail funding decision # 292563 and by the Strategic Research Council at the Academy of Finland, project CloseLoop, funding decision #303453. A part of this work utilized Tampere Microscopy Center facilities at Tampere University. Thermal spray processing of the coatings were done at Thermal Spray Center Finland (TSCF) in Tampere. The authors would like to thank Ms. Hanna-Mari Sinilehto for participating in the experimental work and characterization and M.Sc Tommi Varis for coatings porosity determinations.

References

[1] R. Dal Maschio, B. Fabbri, C. Fiori, Industrial applications of refractories containing magnesium aluminate spinel, Trans. Indian Ceram. Soc. 8 (3) (1988) 121–126.
[2] I. Ganesh, A review on magnesium aluminate (MgAl2O4) spinel: synthesis, processing and applications, Int. Mater. Rev. 58 (2) (2013) 63–112.
[3] G. Bertrand, C. Meunier, P. Bertrand, C. Coddet, Dried particle plasma spray in-flight synthesis of spinel coatings, J. Eur. Ceram. Soc. 22 (6) (2002) 891–902.
[4] M. Niittymäki, K. Lahti, T. Suhonen, J. Metsäjoki, Dielectric breakdown strength of thermally sprayed ceramic coatings: effects of different test arrangements, J. Therm. Spray Technol. 24 (3) (2015) 542–551.
[5] C. Petot, M. Ducos, G. Petot-Ervas, Thermal spray spinel coatings on steel substrates: influence of the substrate composition and temperature, J. Eur. Ceram. Soc. 15 (7) (1995) 637–642.
[6] G. Mauer, R. Vaßen, D. Stöver, Thin and dense ceramic coatings by plasma spraying at very low pressure, Proc. Int. Therm. Spray Conf. 19 (January) (2009) 773–778.
[7] F.L. Toma, S. Scheitz, L.M. Berger, V. Sauchuk, M. Kusnezoff, S. Thiele, Comparative study of the electrical properties and characteristics of thermally sprayed alumina and spinel coatings, J. Therm. Spray Technol. 20 (1–2) (2011) 195–204.
[8] M. Niittymaki, I. Rytoluoto, K. Lahti, J. Metsajoki, T. Suhonen, Role of microstructure in dielectric properties of thermally sprayed ceramic coatings, Proc. 2016 IEEE Int. Conf. Dielectr. ICD 2016 vol. 2, (2016) 1102–1105.
[9] M. Niittymaki, K. Lahti, T. Suhonen, J. Metsajoki, DC conduction and breakdown behavior of thermally sprayed ceramic coatings, IEEE Trans. Dielectr. Electr. Insul. 24 (1) (2017) 499–510.
[10] M. Niittymaki, T. Suhonen, K. Lahti, J. Metsajoki, U. Kanerva, Influence of Humidity and Temperature on the Dielectric Properties of Thermally Sprayed Ceramic $MgAl_2O_4$ Coatings, (2014), pp. 94–97.
[11] S. Sampath, J. Longtin, R. Gambino, H. Herman, R. Greelaw, E. Toremy, direct-write thermal spraying of multilayer electronics and sensor structures, direct-write technologies for Rapid prototyping applications, in: A. Pique, D. Chrisey (Eds.), Direct-Write Technologies for Rapid Prototyping Applications: Sensors, Electronics, and Integrated Power Sources, Academic Press, New York, 2002, pp. 261–302.
[12] S.A. Walling, J.L. Provis, Magnesia-based cements: a journey of 150 years, and cements for the future? Chem. Rev. 116 (7) (2016) 4170–4204.
[13] European Commission, Annexes to the Report on Critical Raw Materials for the EU, May 2014 (2014).
[14] USGS, Mineral commodity summaries 2015, US Geol. Surv. (2015) 196.
[15] B.G. Lottermoser, Mine Wastes (third Edition): Characterization, Treatment and Environmental Impacts, (2010).
[16] M. Edraki, T. Baumgartl, E. Manlapig, D. Bradshaw, D.M. Franks, C.J. Moran, Designing mine tailings for better environmental, social and economic outcomes: a review of alternative approaches, J. Clean. Prod. 84 (1) (2014) 411–420.
[17] B.G. Lottermoser, Recycling, reuse and rehabilitation of mine wastes, ELEMENTS 7 (2011) 405–410.
[18] M. Räisänen, Magnesiittirikastushiekan Ympäristökelpoisuus, (2004).
[19] S. Solismaa, et al., Valorization of Finnish mining tailings for use in the ceramics industry, Bull. Geol. Soc. Finl. 90 (1) (2018) 33–54.
[20] A. Ismailov, N. Merilaita, S. Solismaa, M. Karhu, E. Levänen, Utilizing mixed-

mineralogy ferroan magnesite tailings as the source of magnesium oxide in magnesium potassium phosphate cement, Constr. Build. Mater. (2019).
[21] A.S. Vusikhis, R.I. Gulyaeva, L.I. Leont'ev, L.A. Ovchinnikova, E.N. Selivanov, Kinetic features of breunnerite decarbonization, Russ. Metall. 2016 (9) (2016) 793–797.
[22] P. Vuoristo, Thermal spray coating processes, Compr. Mater. Process. (Janauary) (2014) 229–276.
[23] T. Yoshida, T. Tanaka, H. Yoshida, T. Funabiki, S. Yoshida, T. Murata, Study of dehydration of magnesium hydroxide, J. Phys. Chem. 99 (27) (1995) 10890–10896.
[24] S.J. Wilson, The dehydration of boehmite, γ-AlOOH, to γ-Al2O3, J. Solid State Chem. 30 (November 2) (1979) 247–255.
[25] P. Orosco, L. Barbosa, M.D.C. Ruiz, Synthesis of magnesium aluminate spinel by periclase and alumina chlorination, Mater. Res. Bull. 59 (2014) 337–340.
[26] Ž. Živković, B. Dobovišek, Kinetics of aluminium hydroxide dehydration, J. Therm. Anal. 12 (207) (1977), https://doi.org/10.1007/BF01909477.
[27] K. Stern (Ed.), Metallurgical and Ceramic Protective Coatings, Chapman & Hall, London, 1996.
[28] M. Niittymaki, K. Lahti, T. Suhonen, J. Metsajoki, Effect of temperature and humidity on dielectric properties of thermally sprayed alumina coatings, IEEE Trans. Dielectr. Electr. Insul. 25 (3) (2018) 908–918.
[29] F.L. Toma, et al., Comparison of the microstructural characteristics and electrical properties of thermally sprayed Al 2O 3 coatings from aqueous suspensions and feedstock powders, J. Therm. Spray Technol. 21 (3–4) (2012) 480–488.

PUBLICATION V

Ferrochrome slag feasibility as a raw material in refractories: evaluation of thermophysical and high temperature mechanical properties

Marjaana Karhu, Bob Talling, Patrycja Piotrowska, Alba Matas Adams, Abirami Sengottuvelan, Elina-Huttunen-Saarivirta, Aldo R. Boccaccini, Pertti Lintunen

Waste and Biomass Valorization (2020)

https://doi.org/10.1007/s12649-020-01092-4

Publication reprinted with the permission of the copyright holders.

Waste and Biomass Valorization
https://doi.org/10.1007/s12649-020-01092-4

ORIGINAL PAPER

Ferrochrome Slag Feasibility as a Raw Material in Refractories: Evaluation of Thermo-physical and High Temperature Mechanical Properties

Marjaana Karhu[1] · Bob Talling[2] · Patrycja Piotrowska[2] · Alba Matas Adams[3] · Abirami Sengottuvelan[4] · Elina Huttunen-Saarivirta[1] · Aldo R. Boccaccini[4] · Pertti Lintunen[1]

Received: 31 July 2019 / Accepted: 18 May 2020
© The Author(s) 2020

Abstract
This paper reports the characteristics of ferrochrome slag and its feasibility as aggregate in refractories aiming to substitute virgin refractory raw materials. Refractory castable specimens were formulated with ferrochrome slag as an aggregate and commercial calcium aluminate cement as a binder. Objective was to prepare refractory specimens with a maximum slag utilization but simultaneously to sustain good properties, comparable to those of virgin raw material refractory products. Mechanical and thermo-physical properties of the cured, dried and sintered specimens were characterized. Cold crushing strengths of best performing ferrochrome slag containing specimens were higher than 90 MPa and compressive strength values measured at 1200 °C were over 9 MPa. Thermal insulation properties were even better than those of commercial refractory reference, showing thermal conductivity values as low as $\lambda_{RT-1000\,^{\circ}C} = 1.3 - 0.9$ W/m K. The liquid phase formation above 1200 °C limits the ferrochrome slag use for refractory applications. Results suggest ferrochrome slag's feasibility as an aggregate raw material for refractory materials up to temperatures of 1200 °C in air and up to temperatures of 700 °C in acidic gaseous atmosphere. Possible applications for this kind of novel refractory materials are, e.g., insulating secondary layers or bottom zones in metallurgical processes to substitute virgin refractories. A direct contact to molten metal must be avoided, but they are applicable as, e.g. floorings when exposed only to occasional melt droplets.

Graphic Abstract

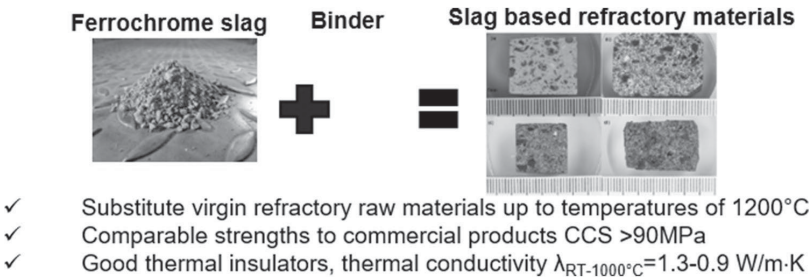

Keywords Slag valorisation · Refractory ceramics · Ferrochrome slag · Electric arc furnace slag

Statement of Novelty

Thus, very limited studies have been conducted to investigate FeCr slag feasibility in high temperature applications, such as in refractory products. This study addressess FeCr

✉ Marjaana Karhu
marjaana.karhu@vtt.fi

Extended author information available on the last page of the article

Published online: 21 May 2020

slag use as aggregate in refractory castables by investigating comprehensively refractory castables thermo-physical and mechanical properties. To authors' knowlewdge, there is a lack of information of ferrochrome slag utilizing refractory materials behaviour at elevated temperatures. For this reason, mechanical and thermal properties of ferrochrome slag based refractories were evaluates also at high temperatures, resulting novel information about their high temperature behaviour.

Introduction

Globally 1.6 Gt of steel was produced in 2014 creating 250 Mt of steel slag as residue [1]. Disposal of the slag is the major issue for steel industry and the utilization of steel slags has been under active research in many years [2]. Most of the slag (50%) is used for road projects, sintering, iron making and recycling within the steel plant [3]. High Carbon Ferrochrome (HCFeCr) is the most common alloying material used for the production of different grades of stainless steel. World high carbon ferrochrome production was 6.0 Mt in 2005 and the generation of ferrochrome (FeCr) slag, the residue generated from HCFeCr production, amounted 1.1–1.6 t/t FeCr depending on feed materials [4]. Numerous studies are available in the literature about FeCr slag utilization in road and civil construction purposes, such as coarse aggregate in concrete applications and pavement layers [5–9], partial substitution of fine aggregate sand in concrete [10, 11] and raw material in bricks [12]. Kumar et al. [13, 14] have reported FeCr slag use as aggregate in refractory castables replacing partly commercial aggregates use. They reported 50 wt% of slag use together with 35 wt% of calcined bauxite in [13] and 45 wt% of slag and 40 wt% of calcined bauxite use in [14]. Results for such refractories disclosed compressive strengh values as high as 60 MPa, indicating the potential for ferrochrome slag use in refractory products. Thus, very limited studies exist of FeCr slag feasibility in high temperature applications. This study addresses FeCr slag use as aggregate in refractory castables by investigating comprehensively refractory castables thermo-physical and mechanical properties. To authors' knowlewdge, there is a lack of information of ferrochrome slag utilizing refractory materials behaviour at elevated temperatures. For this reason, mechanical and thermal properties of ferrochrome slag based refractories were evaluates also at high temperatures, resulting novel information about their high temperature behaviour.

Refractories are ceramic materials that withstand a variety of harsh conditions, including high temperatures, corrosive liquids and gases, abrasive wear, and mechanical and thermal stresses [15]. They are indispensable to all high temperature processes in the production of metals, cement, glass and ceramics as in lining materials for furnaces, kilns, incinerators, and reactors. An enormous variety of refractories exists, designed to meet the temperature and process requirements of each application. Refractory materials are designed so that their properties will be appropriate for the application [16]. Refractory industry is heavily dependent on raw material imports and, within the last years, there has been significant increase in material prices [17]. For refractory industry, the need to secure the availability of raw materials at competitive price has created a strong incentive for exploration of alternative sources of raw materials to substitute virgin raw materials [18] as well as to develop recycling of spent refractories [19].

This paper reports the characteristics of ferrochrome slag and its feasibility as aggregate in refractories aiming to substitute virgin raw materials. Refractory castable specimens were formulated with ferrochrome slag as an aggregate and commercial calcium aluminate cement as a binder. Objective in this study was to prepare refractory specimens with a maximum slag utilization but simultaneously to sustain good properties, comparable to those of virgin raw material products. The testing of refractory properties, in most cases, indicate the performance of a refractory in actual application. Hence, appropriate testing of refractories for predicting properties, closely simulative to their applications, is of great importance [16]. As this study aimed to determine the feasibility of ferrochrome slag to substitute the virgin raw materials in refractories, the effect of slag on refractory specimen properties was investigated and compared with conventional, commercial reference material targeted for similar applications. Mechanical and thermo-physical properties of the cured, dried and sintered specimens were characterized in terms of cold crushing strength, bulk density, porosity, thermal expansion, specific heat capacity and thermal conductivity. Mechanical and thermal properties were evaluated also at high temperatures. In addition, mechanical properties were defined for FeCr slag based refractories exposed to corrosive gaseous atmosphere.

Table 1 Approximate chemical composition of the raw materials (%)

	FeCr slag	EAF slag	Secar71	Reference
SiO_2	30	10	–	44.5
Al_2O_3	26	29	70	52
MgO	23	7	–	–
CaO	2	45	30	1.5
Cr_2O_3	8	–	–	–
Fe_2O_3	4	2	0.1	0.5

Materials and Experimental Procedures

Raw Materials

In this study, ferrochrome slag, originating from high carbon ferrochrome production, was used as aggregate and commercially available calcium aluminate cement (Secar 71 provided by Kerneos) was used as a hydraulic binder in refractory castable specimen formulation. Another steel industry slag, electric arc furnace, EAF, slag originating from carbon steel production was used as fine fraction for castables. As a reference, commercial refractory castable Calde Flow LF50A provided by Calderys was used. Table 1 shows approximate chemical compositions of the raw materials, the total oxide concentrations measured with X-ray fluorescence (XRF) method.

Particle packing optimization of refractory castables covers the selection of right size and amount of various particles [20]. The particles size distribution is selected to fill up the voids between large particles with smaller particles and thus to increase the particle packing density. In this study, Elkem Materials Mixture Analyser Software (EMMA) was used for optimal particle packing calculations in order to formulate the optimal recipes with the right size and amount of various particles using distribution coefficient (q) value of 0.30. Particle size distribution optimization was based on packing models and curves developed by Andreassen [21]. The optimization curves were combined in such a way that the total particle size distribution of the mixture is closest to an optimum curve. In this study, maximum slag utilization was targeted and the FeCr aggregate percentage of 81.8 wt% was kept constant throughout the study. The ratio between cement and the aggregates was locked to 1:4.5 on weight basis. The batch compositions listed in Table 2 were formulated. The composition of Castable1 was formulated using only FeCr slag as aggregate and commercial cement as binder. Castable2 was prepared using 0.15 wt% commercial dispersant (provided by BASF, Castament [22]) in order to evaluate the effect of dispersant use on aggregate binder compatibility and hence strength values. BASF Castament dispersants consisted of polymers based on polyethylene glycol. They are developed to disperse calcium aluminate cement particles and aggregates in order to improve the rheological properties of castables in refractory applications [22]. In the compositions of Castable3 and Castable4, part of the commercial cement (10% and 20%) was replaced by fine EAF slag fraction. Water to cement ratio was experimentally locked to 0.51 for Castables1, 3 and 4 and to 0.44 for Castable2.

Table 2 Batch composition of slag based specimens as wt%

Sample code	FeCr slag	EAF slag	Secar71	Dispersant	w/c (g/g)
Castable1	81.8	–	18.2	No	0.51
Castable2	81.8	–	18.2	Yes	0.44
Castable3	81.8	1.8	16.4	No	0.51
Castable4	81.8	3.6	14.5	No	0.51

Preparation of Refractory Castable Specimens

The FeCr slag fine aggregates 0–4 mm were selected for study. At first, the FeCr slag was dried for 7 h at 105 °C and sieved to the particle size below 4 mm. EAF slag was milled by means of the disintegrator DESI 15/16 C to the particle size below 75 µm. Refractory castable specimens were prepared according to standard EN 196-1 [23]. A standard steel mould with the size of $40 \times 40 \times 160$ mm^3 was used for mixed compositions. Castable were perepared by mechanical mixing and compacted in a mould using a standard jolting apparatus as described in standard. Specimens were first cured for 24 h in the moulds in a curing cabinet (RH > 95%) at room temperature. Then the specimens were removed from the mould and left for another 24 h in the curing cabinet in a plastic bag at room temperature. After that, specimens were moved to drying oven for 7 h at 105 °C. The dried specimens were then sintered in air atmosphere by slowly heating them to 540 °C and kept at this temperature for 3 h, then heated to 1200 °C and kept there for another 3 h.

Characterization Methods

FeCr slag was characterized by microstructural and compositional studies as well as thermal analyses to find out its characteristics. Microstructural investigations were performed using a field-emission scanning electron microscope (FESEM Zeiss ULTRAplus) equipped with an energy dispersive spectrometer (EDS, INCA x-act silicon-drift detector (SDD), Oxford Instruments). The identification of crystalline phases was done by using an X-ray diffractometer (XRD, Empyrean, PANanalytical B.V., ALMELO, Netherlands) with Cu-Kα radiation source, and analysed using HighScore Plus software. The thermal behaviour was studied using thermogravimetric analysis (TGA, Netzsch STA 449 F1 Jupiter) giving also a simultaneous Differential Scanning Calorimetry (DSC) signal. The measurements were made in air and argon atmospheres at a heating rate of 10 °C/min.

In order to evaluate the strength behaviour for slag-based refractory specimens, six specimens were prepared from the Castable1 composition mixture, and their compressive strengths were recorded after chosen steps. The preparation of six specimens took place on day 1. After 24 h of curing in the moulds placed in the curing cabinet, specimens were removed from moulds and the compression test was carried out for one of the six specimens, with the strength

value being recorded as the 1-day compressive strength (step1). On day 2, five of the specimens were left in the curing cabinet in a plastic bag. One of the five specimen was kept separately in the curing cabinet for the measurement of 7-day compressive strength (step2). On day 3, four remaining specimens were moved to drying oven where they are kept for 7 h at 105 °C. At the end of the day after drying, one of the specimens was subjected to the determination of compression strength at 105 °C (step3). On day 4, three of the dried specimens were slowly heated to 540 °C and kept at the temperature for 3 h. On day 5, one specimen from day 4 was heated to 1000 °C, the second specimen was heated to 1200 °C, and the third specimen from day 4 was used for the compression test at 540 °C (step4). On the next day, the cooled specimens were subjected to compression strength determination, and their strength values were recorded for 1000 °C (step5) and for 1200 °C (step6).

The microstructural, physical, mechanical and thermal properties of cured, dried and sintered refractory castable specimens were characterized. Metallographic cross sections were produced by casting the cut sections of specimens in Epofix cold setting resin under low pressure. The castables were then ground and polished. An OLYMPUS digital camera was used for photographing of cross sections. The cross sections were also analysed using FESEM, for which the castables were carbon coated for electrical conductivity. Apparent solid density, bulk density and open porosity of the specimens were investigated according to Archimedes principle following the ISO18754 standard. Thermal expansion coefficient α for the specimens was measured by dilatometry using a Netzsch Dilatometer DIL 402C. The used sample size for the measurements was rectangular 25 mm × 5 × 5 or cylindrical, 25 × 5 mm diameter, cut by a diamond saw, and the heating rate was 5 °C/min. Specific heat capacity and thermal conductivity were measured by laser flash analysis (LFA 457 Microflash, Netzsch) in argon atmosphere for the samples of the size 10 × 10 × 2 mm^3. Samples were prepared by a hollow drill and measured in the temperature range from 21 °C up to 1000 °C. Cold crushing strength of the specimens was tested based on the standard EN 196-1 [23] using uniaxial strength tester. The compression tests were carried out at the constant load rate of 2.4 kN/s as indicated in the standard. For high temperature mechanical tests, cubic samples were prepared from sintered castables. To obtain the desired sample size (10 × 10 × 10 mm^3), a diamond saw with a blade thickness of 0.5 mm was used using a slow cutting speed. The tests were done under argon atmosphere at 1200 °C, with an initial pinchload of − 0.05 kN and a heating rate of 10 °C/min. Once the temperature was reached, compression was performed at a displacement rate of 0.2 mm/min. All the measurements were done in furnace using an Instron frame with a 4 MPa loading cell. Exposure tests for the samples of size 20 × 20 × 2 4 mm^3 were performed in

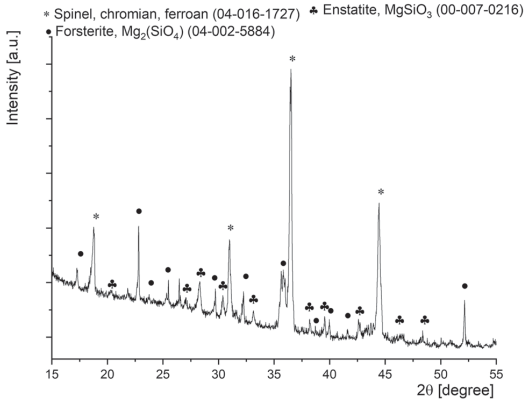

Fig. 1 XRD pattern for the ferrochrome slag

HCl/SO_x gas mixture with 15% humidity at 700 °C temperature for 168 h, after which the strength values were recorded for the exposed specimens.

Results and Discussion

Characterization of the FeCr Slag

Figure 1 presents X-ray diffraction (XRD) pattern for FeCr slag. Spinel phases (chromian, ferroan) $(Mg)(Al,Cr)_2O_4$ appeared as main crystalline peaks. Other identified phases included forsterite Mg_2SiO_4 and enstatite $MgSiO_3$. Additionally, the XRD spectra showed a slight increase in the overall intensity of the curve at low 2θ values which indicates the presence of an amorphous phase.

Figure 2 shows FESEM (AsB) micrographs of the FeCr slag cross section with two different magnifications. Microstructural examinations revealed clearly that microstructure of the slag includes several crystalline phases surrounded by an amorphous glassy phase. Elemental maps disclosed that aluminium is concentrated, together with chromium and magnesium, on larger separate quadrilateral-shaped crystals, most likely spinel $(Mg)(Al,Cr)_2O_4$ phase. Magnesium was concentrated on elongated needle-like crystals together with silicon, most likely being forsterite, Mg_2SiO_4, or enstatite, $MgSiO_3$, phases detected by XRD analyses. Iron was detected in separate spots, seen in the brightest contrast in SEM images. Crystalline phases were surrounded by silicon-rich amorphous glass phase, seen in darker contrast in SEM images. The shape of the XRD curve supports the presence of amorphous phase besides the crystalline phases. The mineralogy of FeCr slag was characterized in detail by Makkonen and Tanskanen [24] who have suggested similarly that common phases in the slag are Fe–Mg–Cr–Al-spinels,

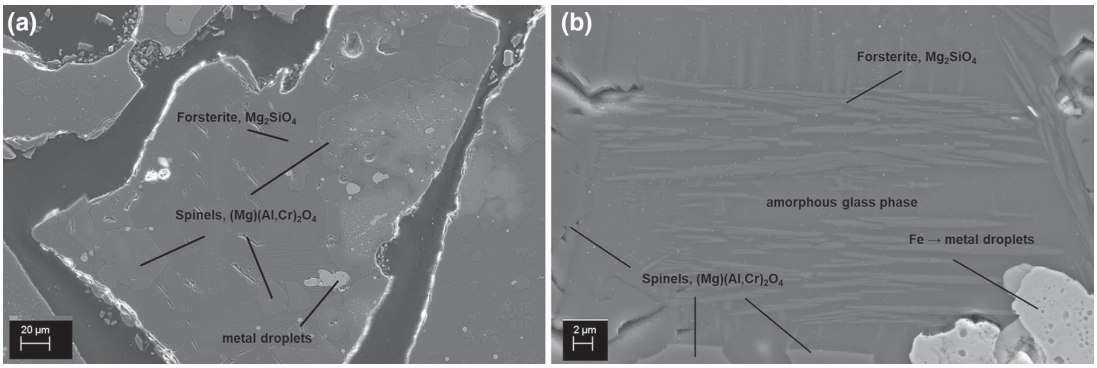

Fig. 2 FESEM images (AsB) of the cross-section of FeCr slag with different magnifications

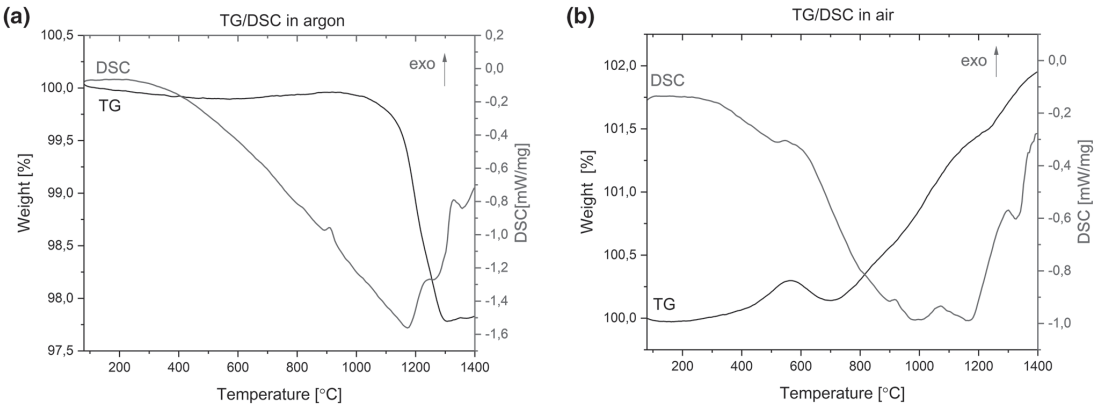

Fig. 3 TG/DSC curves for FeCr slag **a** in argon and **b** in air

forsterite (Mg_2SiO_4), Mg-silicates and metal droplets. With fast cooling rates, the slag is not totally crystalline, with amorphous glass phase being solidified between the grains. The amount of amorphous glass phase depends on the cooling rate being typically between 60 and 70% in FeCr slag [24].

Figure 3 shows the TG/DSC measurement curves of the FeCr slag measured in argon and air atmospheres. In both atmospheres, an exothermic peak was detected in DSC curves above 900 °C similarly than in the study Zelic [5]. Additionally, in air, the weight loss curve started to increase slightly above 400 °C showing also a small exothermic peak in the DSC curve. In air, the weight loss curve continued to increase with increase in temperature, relating most probably to metal iron droplets oxidation detected in microstructure observations. In both atmospheres, peaks observed in DSC curves above 1200 °C were probably related to liquid slag phase formation, with temperature increases increasing the content of liquid phase. In the study by Zelic [5] FeCr slag melting point was reported to fall in the temperature range of 1200–1400 °C. The liquid phase formation at high temperatures restrains the use of FeCr slag-based materials for structural applications. Refractory systems should be designed in such a way that the maximum temperature attainable in the system is lower than the softening or melting temperature of the refractory ingredients: the binder and the aggregates [16]. Thus these results suggest that maximum service temperature for these type of novel FeCr slag based refractory material is 1200 °C.

Properties of the Sintered Refractory Specimens

Figure 4 shows macroscopic cross-sectional images of sintered refractory castable specimens for (a) Reference (b) Castable1 (c) Castable1 after reheating to 1260 °C and (d) Castable1 after reheating to 1320 °C. Images revealed

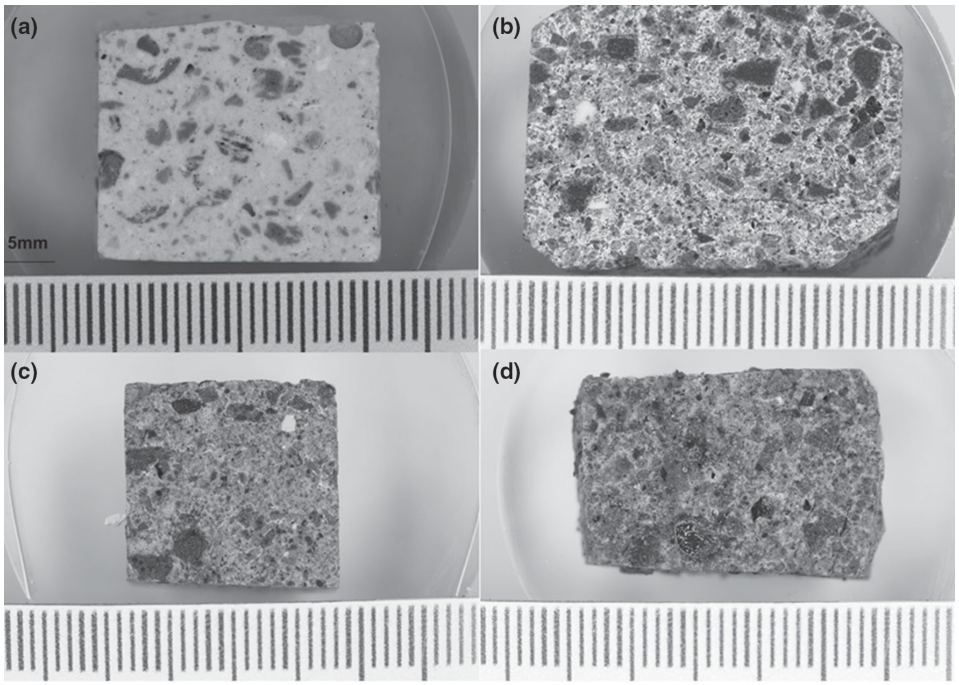

Fig. 4 Macroscopic images of sintered refractory specimen cross sections **a** Reference, **b** Castable1, **c** Castable1 after reheating at 1260 °C and **d** Castable1 after reheating at 1320 °C

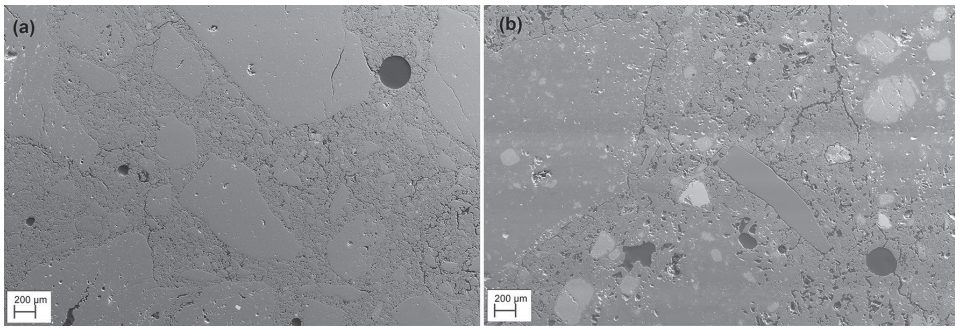

Fig. 5 FESEM cross-sectional micrographs of sintered specimens **a** Reference, **b** Castable2

that both the Reference and Castable1 specimens showed typical refractory material cross-sections, including aggregates and surrounding binder phases. Reheating tests for sintered Castable1 specimens up to temperatures 1260 °C and 1320 °C were made in order to investigate the liquid phase formation which was observed in DSC curves for FeCr aggregates. Reheating to 1320 °C revealed clearly the melting of both slag aggregates and surrounding binder phases, which strengthens the observation of maximum service temperature in DSC curves.

Figure 5 shows FESEM images of sintered cross-sectional specimens of (a) Reference and (b) Castable2. FESEM

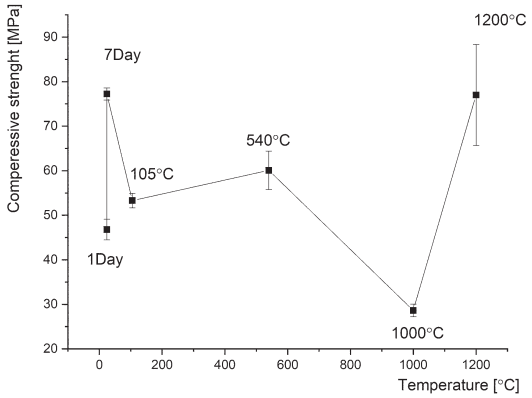

Fig. 6 Strength development curve of slag based Castable1 mixture composition

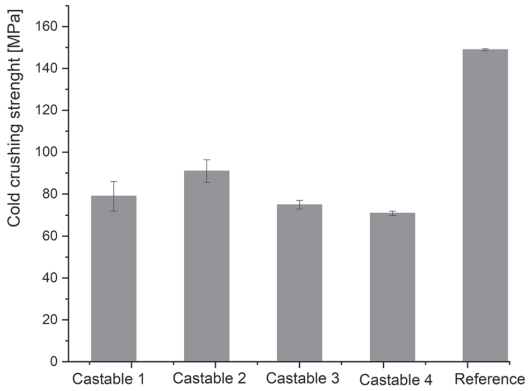

Fig. 7 Cold crushing strengths of slag based-castables and the Reference

micrographs revealed that for the Reference, the compatibility between the binder and the aggregates is good, as charged based on the sharp phase interfaces in Fig. 5a. This is likely a result from long development and surface optimization work for commercial product. For slag-based Castable2 specimen (Fig. 5b), clear cracks at the binder-aggregate interfaces were detected. However, the binder was evenly distributed between the aggregates of different size fractions.

Strength Development Curves

Figure 6 shows strength development curve for Castable1 composition mixture as a function of temperature. Ceramic bonded or fired refractories are formed at high temperatures using binders and a sintering process [19]. As observed at 1000 °C no ceramic bonding has not yet developed. At 1200 °C temperature, higher strength values suggested that ceramic bonds have been formed and full strength of refractory castables has been achieved.

Cold Crushing Strengths

The cold compressive strength or cold crushing strength (CCS) of a refractory material is an indication of its suitability for the use as refractory. It is a combined measure for the strength of the aggregate grains and the bonding system [16]. CCS values recorded for sintered specimens are presented in Fig. 7. The results are average of four specimens. It can be observed that the best performing slag-based Castable2 showed average CCS value of 91 MPa. Strength value was clearly below the strength recorded for the commercial refractory reference material, 149 MPa, but notably higher than the highest strength value, 60 MPa, reported in the studies by Kumar et al. [13, 14] for FeCr slag-utilizing castables. According to CCS values, the use of dispersant (in Castable2) increased the average compressive strength value from 79 (Castable1) to 91 MPa (Castable2). Commercial dispersant (BASF Castament) has been developed to disperse calcium aluminate cement particles and aggregates in order to improve the rheological properties of castables in refractory applications [22]. The differences between the performance of Castable2 and the Reference specimen may be explained by the still poorer compatibility of the binder and aggregate phases of Castable2, as evaluated based on the phase interface appearance (Fig. 5) although the recorded strength values as high as 91 MPa indicate that the strength of the aggregate grains and also of the bonding system are at the acceptable level. By further improving the binder-aggregate compatibility with optimal additives, it can be assumed that

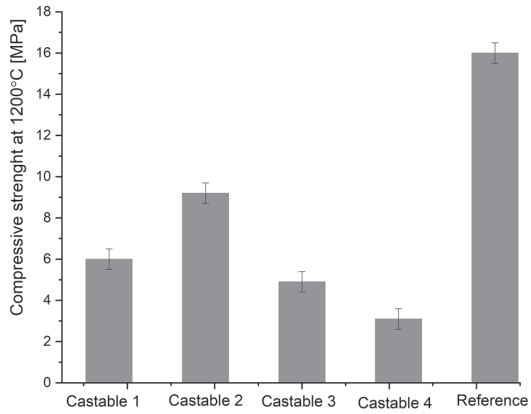

Fig. 8 Compressive strengths measured at 1200 °C

Table 3 Apparent solid density, bulk density and open porosity of refractory specimens

Sample code	Apparent solid density (g/cm^3)	Bulk density (g/cm^3)	Open porosity (%)
Castable1	2.96 ± 0.01	2.35 ± 0.04	20.66 ± 1.32
Castable2	2.92 ± 0.03	2.39 ± 0.07	17.33 ± 1.28
Castable3	2.97 ± 0.03	2.36 ± 0.05	20.57 ± 0.77
Castable4	2.99 ± 0.02	2.33 ± 0.02	22.18 ± 0.88
Reference	2.78 ± 0.01	2.33 ± 0.02	16.12 ± 0.64

even higher strength values may be reached. According to CCS results, it seems that 10% cement replacement by fine EAF slag (Castable3) is possible, still keeping almost the same average strength level for the castables, 75 MPa vs. 79 for Castable1. The higher cement replacement (Castable4) resulted in lower average strength value of 71 MPa.

In recent years, more importance has been given to high-temperature strengths of refractories rather than cold strength values, since refractories are used at elevated temperatures [16]. Figure 8 shows the compressive strengths of sintered slag based castables and the Reference measured at the temperature of 1200 °C. Recorded strengths at 1200 °C were one tenth of corresponding value measured at room temperature. Also at 1200 °C the highest average strength value for slag-based castable was obtained for Castable2, 9.2 MPa, followed by Castable 1 (6.0 MPa). Strength results measured at 1200 °C revealed more clearly that cement replacement by fine EAF slag decreased the strength values. 10% cement replacement by fine EAF slag (Castable3) decreased the average compressive strength to 4.9 MPa and 20% cement replacement (Castable4) even lower, to 3.1 MPa.

Apparent Solid Density, Bulk Density and Open Porosity

The values of apparent solid density, bulk density, and open porosity for slag-based castables and the Reference are shown in Table 3. The results are average of three samples. Typically, the values of density and porosity are used to recommend the refractories for specific applications [16]. In general, the higher the density, the lower the porosity and also, other physical properties, such as strength, are typically related to the density and porosity values. Table 3 shows that bulk density values were of the same order for slag-based castables and the commercial Reference, around 2.35 g/cm^3. These values are typical for the alumino-silicate-based, dense refractory castables used as structural components in heat-treatment furnaces and kilns [16]. The Castable2 showed a slightly higher density value of 2.39 g/cm^3 but featured also the highest variation in the values, which could partly explain the result. Nevertheless, for the best performing (highest strength) slag-based castable, Castable2, the open porosity value of 17.3% was of the same order with the commercial Reference, 16.1%. For other slag-based castables, the porosity values were approximately 20% (Castable1 and Castable3; or even higher (22% for Castable4). Thus by increasing the cement replacement with fine EAF slag fraction, the porosity is increased and the density values of the castable are lowered.

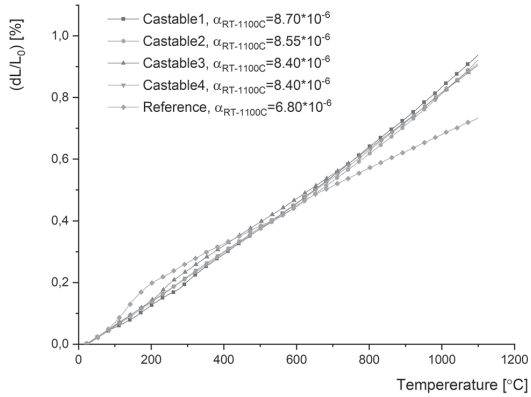

Fig. 9 Thermal expansion of sintered specimens measured by dilatometry

Thermal Expansion

Figure 9 shows the linear thermal expansion of sintered specimens measured by dilatometry. Thermal expansion coefficients, α, of the specimens were determined in the

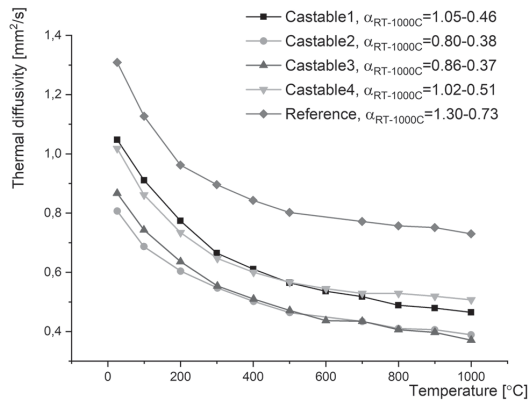

Fig. 10 Thermal diffusivity measured as function of temperature for slag-based castables and Reference

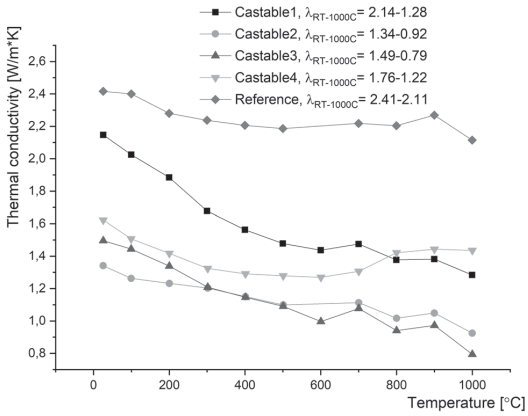

Fig. 11 Thermal conductivity measured as function of temperature for slag based castable and Reference

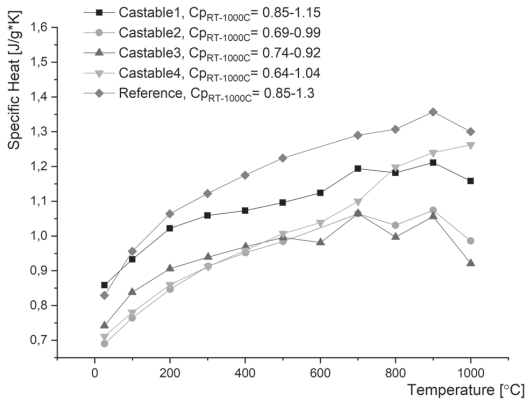

Fig. 12 Specific heat capacity as function of temperature for slag-based castables and the Reference

temperature interval from room temperature up to 1100 °C. Most refractory materials expand when heated and thus, when refractories are installed at room temperature, the whole structure expands and tightens up when heated [16]. Figure 9 shows that all the FeCr slag-based specimens exhibited linear expansion and the recorded thermal expansion coefficient values were at the level comparable to those for the Reference.

Specific Heat Capacity and Thermal Conductivity

Figures 10, 11 and 12 show thermal diffusivity, thermal conductivity and specific heat capacity as a function of temperature for the sintered specimens. In all cases, thermal diffusivity values in Fig. 10 revealed a slight decrease with increase in temperature. Slag-based castables featured somewhat lower thermal diffusivity values as compared to commercial Reference, for which the values ranging between 1.3 and 0.7 mm^2/s were obtained. Among the slag-based castables, the thermal diffusivity values closest to the commercial reference were recorded for Castable1, ranging from 1.1 to 0.5 mm^2/s. The thermal diffusivity values for the slag-based Castable2 (with the best strength properties) showed the lowest thermal diffusivity values, from 0.8 to 0.4 mm^2/s.

Thermal conductivity is a measure of the refractory materials' ability to conduct heat from the hot to the cold face when it is exposed to high temperatures [16]. Low thermal conductivity values implies good thermal insulation capability for refractory materials. Typically when thermal insulation is needed for refractory material, insulating refractory materials are formulated for low relative thermal conductivity and not for strength resistance. The majority of insulating castables are alumino-silicate- based or high alumina castables, having densities between 0.4 and 1.45 g/cm^3 and corresponding porosities of 45–85%. Thus insulating castables show much lower densities and higher porosities than dense castables. Generally when density increases and porosity decreases, thermal conductivity will increase [16]. Thermal conductivity values shown in Fig. 11 disclosed a slight overall decrease in with a shift towards higher temperatures. Slag-based Castable2 exhibited the lowest thermal conductivity values, from 1.3 to 0.9 W/mK, which were much lower than for the commercial Reference (2.4–2.1 W/mK). However, all slag-based castables showed thermal conductivity values lower than the Reference. Thermal conductivity values of slag-based Castable2 are comparable to values shown in literature for alumina based insulating castables which show thermal conductivity value of 1.2 W/mK at 200 °C but have much lower density value of 1.2 g/cm^3 [16]. These results indicate a good thermal insulation capability for FeCr slag based castables and their suitability in the use as aggregate in refractory castables for insulation purposes and simultaneously having sufficient strength for structural component also. Lower thermal conductivity values for FeCr slag compared with natural material granite has been reported also by Niemelä and Kauppi [4] for civil engineering and road construction uses.

The values of specific heat shown in Fig. 12 revealed a slightly increasing values with rise in temperature. Similar results were obtained for EAF slag reported in the literature [25].

Exposure Tests for Corrosive Atmosphere

Corrosion resistance is one of the most important characteristics of refractories, thus the test conditions have to be designed so that they closely simulate the conditions that the

refractories experience during the use [16]. Thermogravimetric analyses of the FeCr slag-based refractories indicate that their maximum service temperature is 1200 °C. Thus in common metallurgical processes that operate at temperatures above 1200 °C, direct exposure to molten metal and slag should be avoided. However, potential applications may involve exposure to gaseous atmosphere, the temperature of which is typically lower than that of liquid phases. For that reason, corrosion tests were performed to predict the behaviour of FeCr based castables in acidic gaseous atmosphere. During the test procedure, samples were exposed to the gas mixture of 15% humidity and HCl/SO_x at 700 °C temperature for 168 h. With visual inspection, no corrosion effects were seen on the surface of the test samples after the exposure. Mechanical tests were performed for the exposed corrosion samples in order to evaluate the effect of corrosive atmosphere on mechanical properties. According to results, corrosion exposure caused no effect on strength values—neither for the slag-based castables nor for the commercial reference. These investigations indicate that the resistance to acidic gaseous atmosphere for FeCr slag based materials is at least at comparable level to the commercial materials.

Conclusion

Refractory castable specimens were formulated using ferrochrome slag as an aggregate and commercial calcium aluminate cement as a binder. Mechanical and thermo-physical properties of the cured, dried and sintered specimens were characterized. The effect of FeCr slag on the properties of refractory specimens was investigated and compared with conventional, commercial reference material targeted for similar applications. From the findings of the study, the following conclusions can be drawn:

- The liquid phase formation above 1200 °C limits the FeCr slag use as aggregate in refractory castables, thus the maximum service temperature for these novel slag-based refractory materials is 1200 °C.
- Cold crushing strength value of FeCr slag-containing specimens was as high as 91 MPa.
- FeCr slag-based specimens sustained their mechanical strength also at high temperatures, with the mechanical strength values at 1200 °C being as high as 9 MPa.
- Thermal properties of the FeCr slag based specimens were even better than those of commercial refractory reference, showing thermal conductivity values as low as 1.3 W/m K.
- FeCr slag-based castables exhibited linear thermal expansion and a low thermal expansion coefficients as low as $\alpha_{RT-1100\,^{\circ}C} = 8.6 \times 10^{-6}$ 1/K.
- FeCr slag-based castables were exposed to corrosive gas mixture with 15% humidity and HCl/SO_x at 700 °C for 168 h. With visual inspection, no corrosion effects were seen on the surface of the test samples. Corrosion exposure caused no effect on strength values.

Results suggested the feasibility of ferrochrome slag to be used as an aggregate raw material for refractory materials up to temperatures of 1200 °C in air and in acidic gaseous atmosphere up to 700 °C to substitute virgin raw materials. Possible applications for this kind of novel refractory materials are, e.g., insulating secondary layers or bottom zones in metallurgical processes up to 1200 °C. A direct contact to molten metal in steel industry must be avoided, but they are applicable as, e.g. floorings when exposed only to occasional melt droplets.

Acknowledgements Open access funding provided by Technical Research Centre of Finland (VTT). The research was has received funding from the European Union's H2020 programme Waste-1-2014, project RESLAG (GA-642067 and by the Strategic Research Council at the Academy of Finland, project CloseLoop, funding decision #303453.

Open Access This article is licensed under a Creative Commons Attribution 4.0 International License, which permits use, sharing, adaptation, distribution and reproduction in any medium or format, as long as you give appropriate credit to the original author(s) and the source, provide a link to the Creative Commons licence, and indicate if changes were made. The images or other third party material in this article are included in the article's Creative Commons licence, unless indicated otherwise in a credit line to the material. If material is not included in the article's Creative Commons licence and your intended use is not permitted by statutory regulation or exceeds the permitted use, you will need to obtain permission directly from the copyright holder. To view a copy of this licence, visit http://creativecommons.org/licenses/by/4.0/.

References

1. McCaffrey, R.: Review of 11th global slag conference. https://www.globalslag.com/conferences/global-slag/review/global-slag-review-2016 (2016). Accessed 22 May 2019
2. Yüksel, İ.: A review of steel slag usage in construction industry for sustainable development. Environ. Dev. Sustain. **19**(2), 369–384 (2017)
3. Dhoble, Y.N., Ahmed, S.: Review on the innovative uses of steel slag for waste minimization. J. Mater. Cycles Waste Manage **20**(3), 1373–1382 (2018)
4. Niemelä, P., Kauppi, M.: Production, characteristics and use of ferrochromium slags, pp. 171–179. INFACON XI, New Delhi (2007)
5. Zelić, J.: Properties of concrete pavements prepared with ferrochromium slag as concrete aggregate. Cem. Concr. Res. **35**(12), 2340–2349 (2005)
6. Lind, B.B., Fällman, A.M., Larsson, L.B.: Environmental impact of ferrochrome slag in road construction. Waste Manage. **21**, 255–264 (2001)
7. Panda, C.R., Mishra, K.K., Panda, K.C., Nayak, B.D., Nayak, B.B.: Environmental and technical assessment of ferrochrome

slag as concrete aggregate material. Constr. Build. Mater. **49**, 262–271 (2013)
8. Acharya, P.K., Patro, S.K.: Utilization of ferrochrome wastes such as ferrochrome ash and ferrochrome slag in concrete manufacturing. Waste Manage. Res. **34**(8), 764–774 (2016)
9. Yilmaz, A., Karaşahin, M.: Mechanical properties of ferrochromium slag in granular layers of flexible pavements. Mater. Struct. Constr. **43**(3), 309–317 (2010)
10. Dash, M.K., Patro, S.K., Rath, A.K.: Sustainable use of industrial-waste as partial replacement of fine aggregate for preparation of concrete—a review. Int. J. Sustain. Built Environ. **5**(2), 484–516 (2016)
11. Dash, M.K., Patro, S.K.: Effects of water cooled ferrochrome slag as fine aggregate on the properties of concrete. Constr. Build. Mater. **177**, 457–466 (2018)
12. Gencel, O., Sutcu, M., Erdogmus, E., Koc, V., Cay, V.V., Gok, M.S.: Properties of bricks with waste ferrochromium slag and zeolite. J. Clean. Prod. **59**, 111–119 (2013)
13. Kumar, A., Srivastava, P.H., Kumar, V., Singh, V.K.: Implementation of industrial waste ferrochrome slag in conventionaland low cement castables: effect of calcined aluminao title. J. Asian Ceram. Soc. **2**, 371–379 (2014)
14. Kumar, P.H., Srivastava, A., Kumar, V., Majhi, M.R., Singh, V.K.: Implementation of industrial waste ferrochrome slag in conventional and low cement castables: effect of microsilica addition. J. Asian Ceram. Soc. **2**(2), 169–175 (2014)
15. Fang, H., Smith, J.D., Peaslee, K.D.: Study of spent refractory waste recycling from metal manufacturers in Missouri. Resour. Conserv. Recycl. **25**(2), 111–124 (1999)
16. Banerjee, S., Schacht, C.A. (eds.): Refractories Handbook. Taylor & Francis Group, Milton Park (2004)
17. Guéguen, E., Hartenstein, J., Fricke-begemann, C.: Raw material challenges in refractory application. In: Proc. Berliner Konf. Miner. Nebenprodukte und Abfaelle (2004), pp. 489–502.
18. European Refractories Producers' and Federation: Refractory ceramics and industrial minerals are critical for european industry, vol. 32. (2009).
19. Horckmans, L., Nielsen, P., Dierckx, P., Ducastel, A.: Recycling of refractory bricks used in basic steelmaking: a review. Resour. Conserv. Recycl. **140**, 297–304 (2019)
20. Fennis, S.A.A.M., Walraven, J.C.: Using particle packing technology for sustainable concrete mixture design. Heron **57**(2), 73–101 (2012)
21. Myhre, B, Hundere, A.M.: The use of particle size distribution in development of refractory castables. In: Proc. XXV ALAFAR Congr. pp. 1–4, (1996).
22. BASF Construction Solutions GmbH: General Information regarding refractory castable application. https://www.dispersions-pigments.basf.com/portal/streamer?fid=823868 (2016). Accessed 29 June 2019. .
23. European Standard: EN 196-1, Methods of testing cement; determination of strength. (1987)
24. Makkonen, H.T.: Tanskanen, Outokumpu Chrome Oy: n Ferrokromikuonan mineralogia ja liukoisuusominaisuudet. University of Oulu (2005).
25. Ortega-Fernández, I., Faik, A., Mani, K., Rodriguez-Aseguinolaza, J., D'Aguanno, B.: Experimental investigation of solid by-product as sensible heat storage material: characterization and corrosion study. AIP Conf. Proc. **1734**(May), 2016 (2016)

Publisher's Note Springer Nature remains neutral with regard to jurisdictional claims in published maps and institutional affiliations.

Affiliations

Marjaana Karhu[1] · Bob Talling[2] · Patrycja Piotrowska[2] · Alba Matas Adams[3] · Abirami Sengottuvelan[4] · Elina Huttunen-Saarivirta[1] · Aldo R. Boccaccini[4] · Pertti Lintunen[1]

[1] VTT Technical Research Centre of Finland Ltd, P.O. Box 1300, 33101 Tampere, Finland

[2] Renotech Oy, Raisionkaari 55, 21200 Raisio, Finland

[3] Imperial College London (UK), Prince Consort Road, London SW7 2BP, UK

[4] FAU Friedrich-Alexander University of Erlangen-Nuremberg, Cauerstr. 6, 91058 Erlangen, Germany